LOW PROFILE, PRINTED CIRCUIT, DUAL-BAND, DUAL-POLARIZED ANTENNA ELEMENTS AND ARRAYS

William Mark Dorsey

Dissertation submitted to the faculty of the Virginia Polytechnic Institute and State University in partial fulfillment of the requirements for the degree of

Doctor of Philosophy

In

Electrical Engineering

Advising Committee
Dr. Amir I. Zaghloul (Chair)
Dr. Gary S. Brown
Dr. William A. Davis
Dr. Scott F. Midkiff
Dr. Pamela Marie Murray-Tuite

April 3, 2009

Falls Church, VA

Keywords: antennas, dual-polarization, dual-band, antenna array, printed circuit antenna, low profile antenna, circularly polarized antennas, multifunction array

LOW PROFILE, PRINTED CIRCUIT, DUAL-BAND, DUAL-POLARIZED ANTENNA ELEMENTS AND ARRAYS

William Mark Dorsey

ABSTRACT

Dual-band antenna elements that support dual-polarization provide ideal performance for applications including space-based platforms, multifunction radar, wireless communications, and personal electronic devices. In many communications and radar applications, a dual-band, dual-polarization antenna array becomes a requirement in order to produce an electronically steerable, directional beam capable of supporting multiple functions. The multiple polarizations and frequency bands allow the array to generate multiple simultaneous beams to support true multifunction radar. Many of the applications in spaced-based systems and personal electronic devices have strict restraints on the size and weight of the antenna element, favoring a low-profile, lightweight device.

The research performed in this dissertation focuses on the design of a dual-band, dual-polarized antenna element capable of operating as an isolated element or in an array environment. The element contains two concentric, dual-polarized radiators. The low band radiator is a shorted square ring antenna, and the high band radiator is a square ring slot. Each constituent element achieves circular polarization through the introduction of triangular perturbations into opposing corners of the radiating element. This technique has been shown to introduce two, near-degenerate modes in the structure that – when excited in phase quadrature – combine to form circular polarization. The perturbations allow circular polarized operation with only a single feed point. The sense of the circular polarization is determined by the location of the feed point with respect to the perturbations. Both senses of circular polarization are excited by the introduction of orthogonal feeds for each of the two radiating elements. Thus, dual-ban, dual-circular polarization is obtained.

The element achieves a low-profile from its printed circuit board realization. The high band square ring slot is realized in stripline. The orthogonal feeding transmission lines are printed on opposing sides of an electrically thin dielectric layer to allow them to cross without physically intersecting. This thin feeding substrate is sandwiched between two dielectric layers of matched dielectric constant. A ground plane is located on the top and bottom of the sandwiched dielectric structure, and the top ground plane contains the square ring slot with perturbed corners. Slotted stripline structures have been shown in

the literature to excite a parallel-plate mode that can degrade overall performance of the antenna. Plated through holes are introduced at the outer perimeter of the square ring slot to short out this parallel-plate mode. The plated through holes (also called vias) serve as the shorting mechanism for the low band microstrip shorted square ring radiator. This element also contains triangular perturbations at opposing corners to excite circular polarization with a single feed point. In this element, orthogonal probe feeds are present to excite both senses of circular polarization.

A dual-band, dual-polarized antenna element was built, tested, and compared to simulations. The constructed element operated at two distinct industrial, scientific, and medical (ISM) frequency bands due to their popularity in low power communications. The antenna element was realized in a multilayer printed circuit layout. A complex design procedure was developed and submitted to a printed circuit board company who manufactured the antenna element. The s-parameters of the antenna were measured using a Network Analyzer, and the results show good agreement with simulations. The radiation and polarization characteristics were measured in a compact range facility. These results also agreed well with simulations. The measured results verify the simulation models that were used in the simulations and establish a confidence level in the feasibility of constructing this element. The dual-band, dual-polarization nature of this element was established through the construction and measurement of this element.

A novel size reduction technique was developed that allows for significant reduction of the element's footprint. This size reduction facilitates the placement of this element within an array environment. The loading technique utilizes a structure analogous to a parallel-plate capacitor to drastically reduce the overall size of the low frequency shorted square ring. The loading structure uses a substrate that is separate from that of the radiating elements. This allows the load to use a high dielectric material to achieve a high capacitance without requiring the radiating elements to be printed on high dielectric material that is potentially expensive and lossy at microwave frequencies.

The two frequency bands were selected to be in separate industrial, scientific, and medical (ISM) bands. These frequency bands are increasingly popular in low power communication devices because unlicensed operation is permitted. The 2.45 GHz and 5.8 GHz ISM bands are commonly used for applications including Bluetooth technology, multiple 801.11 protocol, cellular phone technology, and cordless phones. The ISM bands were chosen for this antenna element due to their popularity, but this antenna is not restricted to these bands. The frequency ratio can be altered by controlling the dielectric constant used in the printed circuit board design, the parameters of the capacitive loading structure, and the size of the constituent elements that are used.

After the size reduction technique is applied, the dual-band, dual-polarized elements can be placed in an array environment resulting in an array capable of generating both senses

of circular polarization in the two, distinct ISM bands. This provides an aperture capable of supporting multiple functions. Depending on the applications required, the frequency bands of the antenna element can be altered to suit the particular system needs.

The array analysis performed in this dissertation used a unique hybrid calculation technique that utilizes nine active element patterns to represent the patterns of the individual elements within a large antenna array. A common first look at array performance is achieved by multiplying the element pattern of an isolated element by an array factor containing the contributions of the geometrical arrangement of the antenna elements. This technique neglects mutual coupling between elements in the array that can alter the impedance match and radiation characteristics of the elements in the array. The active element pattern defines the radiation pattern of a given element in an array when all other elements are terminated in a matched impedance load. The active element pattern is unique for each element in an array. When these patterns are summed, the exact array pattern is obtained. While this technique has the advantage of accuracy, it is not ideal because it requires the simulation, calculation, or measurement of the pattern for each element in the array environment. The technique developed in this dissertation uses only nine active element patterns. These elements are then assigned to represent the active element patterns for all elements in the array depending on the geometrical region where the given element resides. This technique provides a compromise between the speed of using a single element pattern and the accuracy of using the unique active element pattern for each element in the array.

The application of these two concentric, coplanar radiators along with the capacitive loading technique provides a unique contribution to the field of antenna engineering. The majority of dual-band antenna elements in the literature operate with a single polarization in each band. The ones that operate with dual-polarization in each band are typically limited to dual-linear polarization. Circular polarization is preferable to linear in many applications because it allows flexible orientation between the transmitting antenna and receiving antenna in a communications system, while also mitigating multipath effects that lead to signal fading. The ability to operate with two, orthogonal senses of circular polarization allows a system to reuse frequencies and double system capacity without requiring additional bandwidth. The uniqueness of this element lies in its ability to provide dual-circular polarization in two separate frequency bands for an individual element or an antenna array environment. The arrangement of the two element geometries with the addition of the novel capacitive loading technique is also unique. The performance of this element is achieved while maintaining the light weight, low profile design that is critical for many wireless communications applications.

This dissertation provides a detailed description of the operation of this dual-band, dual-polarized antenna element. The design of the constituent elements is discussed for several polarization configurations to establish an understanding of the building blocks

for this element. The dual-band, dual-polarized element is presented in detail to show the impedance match, isolation, and axial ratio performance. The capacitive loading technique is applied to the dual-band, dual-polarized element, and the performance with the loading in place is compared to the performance of the unloaded element. Next, there is an in-depth description of the array calculation technique that was developed to incorporate mutual coupling effects into the array calculations. This technique is then applied to the dual-band, dual-polarized array to show the performance of several array sizes.

ACKNOWLEDGEMENTS

The four years of research presented in the many pages of this dissertation were made possible by the teaching, motivation, and support of many people. Since I devoted countless hours to the remaining 200-plus pages of this dissertation, I felt it was appropriate to dedicate a few more to thank those who – knowingly or not – provided valuable help in one way or another. While I couldn't begin to thank everyone who helped me along the way, I'm going to give it a shot.

I'd like to express many thanks to my advisor, Dr. Amir Zaghloul, who has dedicated countless hours to mentoring, teaching, and guiding me over the last four years. Your assistance and motivation reach far beyond academia, and you made the potentially arduous path to a doctorate degree enjoyable. When I first met with you to discuss what the extended campus program had to offer, I never envisioned all I would get out of it. Your assistance has been invaluable to my academic and professional career. While I am thrilled to have completed my degree, it also represents the end of an extremely enjoyable experience. I certainly hope that we can find other avenues to continue research in the future.

I'd like to thank the U.S. Naval Research Laboratory and the Edison Program for investing in my education and providing me with the time necessary to complete my degree. Mark Parent and Dr. Bruce Danly have permitted me to use the full time available for pursuing my studies even though it meant more time away from work. My co-worker John Valenzi was very helpful in assembling and measuring many of the antenna elements discussed in this dissertation. Dr. Joon Choe and Dr. Eric Mokole provided me with valuable advice that helped me persevere through several obstacles along the way.

I'd like to thank my classmates at the Northern Virginia Campus of Virginia Tech. At a small satellite campus, it was extremely helpful to have a close-knit group of graduate students to study with, seek advice from, and – in some cases – commiserate with. Good luck to you all in the remainder of your studies.

I'd like to extend my thanks and appreciation to the members of my advisory committee – Dr. Gary S. Brown, Dr. William A. Davis, Dr. Scott F. Midkiff, Dr. Pamela Marie Murray-Tuite, and Dr. Steven J. Weiss – for the advice and assistance provided throughout my research. Coordinating exams and presentations between two – and sometimes three – campuses with participants already bogged down with their own obligations is a difficult task. But, you have all been extremely accommodating throughout this process.

I'd like to thank Dr. Kawthar Zaki who served as my advisor at the University of Maryland for both my undergraduate and graduate studies. As an undergrad at Maryland,

I wasn't sure what area of E.E. I was the most interested in. Your teaching helped me find a great interest in Microwave Engineering that eventually led to my interest in antenna design. Thank you for the guidance you provided me during the completion of by B.S. and M.S. in E.E.

I am very lucky to have such a close-knit family that has always been there to provide encouragement and support. I'd like to thank my sisters, Anne and Laura, for tolerating my "adolescent years" as a bratty, troublemaking kid. You probably never imagined I would end up getting a doctorate degree (I know I didn't). Whether you know it or not, you two have served as role models for me over the years, and I've always looked up to you for advice and encouragement.

I have to mention my four wonderful nieces – Samantha, Katie, Natalie, and Allison – and my terrific nephew Henry. The five of you have been an endless source of humor and entertainment that help lighten any stressful times.

I'd like to thank the illustrious *Team 8* – including my brother-in law Jeff and my Dad – for my weekly Tuesday night distraction from the stresses of dissertation writing…even if it does come with the added stress of trying to pick up a ten pin.

To my parents, Bill and Karen Dorsey: Thank you for the endless support and encouragement you have provided me throughout all of my academic pursuits. You have always provided me with a shining example of the hard work, dedication, and discipline that I needed to succeed in all of my academic endeavors. While I may not have always taken things as "serious" as I should, I eventually figured it out (with a little bit of help and guidance)! From long tutoring sessions in Complex Variables, to home cooked meals, to supporting phone calls, to the new suit worn to my defense, you have made all of this possible. I couldn't have asked for more support thank you have given me over the years.

To my wife, Tess: Thank you for the daily encouragement and understanding you have given me. You provided me the time and seclusion I needed to complete this dissertation while somehow always knowing when I needed a distraction to keep my sanity. You always expressed the utmost confidence in me during this process, and you have been an endless source of care and support. I promise…we don't have to keep Antenna Engineering textbooks on the floor in the computer room any more…and I might even have time to change the light bulbs in the laundry room now.

To my beautiful daughter and littlest cheerleader, Angelina: Throughout the countless hours I spent writing this dissertation, your smile served as the most welcome of distractions. The time spent reading Gerald McBoing Boing and The Diggingest Dog, assembling an exersaucer, and changing diapers proved to be the perfect stress-reliever.

With the completion of this dissertation, I look forward to having even more time to spend with you as your grow and learn.

For those who know me well, I'm sure you know that anything I say or write has to tie into sports in one way or another. As I grew up, my father would always tell me stories about Johnny Unitas and the Baltimore Colts' championship teams while we watched football. So, what better athlete to quote than the finest QB to ever step on the field?

When Johnny Unitas was inducted in the Hall of Fame in 1979, he famously said that a "man never gets to this station in life without being helped, aided, shoved, pushed, and prodded to do better." He continued to say that "the players I played with and the coaches I had…they are directly responsible for me being here." While I don't think I will ever have a bronze bust displayed in Canton or Cooperstown, I think the sentiments expressed by the legendary Baltimore quarterback apply to my situation as well. I have been extremely lucky to have professors, mentors, and family who helped, aided, shoved, pushed, and prodded me to completion of my doctorate degree. I guess that in my analogy, you all have served as my Raymond Berry and Lenny Moore, and that's some good company to keep. You all have made this possible. Thank you!

Table of Contents

LIST OF FIGURES

LIST OF TABLES

CHAPTER 1. INTRODUCTION

As the field of wireless communications grows, electronic devices are required to support multiple functions that require communications within multiple, distinct frequency bands. As the requirements for personal wireless devices increases, the desired footprint for the device seemingly decreases. These size restraints make dual-band antenna elements virtually a necessity in order to minimize the number of antenna elements required within the device to conserve valuable real estate. Moreover, personal communications devices operate within restricted frequency bands of the electromagnetic spectrum. An antenna element capable of simultaneously operating with two orthogonal senses of polarization can efficiently use the allotted frequency spectrum by reusing frequencies. This increases the capacity of the system without requiring additional frequency coverage. A dual-band antenna element capable of operating with dual-orthogonal polarization in each frequency band provides invaluable flexibility to a system. Additionally, if this element is realized in printed circuit board technology, it can be made low profile and lightweight while allowing for easy integration with the accompanying electronics in the system and providing affordable manufacturing costs.

Antenna arrays are used to provide highly directional beams that can be scanned electronically. Applications requiring large arrays range from communications, to radar, to target tracking, to electronic warfare (EW). As the number of required functions increases, the number of required potentially large array apertures increases as well. Significant research has been completed to minimize the number of arrays on various platforms. For example, the U.S. Naval Research Laboratory (NRL) carried out the Advanced Multifunction RF System (AMRFS) program to develop a broadband array capable of performing multiple communications, radar, and EW functions in an effort to reduce the number of topside antenna arrays on a U.S. Navy ship [1, 2]. The AMRFS effort was chosen to have broadband, dual-linearly polarized coverage in order to provide adequate frequency coverage for multiple functions. A dual-band, dual-polarized antenna array would also permit one array to carry out a number of functions, thus reducing the number of large arrays required in a system. If the frequency bands were chosen to satisfy multiple needs aboard the ship, a large array of dual-band, dual-polarized antenna elements would reduce the number of expensive – both in money and real estate – on the ship.

The research performed in this dissertation is aimed at designing a dual-band, dual-polarized antenna element that can operate as an isolated element as well as in an array environment. The element achieves a low profile from its printed circuit board realization and contains two concentric, coplanar, dual-polarized radiators. The low band radiator is a shorted square ring antenna, and the high band radiator is a square ring slot. A novel size reduction technique was developed that allows for significant reduction of the element's footprint by introducing a large

capacitive effect into the low band element. This size reduction facilitates the placement of the element within an array environment. The design discussed in this dissertation uses frequencies contained in separate industrial, scientific, and medical (ISM) bands. These frequency bands are increasingly popular in low power communication devices because unlicensed operation is permitted. These bands were chosen due to their popularity, but this antenna is not restricted to these bands. The element is shown to have extreme flexibility in the selection of the ratio between the high and low band frequencies.

The research for the design of this element dates back to the late 1980s when Sorbello and Zaghloul completed research on introducing perturbations to the corners of square ring slot antennas to produce single-feed circular polarization [3]. Their work discussed the addition of orthogonal feed lines to generate dual-linear or dual-circular polarization from a square ring slot in an array environment, and it received a patent in 1996 [4]. Ravipati, Kawser, and Zaghloul discussed a dual-band antenna element in 1994 that was suitable for wide-angle scanning in a phase array environment [5]. This element was a hybrid of micorstrip and waveguide radiators that involved the placement of an open-ended waveguide inside of the shorted region of a shorted annular ring antenna. Their element was capable of operating with dual-linear polarization in each of the two frequency bands, but was unable to use dual-circular polarization. The presence of the waveguide radiator increased the profile, and weight of the design while providing a difficult to design to include in an array.

In 2007, Dorsey and Zaghloul combined the two previously mentioned elements by placing a square ring slot in the center of a shorted square ring antenna element [6]. This element used a size reduction technique designed by Dorsey and Zaghloul [7, 8] to reduce the size of the element and allow for wider frequency ratios than the design presented in [5]. In order to accurately analyze the performance of this complex element in an array environment, Dorsey derived an array analysis approach that uses multiple active element patterns to approximate the exact active element pattern for elements in given geometrical regions within the array [9].

This dissertation discusses the development of a dual-band antenna element capable of operating with dual-polarization in each frequency band. A thorough description of the constituent element design is presented. In many cases, antenna elements were built and tested to validate the computational tools and techniques that were used in the design process. After establishing a firm understanding in the operation of the shorted square ring and square ring slot elements, the constituent elements were then combined in a unique way to form a complex element capable of providing flexible, dual-band, dual-polarized operation. A dual-band, dual-CP antenna element operating at two ISM frequency bands was built, tested, and compared to simulated results. The s-parameters of the four port antenna were measured with a Network Analyzer, and the polarization characteristics were confirmed in a compact range facility. The measured results agree well with the simulations, thus verifying the operation and functionality of the dual-band, dual-CP antenna element design. The ability to show agreement between the simulations and measurements establishes the validity of the simulation models used in this dissertation.

Additionally, the ability to generate dual-CP in the two frequency bands of the dual-band antenna element was proven and realized in a low-profile, printed circuit design.

The element can be used in a multifunction phased array requiring wide scanning performance once a size reduction technique is added to reduce the footprint of the element. The array analysis approach is detailed, and the element is shown to provide excellent array performance.

The remainder of this section introduces the electromagnetic concepts that are critical in the design and analysis of the dual-band, dual-polarized antenna element. The concept of polarization for electromagnetic waves is discussed to establish some key parameters and terms that will be used throughout the remainder of the dissertation. This discussion is followed by a definition of parameters that are used to characterize dual-polarized electromagnetic systems. These parameters will be used in later sections to analyze the performance of the dual-band, dual-polarized antenna element and array. Printed circuit antennas are introduced to show the advantages of using the ever-advancing technology to facilitate antenna design. A survey of existing dual-band, dual-polarized antenna elements from the literature is provided. These elements serve as a point of comparison for the element detailed in this dissertation. An introduction to antenna arrays and their analysis is provided to introduce key concepts that will be used in Chapter 4. Finally, there is a discussion of the computational electromagnetic (CEM) tools that exist for use in antenna design.

1.1 Discussion on Polarization

Electromagnetic fields are functions of both time and space that are composed of electric and magnetic fields. The electric and magnetic fields are related through Maxwell's equations shown in (1-1)-(1-4). The six field quantities used in Maxwell's equations are the electric intensity (**E**), magnetic intensity (**H**), electric flux density (**D**), magnetic flux density (**B**), electric current density (**J**), and the electric charge density (Q_v). The bolded font indicates vector quantities. In addition to satisfying Maxwell's equations, electromagnetic fields also satisfy the wave equation (1-5)-(1-6), where k is the wave number of the medium as defined in (1-7).

$$\nabla \times \boldsymbol{E} = -j\omega \boldsymbol{B} \quad \textbf{(1-1)}$$

$$\nabla \times \boldsymbol{H} = j\omega \boldsymbol{B} + \boldsymbol{J} \quad \textbf{(1-2)}$$

$$\nabla \cdot \boldsymbol{B} = 0 \quad \textbf{(1-3)}$$

$$\nabla \cdot \boldsymbol{D} = Q_v \quad \textbf{(1-4)}$$

$$\nabla \times \nabla \times \boldsymbol{E} - k^2 \boldsymbol{E} = \boldsymbol{0} \quad \textbf{(1-5)}$$

$$\nabla \times \nabla \times \boldsymbol{H} - k^2 \boldsymbol{H} = \boldsymbol{0} \quad \textbf{(1-6)}$$

$$k = \frac{2\pi}{\lambda} \quad \textbf{(1-7)}$$

The wave equation can be written in another form by applying the identity shown in (1-8). In a source free medium, the divergence of the electric and magnetic fields is zero according to (1-3) and (1-4). As a result, the wave equations in (1-5) and (1-6) can be written in the form shown in (1-9) and (1-10). These equations are called the vector wave equation [10, 11]. Equations (1-9) and (1-10) coupled with (1-3) and (1-4) are equivalent to (1-5) and (1-6). The rectangular components of **E** and **H** satisfy the scalar wave equation (1-11), commonly referred to as the Helmholtz equation [10].

$$\nabla^2 \boldsymbol{A} = \nabla(\nabla \cdot \boldsymbol{A}) - \nabla \times \nabla \times \boldsymbol{A} \quad \textbf{(1-8)}$$

$$\nabla^2 \boldsymbol{E} + k^2 \boldsymbol{E} = 0 \quad \textbf{(1-9)}$$

$$\nabla^2 \boldsymbol{H} + k^2 \boldsymbol{H} = 0 \quad \textbf{(1-10)}$$

$$\nabla^2 \psi + k^2 \psi = 0 \quad \textbf{(1-11)}$$

A plane wave is a solution to the wave equation where the phase of the electric and magnetic fields is constant over a set of planes. For this discussion, we will focus on plane waves that travel in the z-direction. If there are no materials in the vicinity of the propagation path to act as a guide, the wave will be a transverse wave [12]. This means that the electric and magnetic fields are perpendicular to each other and the direction of propagation. The direction of the electric and magnetic fields can change with respect to time, but they remain perpendicular to each other and to the direction of propagation. The behavior of the instantaneous electric field vector with respect to time at a given point in space is referred to as the *polarization* of the wave.

An instantaneous transverse electric field traveling in the z-direction can be decomposed into a summation of orthogonally polarized components. E_1 and E_2 are the amplitudes of the instantaneous electric field in the x,y directions (real numbers), ω is the radian frequency, β is the phase constant, and δ is the phase by which the y component leads the x (phase angle).

$$\boldsymbol{E}(t,z) = \hat{x}E_x(t,z) + \hat{y}E_y(t,z) \quad \textbf{(1-12)}$$

$$E_x(t,z) = E_1 cos(\omega t - \beta z) \quad \textbf{(1-13)}$$

$$E_y = E_2 cos(\omega t - \beta z + \delta) \quad \textbf{(1-14)}$$

If there is no y-component (i.e. E_2=0), the wave is linearly polarized in the x-direction. This polarization is often referred to as "horizontal" polarization implying that the electric field is parallel to the horizon. Similarly, if there is no x-component (i.e. E_1=0), the wave is y-polarized (commonly referred to as vertically polarized). If the phase angle is equal to zero, the electric field can be linearly polarized in an arbitrary direction determined by the tilt angle, τ. The electric field for an arbitrary polarization is defined in (1-15), and the tilt angle for linear polarizations is defined in (1-16).

$$\boldsymbol{E}(t) = (\hat{x}E_1 + \hat{y}E_2)cos(\omega t) \quad \textbf{(1-15)}$$

$$\tau = tan^{-1}\frac{E_2}{E_1} \quad \textbf{(1-16)}$$

If the phase angle is ±90°, the orthogonal field components are in phase quadrature resulting in elliptical polarization. If the phase angle is +90 degrees, the polarization is left-hand elliptical polarization (LHEP). The electric field rotates in the direction of the curl of the fingers on the left hand when the thumb points in the direction of propagation. Conversely, right-hand elliptical polarization (RHEP) results when the phase angle is -90 degrees. This is illustrated in Figure 1-1. The electric field vector is plotted at multiple instants in time. From this figure it is evident that the tip of the instantaneous electric field vector traces an elliptical shape. Moreover, the field vector rotates counter-clockwise, resulting in LHEP. Circular polarization (CP) results when the x- and y-field components are in phase quadrature and have equal magnitude. The wave is right-hand circularly polarized (RHCP) when δ=+90° and left-hand circularly polarized (LHCP) when δ=-90° for the same arguments made for elliptical polarization.

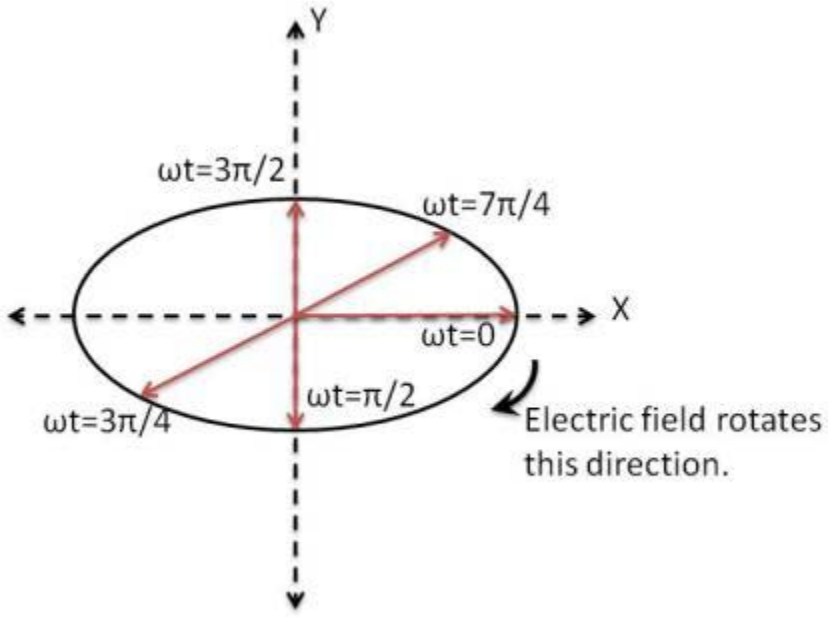

Figure 1-1: Illustration of the electric field vector rotation for left-hand elliptical polarization (LHEP)

The axial ratio defines the ratio between the major and minor axis lengths of the polarization ellipse, and thus it quantifies the shape of the ellipse. Elliptically polarized waves are viewed as having two degrees of freedom: ellipticity is defined by the axial ratio, and the polarization of the ellipse is defined by the tilt angle [13]. The polarization ellipse for an elliptical polarization is shown in Figure 1-2 with the pertinent polarization parameters defined. When the axial ratio is at its minimum value of 1, the polarization ellipse becomes a circle. As the axial ratio tends

towards infinity, the polarization approaches perfect linear polarization in the direction of the tilt angle.

$$|R| = \frac{major\ axis\ length}{minor\ axis\ length} = \frac{E_{max}}{E_{min}} = \frac{OA}{OB} \geq 1 \quad \textbf{(1-17)}$$

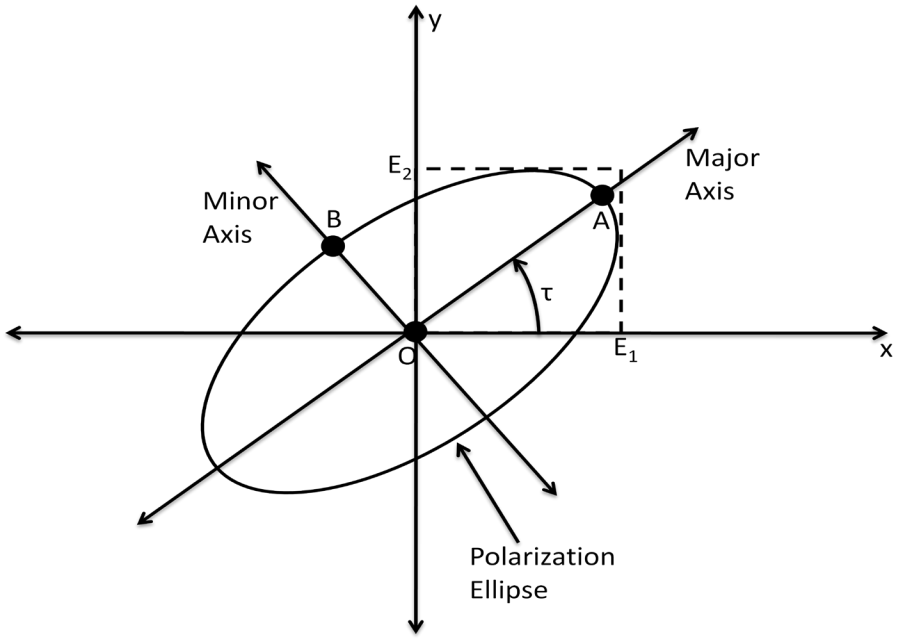

Figure 1-2: Polarization ellipse showing tilt angle, axial ratio, major axis, and minor axis

Polarization states are orthogonal if one state contains no component of the other. For example, horizontal and vertical polarization states are orthogonal. Linear polarization states with tilt angles (ξ) and ($\xi \pm \pi/2$) are also orthogonal. Additionally, RHCP and LHCP are orthogonal polarizations. Two arbitrary polarization states are orthogonal if (1-18) is satisfied. In antenna measurements, copolarized and cross-polarized states are defined. Typically, the copolarized state is defined as the "intended" polarization state, and the cross-polarized state is the state orthogonal to the copolarized state. The co- and cross-polarized antenna patterns are defined as (1-19) and (1-20) respectively, where $\hat{e}_{co}$ and $\hat{e}_{cr}$ are the co- and cross-polarized unit vectors. As an example, the copolarized and cross-polarized unit vectors for LHCP are defined in (1-21) and (1-22). These two unit vectors satisfy (1-18).

$$\hat{e}_A \cdot \hat{e}_A^{ortho} = 0 \quad \textbf{(1-18)}$$

$$F_{co}(\theta, \varphi) = \bar{E}(\theta, \varphi) \cdot \hat{e}_{co} \quad \textbf{(1-19)}$$

$$F_{cr}(\theta, \varphi) = \bar{E}(\theta, \varphi) \cdot \hat{e}_{cr} \quad \textbf{(1-20)}$$

$$\hat{e}_{co}^{LHCP} = \frac{1}{\sqrt{2}}\left[(sin\varphi - jcos\varphi)\hat{\theta} + (cos\varphi + jsin\varphi)\hat{\varphi}\right] \quad \textbf{(1-21)}$$

$$\hat{e}_{cr}^{LHCP} = \frac{1}{\sqrt{2}}\left[(sin\varphi + jcos\varphi)\hat{\theta} + (cos\varphi - jsin\varphi)\hat{\varphi}\right] \quad \textbf{(1-22)}$$

1.2 Definition of Terms Used in Analyzing Dual-Polarized System Performance

A thorough discussion of common quantities used to evaluate the performance of dual-polarized systems is provided in [12], and the discussion in this section follows from the work detailed by Stutzman.

Any electromagnetic wave can be decomposed into the sum of two orthogonal polarization states satisfying (1-18). In dual-polarized systems, these two states are commonly referred to as the *copolarized* and *cross-polarized* state. The *copolarized* component typically refers to the state that is closest to the "desired" polarization in the system.

An electromagnetic wave propagating in polarization state *w* can be decomposed into a sum of the *copolarized* and *cross-polarized* components as shown in (1-23). In (1-23), the subscript *co* refers to the *copolarized* state, the subscript *cr* refers to the *cross-polarized* state, and the subscript *w* denotes the *w-polarized* vector.

$$\overline{E}_w = E_{co}\hat{e}_{co} + E_{cr}\hat{e}_{cr} \quad \textbf{(1-23)}$$

The *cross-polarization ratio* (CPR) defines the ratio of the power density in the *cross-polarized* component to that in the *copolarized* component.

$$CPR = \frac{S_{cr}}{S_{co}} = \frac{\left|E_{cr}\right|^2}{\left|E_{co}\right|^2} \quad \textbf{(1-24)}$$

In elliptically polarized (EP) electromagnetic waves, the CPR is defined as the ratio of the linear components along the principle axes. Therefore, the CPS is related to the axial ratio for polarization state *w* as shown in (1-25).

$$CPR = \left[\frac{E_{\min or}}{E_{major}}\right]^2 = \frac{1}{\left|R_w\right|^2} \quad \textbf{(1-25)}$$

The EP wave can be decomposed into two CP components. In this case, the CPR_c (where the subscript *c* denoted circular polarization), is defined as (1-26) where *R* is the wave axial ratio.

$$CPR_c = \left[\frac{|R|-1}{|R|+1}\right]^2 \quad \textbf{(1-26)}$$

In system applications, it is sometimes more convenient to define a *Cross-Polarization Isolation* (XPI). XPI is the ratio of the "wanted" power level to the "unwanted" power level in the same

channel when the transmitting antenna is radiating nominally orthogonally polarized signals of the same frequency and power level. A related quantity is the *Cross-Polarization Discrimination* (XPD), which defines the ratio of the signal level at the output of a receiving antenna that is nominally copolarized to the transmitting antenna to the output of a receiving antenna that is the same gain but nominally orthogonally polarized to the transmitter. A general expression for XPD is provided in (1-27). In antenna states that are near CP, XPD can be approximated by (1-28). In these expressions, τ refers to the tilt angle for the polarization.

$$XPD = \frac{R_{cr}^2 + 1}{R_{co}^2 + 1} \bullet \frac{\left(R_{co}^2 + 1\right)\left(R_w^2 + 1\right) + 4R_{co}R_w + \left(R_{co}^2 - 1\right)\left(R_w^2 - 1\right)\cos\left(2\Delta\tau_{co}\right)}{\left(R_{cr}^2 + 1\right)\left(R_w^2 + 1\right) + 4R_{cr}R_w + \left(R_{cr}^2 - 1\right)\left(R_w^2 - 1\right)\cos\left(2\Delta\tau_{cr}\right)} \quad \textbf{(1-27)}$$

$$XPD \approx \frac{R_{cr}^2 + 1}{R_{co}^2 + 1} \bullet \frac{\left(R_{co}^2 + 1\right)\left(R_w^2 + 1\right) + 4R_{co}R_w}{\left(R_{cr}^2 + 1\right)\left(R_w^2 + 1\right) + 4R_{cr}R_w + \left(R_{cr}^2 - 1\right)\left(R_w^2 - 1\right)\cos\left(2\Delta\tau_{cr}\right)} \quad \textbf{(1-28)}$$

If the incoming wave has perfect circular polarization, XPD becomes independent of the tilt angle. In this case, the XPD is related to the axial ratio as defined in (1-29). In this case, the XPD is also related to the *cross-polarized ratio* for the circular polarized wave (CPR_c) as shown in (1-30). XPD is plotted as a function of axial ratio in Figure 1-3. This figure shows that as the axial ratio approaches unity (0dB), the XPD tends towards infinity.

$$XPD = \left[\frac{|R_{co}| + 1}{|R_{co}| - 1}\right]^2 \quad \textbf{(1-29)}$$

$$XPD = \frac{1}{CPR_c} \quad \textbf{(1-30)}$$

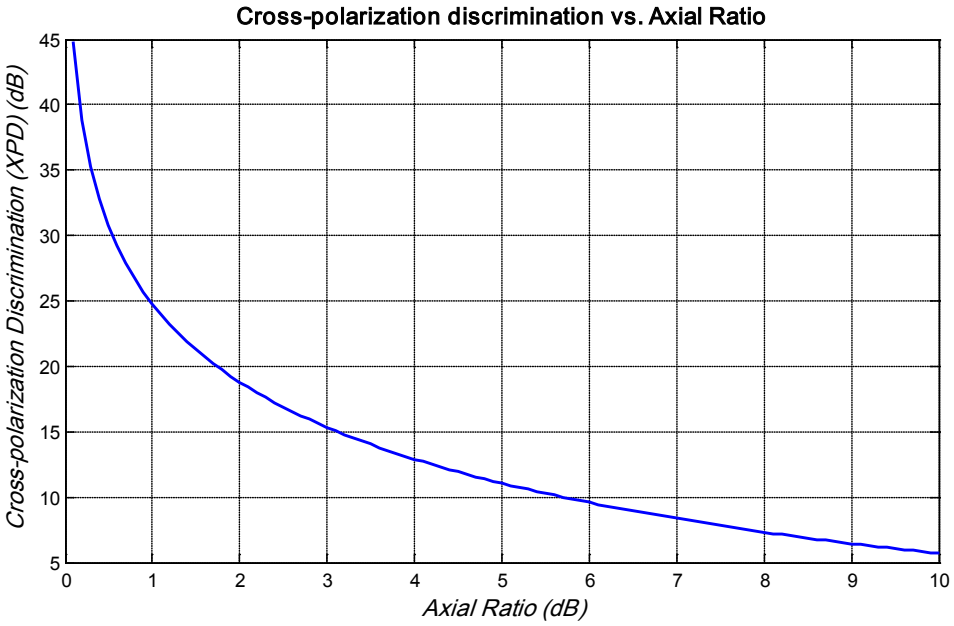

Figure 1-3: Cross-polarization discrimination (XPD) as a function of axial ratio

The parameters defined in this section will be used to characterize the performance of the dual-band, dual-CP antenna array discussed later in this dissertation.

1.3 Introduction to Printed Circuit Antenna Elements

Many RF applications place a size and weight restriction on the antenna. For instance, a payload that is to be deployed on a satellite has a restricted overall mass and volume [14]. Thus, a lighter antenna leaves more weight available for pertinent electronics on the payload. Another example stems from the ever-advancing technology in the field of cellular communications. With the increased popularity of compact cellular handsets and portable satellite communication devices, the antenna needs to be able to easily integrate with the accompanying circuitry in the device. Additional restraints on the antenna size have resulted from the need for antenna diversity, which requires the placement of multiple antennas within a single handset. A printed circuit realization is ideal for wireless applications due to low profile, simple fabrication, low cost, and compatibility with integrated circuits [15]. Printed circuit antennas are also gaining increase popularity because they provide a low cost method of producing high volume of devices with tight tolerances [16].

The use of printed circuit technology is not without drawbacks. The power handling capability is limited by the loss tangent of the dielectric, limitation of current in narrow conductors, and high field strengths associated with sharp edges of etched conducting tracks. The performance can vary due to tolerances in material properties, etching tolerances, and errors in registration between faces of a multi-layer structure. Most personal wireless devices operate at low to medium power levels reducing the significance of the power handling limitations. [16]

Printed circuit boards consist of conducting layers separated by dielectric substrates. The thickness of the conducting layers is determined by the weight of copper per square foot that is deposited onto the substrate layer. The electrical properties (ε_r, tanδ) and height of the substrate (h) depend on the material that is used.

Printed circuit antennas are typically fed by a planar microwave transmission line. Three commonly used transmission lines are shown are illustrated in Figure 1-4. Stripline circuits consist of a conductor of width *w* sandwiched between two ground plane layers, while a microstrip circuit consists of a conductor of width *w* and a single ground plane layer. Stripline circuits have minimal leakage, thus minimizing losses that can occur via radiation. The center conductor in a stripline circuit is immersed in a uniform dielectric medium which allows it to support a transverse electromagnetic (TEM) propagation mode. This is ideal because this mode has a lower attenuation than the transverse modes supported in microstrip circuits. Despite these advantages, microstrip is more widely used than stripline due largely to convenience. The feed line is easily accessible because it is not buried inside of a dielectric layer. This makes installation of a connector simpler. It is also more convenient to construct microstrip circuits because they require a single dielectric layer. Stripline circuits require two microwave substrates (one above the feed line and one below) to be etched and bonded together, whereas a microstrip circuit requires only a single layer. [17]

In microstrip and stripline circuits, the ground plane and the feeding conductor are separated by a microwave substrate. This causes significant energy to be coupled into the substrate resulting in loss due to the dissipative nature of the material. Coplanar waveguide consists of three conductors printed on the top side of a microwave substrate. The center conductor (width *s*) is printed in between two ground traces. The ground traces are separated from the center conductor by a distance *w*. [17]

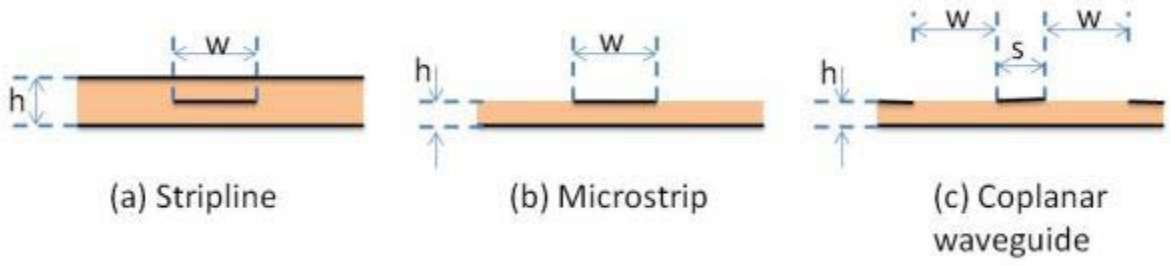

Figure 1-4: Illustration of common planar microwave transmission lines

The impedance of the microwave transmission lines is controlled by the height of the substrate and width of the conductors. In printed circuit antenna design, the impedance of the feeding transmission line is chosen to match the input impedance of the antenna to minimize the reflection coefficient. The most common printed antenna is a microstrip patch antenna due to its broadside radiation pattern and simplicity of construction. However, the ever-advancing field of wireless antennas has placed size, shape, and weight restrictions on the antenna while increasing

the technological requirements. The increased restrictions resulted in the need for new antenna designs that can meet the specifications required for the system while conforming to the available space.

1.4 Discussion on Dual-Polarized, Dual-Band Antenna Elements and Arrays

Antennas capable of operating at multiple frequency bands are advantageous to many applications ranging from space-based radar to personal wireless communications. Synthetic aperture radar (SAR) typically operates in L- and C-bands [18]. For space-based SAR applications where minimizing the mass and weight of the radar system is essential to reducing the overall weight of the payload and cost of the mission, antennas capable of operating in multiple frequency bands with multiple polarizations are beneficial [14]. Dual-band antenna elements are also desirable in radar applications because of their ability to improve data collection rates [19, 20] while also allowing for true multifunction radar (MFR) operation [21].

Wireless communications networks have shown an increased number of subscribers as well as an increased demand for multi-band equipment [22]. Wireless access points and laptops are both turning towards antennas capable of operating in multiple frequency bands in order to support multiple protocol [23, 24]. The 2.45 GHz ISM band is quickly growing in popularity for wireless communications devices due to its use in Bluetooth technology and 802.11b/g protocol. For higher data rates, the frequency band from 5.15-5.85 GHz is often used, and the 802.11a protocol operates within the 5.2GHz ISM band [24]. Moreover, the cell phone industry is incorporating multi-band antennas into handsets to reduce the number of antennas required to provide operation for different services [25].

Dual-band and dual-polarized antennas have gained increasing popularity in the literature. These element architectures can typically be placed into two categories: 1) a single element with a wide operational bandwidth capable of covering multiple bands or 2) an element comprised of two separate radiators, each of which is optimized for a specific frequency band [21]. The majority of the work done on dual-band elements focuses on elements that operate with a single polarization state in each frequency band. There is some work that focuses on dual-band elements capable of supporting dual-linear operation at each band, and a minimal amount of work detailing dual-CP operation at each band. Granholm performed extensive work on dual-band, dual-polarized antenna elements, but his work in [20] dealt with a dual-band element capable of operating with dual-linear polarization in each band.

Circular polarized (CP) antennas are popular choices in wireless communications applications owing to their ability to allow flexible orientation in the plane of the transmitter and receiver antennas and to reduce multipath effects that can lead to signal fading [26-28]. The ability to operate with both senses of CP (RHCP and LHCP) allows frequency reuse to double system capacity [27]. In two-way data link systems, information is often transmitted by means of polarization shift keying, a technique that utilizes orthogonal senses of CP [27]. There has been limited work presented in the literature dealing with elements capable of simultaneously

operating with orthogonal senses of CP. For example, Jefferson and Smith [29] discuss a nearly square microstrip patch element utilizing orthogonal feed locations to simultaneously generate right hand CP (RHCP) and left hand CP (LHCP). This element operates over a single frequency band. Another dual-CP antenna is presented by Sharma and Mital [30, 31]. This element provides dual-CP operation with a diamond shaped patch with a diagonal slot. The element has a coupled feed using dumbbell shaped apertures, and it provides an axial ratio bandwidth of 20.4%. However, the operation is limited to a single frequency band. Aloni presents a dual-CP microstrip patch fed with crossing slots [32] that provides an even wider bandwidth than that presented by Sharma and Mital. However, it has the same limitation of operating over a single frequency band. The work presented in this dissertation will show the development and analysis of a dual-band element capable of simultaneously generating dual-CP in each frequency band.

Microstrip patch antennas using the reactive stub loading has been shown to provide dual-band operation [33]. However, each frequency band for this element operates with the same sense of linear polarization. If multiple feed locations and stubs are used, dual-linear polarization is possible. This type of elements has been shown to provide limited control of the frequency ratio between the two operational bands [14].

An annular ring patch radiator is capable of providing CP behavior at two separate frequency bands [34]. When this type of element is operated in CP, the magnetic currents flow clockwise around the ring slot in a given frequency band, but they will flow counterclockwise at another frequency band. This behavior provides dual-band behavior, but each band only operates with a single sense of CP. There is also limited control over the ratio of frequencies for the two bands.

The cell phone industry has led to the design of several dual-band antennas. Liu and Gaucher present a design capable of covering multiple frequency bands for cellular and WLAN applications [24]. This element uses a combination of inverted-F and L-shaped radiators to cover the multiple bands. Lindmark published a dual-band antenna capable of covering GSM and DCS frequency bands consisting of an aperture coupled stacked patch design [22]. Jeon and Park discuss a triangular shaped patch employing a U-shaped slot and L-shaped feed in order to provide a wide bandwidth capable of covering the PCS and IMT-2000 frequency bands [35]. In each of these elements, the given frequency bands operate with only a single sense of linear polarization.

Many of the dual-band elements with CP polarization require complex feed networks consisting of diplexers and hybrids. Helms, *et al* patented a design for a dual-band stacked patch design where each band operates with a single sense of CP [36]. In this design, the outputs of a 90°-hybrid feed orthogonal locations on the element to generate CP. Lee *et al* earned a patent for a wideband element capable of operating with linear, CP, dual-linear, or dual-CP polarization [37]. The possible polarization states in this element depend on the configuration of a complex feed network consisting of 90° and 180° hybrids. The dual-band element patented by Cha et al provides linear or CP operation with a hybrid feeding network [38].

Antenna arrays are used in applications requiring a highly directional beam with electronic steering capability. Phased arrays can also be used to produce several beams simultaneously, thus allowing one aperture to perform multiple functions. For example, the U.S. Naval Research Laboratory developed the Advanced Multifunction RF System (AMRFS), a system capable of performing multiple radar, communications, and electronic warfare (EW) functions simultaneously [1, 2]. In AMRFS, a broadband antenna element was used to cover the necessary bands for the multiple functions. However, a dual-band dual-polarized antenna could also be beneficial in such a system. The two bands could be selected to cover the operational frequencies of several necessary functions, and the element could operate with orthogonal polarizations simultaneously in each band to further enhance the capabilities of the array.

Dual-band radiating apertures are often achieved by interleaving elements of different sizes, where each type of element has its own array lattice structure. These types of element arrangements are discussed in [4, 19, 21]. In some instances, this is achieved by using perforated patches that enable a series of smaller elements to be placed within holes in the larger, low band elements [18]. Although these publications deal with dual-band apertures, the elements used in the design are inherently single band. The dual-band nature of these apertures stems from the arrangement of single band elements on different lattice structures.

1.5 Introduction to Antenna Arrays

Many individual antenna elements can be arranged into an array to produce a directional antenna pattern. A single, large antenna element (i.e. parabolic reflector) can be used in applications requiring a directional beam. However, using large antennas provides mechanical challenges, and the antenna must be mechanically rotated if the main beam needs to be scanned. An antenna array eliminates the need to physically rotate the array. The excitation of each of the constituent elements can be controlled to electronically scan the main beam. Advancements in the field of solid-state technology have made it possible to realize the complex feed network required to control the excitation of the elements in the array at a reasonable cost [39].

A linear array of elements provides the ability to scan the main beam the plane containing the elements. Multidimensional arrays are typically used for high gain applications requiring scanning of the main beam in an arbitrary direction. The elements in the array are typically spaced in a regular lattice structure. In a rectangular lattice the elements are arranged with spacing Δx and Δy in the principle planes of the array. Another common array lattice used a triangular spacing between elements.

The radiation pattern of the antenna array is calculated from the superposition of the contribution of the elements in the array. The general expression for calculating this expression is shown in (1-31). In this expression $F(\theta, \varphi)$ is the array pattern, I_{mn} is a complex number representing the amplitude and phase excitation of element mn, $g_{mn}(\theta, \varphi)$ is the element pattern of element mn,

and $e^{j\beta\hat{r}\cdot\boldsymbol{r}_{mn}}$ represents the phase weighting given to element *mn* due to its geometrical location in the array. In the exponential term in (1-31), $\hat{r}$ is the unit vector in the direction of the observation angle, $\boldsymbol{r}_{mn}$ is the vector from the center of the array to the element location, α_{mn} is the phase shift at element *mn* used for scanning the mean beam, and $\beta = \omega\sqrt{\mu\varepsilon}$ is the real valued phase constant.

$$F(\theta,\varphi) = \sum_{m=1}^{N_y}\sum_{n=1}^{N_x} I_{mn} g_{mn}(\theta,\varphi) e^{j\beta\hat{r}\cdot\boldsymbol{r}_{mn}+\alpha_{mn}} \quad \textbf{(1-31)}$$

In many array applications, the elements within the array have identical element patterns. If that is the case, (1-31) can be simplified to (1-32). This expression shows that, when the elements within the array are identical, the array pattern can be factored into the product of the element pattern and the array factor $f(\theta,\varphi)$, where the array factor takes the form of (1-33). The array factor can be viewed as the radiation pattern of the array when all elements are replaced with an isotropic radiator (i.e. $g(\theta,\varphi) = 1$). The resulting array pattern will consist of a main lobe pointed in the direction of maximum radiation and many sidelobes. The ability of the array to concentrate power is often characterized by the sidelobe level (SLL) of the array. The SLL is calculated by taking the ratio of the maximum value of the pattern magnitude to the maximum value of the highest sidelobe peak. The half-power beamwidth of the array refers to the angular separation between the points where the main lobe is at half of its maximum value. [39]

$$F(\theta,\varphi) = g(\theta,\varphi)\sum_{m=1}^{N_y}\sum_{n=1}^{N_x} I_{mn}\, e^{j\beta\hat{r}\cdot\boldsymbol{r}_{mn}+\alpha_{mn}} \quad \textbf{(1-32)}$$

$$f(\theta,\varphi) = \sum_{m=1}^{N_y}\sum_{n=1}^{N_x} I_{mn}\, e^{j\beta\hat{r}\cdot\boldsymbol{r}_{mn}} \quad \textbf{(1-33)}$$

The main beam of the array pattern in (1-32) can be scanned to an arbitrary (θ_0, φ_0) location by using the phase shift defined in (1-34). Additional main lobes appear in the visible region of the array factor if the spacing becomes larger than a half-wavelength. The grating lobe-free region of the array is limited to scan angles less than θ_0, where is determined from the element spacing (*d*) using (1-35).

$$\alpha_{mn} = -\beta(x_{mn}sin\theta_0 cos\varphi_0 + y_{mn}sin\theta_0 sin\varphi_0) \quad \textbf{(1-34)}$$

$$\theta_0 < sin^{-1}\left(\frac{\lambda}{d} - 1\right) \quad \textbf{(1-35)}$$

The array factor for a 10 element array of elements is plotted in Figure 1-5 for three beam locations: θ_0=0°, θ_0=30°, and θ_0=60°. The element spacing in this array is 0.58λ, so grating lobes are expected for scan angles greater than 46°. This is reflected in the pattern plot in Figure 1-5 for θ_0=60°. The main beam is located at θ=-60°, and a grating lobe is present near θ_0=60°. The θ_0=0° and θ_0=30° cases show no grating lobes.

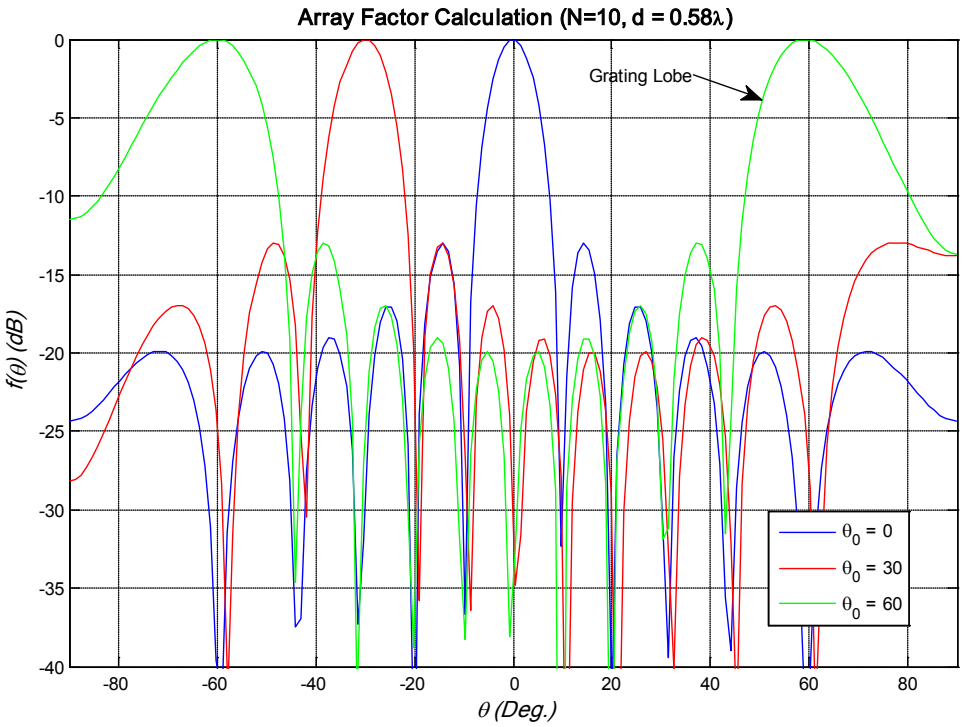

Figure 1-5: Array pattern for 10-element array with 0.58λ spacing

In high performance arrays requiring precise determination of the current distribution across the element in the array, it is important to include the effects of the coupling between elements in the array. The mutual coupling between elements in the array can change the impedance of the array element. In an n-element array, the terminal voltages and currents are related as shown in (1-36). In this expression, V_m is the impressed voltage on element *m*, I_m is the current flowing on element *m*, Z_{mm} is the self-impedance of element *m*, and Z_{nm} is the mutual impedance between element *n* and element *m*. The feed network in an array should be designed to match the input impedance of each element rather than the self-impedance. The input impedance is defined in (1-37). [40]

$$\begin{aligned} V_1 &= I_1 Z_{11} + I_2 Z_{21} + \cdots + I_n Z_{n1} \\ V_2 &= I_1 Z_{12} + I_2 Z_{22} + \cdots + I_n Z_{n2} \\ &\vdots \\ V_n &= I_1 Z_{1n} + I_2 Z_{2n} + \cdots + I_n Z_{nn} \end{aligned} \tag{1-36}$$

$$Z_1^{input} = \frac{V_1}{I_1} = Z_{11} + \frac{I_2}{I_1} Z_{12} + \cdots + \frac{I_n}{I_1} Z_{1n} \tag{1-37}$$

Mutual coupling between elements in an array impacts the radiation pattern as well as the impedance. An accurate representation of the array pattern will include the variations in the excitation currents that result from mutual coupling. The exact element pattern can be calculated

by using the active element pattern for each individual element in (1-31). The active element pattern for element *m* is obtained by exciting element m with all other elements terminated in the generator impedance. In an array with N elements, all N active element patterns are unique. Thus, each active element needs to be simulated or calculated. Evaluating the active element pattern for every element in a large array is a difficult task. As a result, approximations are typically used. The array analysis in this dissertation makes use of a hybrid technique using multiple active element patterns to represent elements in several regions within the array. A comprehensive description of this technique is provided in later sections of this dissertation.

1.6 Introduction to Antenna Analysis Tools

The advancement of computational electromagnetics (CEM) has provided the antenna engineer with a wide array of tools to aid in the design of complex radiating structures. CEM methods fall into one of two categories. Full-wave analysis tools provide an exact solution to Maxwell's equations. The second category of simulation tools applies physically justifiable assumptions to arrive at approximate solutions.[41]

The CEM tools available to antenna engineers can be divided into time domain (TD) and frequency domain (FD) solvers. The TD techniques consist of the Finite Integration Technique (FIT), Finite Difference-Time Domain (FD-TD), Time Domain-Integral Equation (TD-IE), Time-Domain-Finite Element (TD-FE), among other – less frequently used – techniques. The majority of the TD solvers use the point form of Maxwell's equations. These equations are a set of first order, coupled partial differential equations (PDEs) as shown in (1-37)-(1-40).

The FD solvers consist of the Finite Element Method (FEM) and the Method of Moments (MoM). FEM solves Maxwell's equations by solving the vector wave equation. FEM can be used to solve antenna problems consisting of only conducting bodies, but MoM is more efficient for these problems. One of the most popular commercially available CEM package employing a FD solver is Ansoft HFSS.

The simulation work in this report was performed using CST Microwave Studio [42], a commercially available electromagnetic simulation tool. CST Microwave Studio employs the Finite Integration Technique (FIT) which was introduced by Weiland in 1977 [43]. The traditional finite difference time domain (FDTD) technique solves electromagnetic problems by discretizing the differential form of Maxwell's Equations. Ampere's Law (1-38), Faraday's Law (1-39), and the two divergence equations (1-40), (1-41) are shown below. In linear, isotropic, time-invariant, non-dispersive media, (1-38) and (1-39) can be re-written as (1-42) and (1-43) respectively. These equations can be combined to form a hyperbolic system of coupled partial differential equations (PDEs) that are first order in space and time [44]. The FDTD method utilizes an algorithm that approximates the continuous derivatives in both time and space using centered two-point finite differences illustrated in (1-44).

$$\frac{\partial \boldsymbol{B}}{\partial t} = \nabla x \boldsymbol{H} - \boldsymbol{J} \quad \textbf{(1-38)}$$

$$\frac{\partial \boldsymbol{B}}{\partial t} = -\nabla x \boldsymbol{E} \quad \textbf{(1-39)}$$

$$\nabla \cdot \boldsymbol{D} = \rho \quad \textbf{(1-40)}$$

$$\nabla \cdot \boldsymbol{B} = 0 \quad \textbf{(1-41)}$$

$$\varepsilon \frac{\partial \boldsymbol{E}}{\partial t} = \nabla x \boldsymbol{H} - \boldsymbol{J} \quad \textbf{(1-42)}$$

$$\mu \frac{\partial \boldsymbol{H}}{\partial t} = -\nabla x \boldsymbol{E} \quad \textbf{(1-43)}$$

$$\left.\frac{df}{dz}\right|_{z=z_0} = \frac{f\left(z_0+\frac{\Delta z}{2}\right)-f\left(z_0-\frac{\Delta z}{2}\right)}{\Delta z} + O(\Delta z^2) \quad \textbf{(1-44)}$$

An alternative derivation of the FDTD method can be obtained by using an approximation of the integral forms of Maxwell's curl equations (1-45), (1-46). The approximation of these equations forms the basis of FIT.

$$\iint_A \boldsymbol{D} \cdot \hat{n} dA = \oint_{\partial A} \boldsymbol{H} \cdot \boldsymbol{dl} \quad \textbf{(1-45)}$$

$$\iint_A \boldsymbol{B} \cdot \hat{n} dA = -\oint_{\partial A} \boldsymbol{E} \cdot \boldsymbol{dl} \quad \textbf{(1-46)}$$

Classical FDTD simulation tools have the disadvantage of utilizing a staircase mesh approximation for complex boundaries. FIT can be considered a generalization of the FDTD method, while also maintaining links to the Finite Element Method (FEM). This link deals with the multiple mesh configurations that can be utilized with FIT. The staircase mesh provides good performance when applied to structures without curved or slanted boundaries. However, when the boundaries become complex, this mesh type has convergence problems and requires more computational resources. The Perfect Boundary Approximation (PBA) mesh posses excellent convergence properties and reduces the simulation time on designs with complex boundaries compared to the time required when using a staircase mesh. The PBA mesh allows efficient simulation of electrically large structures. Finally, FIT can also use a tetrahedral mesh similar to that used in FEM simulation tools. This mesh has excellent convergence properties, but it requires extensive computational resources. When used in large structures, the tetrahedral mesh requires an iterative mesh solution further increasing the computational cost [45].

FIT was first proposed as an application to frequency domain solutions and was the first eigenmode solution algorithm that showed the ability to reduce all spurious modes [45]. Later, FIT was extended to the time domain. FIT gained international recognition in the early 1980s when it became the first code capable of calculating transient fields of charged particles at ultra-realistic energies. This breakthrough led to the MAFIA collaboration ("solving **MA**xwell's

equations with the **F**inite **I**ntegration **A**lgorithm"). The result of this collaboration was a full electromagnetic, thermal, and partical tracking software package [45].

The simulation work performed in this research project was completed utilizing CST Microwave Studio. This software package allows the simulation of complex electromagnetic problems using the FIT algorithm. It contains three solvers: time domain, frequency domain, and eigenmode. The time domain solver allows the use of the PBA mesh, which enables the solution of large and/or complex electromagnetic problems such as finite arrays. The solution of Maxwell's Equations via FIT using the time domain solver requires less numerical effort than FEM solvers [46]. The time domain solver provides fast solutions to typical antenna problems. Infinite array simulations can be performed using periodic boundary conditions, but scanned performance is not available utilizing this technique. The frequency domain solver allows the simulation of a unit cell of an antenna array. These boundary conditions allow the investigation of a scanned array by placing a phase shift across adjacent boundaries to simulate a scanned plane wave. In the course of this report, a dual-band, dual-polarized element will be studied as an isolated element, as an element in an infinite array, and as an element in a finite antenna array.

1.7 Outline for Remainder of the Dissertation

The remaining sections of this dissertation detail the design and analysis of dual-band, dual-polarized antenna elements and arrays. The analysis begins with a detailed look at the constituent elements that serve as the building blocks for the dual-band, dual-polarized antenna element. This analysis includes an investigation into several polarization configurations, including dual-polarization and reconfigurable polarization. A detailed description is provided of a novel size reduction technique using capacitive loading. The analysis includes modal analysis and simulations. Several antenna elements were built and tested to provide experimental verification.

After a thorough understanding of the constituent elements is established, the elements are combined to form a dual-band element capable of simultaneous operating with orthogonal polarizations. Several polarization combinations are explored through simulations. The performance of this element is compared to existing elements in the literature.

The element is also analyzed in an array environment. A hybrid technique is developed that uses multiple active element patterns in the analysis. This technique is applied to the dual-band, dual-polarized antenna array to show that the array maintains excellent polarization characteristics at wide scan angles in both frequency bands.

CHAPTER 2. CONSTITUENT ELEMENT ANALYSIS

The proposed coplanar, dual-band, low-profile element is capable of operating in multiple polarization configurations, and it can be placed in an array environment while still maintaining the ability to scan to wide angles without the introduction of grating lobes in the high frequency band. The basic building blocks for this design are the shorted annular ring antenna and the square ring slot antenna. The former will be used as the low band radiator, while the latter has been selected as the high band radiator. Before beginning with the design of the dual-band, dual-polarized antenna element, a comprehensive understanding of the fundamental operation of the constituent elements must be established. In order to achieve the desired goals with these elements, modified elements and novel techniques have been designed that will enhance the flexibility of the design. This chapter provides a thorough description of the elements and techniques that will be utilized in the design of the dual-band low profile elements.

2.1 Square Ring Slot

The square annular ring slot serves as the primary building block for the high band element of the dual-band, dual-polarized element described in this dissertation. The element is designed using a resonant ring of slotline transmission line, but it can also be realized with other transmission lines such as microstrip, stripline, or coplanar waveguide.

Circular polarized (CP) antennas are popular choices in mobile wireless communications applications owing to their ability to reduce multipath effects and allow flexible orientation of the transmitter and receiver antennas [47]. Microstrip antennas are often used for such applications due to their low profile and inexpensive manufacturing. However, these antennas provide limited CP bandwidth. Printed slot antennas can be provide a wider impedance bandwidth than traditional microstrip antennas. If perturbations are added to the structure, they can result in single-feed CP operation. An illustration of a microstrip line fed square ring slot antenna is shown in Figure 2-1.

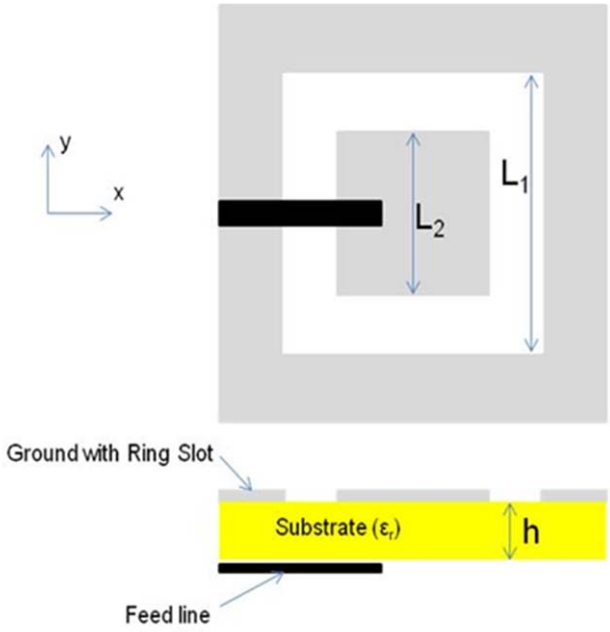

Figure 2-1: Illustration of Microstrip Fed Ring Slot Antenna

In this section, the operation of square ring slots will be investigated, and several designs dealing with modified polarization will be discussed.

2.1.1 Modal Analysis of Square Ring Slot Antennas

The resonant frequency of the square annular ring antenna can be derived by utilizing a transmission line analysis following from [48]. The square annular ring antenna can be divided into two transmission line sections of lengths l_1 and l_2, where the total length of the ring is $l=l_1+l_2$ as shown in Figure 2-2. Each of these sections is viewed as a length of transmission line, and $z_{1,2}$ measures the distance along the corresponding line as measured from the $z_{1,2}=0$ point. If the transmission line is taken to be lossless, the voltage and current on the line can be defined by (2-1) and (2-2). In these equations, Z_0 is the characteristic impedance of the line, and $\beta_{1,2}$ is the propagation constant of the specified line.

$$V_{1,2}(z_{1,2}) = V_0^+\left(e^{-j\beta z_{1,2}} + \Gamma_{1,2}(0)e^{j\beta z_{1,2}}\right) \quad \textbf{(2-1)}$$

$$I_{1,2}(z_{1,2}) = \frac{V_0^+}{z_0}\left(e^{-j\beta z_{1,2}} - \Gamma_{1,2}(0)e^{j\beta z_{1,2}}\right) \quad \textbf{(2-2)}$$

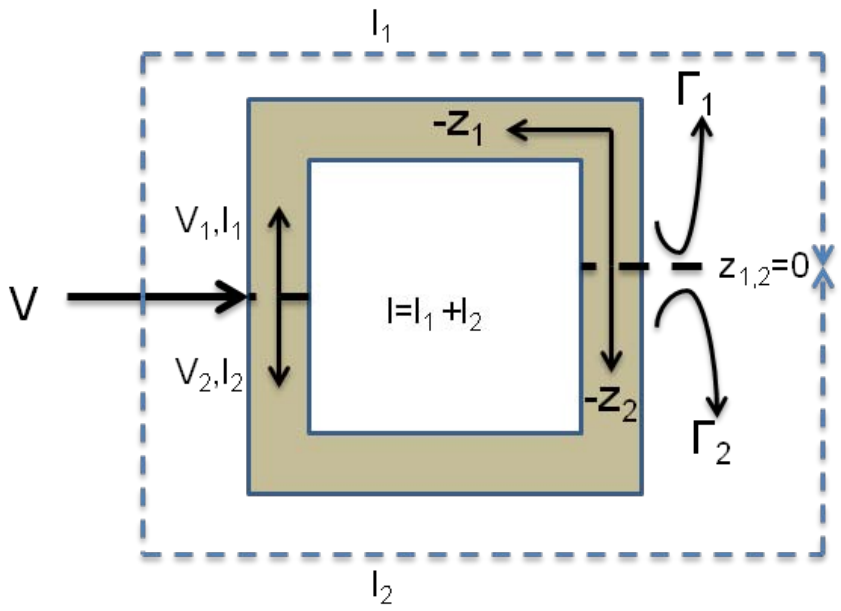

Figure 2-2: Transmission Line Model of Square Annular Ring

The resonant frequency of this structure corresponds to the frequency where a standing wave exists on the transmission lines. The length of the ring that supports a standing wave can be found by taking the derivative of the voltage from (2-1) with respect to the distance along the line (z). To find the locations of the critical points of the voltage along the transmission line, the derivative of (2-3) is set equal to zero. In order for this condition to hold, the reflection coefficients, $\Gamma_{1,2}(0)$, must equal unity. The expression for the reflection coefficients at resonance can be substituted into (2-1) and (2-2) to arrive at an expression for the voltages and currents on the transmission line at resonance shown in (2-4) and (2-5).

$$\frac{\partial V_{1,2}(z_{1,2})}{\partial z} = -j\beta_{1,2}V_0^+\left(e^{-j\beta z_{1,2}} - \Gamma_{1,2}(0)e^{j\beta z_{1,2}}\right) \quad \textbf{(2-3)}$$

$$V_{1,2}(z_{1,2}) = 2V_0^+ cos(\beta z_{1,2}) \quad \textbf{(2-4)}$$

$$I_{1,2}(z_{1,2}) = \frac{-j2V_0^+}{z_0} sin(\beta z_{1,2}) \quad \textbf{(2-5)}$$

The standing wave on each section of the transmission line repeats for multiples of the half-wavelength in the guide. As a result, the shortest length of the ring that can support the standing wave is one guided wavelength as shown in (2-6).

$$l = n\lambda_g \quad \textbf{(2-6)}$$

There are several expressions used in the literature for the guided-wavelength in the microstrip-fed slotline annular ring. A common technique is to use the expression in (2-7), where the resonant frequency is defined in terms of the slot length, width, and a correction factor. Wong,

et al [49] use the correction factor of (2-8), while Row [47] uses the correction factor of (2-9). Another explanation of the guided wavelength is presented in [50]. Janaswamy and Schaubert perform extensive computations to arrive at empirical formulas for the slot wavelength and characteristic impedance as a function of dielectric constant, substrate height, and slot width.

$$f_0 \approx \frac{c}{2(l_1+l_2)} R \qquad \textbf{(2-7)}$$

$$R_1 = \left(\frac{1+\varepsilon_r}{2\varepsilon_r}\right)^{1/2} \qquad \textbf{(2-8)}$$

$$R_2 = (0.3(\varepsilon_r - 1) + 1)^{-1/2} \qquad \textbf{(2-9)}$$

A microstrip square ring slot example was designed and simulated using CST Microwave Studio [42]. The element used L_1=0.5", and it was printed on a Rogers RO4350 (ε_r=3.48, h=0.06") substrate. The resonant frequency as a function of L_2 was calculated from (2-7) using the correction factors shown in (2-8) and (2-9). The results are plotted in Figure 2-3. The results show that the resonant frequency decreases as the length of the inner side decreases. Intuitively, this trend makes sense. As the inner side gets longer, the mean circumference of the square ring slot increases, thus increasing the wavelength at resonance.

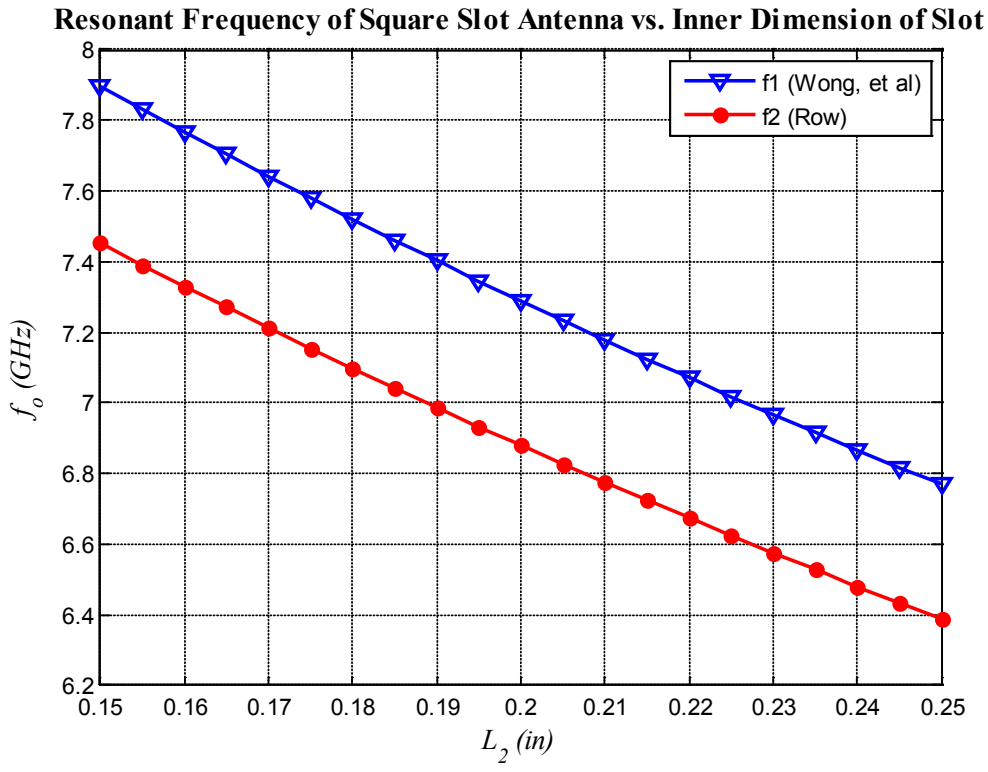

Figure 2-3: Resonant Frequency as a Function of inner slot length (L_2)

This element was simulated using an inner side length of 0.4" (L_2=0.4"). The model used in this simulation is shown in Figure 2-4. A comparison of the calculated and simulated resonant frequencies is provided in Table 2-1. This result shows that the simulated resonant frequency falls in between the two calculated values, but it is closer to the calculated value obtained using Row's formulation of (2-9). The Smith Chart result is shown in Figure 2-5. A marker is placed at 5.0 GHz, and the marker is seen to be very close to the center of the Smith Chart indicating an excellent impedance match.

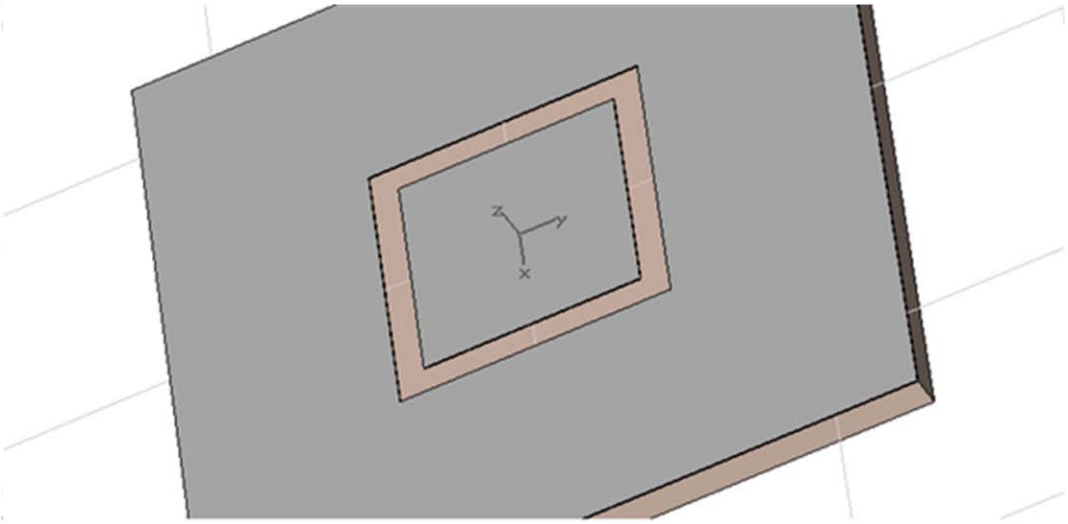

Figure 2-4: CST Model of a Square Ring Slot

Table 2-1: Resonant Frequency Comparison for Square Ring Slot

Evaluation Technique	Resonant Frequency
Calculation (Wong, et al using (2-8))	5.26 GHz
Calculation (Row, using (2-9))	4.97 GHz
CST Microwave Studio Simulation	5.02 GHz

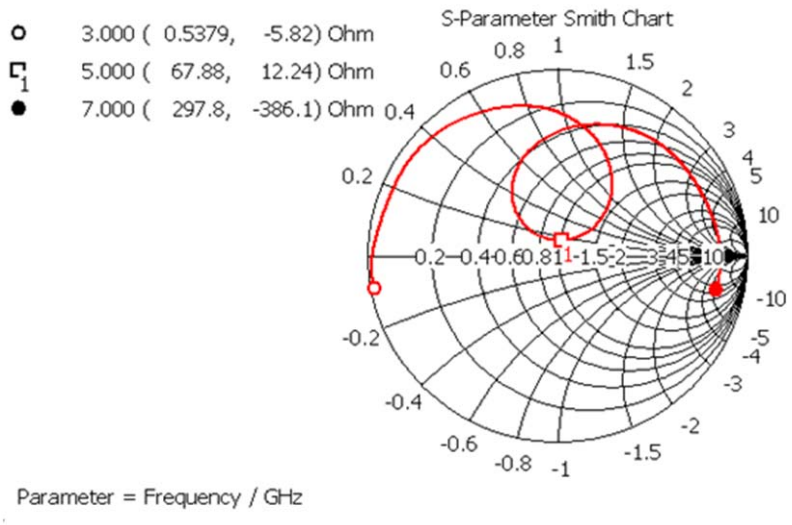

Figure 2-5: Simulated Smith Chart for Square Ring Slot

The fundamental mode of a square ring slot located in the x-y plane radiates with a pattern having a maximum value at broadside. The simulated volumetric pattern is provided in Figure 2-6 for the square ring slot. The slot is fed from a microwave feed along the y-axis ($\varphi=90^0$). The E-plane is parallel to the feed direction. The element is seen to have excellent radiation efficiency of 98.39%.

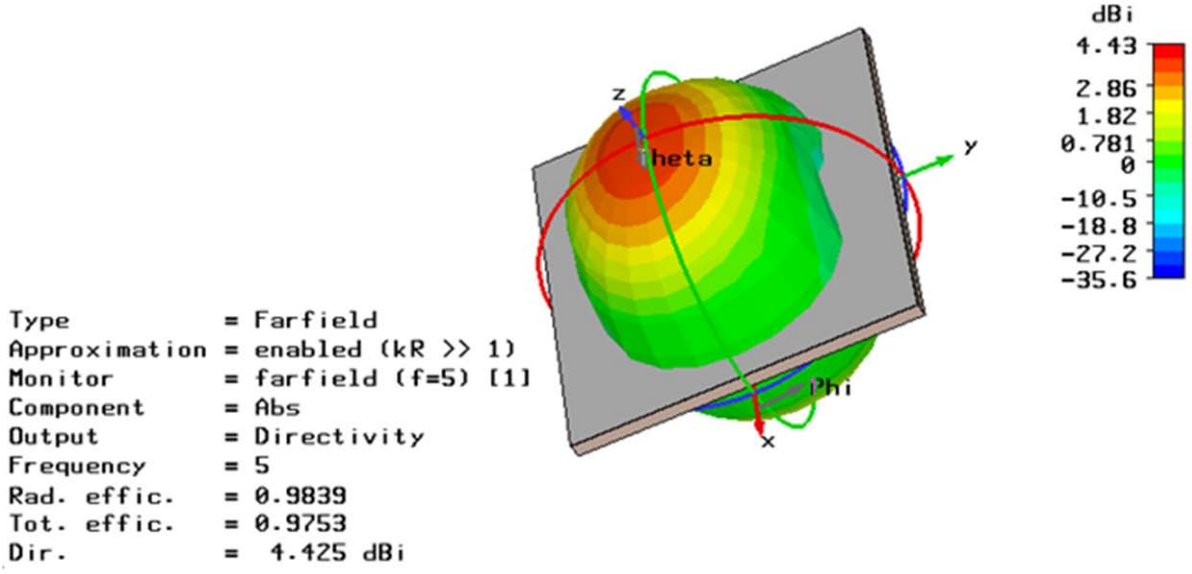

Figure 2-6: Microstrip Square Ring Slot Three-Dimensional Pattern

2.1.2 Stripline Realization of a Square Ring Slot Antenna

The previous section derived the resonant frequency and performance of a square ring slot when implemented in a slotline or microstrip line realization. A slotted stripline restricts the radiated energy to the upper half space, while the microstrip or slotline designs will radiate into the whole space. For this reason, the stripline design can be advantageous for applications requiring a more directive antenna element. However, the stripline – sometimes referred to as triplate – realization of this element presents some interesting obstacles that must be overcome in order to achieve high performance. The triplate configuration is illustrated in Figure 2-7.

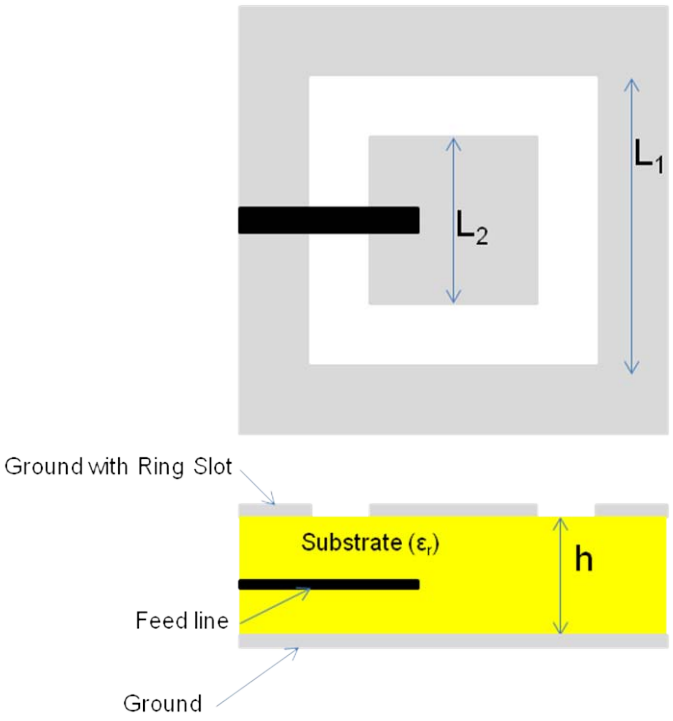

Figure 2-7: Stripline Square Ring Slot Configuration

The most notable difference between the slotline ring slot and the stripline ring slot is the behavior of the resonant frequency. For thin slots (L_1/L_2 near unity), the resonance of the ring slot will occur approximately when the mean circumference is equal to an integer multiple of guided wavelengths. Thus, narrow slotted triplate antennas behave in a similar fashion to the slotline ring antenna discussed in the previous section. However, as the slot width increases, the resonance of the antenna changes significantly [51].

The narrow slot behaves as two slots that are bent and connected at their end point as shown in Figure 2-2. The electric field in these slots is perpendicular to the direction of propagation in the slot and is symmetrical and uniform around the ring. As the slot width increases, some of the electric field begins to bend towards the lower ground plane in a manner analogous to the fringing fields of a traditional microstrip patch. This causes the current density on the inner edge of the slot to have a higher concentration than that on the outer perimeter. Subsequently, the

antenna behavior becomes similar to that of a microstrip patch and resonance occurs when the length of the inner-side of the square ring slot approaches a half-wavelength in the dielectric material that forms the substrate for the stripline circuit. As a result, the overall size of the structure becomes larger making it less than ideal for the dual-band element studied in this research.

The stripline element shown in Figure 2-7 can also have problems with efficiency and a distorted pattern shape due to the excitation of a parallel plate mode between the top and bottom conductors of the triplate design. For example, a simulation of a square ring slot with a stripline feed exhibited a radiation efficiency of less than 24% as seen in Figure 2-8. The source of the inefficiency can be seen by viewing the magnetic field in a plane containing the feeding stripline center conductor. Figure 2-9 shows the magnetic field at four different phase values ranging from 0^0 to 180^0. This figure shows that the fields are not tightly confined to the stripline and the slot. There are high concentrations of field strength away from these desirable locations due to the parallel plate mode that exists between the top and bottom ground planes. In order to improve the efficiency, this mode must be suppressed.

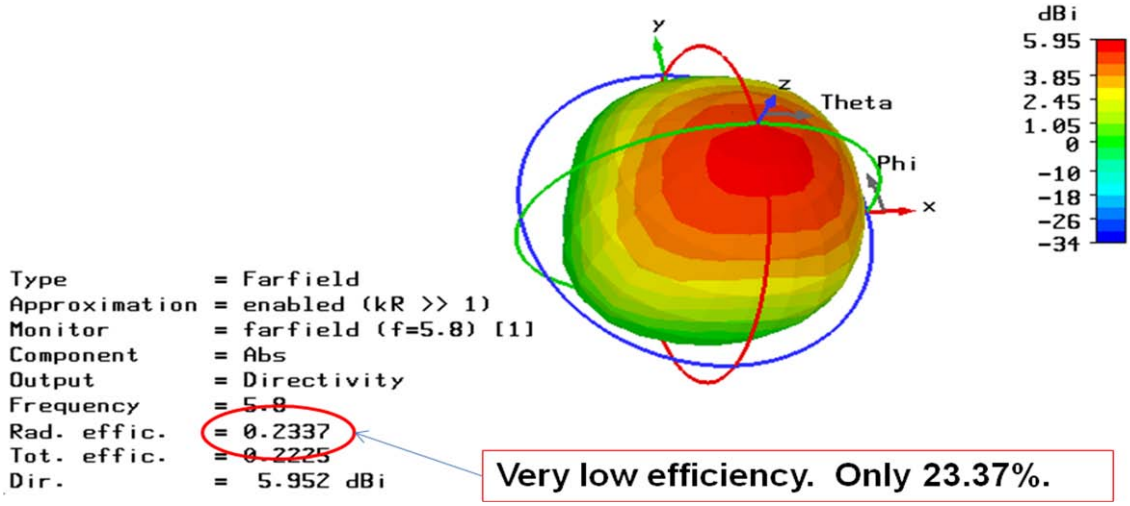

Figure 2-8: 3D Radiation Pattern for Square Ring Slot

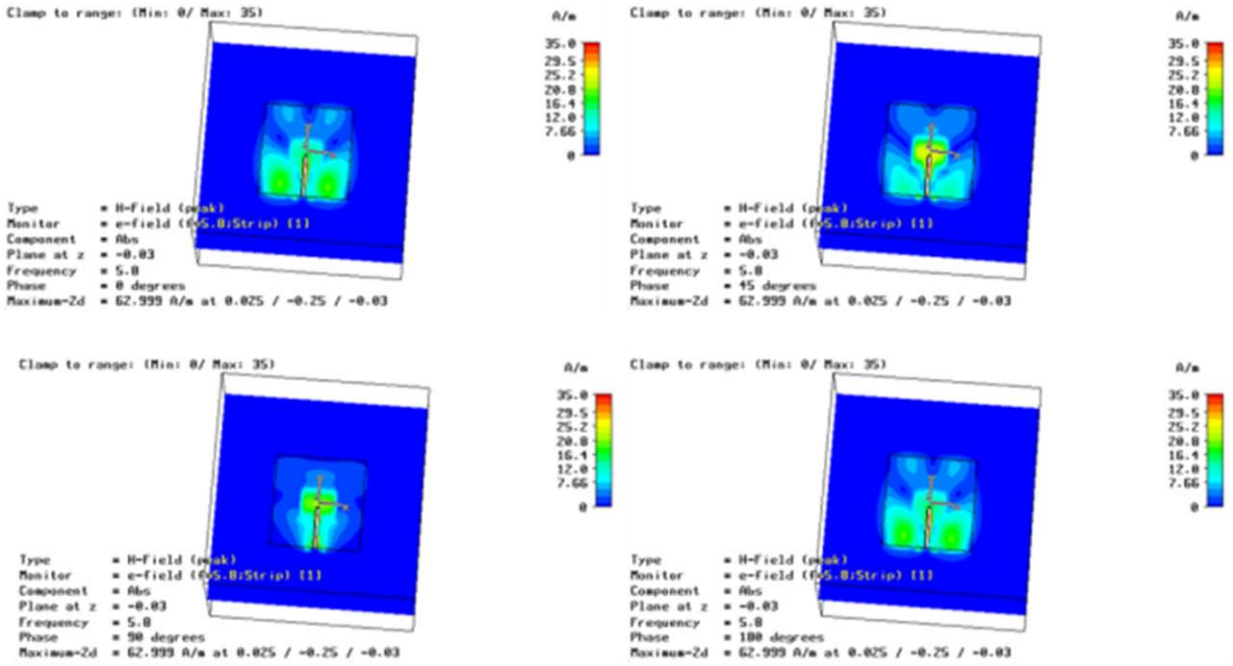

Figure 2-9: H-Field in Stripline of a Tri-Plate Square Ring Slot Antenna

Power loss, inefficiency, and radiation pattern perturbations can be generated in arrays fed by stripline networks by the existence of the parallel plate mode in a stripline configuration [52]. Work by Bhattacharyya, Fordham, and Liu [53] has shown that vias (also referred to as plated-through ground holes) can be used to suppress the parallel plate mode in slot-coupled patch antennas fed by stripline feed networks. Their design contains vias surrounding the slot that coupled energy from the feeding transmission line to the microstrip antenna above. They show that the presence of the vias improves the gain by increasing the available power for radiation. Further work has been done on incorporating vias in stripline circuits [54], and it was again shown to be a technique for suppressing the parallel-plate mode than can exist.

Figure 2-10 illustrates a technique for incorporating shorting vias into the square ring slot antenna. In this design, shorting vias are placed around the outer periphery of the ring slot. This figure contains one view of the model with the upper ground plane removed to reveal the location of the vias around the outer perimeter of the square ring slot. The smith chart and return loss plot in Figure 2-11 and 2-12 respectively show that an excellent match can be obtained using this design. The resulting radiation pattern is provided in Figure 2-13 and shows a drastic improvement in the performance. The pattern is no longer distorted, and the efficiency has increased to 91.76%. Additionally, the directivity has increased from 5.95dBi in the slot with no mode suppressing vias to over 7dBi with the inclusion of the vias. This is a result of the mode suppression. More power is delivered to the fundamental mode in the design with the absence of the parallel plate mode.

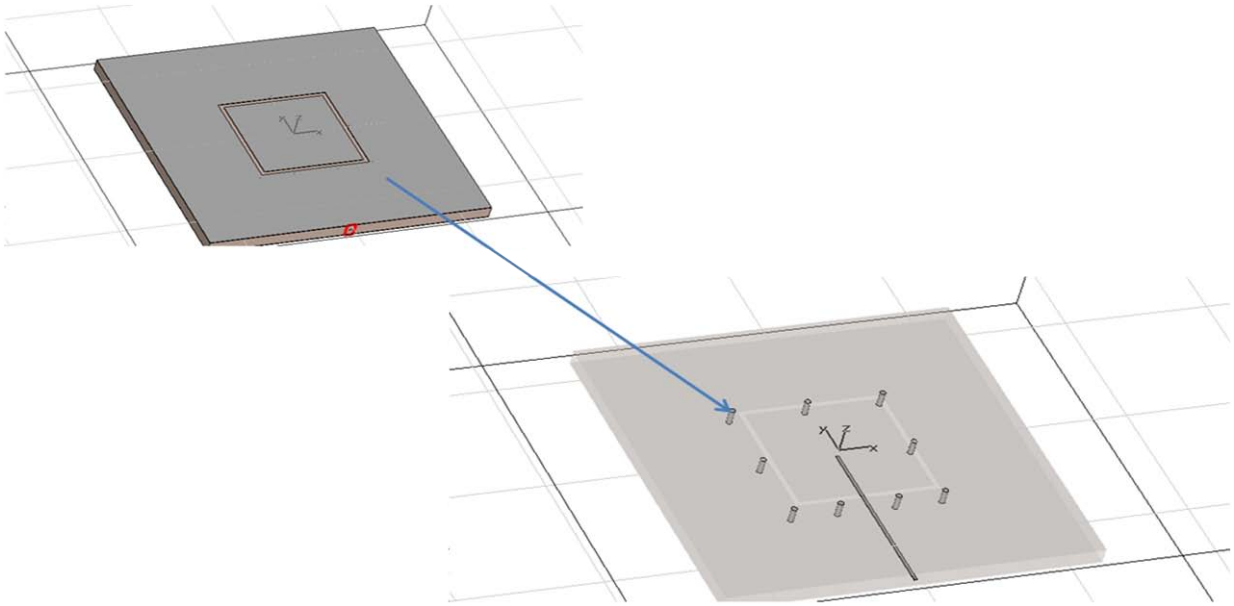

Figure 2-10: Square Ring Slot with Vias for Parallel Plate Mode Suppression

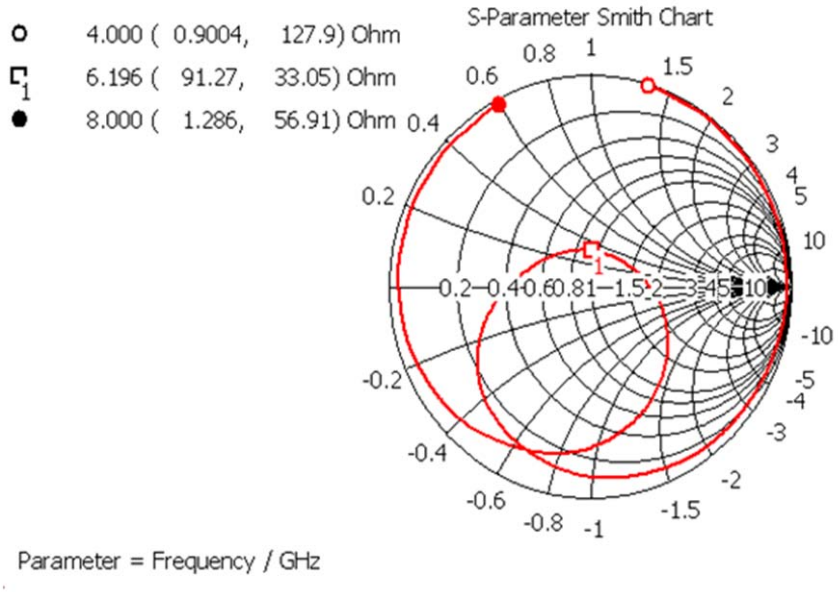

Figure 2-11: Smith Chart for Square Ring Slot with Mode Suppressing Vias

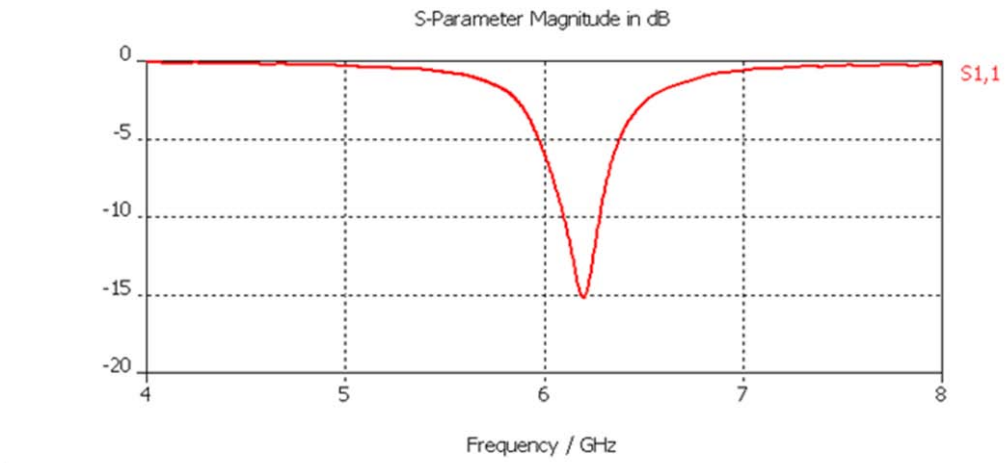

Figure 2-12: Return Loss for Square Ring Slot with Mode Suppressing Vias

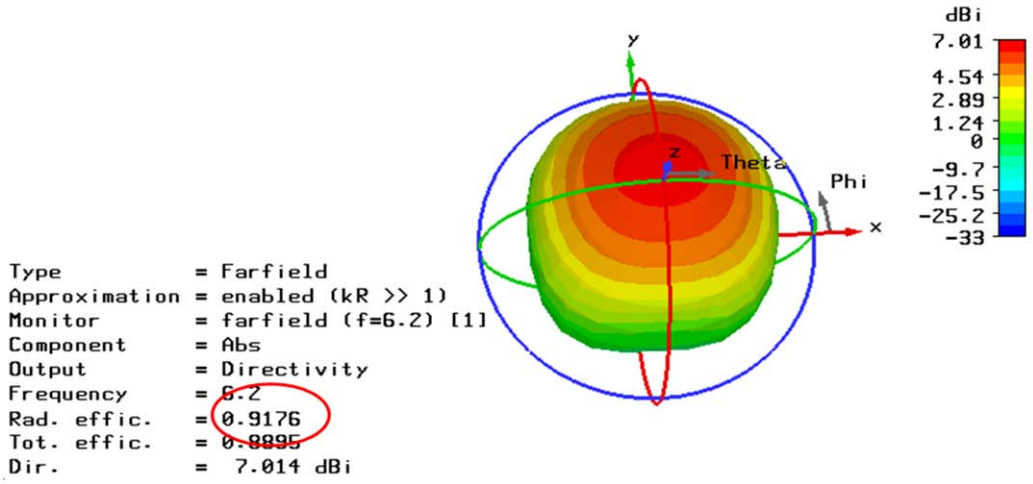

Figure 2-13: Radiation Pattern for Square Ring Slot with Mode Suppressing Vias

We can compare the magnetic field in this design to that shown in Figure 2-9. The same two-dimensional magnetic field cuts are plotted for the design with the mode suppressors in Figure 2-14. It is seen that the fields are tightly bound to the feeding stripline and the slot with a much higher concentration of the fields occurring inside of the slot that was seen in the design with no mode suppression.

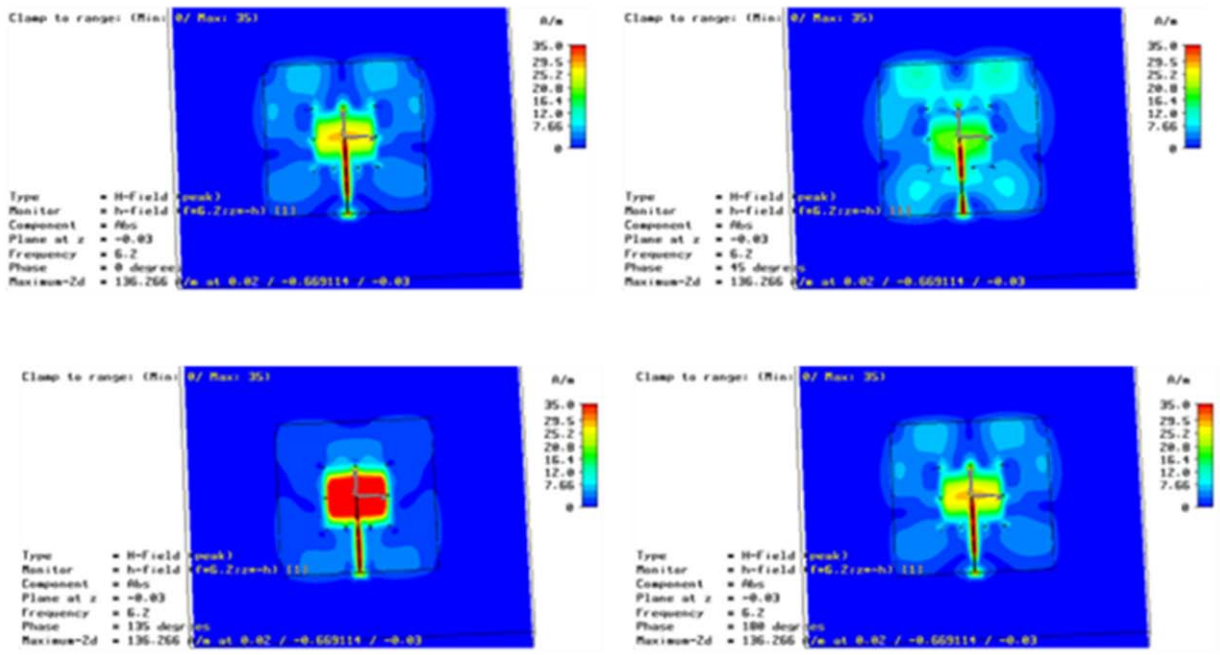

Figure 2-14: H-Field in Stripline of a Tri-Plate Square Ring Slot Antenna with Mode Suppressing Vias

The stripline realization of the square ring slot antenna restricts the radiation to the upper half plane making it advantageous for most array designs. In order to provide a high radiation efficiency, carefully placed vias are introduced into the design to suppress the parallel plate mode that can exist in the design.

2.1.3 Single-Feed CP Operation of the Square Ring Slot Antenna

There has been much work presented in the literature on single feed CP operation of microstrip antennas as well as slots. Row presents a technique for obtaining CP in a square ring slot antenna by using a microstrip line that is electromagnetically coupled to orthogonal sides of the square-ring slot [47]. Wong, *et al* present a technique utilizing a meandered slot section to perturb the slot and create CP operation [49]. Moreover, Sharma and Gupta have performed extensive research in single feed circular polarization for microstrip antennas [55, 56]. One technique they propose involves introducing triangular truncations at opposing corners of a square microstrip radiator. This technique has also been applied to square ring antennas [3, 57, 58]. The perturbed corners technique is used in this research and applied to a square ring slot antenna. An illustration of the square ring slot is provided in Figure 2-15. The truncations are isosceles triangles with the two equal sides having length of Δ.

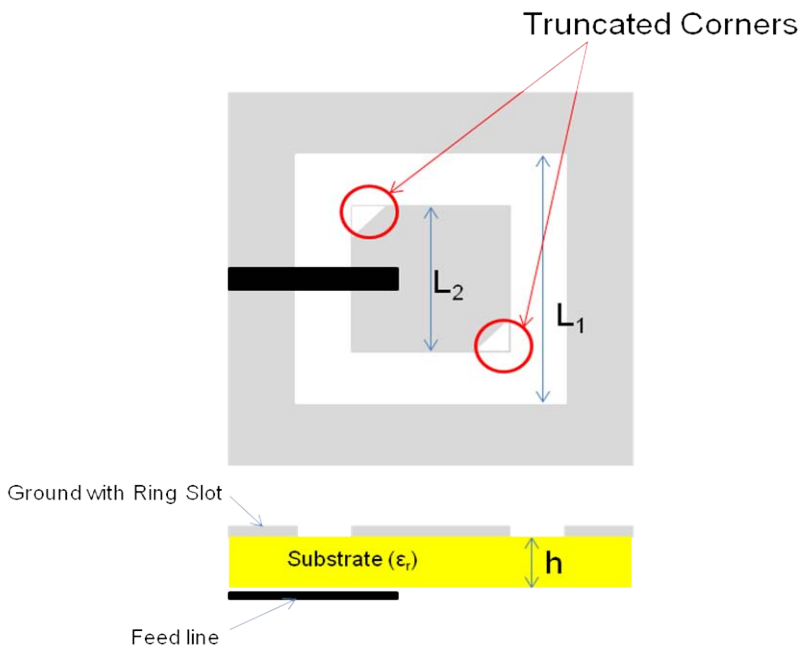

Figure 2-15: Illustration of Square Ring Slot with Truncated Corners for CP Operation

A microstrip perturbed slot was designed to operate within X-Band frequencies. The dimensions for the design are shown in Table 2-2. This element was printed on a Rogers 4350 substrate (ε_r=3.48, h=0.03"). The parameters show a L_1/L_2 ratio of 1.5.

Table 2-2: Dimensions for X-Band Square Ring Slot with Truncated Corners for CP Operation

Parameter	Value
L_1	0.3"
L_2	0.2"
Δ	0.15"
Stub length	0.2"
w_f	0.015"

This element was modeled in CST Microwave Studio using the model shown in Figure 2-16. This model shows that the truncations used in this element are pronounced due to the low quality factor of the design. The low quality factor is reflected in the broad return loss bandwidth shown in Figure 2-17. Designs using a large L_1/L_2 ratio with pronounced truncations have been shown to result in broadband CP operation in [3]. The truncation and feed line were optimized to provide the best Axial Ratio (AR) and impedance match over a wide bandwidth, and excellent results were seen. The return loss of this antenna was below -10dB from 10.2 – 15.4 GHz as

seen in the plot of Figure 2-17. However, not all of this wide bandwidth is usable for CP operation due to the AR.

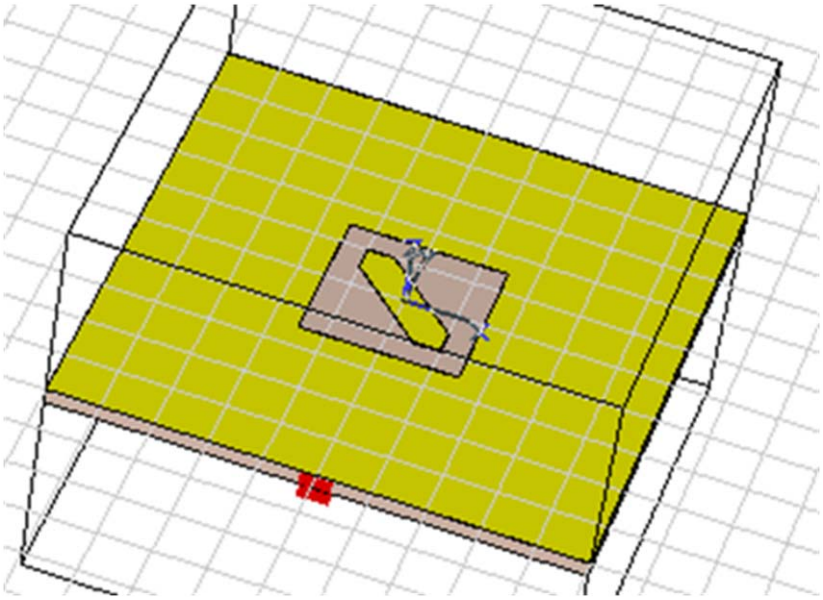

Figure 2-16: Simulation model for microstrip square ring slot with truncated corners

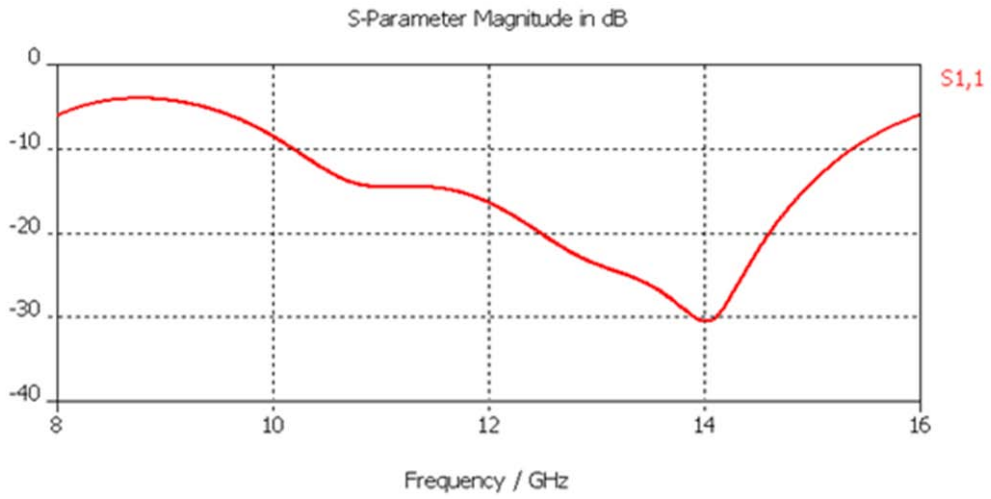

Figure 2-17: Simulated return loss for square ring slot with truncated corners

The truncations in this element support RHCP operation. For LHCP operation, the truncations could be moved to the orthogonal corners. The AR plot shown in Figure 2-18 indicates excellent

CP operation at broadside for this element. The fractional CP bandwidth depends on the acceptable axial ratio limit. The CP bandwidths for several commonly used AR thresholds are shown in Table 2-3. If a 3dB threshold is acceptable for the axial ratio, then a fractional bandwidth of almost 9% can be obtained. The entirety of the axial ratio bandwidth falls within the usable impedance bandwidth.

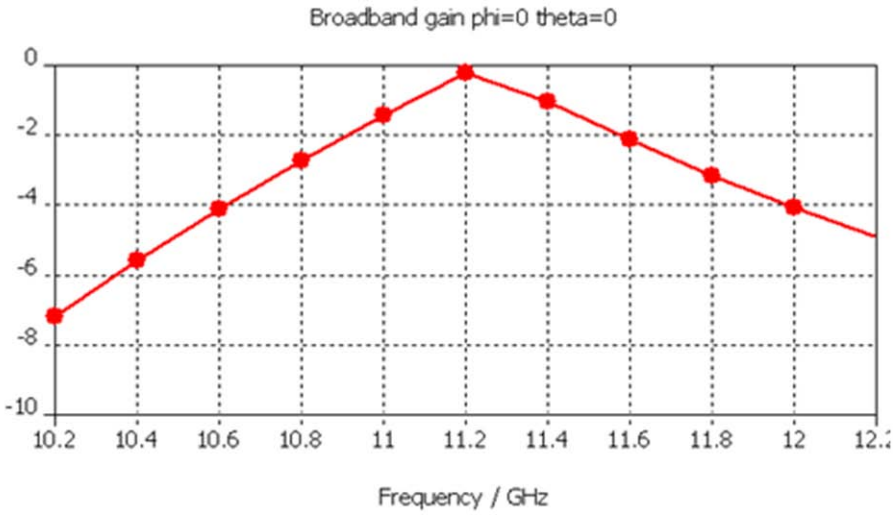

Figure 2-18: Axial Ratio vs. Frequency for X-Band Square Ring Slot with Truncated Corners for CP Operation

Table 2-3: Fractional Axial Ratio Bandwidth for X-Band Square Ring Slot with Truncated Corners for CP Operation

Axial Ratio Threshold	Fractional Bandwidth
-1dB	2.9%
-1.5dB	4.5%
-2dB	6.3%
-3dB	8.9%

The optimal AR location is at 11.2GHZ, where the axial ratio is -0.2dB. The RHCP and LHCP plots for cuts in the $\varphi=0^0$ and $\varphi=90^0$ planes are compared in Figures 2-19 and 2-20 respectively. These patterns indicate excellent cross-polarization discrimination (XPD) of almost 40dB at broadside, which was expected by the axial ratio near 0dB. Figure 1-3 shows that an XPD of 40dB corresponds to an AR close to unity, so the simulated polarization performance is reinforced by the theoretical results. The axial ratio also extends over wide angles as shown in Figure 2-21. The broad angular coverage will be extremely important when the design is ultimately included in an array environment. When the array is scanned to wide angles, its axial ratio will depend largely on the axial ratio of the constituent elements at the given θ value.

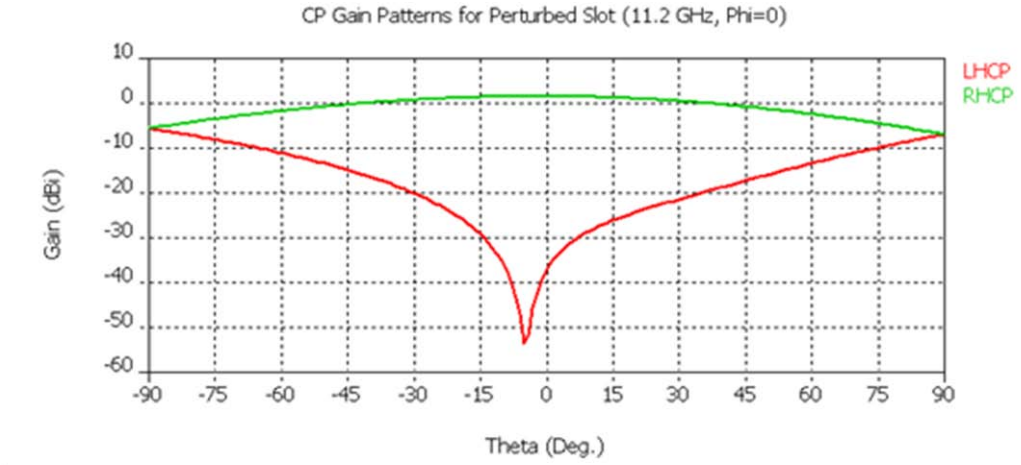

Figure 2-19: CP Radiation Patterns for Square Ring Slot with Truncated Corners at 11.2 GHz (Phi=0)

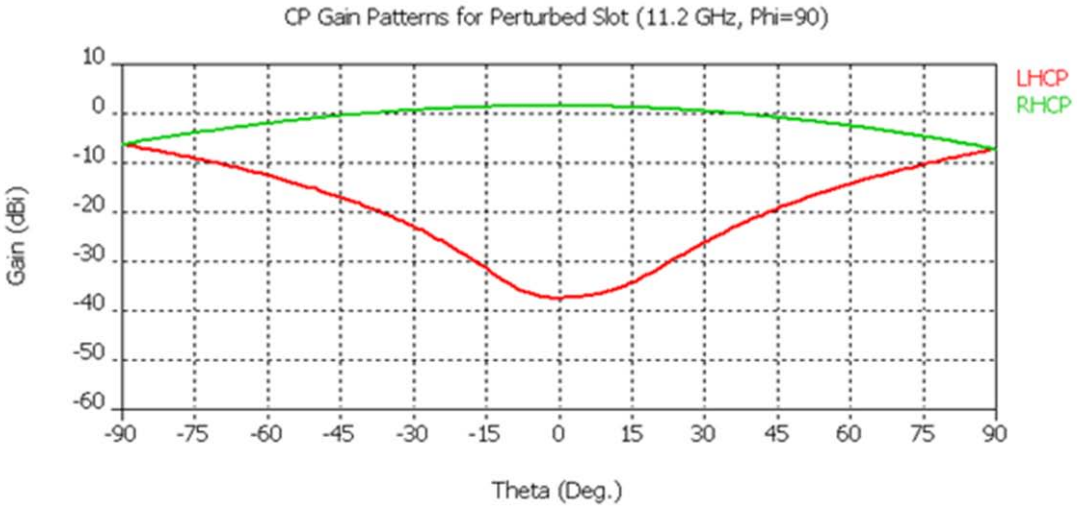

Figure 2-20: CP Radiation Patterns for Square Ring Slot with Truncated Corners at 11.2 GHz (Phi=90)

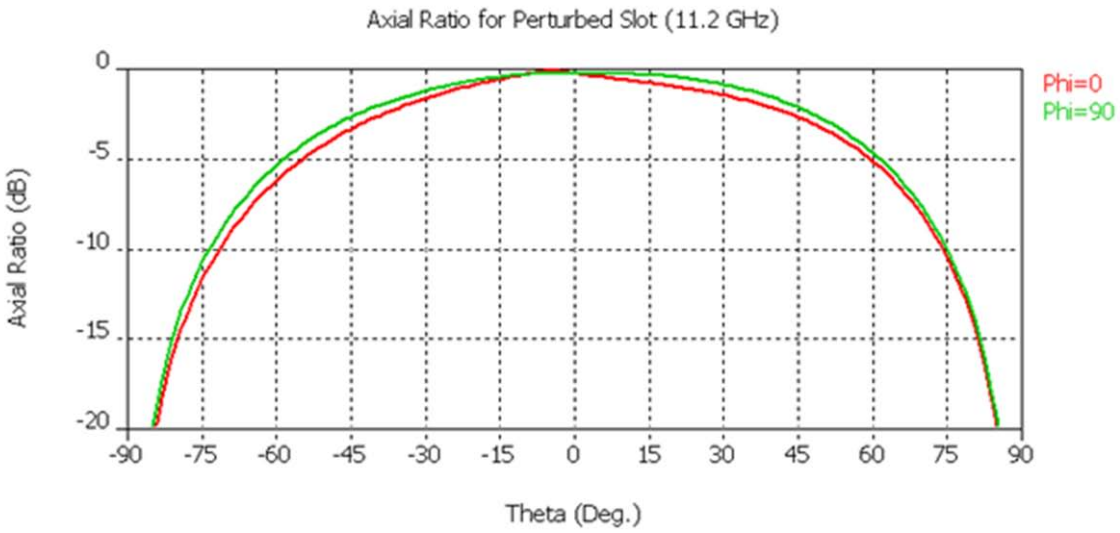

Figure 2-21: Axial Ratio vs. Theta for Square Ring Slot with Truncated Corners at 11.2GHz

2.1.4 Square Ring Slot Antenna with Reconfigurable Polarization

Circularly polarized (CP) antennas are popular choices in mobile wireless communications applications owing to their ability to allow flexible orientation between the transmitter and receiver antennas and in reducing multipath effects that can lead to signal fading in multipath environments [26-28, 59]. The ability to operate with both senses (left and right hand) of CP allows the system to reuse frequencies and double the system capacity [60]. Moreover, if the antenna can be switched between two senses of CP as well as linear polarization, it will allow the user to roam to virtually any existing network operating in the operational band of the antenna [28]. A printed circuit realization is ideal for wireless applications due to low profile, simple fabrication, low cost, and compatibility with integrated circuits. An element that combines the printed circuit realization and the reconfigurable polarization would be attractive for wireless and personal communication applications.

A common technique for achieving circular polarization is to feed the antenna in two locations with a 90 degree phase shift between the antenna ports. This technique has the drawbacks of requiring two feed lines as well as a hybrid network of some kind to provide the necessary phase shift. Single feed CP has been realized in microstrip antennas through the introduction of a perturbation in opposing corners of the antenna [55-57]. These perturbations introduce a second near-degenerate mode. If the antenna is fed correctly, these modes can be generated with the same amplitude and a 90 degree phase difference resulting in CP. In these designs, the polarization is either RHCP or LHCP depending on the relationship between the feeding microstrip line and the truncated corners.

While traditional microstrip antennas provide a limited CP bandwidth, printed slot antennas can prove to be more attractive elements in some cases because they provide an improved operating bandwidth without increasing the overall size of the element [47]. These elements can then be perturbed to provide a wideband CP operation by applying the principle of complementary structures to the previously mentioned perturbed class of microstrip structures [3]. A perturbed square-ring slot antenna is proposed that can be switched between RHCP, LHCP, or linear polarization (LP) by biasing a series of PIN diode switches. The perturbations used in this element are triangular truncations at opposing inner corners of the square ring slot. A prototype antenna using manual switches was designed, built, and measured to reveal the electromagnetic feasibility of the switching technique. The actual PIN diode switching circuitry is not implemented, but a possible layout using a biasing scheme similar to that used in [61, 62] is provided. The details of the control circuit designs are beyond the scope of this paper. On the other hand, the performance and effects of the PIN chip diode switches are included in the simulation.

The proposed reconfigurable square ring slot antenna is illustrated in Figure 2-22. Figure 2-22(a) shows the ground plane and the feeding microstrip line, which are printed on opposite sides of a microwave substrate. The microstrip line contains a shunt stub for impedance matching. The stub was added because the optimal axial ratio (AR) occurred outside of the optimal return loss bandwidth. The perturbed slot is separated into five conducting patches as seen in Figure 2-23(b). Small conducting pads and PIN diode switches are located in the gap between the center conducting patch (C_1) and the other four conducting patches (C_2, C_3, C_4, and C_5). These switches consist of a PIN diode in series with a large capacitor which is used to maintain continuity between the RF grounded conductors while maintaining DC isolation. A patch is located in between the PIN diode and the large capacitor, and is connected to the positive voltage through an inductor used as a RF choke. The five conducting patches are also DC grounded through inductors. This biasing scheme is similar to that used in [61, 62].

The design presented in this section operates at X-band frequencies resulting in small slot dimensions. These small dimensions do not leave sufficient room in the slot for the switching components, so these components are integrated on the feed line layer of the dielectric substrate. A conceptual view of the feed line layer for a design, including the lumped elements, is provided in Figure 2-23. This figure shows that the control lines and lumped elements can be integrated without interfering with the microstrip feed. Electrical continuity with the ground plane layer is maintained through the use of plated through holes. Figure 2-23(a) shows the bottom view of the printed circuit element, and Figure 2-23(b) shows a detailed view of one quadrant of the design. The microstrip feed line is outlined in red in Figure 2-23(a). A lumped element illustration of a quadrant of the biasing network is provided in Figure 2-24. This figure illustrates the placement of the diode and capacitor between the pads C_1 and C_3, and it also shows the location of the inductors for applying the DC bias voltage and ground. The dimensions of the components used in this schematic are based on commercially available chips. Avago PIN chip diodes are used

due to their small footprint and low series resistance. The dimensions for surface mount inductors and capacitors from Vishay are used in the layout of Figure 2-23 and their circuit parameters are used in the simulations shown below.

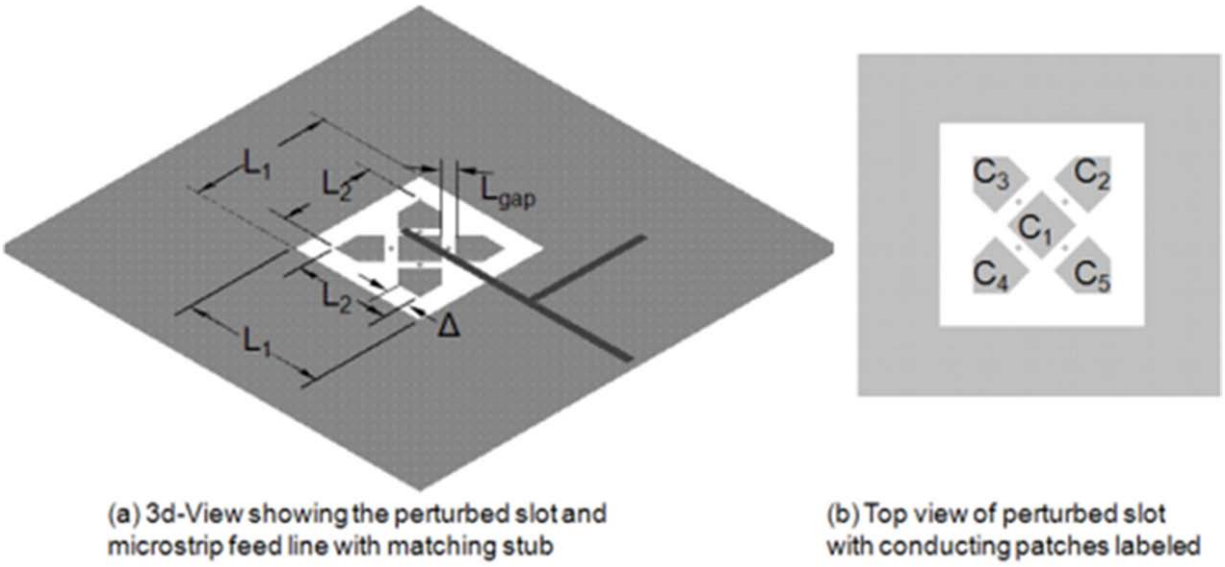

Figure 2-22: Topology of Perturbed Square Ring Slot with Reconfigurable Polarization (L1=0.762cm, L2=0.508cm, Lgap=0.046cm, Δ=0.127cm)

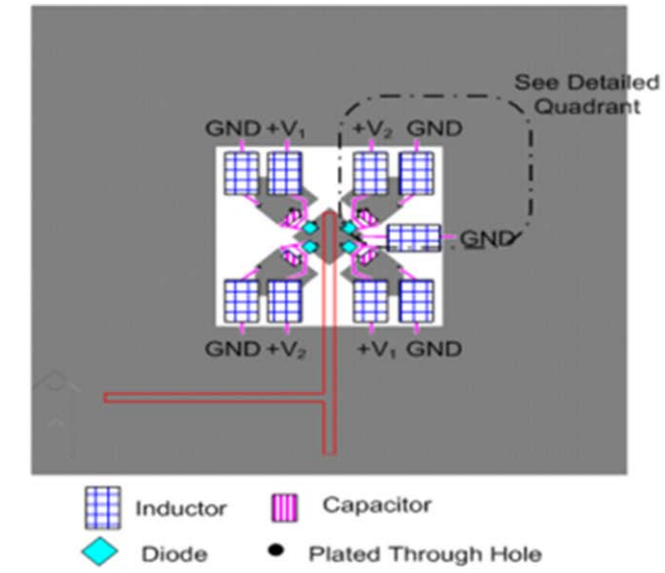

(a) Lumped Element and Control Line Layout for Perturbed Square Ring Slot with Reconfigurable Polarization

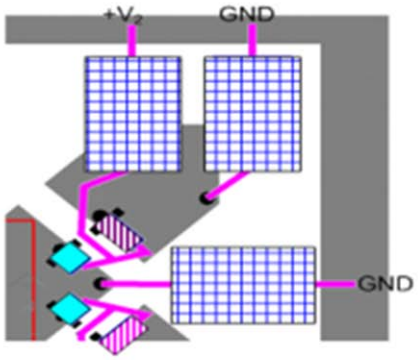

(b) Detailed Quadrant View

Figure 2-23: Conceptual View of Feed Line Layer Including Lumped Elements

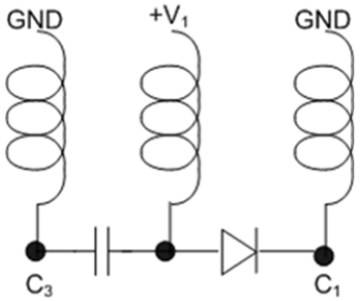

Figure 2-24: Lumped Element Illustration for a Quadrant of the Biasing Network

The switching can also be realized with MEMS switches placed between the conducting pads. The effective shape of the perturbed center region – and thus the polarization – can be controlled by biasing the proper switches. The possible polarization states (RHCP, LHCP and LP) and the corresponding diode switch states are tabulated in Table 2-4.

Table 2-4: Switching States for Perturbed Square Ring Slot with Reconfigurable Polarization

Polarization State	Switch from C_1 to C_2	Switch from C_1 to C_3	Switch from C_1 to C_4	Switch from C_1 to C_5
RHCP	OFF	ON	OFF	ON
LHCP	ON	OFF	ON	OFF
LP	ON	ON	ON	ON

An X-Band element was designed and simulated using CST Microwave Studio [42], a computational electromagnetic software package employing the Finite Integration Technique (FIT). The element is printed on a Rogers RO4350 microwave substrate (h=0.076cm, ε_r=3.48). In the simulations, the diode switches were modeled as lumped elements with the capacitance and resistance values close to those of PIN diode switches in either the ON or OFF state depending on the given polarization. The resistances were 1.5Ω for the ON state and 100MΩ for the OFF state; the capacitances were 0.025pF for the OFF state and 0 pF for the ON state. This element was designed with CP operation in mind, thus the matching stub was optimized to provide a low VSWR in this mode. If LP was more important for a given application, the matching network would be redesigned to lower the VSWR in the LP mode. A single matching stub was used in this design, but it is feasible to have multiple matching stubs optimized for each polarization state. These stubs would then be selected by additional switches.

After simulating the element using PIN diode switch characteristics, an element was built and tested using thin conducting wires to mimic electronically controlled switches to test each of the polarization states. The VSWR of the measured design is compared to the simulated results in Figure 2-25. These results show a favorable comparison between the simulated and measured impedance match for all three polarization states.

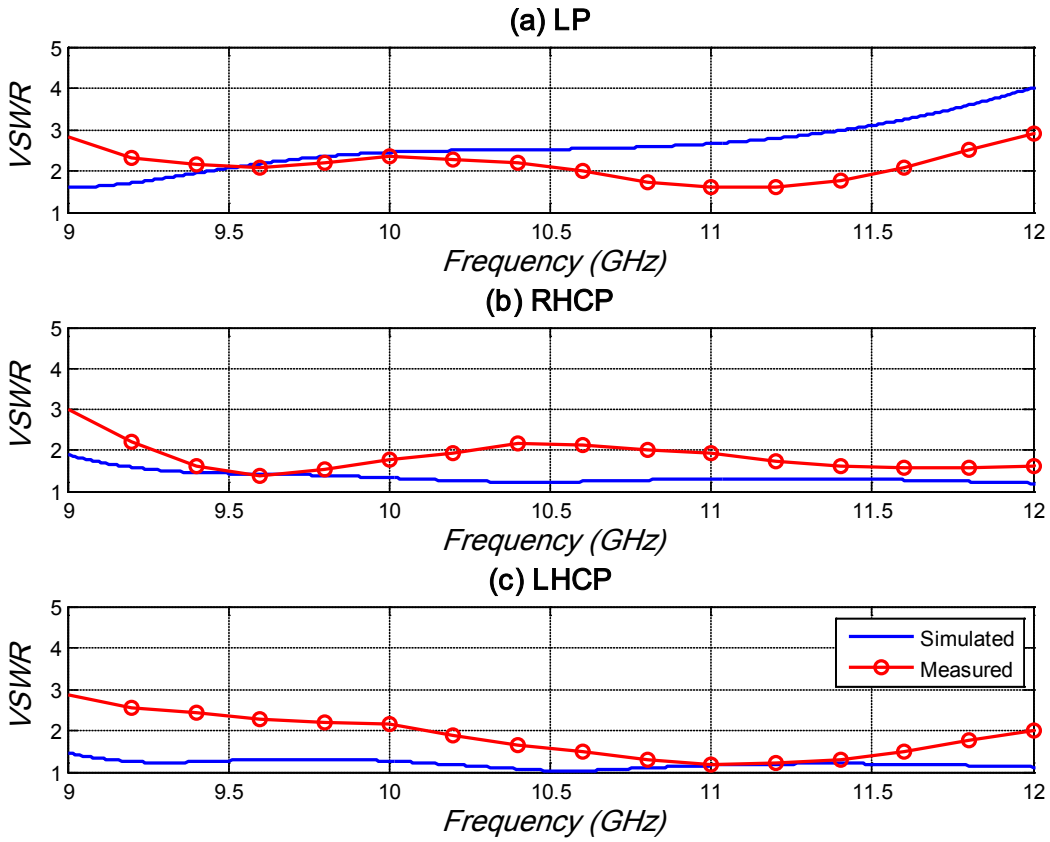

Figure 2-25: VSWR for Perturbed Square Ring Slot with Reconfigurable Polarization

Each of the CP modes showed 3dB axial ratio bandwidths of greater than 5% (5.1% for RHCP, 5.8% for LHCP) as seen in the simulated results of Figure 2-26. The plots of Figure 2-26 also show the measured AR for the RHCP configuration; the measurement is in agreement with the simulations over most of the operational frequency band. This usable axial ratio bandwidth lies entirely within the region where the simulations showed a VSWR<1.5:1. In the measured results, the VSWR in the usable CP regions were better than 2.0:1.

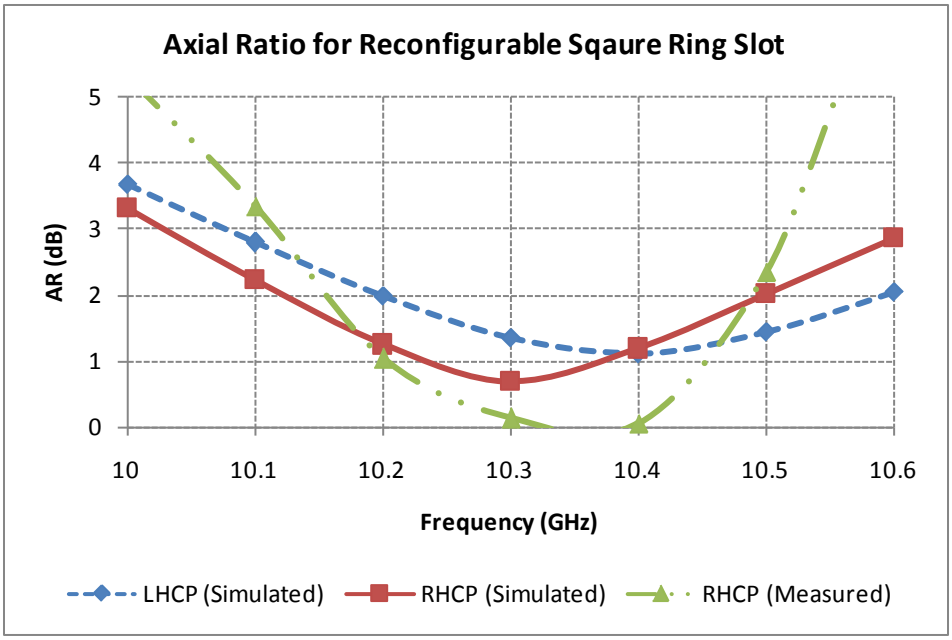

Figure 2-26: Axial Ratio for Perturbed Slot with Reconfigurable Polarization

Figure 2-27 shows the simulated co- and cross-pol gain pattern and the electric field in the slot for all three polarization configurations of this antenna. The two CP states radiate the desired CP state in the upper half plane ($|\theta|<90^{o}$), and the opposite sense in the lower half plane ($|\theta|>90^{o}$). This is reflected by the increased cross-polarization levels in the lower half plane, and it results from the observation points in the lower half plane seeing the mirror image of the surface currents on the antenna's conducting surface seen in the upper half plane [61]. The reversed polarization in the lower half plane causes the patterns in the CP states to appear different than the LP state. The LP gain pattern of Figure 2-28(c) shows a cross-pol level of -35dB on broadside. For applications requiring radiation in only a half-plane, the perturbed slot with switchable polarization could be realized using a stripline design to minimize the radiation in the lower half-plane.

The electric field distributions provided in Figure 2-28(d)-(f) illustrate the effect the switching on the electromagnetic operation of the slow antenna. When operating in RHCP mode, the switches from C_1 to C_3 and C_5 are ON causing the electric field in the slot to rotate in a counter clockwise manner as illustrated in Figure 2-28(d). Conversely, Figure 2-28(e) shows the electric field in the slot rotating clockwise when the switches from C_1 to C_2 and C_4 are ON for LHCP operation. When all switches are ON, the antenna operates with linear polarization in the y-direction. This is reflected in the electric field distribution shown in Figure 2-28(f).

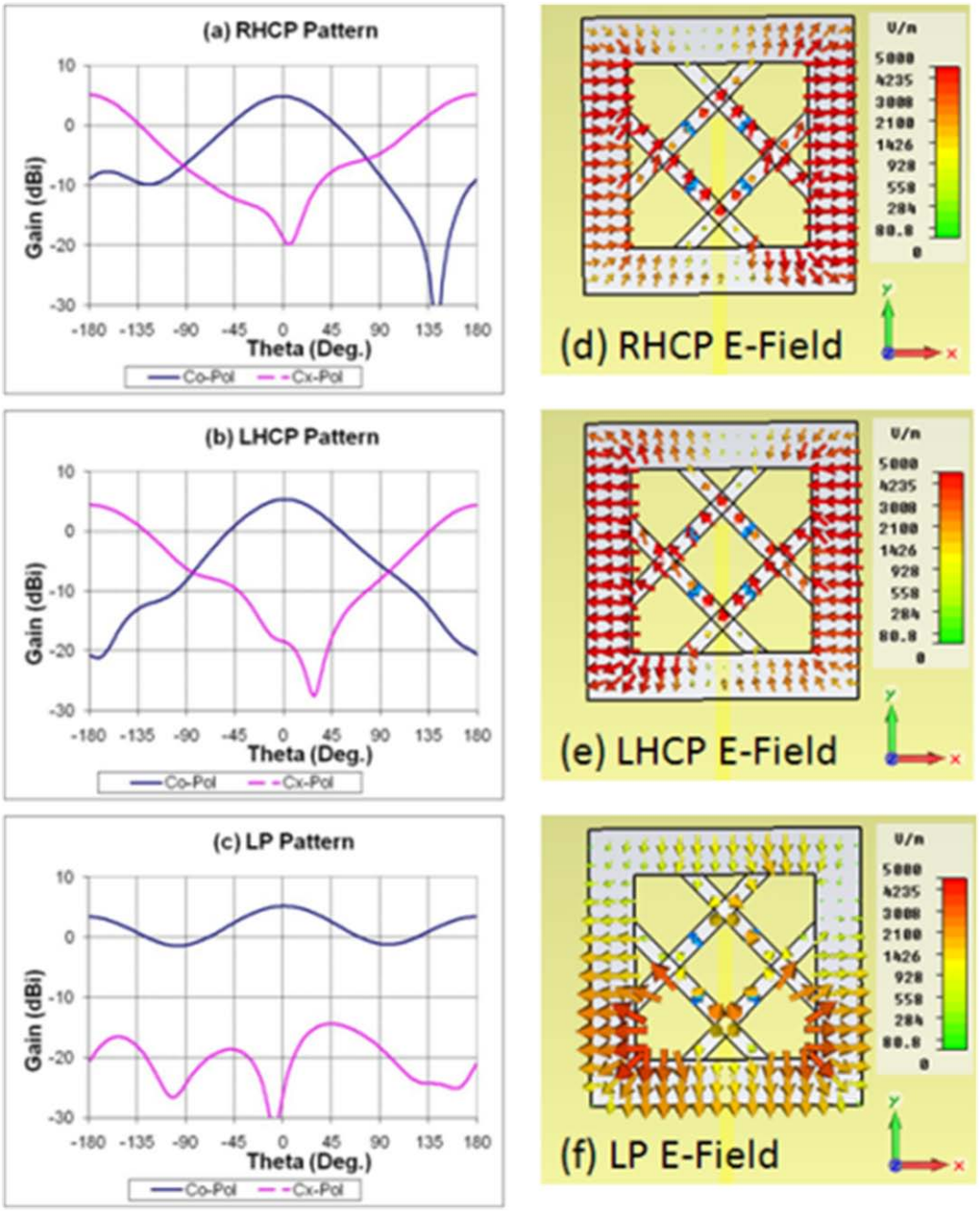

Figure 2-27: Radiation Pattern and Slot Electric Field for Perturbed Slot with Reconfigurable Polarization

The polarization pattern was measured for this antenna in each of the three polarization states. This pattern provides the amplitude response of the antenna as it is rotated about its axis ($-180° < \theta_{feed} < 180°$) when illuminated by a linearly polarized plane wave [12]. The measured polarization patterns for the LHCP and LP modes are plotted in Figure 2-28. These measured patterns can be used to determine the polarization ellipse for each sense of polarization as shown in Figure 2-29. The shape and orientation of this ellipse highlights key polarization parameters.

The ratio of the major axis length to the minor axis length defines the axial ratio, and the orientation of the major axis is referred to as the tilt angle [12]. For this antenna, the polarization ellipse for the LP mode shows that this element is vertically polarized with a 0-degree tilt angle. The small minor axis value for the polarization ellipse results from a cross-polarization level that is more than 20dB down from the co-polarized component. The LHCP mode has a polarization ellipse that is nearly circular, indicating excellent axial ratio performance. A unit circle is also plotted in Figure 2-29 to show the polarization ellipse for perfect CP operation. The deviation between the LHCP polarization ellipse and the ideal polarization ellipse reflects an axial ratio less than 1.5dB.

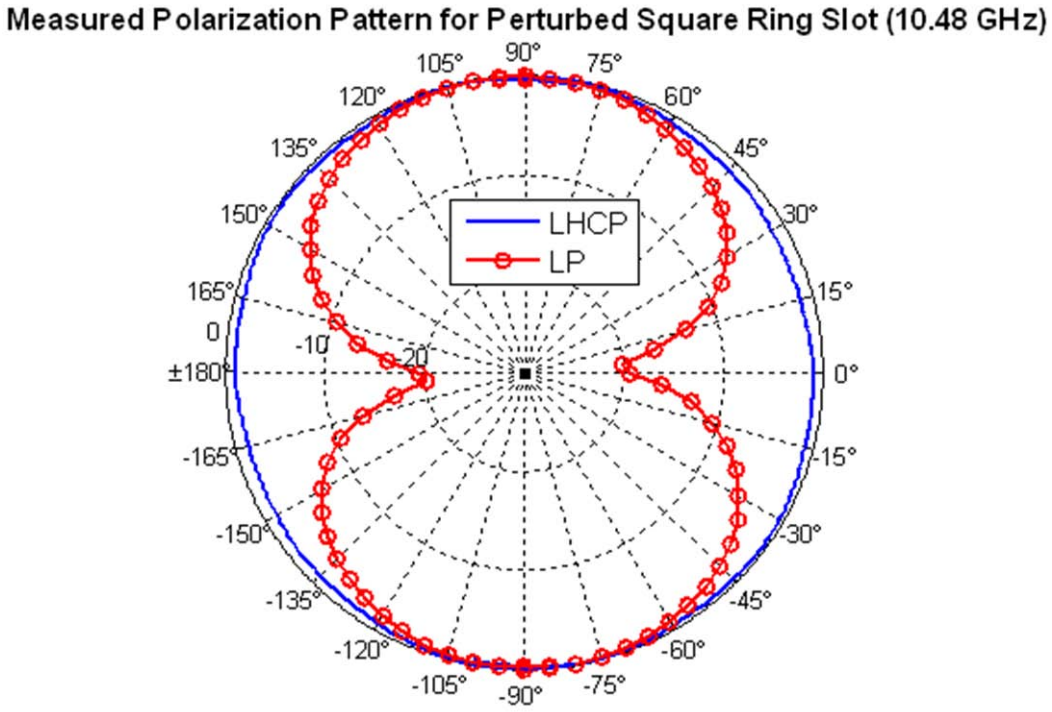

Figure 2-28: Measured Polarization Pattern for Perturbed Square Ring Slot with Reconfigurable Polarization

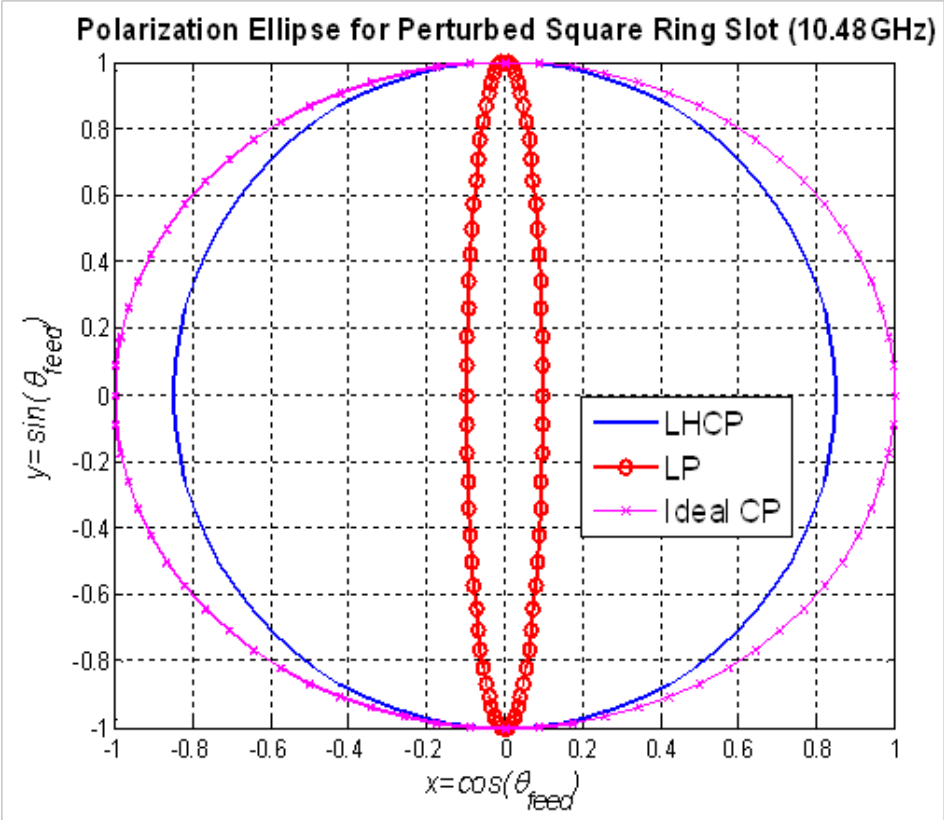

Figure 2-29: Measured Polarization Pattern for Perturbed Square Ring Slot with Reconfigurable Polarization

A perturbed square ring slot with reconfigurable polarization that is capable of switching between LHCP, RHCP, and LP has been proposed. In the simulations, the switching was obtained by changing the DC bias on a series of PIN diode switches. The simulations accounted for the capacitance and resistance of the PIN diodes in the given state. The two CP states exhibited 3dB AR bandwidths greater than 5%. A matching stub was added to improve the VSWR of the radiator in the frequency region containing the usable CP bandwidth.

An element was built and tested showing excellent polarization results for each state. Although this element utilized a simplified switching technique, it illustrated that the element has excellent polarization performance in all three polarization states. Although the actual switching and control was not constructed and the details of the biasing and control circuits were not addressed, an illustrative layout for the integration with the antenna element was provided.

2.1.5 Dual-Circularly Polarized Square Ring Slot Antenna

The element discussed in the previous section has the ability to switch between linear polarization and both senses of circular polarization, using a single polarization at a time. In some cases, it could be more desirable to operate with both sense of CP simultaneously. This has the advantage of allowing frequency reuse, which effectively doubles the capacity in a wireless communications system.

A stripline element providing dual-CP operation was designed and simulated to illustrate the concept. The model used in these simulations is shown in Figure 2-30. From above, the element looks like the traditional perturbed ring slot element that has been discussed previously. The alteration providing the dual-CP performance is revealed from inspection of the feed network.

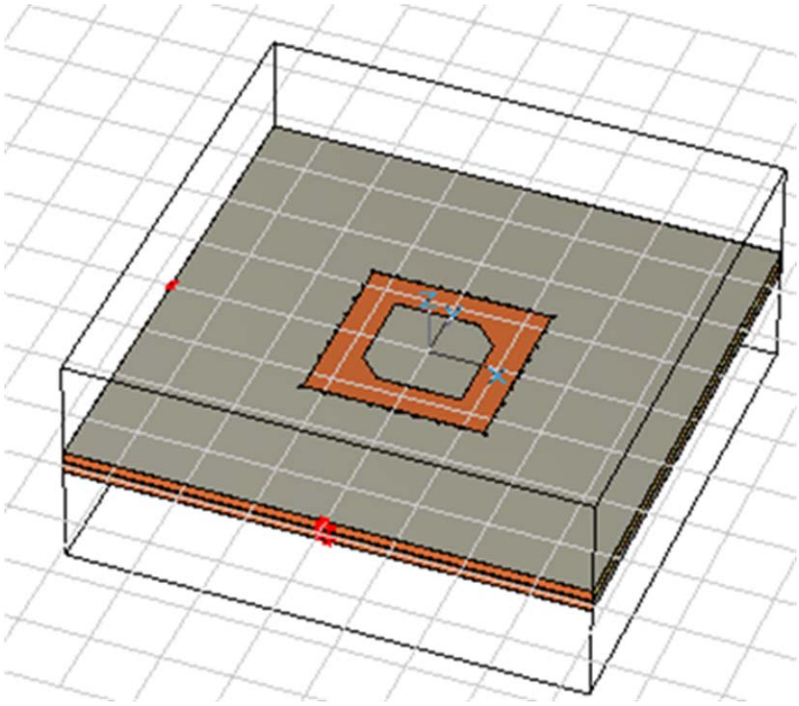

Figure 2-30: Simulation Model for Dual-CP Square Ring Slot with Stipline Realization

The stripline design uses shorting ground vias around the outer periphery of the slot to increase the efficiency as discussed previously. The stripline feed passes in between the vias and underneath of the slot. Two orthogonal feeds are used to generate the orthogonal senses of circular polarization. The optimal feed location is beyond the center of the element. Thus, if the two feeds are contained in the same vertical plane, they will physically intersect. In order to avoid this, a very thin dielectric layer is placed at the center of the stripline design. This layer is referred to as the *feed substrate*. One of the feed lines can be printed on the top of the *feed substrate*, and the other feed is printed on the bottom side. This allows them to be in close proximity electrically without physically intersecting.

In Figure 2-31, the upper ground plane is removed to reveal the shorting vias and the orthogonal feed lines. The dielectric layers are illustrated in Figure 2-32. All three substrates (upper, feed, and lower) are Rogers RT5870 material with a dielectric constant of 2.33. The upper and lower substrates are 0.031" thick, while the feed substrate is only 0.004" thick.

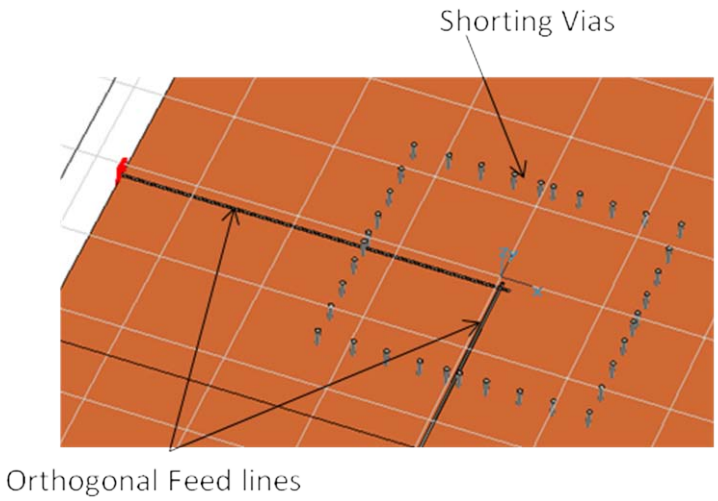

Figure 2-31: Location of Orthogonal Feed Lines in Dual-CP Square Ring Slot with Stipline Realization

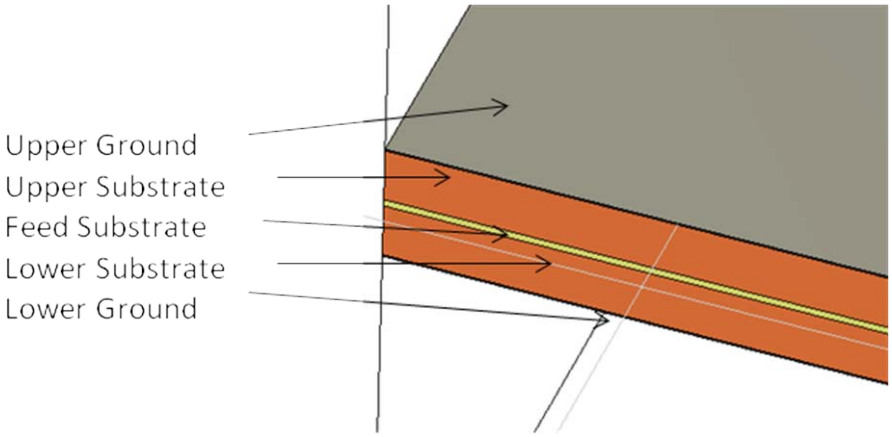

Figure 2-32: Dual-Substrate Dielectric Stack-up for Dual-CP Square Ring Slot with Stipline Realization

The two polarizations operate with a good impedance match as illustrated by the Smith Chart of Figure 2-33. In these simulations, Port 1 excites RHCP and is printed on the bottom of the feed substrate. Conversely, Port 2 excites LHCP and is printed on the top of the feed substrate. Inspection of Figure 2-33 reveals that the LHCP match is farther away from the center of the Smith Chart than the RHCP match. The feed line printed on the bottom of the feed substrate experiences a slightly degraded performance than the feed printed on the top. This slight degradation in match is shown in the VSWR plot of Figure 2-34. In this plot, *VSWR1* is the LHCP curve, and *VSWR2* is the RHCP curve.

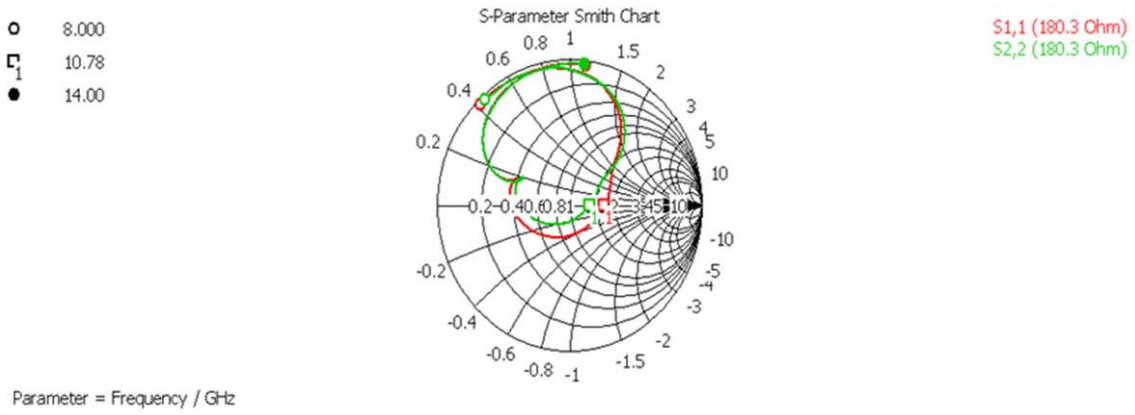

Figure 2-33: Smith Chart for Dual-CP Square Ring Slot with Stipline Realization

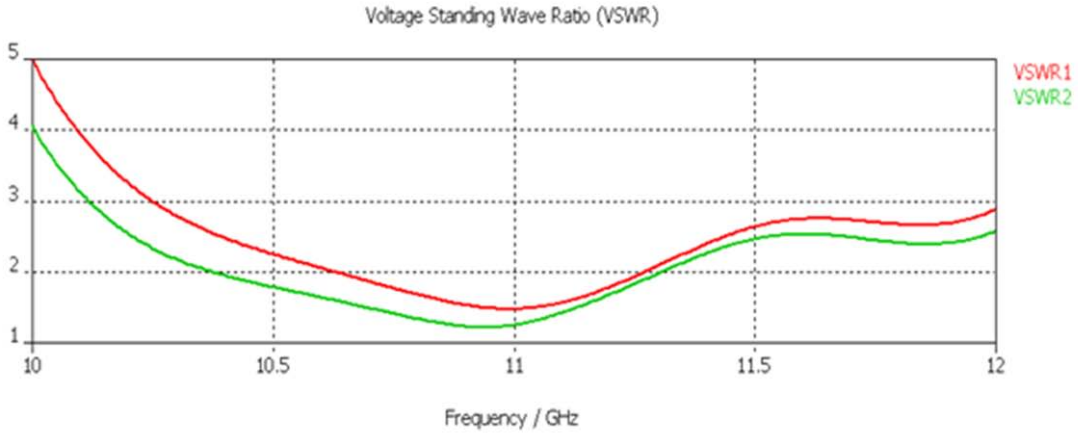

Figure 2-34: VSWR for Dual-CP Square Ring Slot with Stipline Realization

Although the two transmission lines are physically close to each other at the center of the element, there is a high level of inter-polarization isolation. The S-parameters of this two-port network are shown in Figure 2-35. The isolation is greater than 10dB over a band from 10.5 GHz to 11.4 GHz, and the peak isolation exceeds 43dB at 10.79 GHz. This band of high isolation corresponds to the 3dB Axial Ratio bandwidth as seen in Figure 2-36. The two polarizations have a 3dB Axial Ratio bandwidth of greater than 7.5%. RHCP operation exhibits slightly improved performance compared to LHCP. The RHCP feed line is printed on the top side of the feed substrate, and it passes above the LHCP feed line. This interaction has a greater impact on the LHCP feed line since it has a conductor between it and the slotted element. However, this degradation is not severe as both polarizations exhibit high performance.

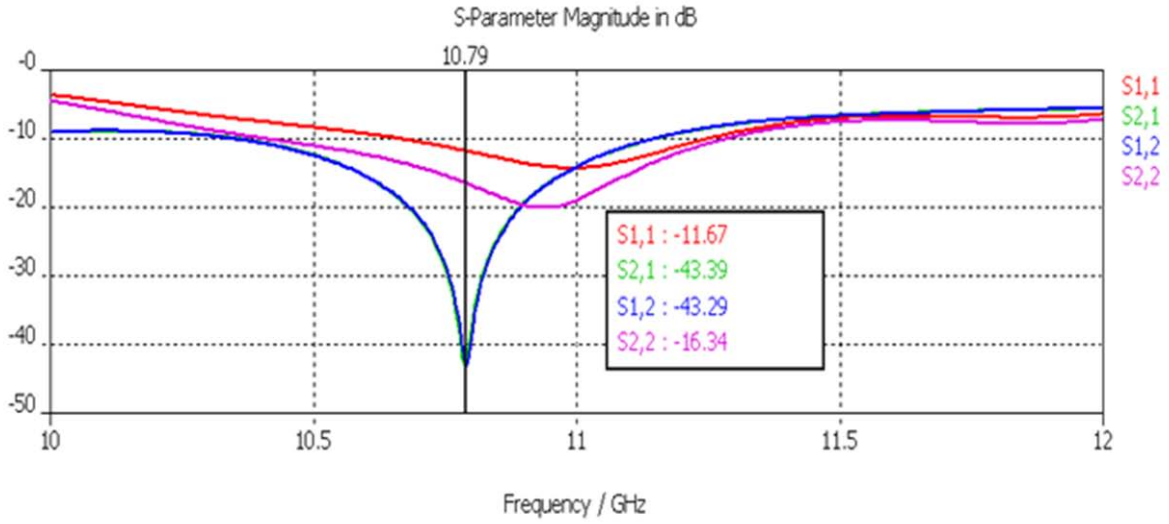

Figure 2-35: Dual-CP Square Ring Slot with Stipline Realization S-Parameters

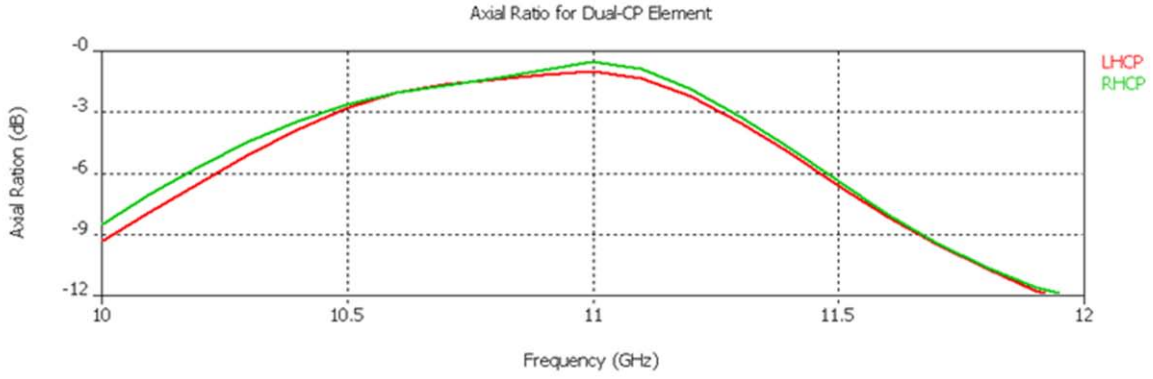

Figure 2-36: Dual-CP Square Ring Slot with Stipline Realization Axial Ratio

The three-dimensional radiation patterns for the LHCP (Figure 2-37) and RHCP (Figure 2-38) show a clean, broadside pattern and high radiation efficiency. The high efficiency indicates that the shorting vias are effectively minimizing the propagation of any parallel plate mode that could exist between the ground plane layers of the stripline design.

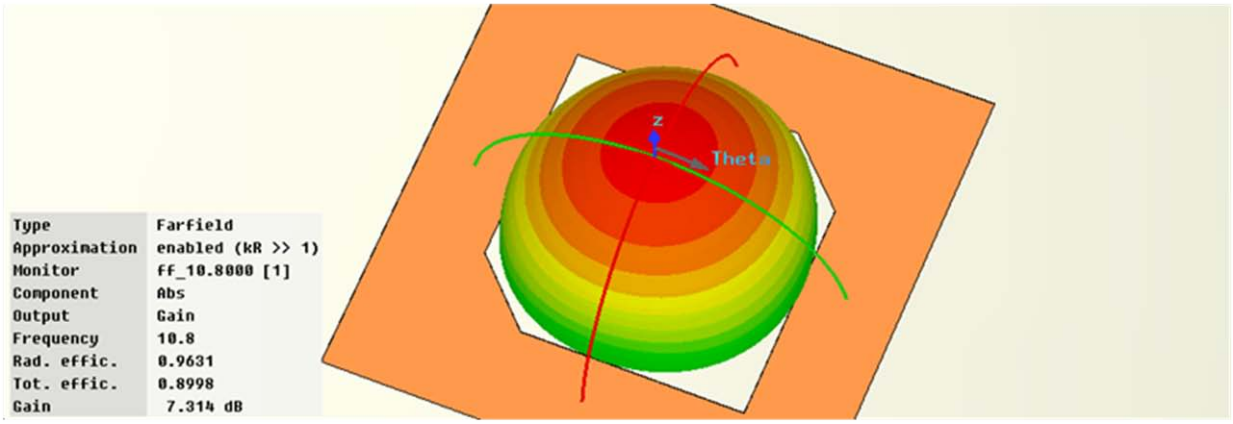

Figure 2-37: 3D Radiation Pattern for LHCP Port of the Dual-CP Element

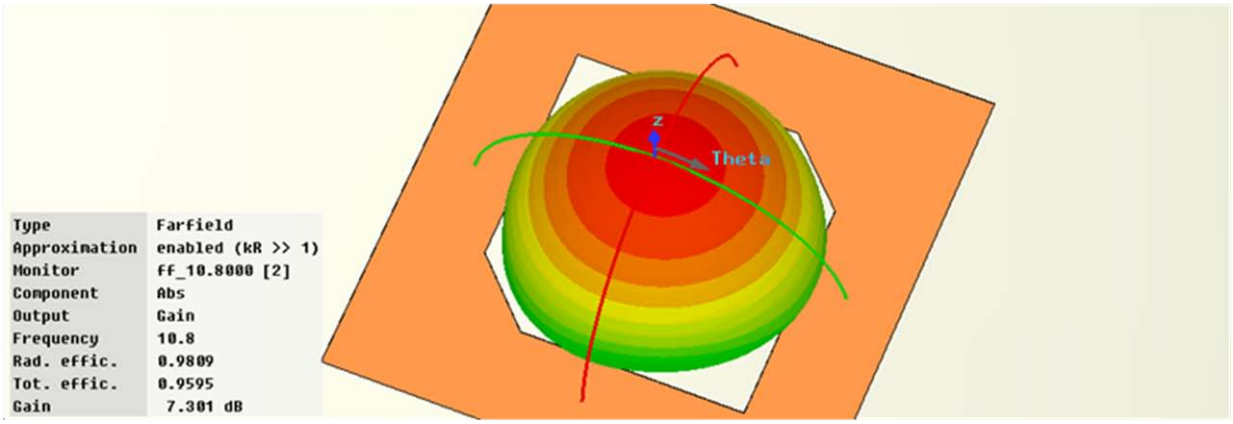

Figure 2-38: 3D Radiation Pattern for RHCP Port of the Dual-CP Element

2.2 Shorted Ring Antenna

The shorted annular ring antenna serves as the basic element for the low band operation of the proposed dual-band element. This element consists of an annular aperture printed on a microwave substrate shorted at the inside of the annular to the ground plane. The radiator is commonly circular (Figure 2-39), but it can also take on a square shape as shown in Figure 2-40. This element provides a broadside pattern and impedance bandwidth similar to that of a conventional microstrip patch when operated at the TM_{11} mode. By shorting this element at the inner radius, the power coupled into surface wave modes in the substrate is minimized. The reduction in energy transferred to surface waves maximizes the power available for radiation, and thus the efficiency of the antenna is increased. Moreover, the reduction of surface wave modes increases the performance of the element in an array environment by reducing the energy that will be coupled to neighboring elements within the array [63].

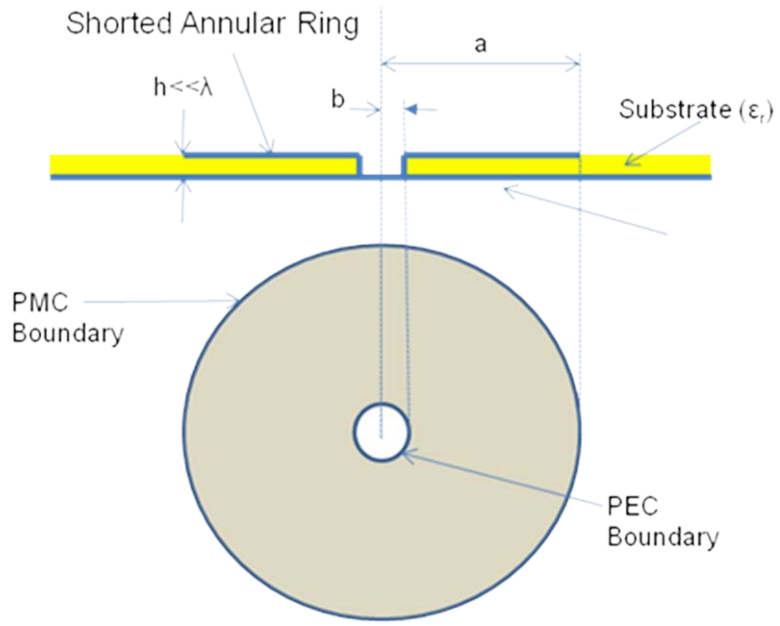

Figure 2-39: Shorted Annular Ring Antenna (Circular Radiator)

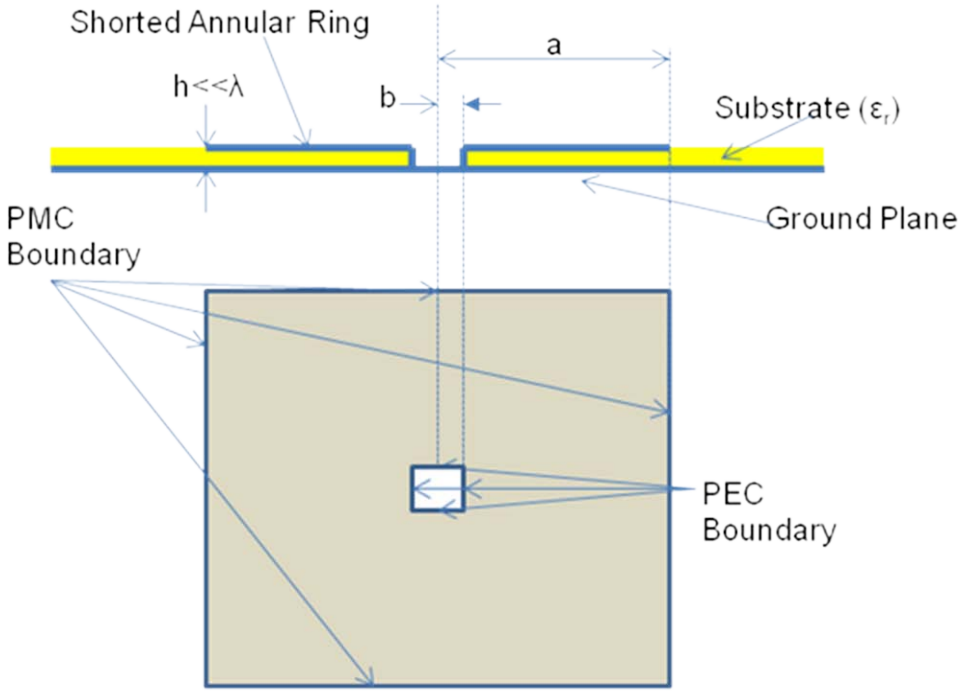

Figure 2-40: Shorted Annular Ring Antenna (Square Radiator)

2.2.1 Modal Analysis for Shorted Annular Ring Antenna

The modes of a circular shorted annular ring antenna can be calculated by viewing the region between the annular ring and the ground plane as a cavity. This cavity has perfect electric conductors (PEC) at z=0,h and at the inner radius, ρ=b. This structure also has a perfect magnetic conductor (PMC) at the outer radius, ρ=a. An illustration of the dimensions and boundaries is shown in Figure 2-39.

We assume that only Transverse Magnetic (TM) modes will exist in this cavity by defining the electric field in the cavity to be parallel to the z-axis. In order to solve for these modes, we solve the Helmholtz Equation of (2-10) for E_z. The geometry of this problem lends itself to cylindrical coordinates, so we define the ∇^2 operator in cylindrical coordinates (2-11).

$$\nabla^2 E_z + \mathrm{k}^2 E_z = 0 \quad \textbf{(2-10)}$$

$$\nabla^2 = \frac{\partial^2}{\partial \rho^2} + \frac{1}{\rho}\frac{\partial}{\partial \rho} + \frac{1}{\rho^2}\frac{\partial^2}{\partial \varphi^2} + \frac{\partial^2}{\partial z^2} \quad \textbf{(2-11)}$$

In microstrip antenna designs, the substrate thickness is typically much smaller than a wavelength (h<<λ). As a result, we will neglect the z-variation by making the assumption that the fields remain constant in this dimension, and we will focus on the ρ- and φ-components. If we set the z-variation equal to zero, we can simplify (2-11) by removing the z=dependency. We now apply this operator to E_z and solve using the separation of variables shown in (2-13).

$$\left(\frac{\partial^2}{\partial \rho^2} + \frac{1}{\rho}\frac{\partial}{\partial \rho} + \frac{1}{\rho^2}\frac{\partial^2}{\partial \varphi^2}\right) E_z + k^2 E_z = 0 \quad \textbf{(2-12)}$$

$$E_z(\rho, \varphi) = f(\rho) g(\varphi) \quad \textbf{(2-13)}$$

We can substitute (2-13) into (2-12) and arrive at two ordinary differential equations (ODEs). One of these ODEs can be solved for f(ρ), while the other can be solved for g(φ).

$$\nabla^2\big(\mathrm{f}(\rho)\mathrm{g}(\varphi)\big) + \mathrm{k}^2\big(\mathrm{f}(\rho)\mathrm{g}(\varphi)\big) = 0 \quad \textbf{(2-14)}$$

$$\left(\frac{\partial^2}{\partial \rho^2} + \frac{1}{\rho}\frac{\partial}{\partial \rho} + \frac{1}{\rho^2}\frac{\partial^2}{\partial \varphi^2}\right)\big(\mathrm{f}(\rho)\mathrm{g}(\varphi)\big) + k^2\big(\mathrm{f}(\rho)\mathrm{g}(\varphi)\big) = 0 \quad \textbf{(2-15)}$$

$$\frac{\rho^2}{f(\rho)}\frac{d^2 f(\rho)}{d\rho^2} + \frac{\rho}{f(\rho)}\frac{df(\rho)}{d\rho} + \rho^2 k^2 = -\frac{1}{g(\varphi)}\frac{d^2 g(\varphi)}{d\varphi^2} \quad \textbf{(2-16)}$$

The left hand side of (2-16) depends only on the variable ρ, while the right hand is strictly a function of φ. Therefore, in order to satisfy the expression at all values of ρ and φ, each side must be equal to a constant as defined in (2-17) and (2-18).

$$k_\varphi^2 = -\frac{1}{g(\varphi)}\frac{d^2 g(\varphi)}{d\varphi^2} \quad \textbf{(2-17)}$$

$$\frac{\rho^2}{f(\rho)}\frac{d^2 f(\rho)}{d\rho^2} + \frac{\rho}{f(\rho)}\frac{df(\rho)}{d\rho} + \left(\rho^2 k^2 - k_\rho^2\right) = 0 \quad \textbf{(2-18)}$$

The general solution to (2-17) is the sinusoidal variation shown in (2-19). The differential equation of (2-18) is known as Bessel's differential equation [64], and the solution is a summation of Bessel functions of the first and second kind as shown in (2-20).

$$g(\varphi) = A_1 sin(k_\varphi \varphi) + B_1 cos(k_\varphi \varphi) \quad \textbf{(2-19)}$$

$$f(\rho) = A_2 J_n(k_\rho \rho) + B_2 Y_n(k_\rho p) \quad \textbf{(2-20)}$$

In geometries containing the origin (i.e. a circular microstrip patch antenna), the Bessel function of the second kind is eliminated from the solution because it tends towards infinity as its argument approaches zero. However, the geometry of this problem does not include ρ=0 in the solution area, so both terms of (2-20) must be included in the solution. We also restrict the φ variation to functions that are periodic in multiples of 2π, so we restrict k_φ to integer values. Since the problem is symmetric in φ allowing an arbitrary reference point to be defined. Thus, we select only the cosine variation for g(φ). Using these simplifications, we can write a new expression for E_z as seen in (2-21).

$$E_z(\rho, \varphi) = cos(m\varphi)\{A_2 J_n(k_\rho \rho) + B_2 Y_n(k_\rho \rho)\} \quad \textbf{(2-21)}$$

In order to solve for the modes in this structure, we enforce the boundary conditions of the geometry. The PEC at the inner radius (ρ=b) forces $E_z(\rho=b,\varphi)=0$. Similarly, the PMC at the outer radius (ρ=a) forces $H_\varphi(\rho=a,\varphi)=0$. Since H_φ is proportional to $\frac{\partial E_z}{\partial \rho}$, we set $\frac{\partial E_z(\rho=a,\varphi)}{\partial \rho} = 0$. By applying these equations, we arrive at the expressions in (2-22) and (2-23). Combining these expressions leads to the characteristic equation in (2-24) that can be solved for the wave numbers of the TM_{n1} modes in the cavity. In these equations, k_φ has been replaced with k_{n1} to indicate that it is the wavenumber of mode TM_{n1}.

$$E_z(\rho = b, \varphi) = 0 \Rightarrow A_2 J_n(k_{n1} b) = -B_2 Y_n(k_{n1} b) \quad \textbf{(2-22)}$$

$$\frac{\partial E_z(\rho=a,\varphi)}{\partial \rho} = 0 \Rightarrow A_2 J_n'(k_{n1} a) = -B_2 Y_n'(k_{n1} a) \quad \textbf{(2-23)}$$

$$Y_n(k_{n1} b) J_n'(k_{n1} a) = J_n(k_{n1} b) Y_n'(k_{n1} a) \quad \textbf{(2-24)}$$

The characteristic equation of (2-24) can be simplified to an expression that does not involve taking the derivatives of Bessel functions by applying the identity of (2-25). In this identity, Z_p can be a Bessel (or Hankel) function of the first or second kind.

$$\frac{d}{dx} Z_p(\alpha x) = \alpha Z_{p-1}(\alpha x) - \frac{p}{x} z_p(\alpha x) \quad \textbf{(2-25)}$$

The simplified form of (2-24) is shown in (2-26). Once the solutions of this equation have been found, they can be substituted into (2-27) to find the resonant frequencies of the TM_{1n} modes in the cavity.

$$\left[k_{n1}J_{n-1}(k_{1n}a) - \frac{n}{a}J_n(k_{n1}a)\right]Y_n(k_{n1}b) - J_n(k_{n1}b)\left[k_{n1}Y_{n-1}(k_{n1}b) - \frac{n}{a}Y_n(k_{n1}b)\right] = 0 \quad \textbf{(2-26)}$$

$$f_{n1} = \frac{ck_{1n}}{2\pi a\sqrt{\varepsilon_r}} \quad \textbf{(2-27)}$$

This expression can be made more precise by incorporating a correction for the fringing fields at the outer radius of the radiating annular ring. The commonly used expression was a larger value for the outer radius to account for these fields as shown in (2-28)[65]. In this expression, *a'* is the outer radius calculated from (2-26), *a* is the physical outer radius of the antenna accounting for the fringing fields, and *h* is the substrate height.

$$a' = a + \frac{3}{4}a \quad \textbf{(2-28)}$$

A Matlab script was written to solve for the resonant frequencies in a shorted annular ring antenna using the above analysis. As an example, we will solve for the resonant frequencies of a shorted annular ring antenna using the parameters shown in Table 2-5. The resonant frequencies of the first four modes that were calculated from the Matlab script are shown in Table 2-6. This antenna was then simulated in CST Microwave Studio, a commercially available software package employing the Finite Integration Technique (FIT) [42]. The model used in this simulation is shown in Figure 2-41. The resonant frequencies from the simulations compared favorably to the analytical values. The plot of Figure 2-42 shows the simulated return loss of the antenna using the dimensions from Table 2-5. This plot also has markers indicating the location of the analytical values. For these markers, the amplitude was taken to make the point close to the corresponding mode.

Table 2-5: Parameter Values for Example Shorted Annular Ring

Parameter	Value
a	0.87"
b	0.25"
h	0.06"
ε_r	2.1

Table 2-6: Parameter Values for Example Shorted Annular Ring

Mode	Frequency (GHz)
TM_{01}	2.29
TM_{11}	2.95
TM_{21}	4.32
TM_{31}	5.84

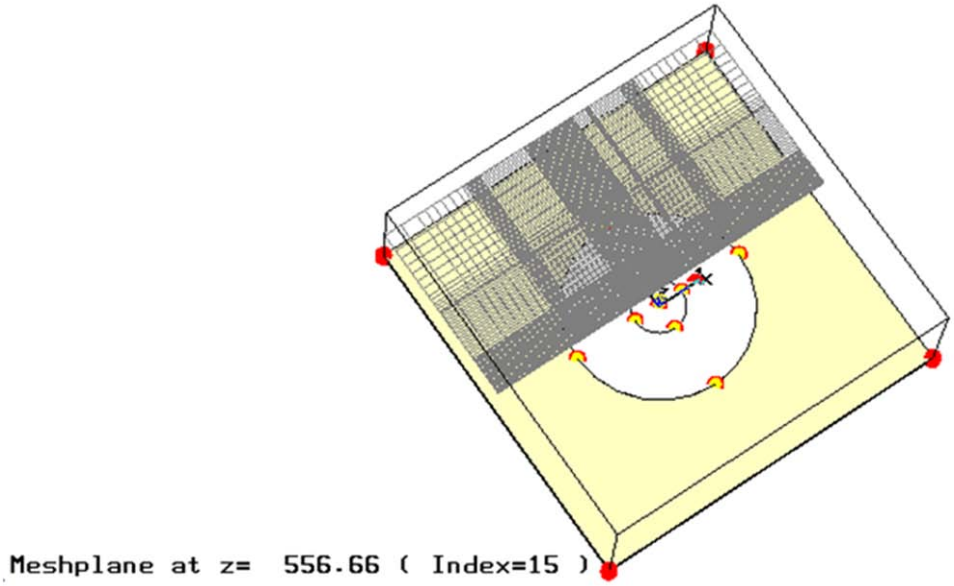

Figure 2-41: Simulation Model of Shorted Annular Ring

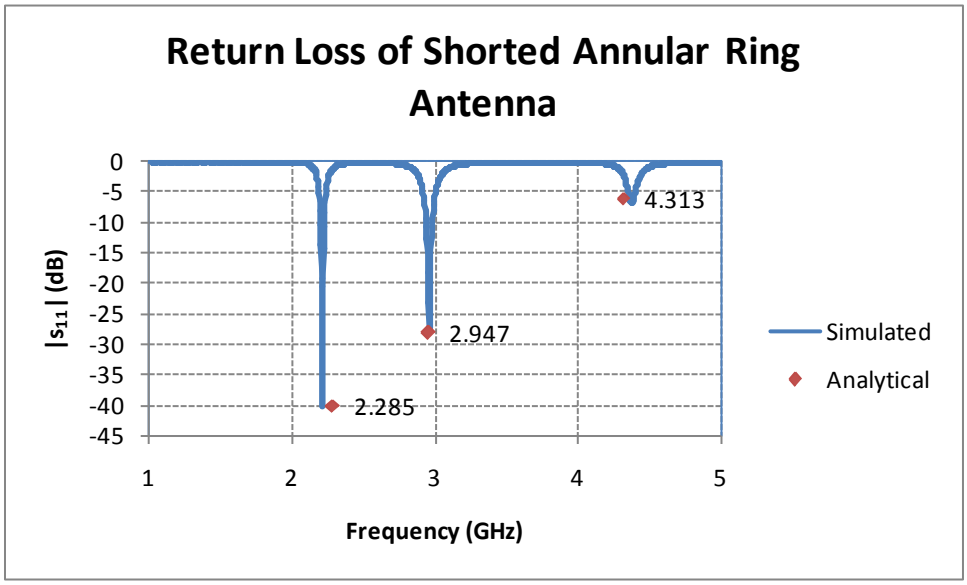

Figure 2-42: Comparison of Resonant Frequencies for the Shorted Annular Ring Having the Dimensions shown in Table 2-5: Simulation vs. Analytical

There are many solution sets for the inner and outer radius of a shorted annular ring that will satisfy (2-26) for the same resonant frequency. Several factors go into the selection of the inner and outer radius for a desired operating frequency. If restraints exist on the outer radius of the structure, a smaller value for '*a*' would be desirable. In some instances, a smaller frequency antenna is placed inside of the shorted inner radius [44-46], and thus a larger 'b' would be desirable in order to leave sufficient room for this second antenna. The separation between the modes depends on the ratio of the radii. Figure 2-43 shows a plot with the ratio of the inner to

outer radius on the horizontal axis. The vertical axis shows the resonant frequency, and there are curves for the first four modes that will exist in this structure. For these calculations, the outer radius, substrate height, and dielectric constant are those from Table 2-5. The inner radius of the structure was varied, and the resonant frequencies were calculated analytically from (2-26) and (2-27). The plot shows that the resonant frequencies are farther apart for smaller b/a ratios. As the outer radius gets closer to the inner radius, the resonant frequencies of the lower order modes grow faster than those of each higher mode, and the modes become much closer together. The results shown in this plot match those described in [42]. These factors must all be considered when selecting the radii of this structure.

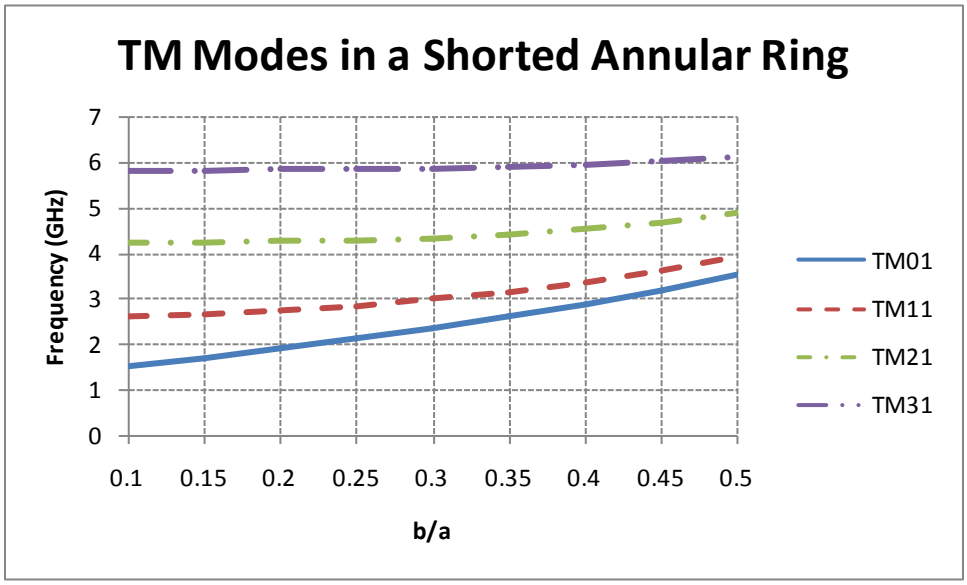

Figure 2-43: Resonant Frequencies in a Shorted Annular Ring as a Function of b/a

The proper mode must be selected in this design to achieve a radiation pattern with the desired characteristics and shape. The fundamental mode, TM_{01}, radiates with a pattern similar to that of a monopole[65]. The TM_{01} surface currents on the annular ring are shown in Figure 2-44. This current distribution shows currents with opposite phase in opposing halves of the annulus resulting in a null at broadside as seen in the patterns of Figure 2-45. The three-dimensional pattern of this mode (Figure 2-46) shows azimuthal symmetry in the radiated fields. The TM_{11} mode radiates with a maximum value at broadside, similar to that of a traditional microstrip patch antenna. The current, principle plane patterns, and three-dimensional pattern of this antenna are shown in Figures 2-47, 2-48, and 2-49 respectively. The TM_{21} currents result in a null at broadside for the radiation pattern in a similar manner to that of the TM_{01} mode. However, they have different azimuthal variation as seen in the three-dimensional pattern. The pattern of this mode contains two full variations in the azimuthal direction. All of the currents

and radiation patterns shown in Figures 2-44 through 2-52 were obtained from CST Microwave Studio simulations utilizing a 50Ω probe feed located on the x-axis.

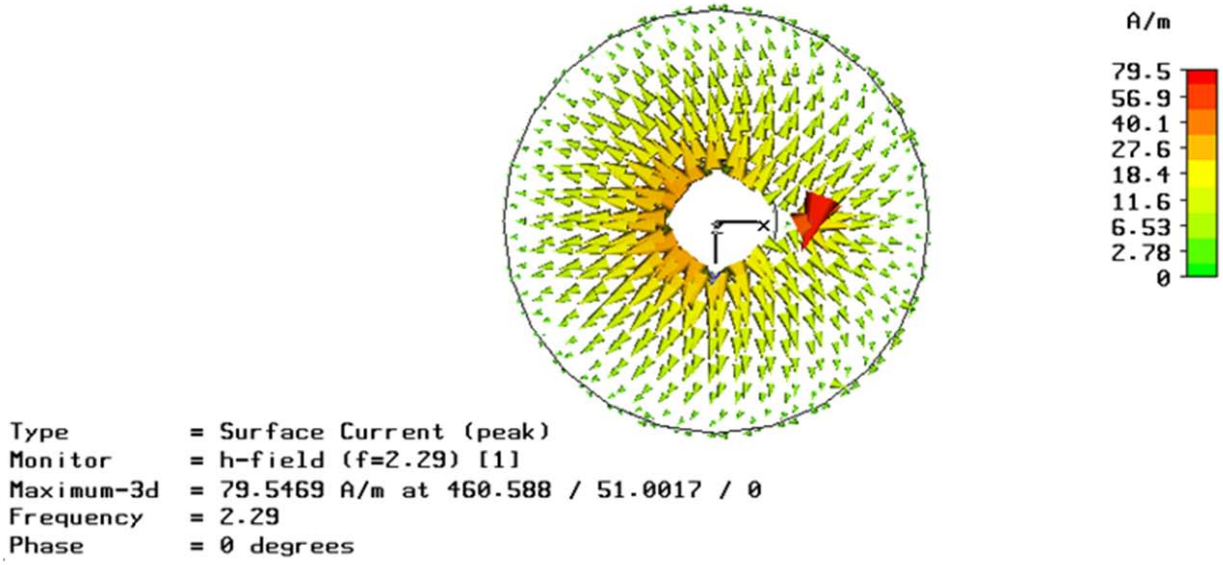

Figure 2-44: TM_{01} Surface Current for Shorted Annular Ring Antenna

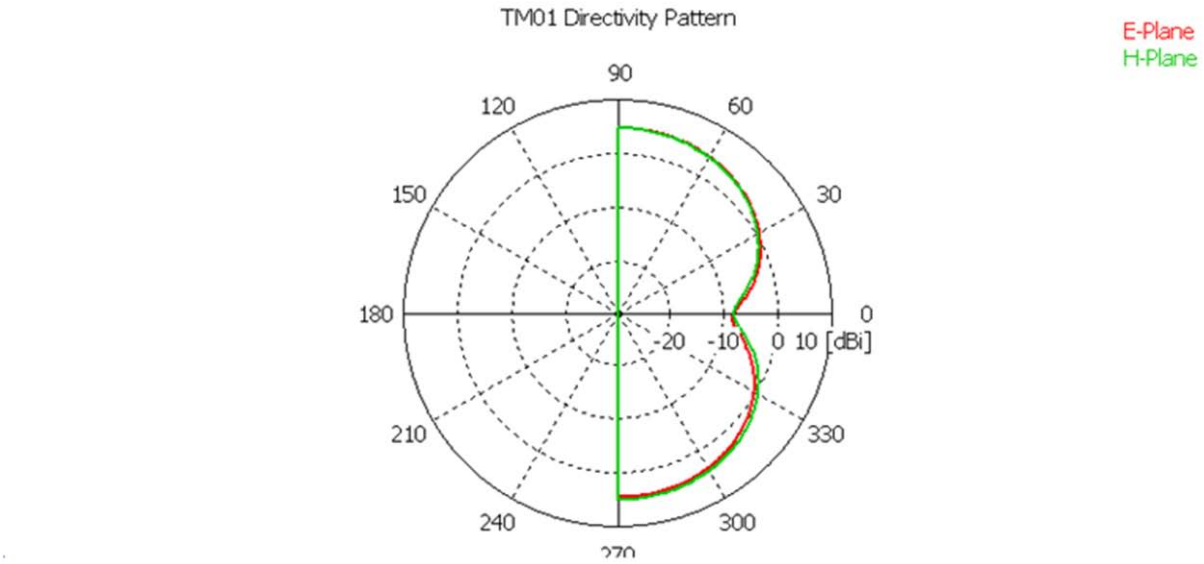

Figure 2-45: TM_{01} Principle Plane Patterns for Shorted Annular Ring Antenna

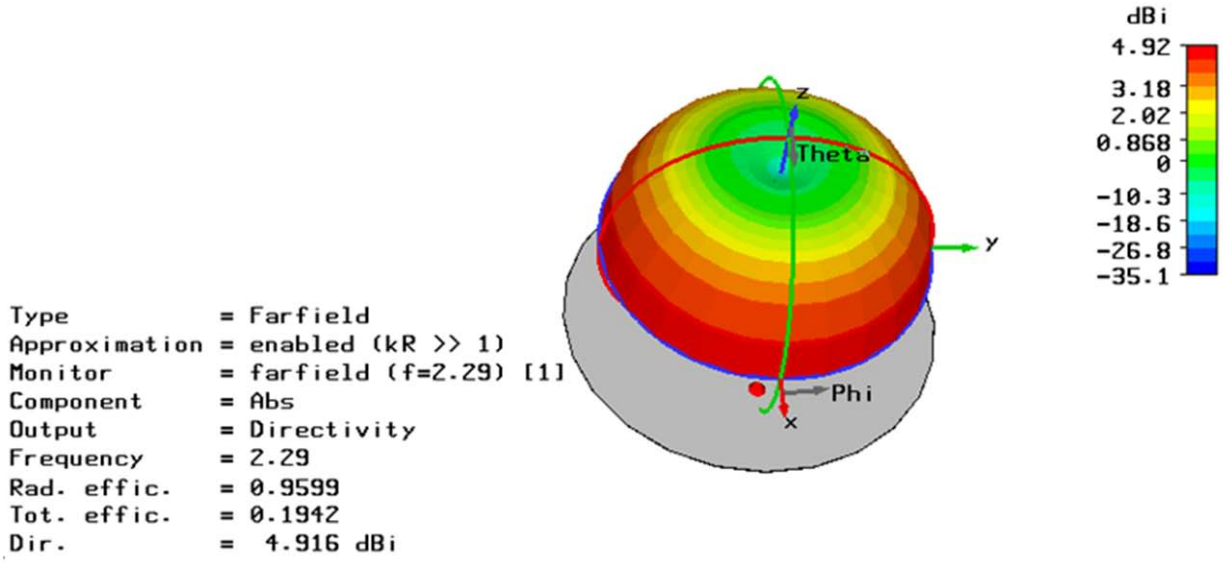

Figure 2-46: TM_{01} 3D Pattern for Shorted Annular Ring Antenna

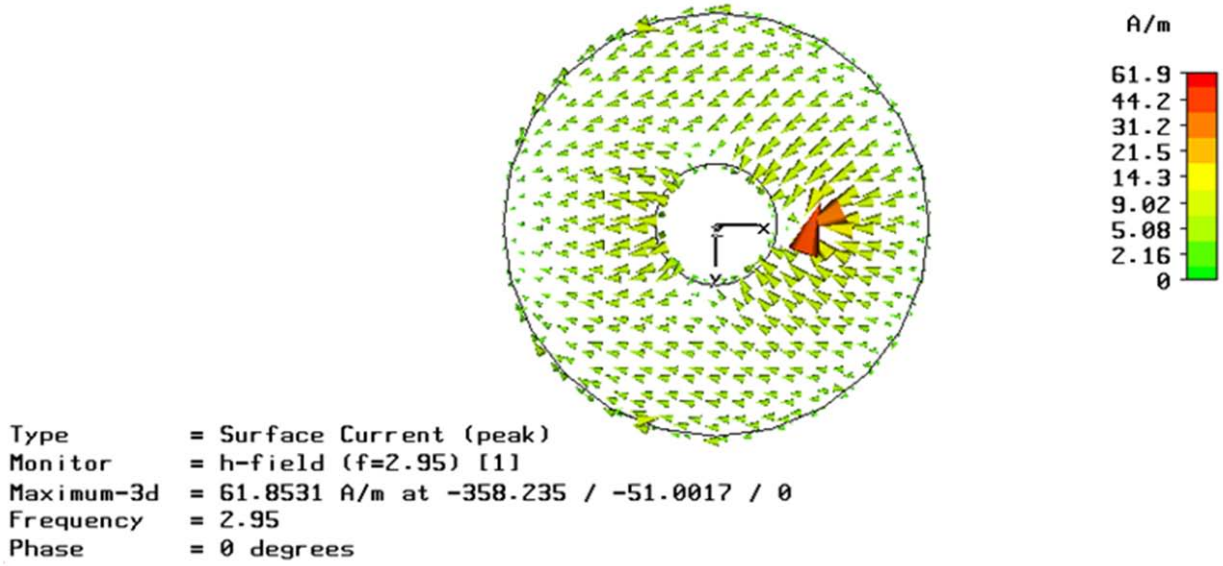

Figure 2-47: TM_{11} Surface Current for Shorted Annular Ring Antenna

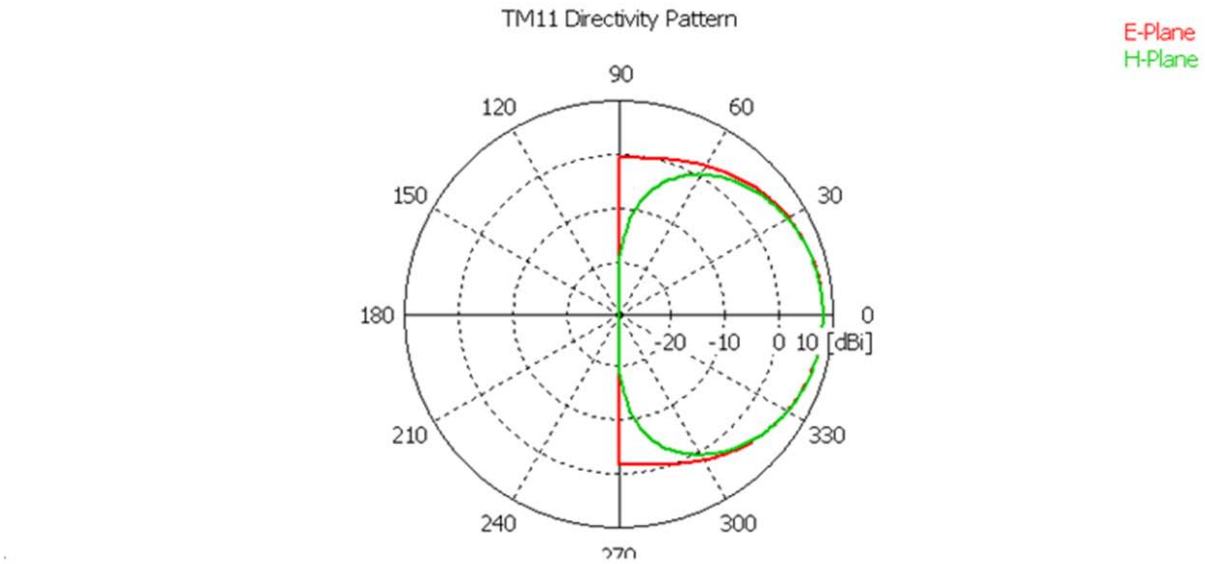

Figure 2-48: TM_{11} Principle Plane Patterns for Shorted Annular Ring Antenna

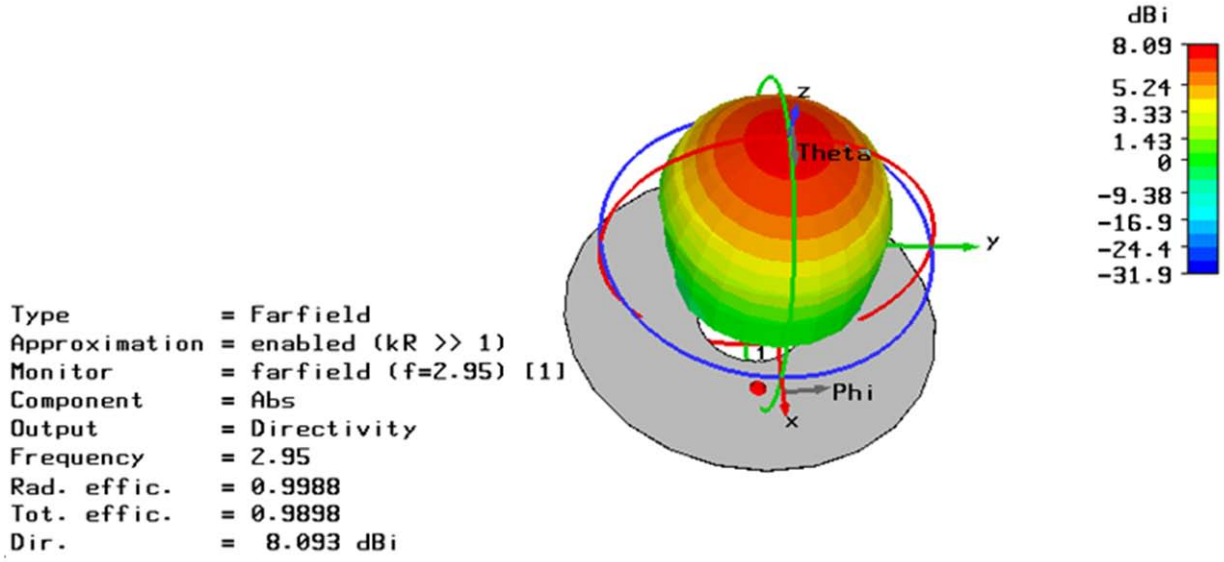

Figure 2-49: TM_{11} 3D Pattern for Shorted Annular Ring Antenna

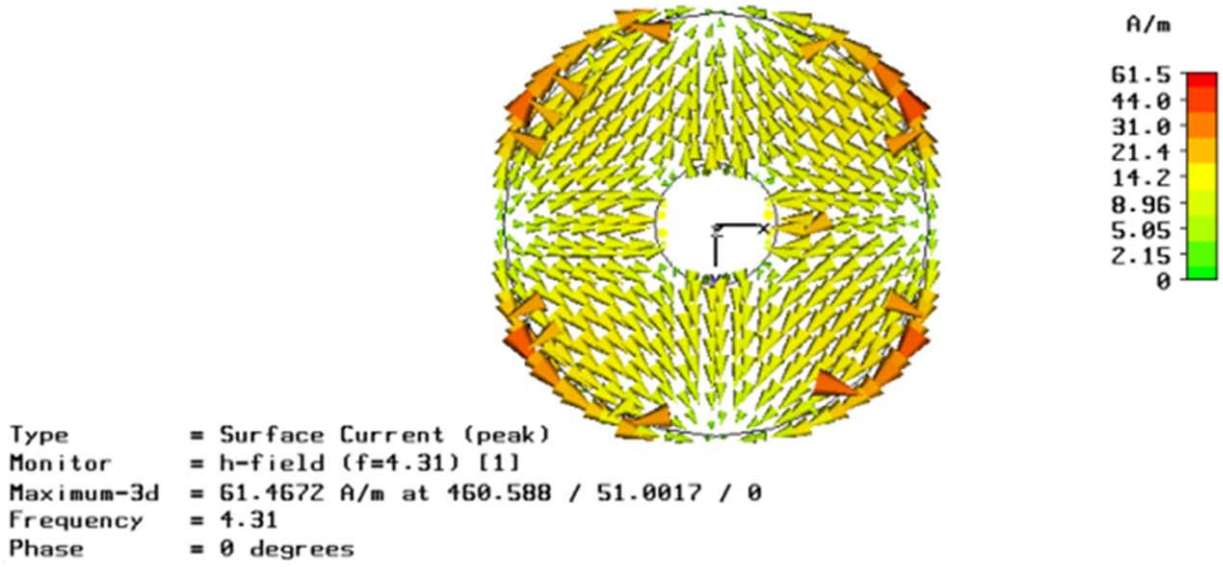

Figure 2-50: TM_{21} Surface Current for Shorted Annular Ring Antenna

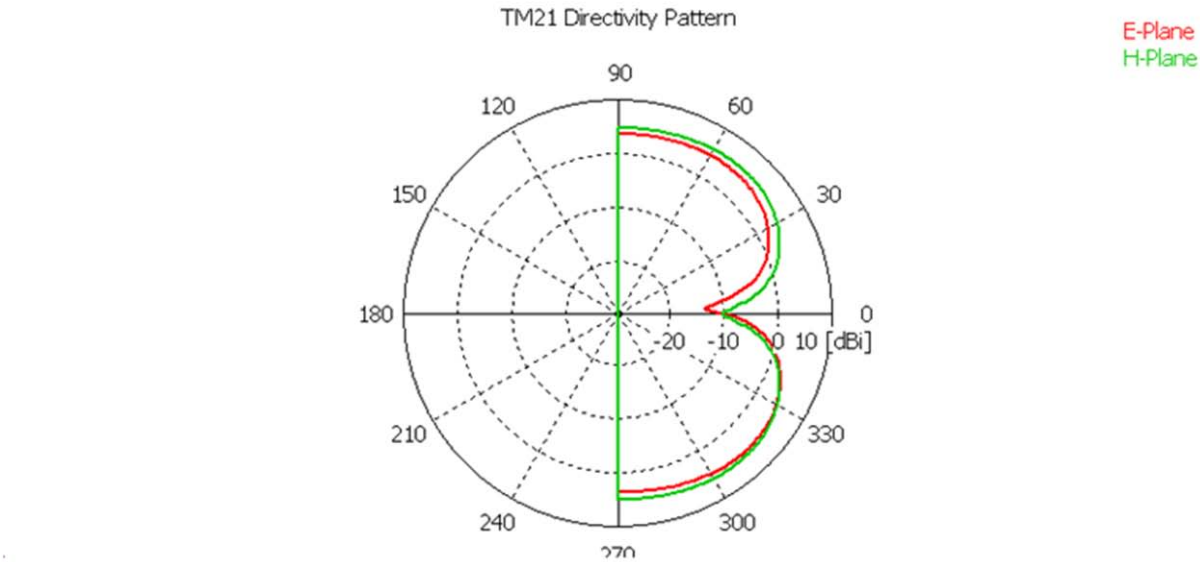

Figure 2-51: TM_{21} Principle Plane Patterns for Shorted Annular Ring Antenna

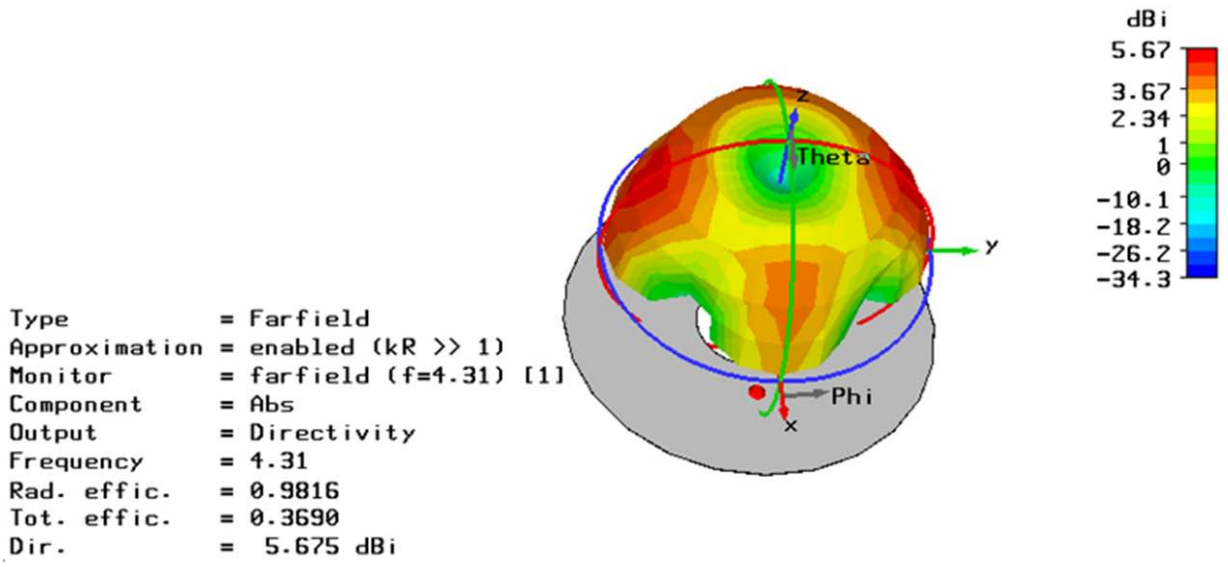

Figure 2-52: TM_{21} 3D Pattern for Shorted Annular Ring Antenna

A shorted annular ring operating in the TM_{11} mode was built and tested in the compact range of the Naval Research Laboratory. Prior to building this element, simulations were performed using a finite ground plane to serve as a comparison to the built element. The analytical work and simulations with the infinite ground plane showed a resonant frequency of 2.95GHz. The finite ground plane slightly increased the resonant frequency of the antenna to 3GHz. Finite ground planes have been seen to increase resonant frequency in other antennas [65]. The constructed element used a CuFlon substrate, a copper-clad Teflon material with a dielectric constant of 2.1.

The dimensions of the antenna are shown in Table 2-7, and a photograph of the antenna is shown in Figure 2-53. The measured performance had excellent agreement with the CST Microwave Studio Simulations. The return loss plot of Figure 2-54 shows a difference in resonant frequency for the TM_{11} mode of less than 1.5%. Also, the measured E- and H-plane gain patterns have excellent agreement in both shape and magnitude with the simulations as seen in Figures 2-55 and 2-56.

Table 2-7: for Shorted Annular Ring Antenna

Parameter	Value
Outer Radius (a)	0.87”
Inner Radius (b)	0.25”
Feed Location	0.4”
Ground Plane Outer Radius	1.25”
Substrate Height	0.062”

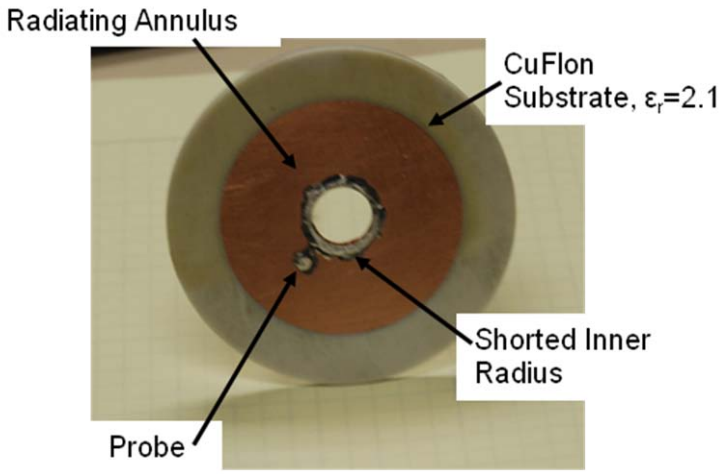

Figure 2-53: Photograph of Constructed Shorted Annular Ring Antenna

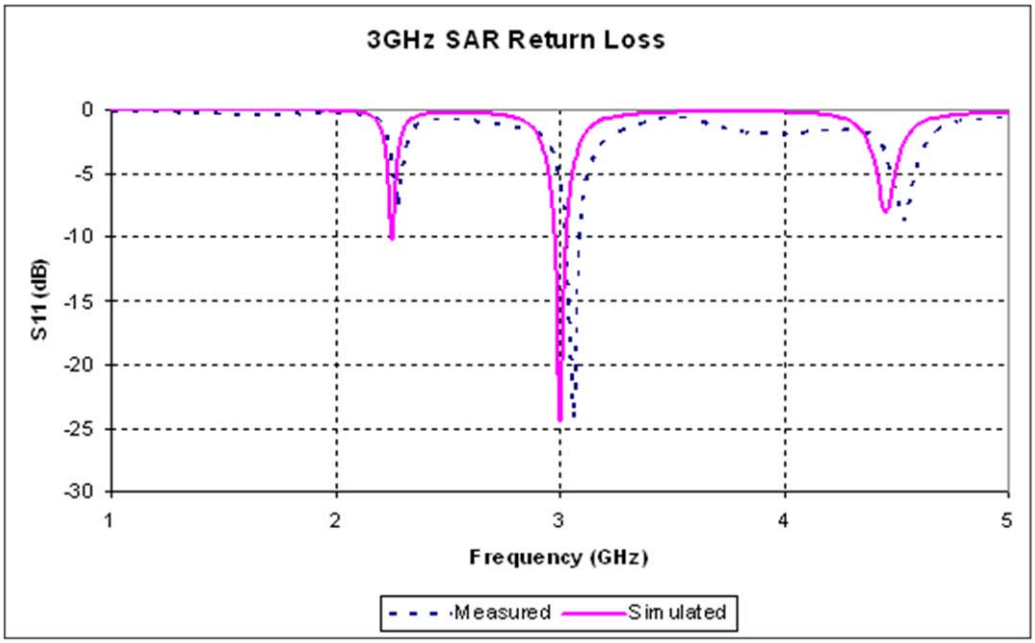

Figure 2-54: Measured and Simulated Return Loss of Shorted Annular Ring

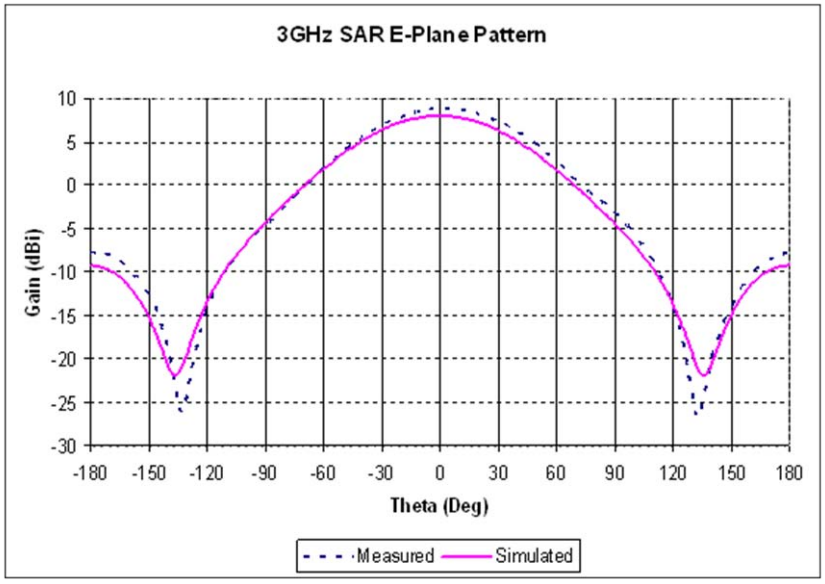

Figure 2-55: Measured and Simulated E-Plane Gain Pattern for Shorted Annular Ring

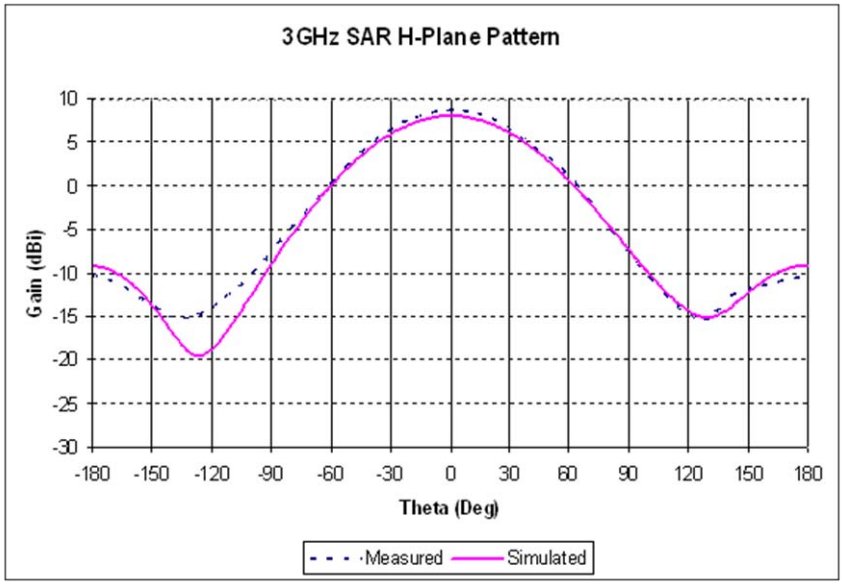

Figure 2-56: Measured and Simulated H-Plane Pattern for Shorted Annular Ring

2.2.2 Modal Analysis for Shorted Square Ring Antenna

The shorted square ring antenna is similar to the shorted annular ring described in the previous section. This antenna has a square radiator of side length 2a shorted by a square aperture of side length 2b. This structure is illustrated in Figure 2-2. This structure has a complex set of boundary conditions that does not lead to a convenient analytical expression for the resonant

frequencies like the shorted annular ring did. As a result, the resonant frequencies can be calculated either numerically or via simulations. A comparison of the boundary conditions between the circular and square shorted ring antennas is provided in Table 2-8.

Table 2-8: Boundary Conditions for Shorted Square Ring

	Circular Shorted Ring	Square Shorted Ring
PEC Location	$\rho = b$	$x = \pm b \; for \; \lvert y \rvert \leq b$ $y = \pm b \; for \; \lvert x \rvert \leq b$
PMC Location	$\rho = a$	$x = \pm a \; for \; \lvert y \rvert \leq a$ $y = \pm a \; for \; \lvert x \rvert \leq a$

As an example, we can begin with the dimensions shown in Table 2-9. The inner side length in this example has been left as a parameter. As the ratio of 'b' to 'a' increases, the modes in this structure grow closer together, just as they did in the shorted annular ring. The resonant frequencies used for the plot in Figure 2-57 were obtained through simulations in CST Microwave Studio.

Table 2-9: Dimensions for Shorted Square Ring Example

Parameter	Value
a	0.655"
b	0.25"
h	0.06"
ε_r	3.48

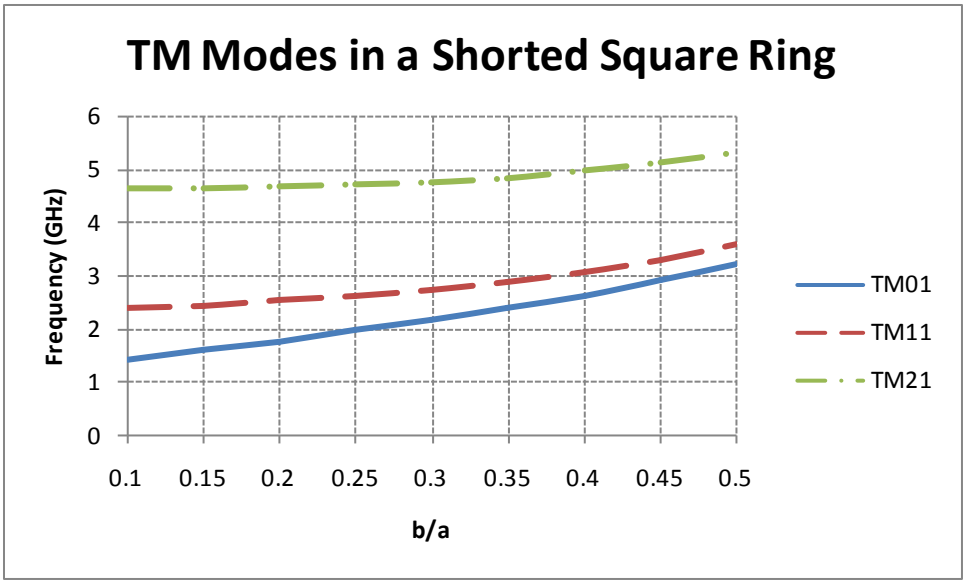

Figure 2-57: Resonant Frequencies in a Shorted Square Ring as a Function of b/a

The CST Microwave Studio model used for simulating this element is shown in Figure 2-58. This structure was fed with an ideal probe feed, and the resulting return loss plot is shown in Figure 2-59. The return loss shows that the TM_{01} mode resonates near 2.5GHz, the TM_{11} mode near 3GHz, and the TM_{21} mode just below 5 GHz. The TM_{11} mode has a return loss below -10dB over a 1.5% frequency bandwidth.

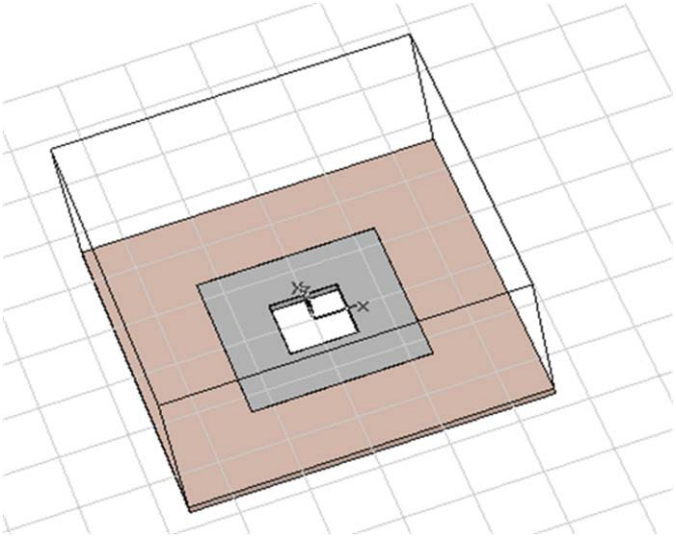

Figure 2-58: CST Model of Square Shorted Ring

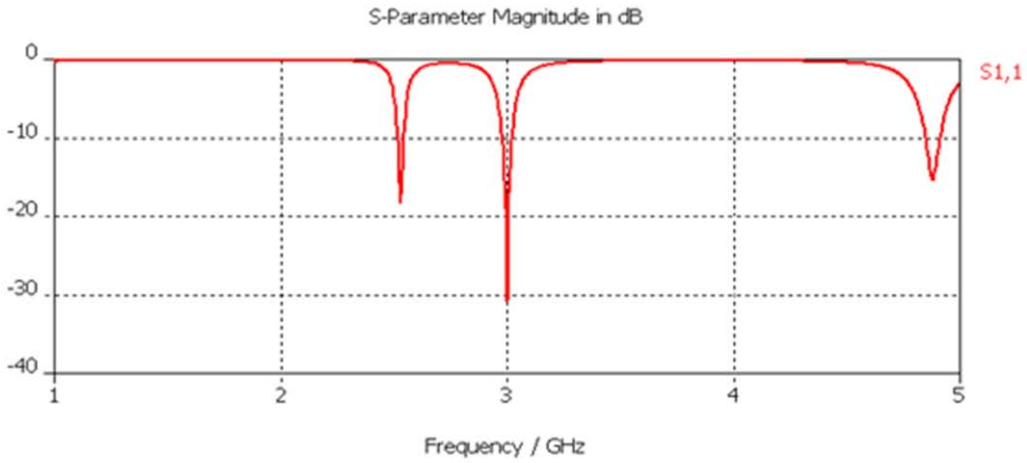

Figure 2-59: Simulated Return Loss of Square Shorted Ring Using Dimensions from Table 2-9

The TM_{01} mode has a radiation pattern with a maximum directed in the endfire direction similar to that of a monopole. The surface current, principle plane patterns, and three-dimensional radiation pattern are shown in Figures 2-60 through 2-62 respectively. This mode could be attractive for vehicle-mounted antennas only concerned with coverage over a limited elevation angle measured from the horizon.

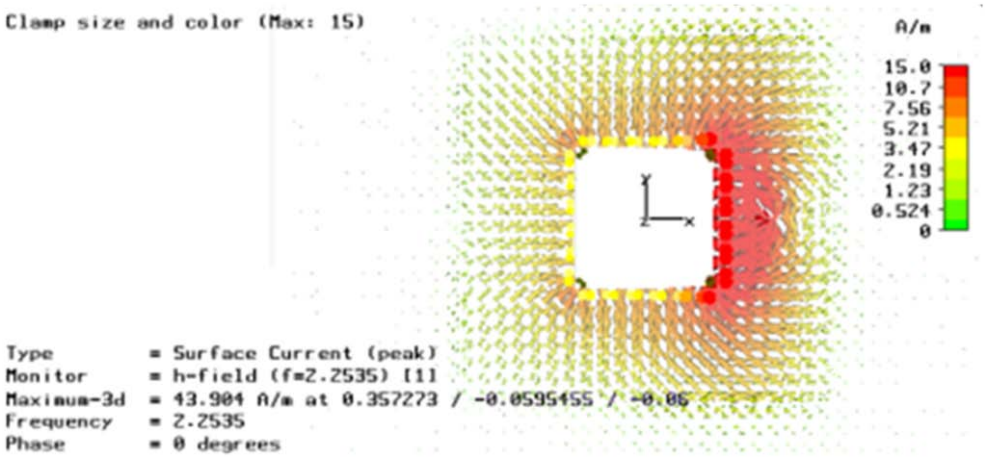

Figure 2-60: Square Shorted Ring TM_{01} Surface Current

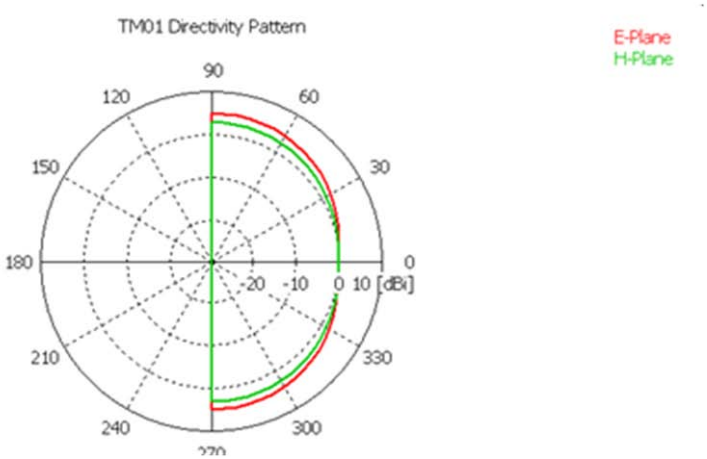

Figure 2-61: Square Shorted Ring TM_{01} Principle Plane Patterns

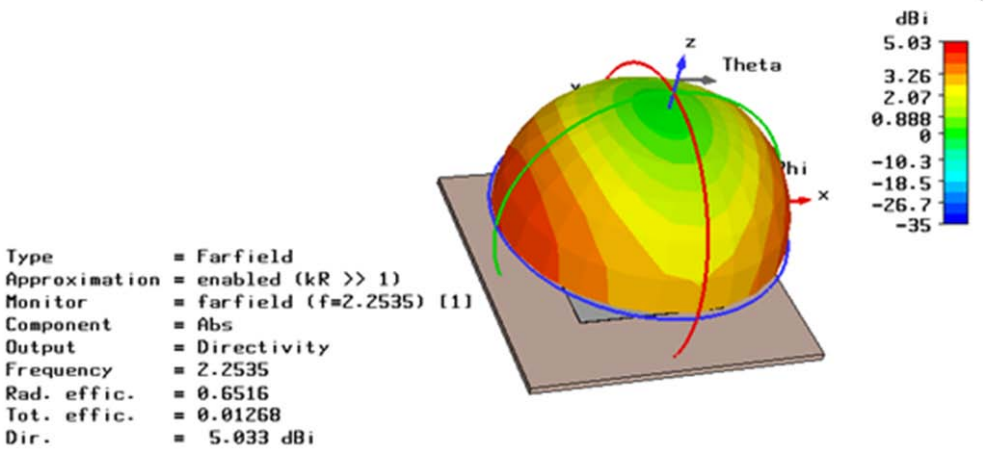

Figure 2-62: Square Shorted Ring TM_{01} 3D Pattern

The TM_{11} mode of the Square Shorted Ring antenna radiates with a broadside pattern similar to that of a traditional microstrip patch antenna. The surface currents, principle plane pattern, and 3D patterns of this device are shown in Figures 2-63 through 2-65. In this simulation, this was the mode that was focused on. As a result, the best match was obtained for this mode.

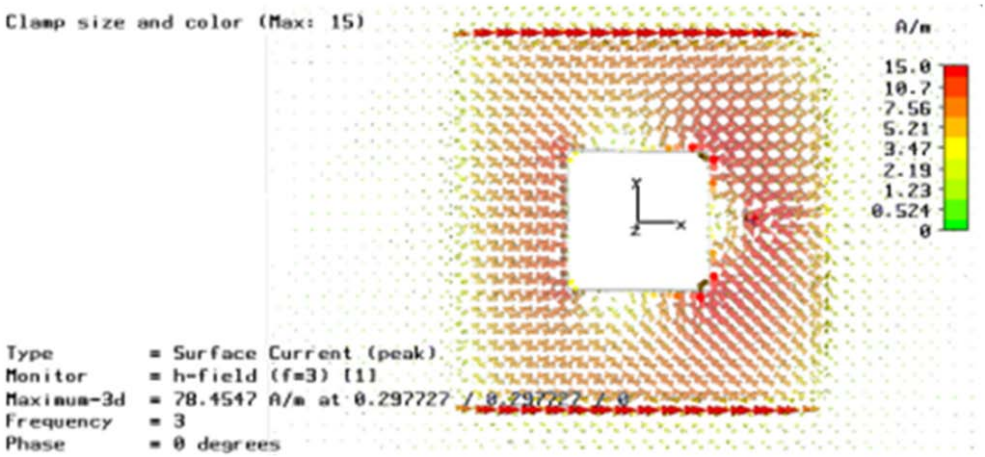

Figure 2-63: Square Shorted Ring TM_{11} Surface Current

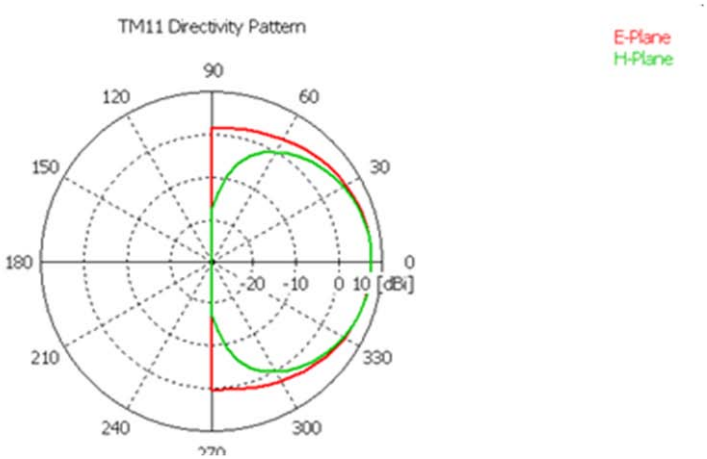

Figure 2-64: Square Shorted Ring TM_{11} Principle Plane Patterns

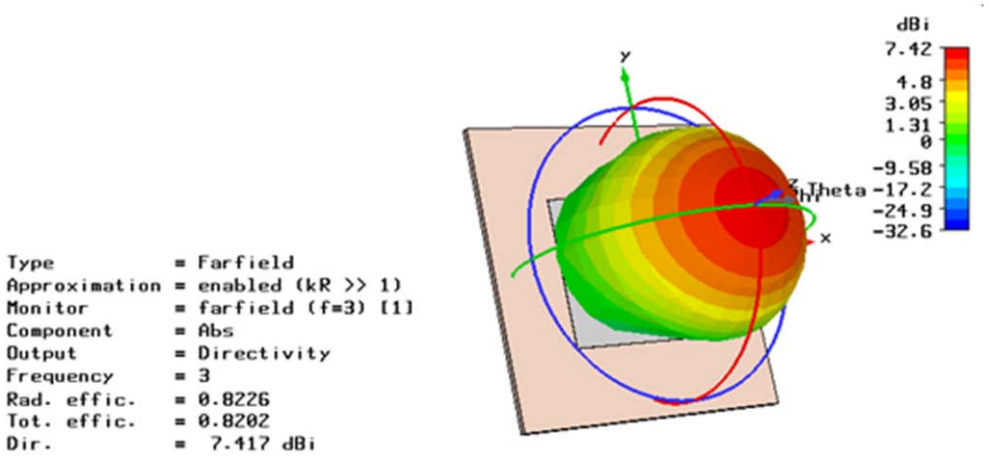

Figure 2-65: Square Shorted Ring TM_{11} 3D Pattern

The third resonant mode, TM_{21}, has a surface current with a higher degree of variation as shown in Figure 2-66. This current distribution results in principle plane patterns with a null at broadside as shown in Figure 2-67. Additionally, the azimuth pattern has nulls in the planes at 45 degrees and 135 degrees and two full variations as shown in Figure 2-68.

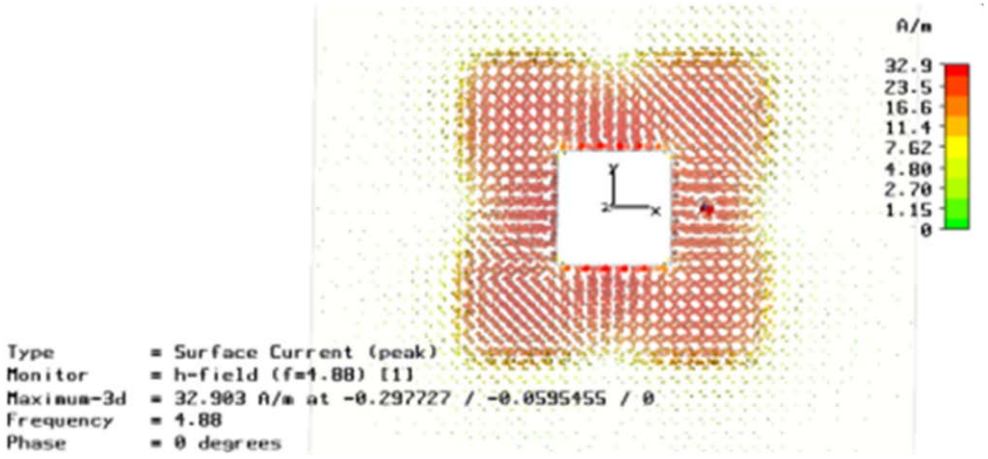

Figure 2-66: Square Shorted Ring TM_{21} Surface Current

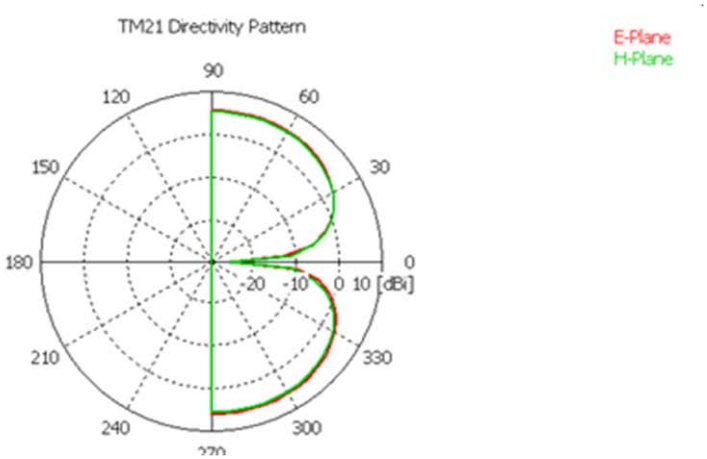

Figure 2-67: Square Shorted Ring TM_{21} Principle Plane Patterns

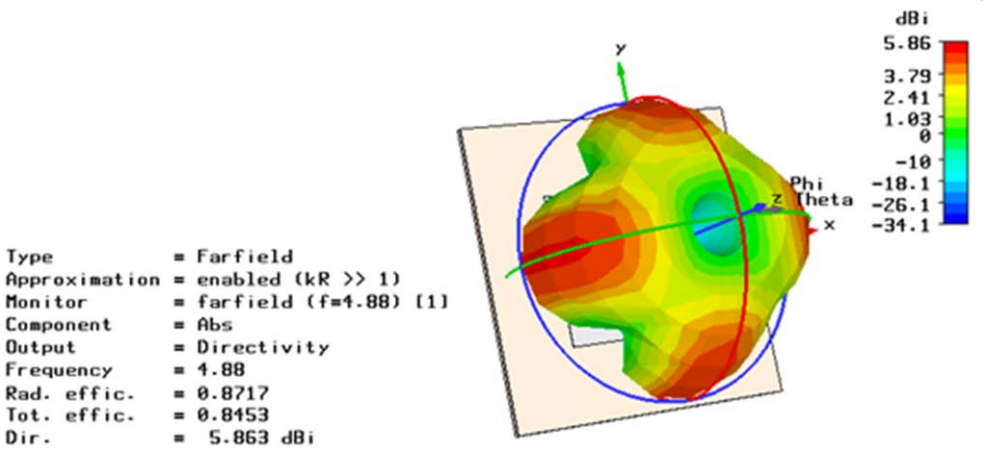

Figure 2-68: Square Shorted Ring TM_{21} 3D Pattern

2.2.3 Single-Feed CP Operation of Shorted Square Ring Antennas

The shorted square ring radiates with linear polarization when fed with a single probe. The polarization is parallel to a line passing from the probe through the center of the antenna. Circular polarization can be obtained through the addition of a second probe fed in phase quadrature. This technique introduces the need for a hybrid and a second probe feed making it non-ideal. Alternatively, circular polarization can be obtained with a single probe feed. This is done by truncating two opposing corners of the ring antenna as shown in Figure 2-69 [55-57].

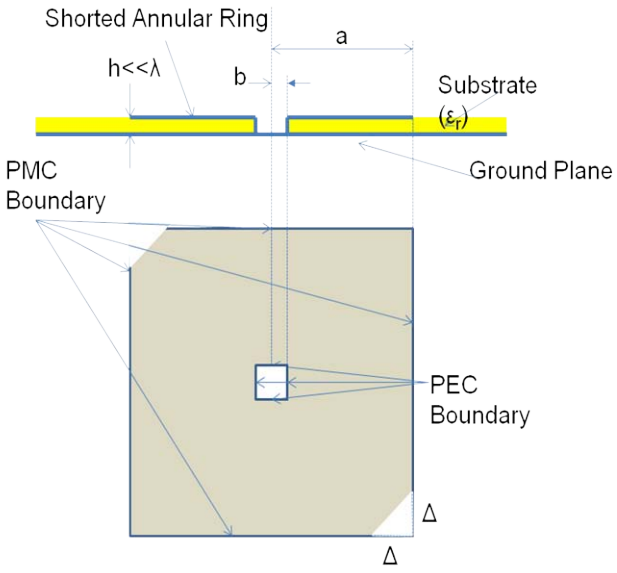

Figure 2-69: Single Feed Circularly Polarized Shorted Square Ring

The truncated corners allow two orthogonal, diagonal modes to exist at slightly different frequencies. The mode in the diagonal containing the chopped corners resonates at a slightly higher frequency than the orthogonal mode due to the shorter length of the diagonal. The feed point of the antenna is chosen to provide the proper phase shift between the two modes which creates the circular polarization. The feed location can be parallel to either the x- or y- axis to provide RHCP or LHCP.

The area of the truncated corner can be calculated from the quality factor of the unloaded antenna [57]. From previous simulations described in 2.2.2, the unloaded antenna was seen to have a frequency bandwidth of 1.5%. This value corresponds to a quality factor of 69.8. Using the equation provided in [57], we can calculate the area of the truncated corner and length (Δ) of the side for the equilateral truncations as shown in (2-29), where Δ_{AREA} is the ratio of the truncation area to the area of the unloaded ring. The area of the truncation results in an equilateral triangle with the length of 0.119". The resonant frequency of the mode in the plane containing the truncations can be calculated from (2-30).

$$\Delta_{AREA} = \frac{1}{2Q} = 0.007 \quad \textbf{(2-29)}$$

$$f_1 = f_0\left(1 + \frac{2\Delta_{AREA}}{((2a)^2-(2b)^2)}\right) = 3.02GHz \quad \textbf{(2-30)}$$

Figure 2-70 provides a plot showing the simulated results for the return loss and axial ratio of the Square Shorted Ring with single feed circular polarization of Figure 2-71. The return loss shows the generation of the second, near degenerate mode, near the calculated value of 3.02 GHz. The curves show an extremely narrow 3dB Axial Ratio bandwidth of 0.75% and a -10dB return loss bandwidth of 2.91%. The dimensions of this antenna are provided in Table 2-10. The value for

Δ obtained through simulations was 0.110”, and it corresponds very well to the calculated value of 0.119”. This configuration resulted in RHCP. The feed could be rotated to the orthogonal plane to obtain LHCP.

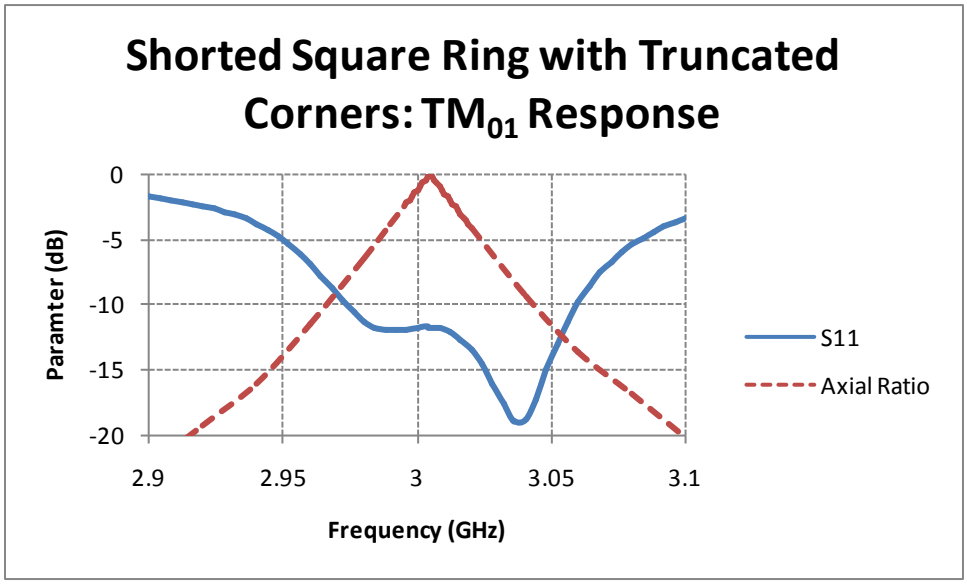

Figure 2-70: Simulated Return Loss and Axial Ratio for Shorted Square Ring with Single Feed CP

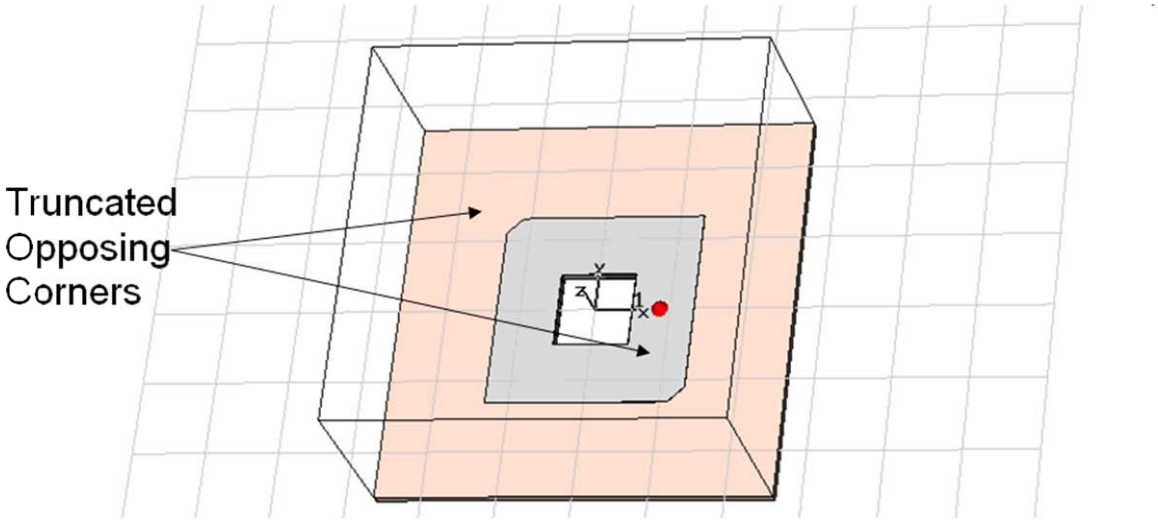

Figure 2-71: Simulation Model for Shorted Square Ring with Single Feed CP

Table 2-10: Dimensions for Shorted Square Ring with Single Feed CP

Parameter	Value
A	0.6575”
B	0.25”
Δ	0.11”
Feed Location	0.42”
h	0.06”
ε_r	3.48

2.2.4 Dual-Substrate Capacitive Loading for Size Reduction in Shorted Annular Ring Antennas

Many RF applications place a size and weight restriction on the antenna. For instance, a payload that is to be deployed on a satellite has a restricted overall mass and volume [14]. Thus, a lighter antenna leaves more weight available for pertinent electronics on the payload. Another example stems from the ever-advancing technology in the field of cellular communications. With the increased popularity of compact cellular handsets and portable satellite communication devices, the ability to reduce the antennas size has become a necessity. Additional restraints on the antenna size have resulted from the need for antenna diversity, which requires the placement of multiple antennas within a single handset. These are two examples of fields where a compact size antenna is ideal.

The shorted annular ring antenna, shown in Figure 2-1, is often used because its two critical radii can be manipulated to satisfy the dominant mode resonance condition of a standard circular patch and also keep from exciting a surface wave mode in the substrate [63]. These two conditions are met as long as the inner radius and outer radius are chosen to satisfy a transcendental equation.

This section discusses an edge loading technique that introduces capacitive loading into a shorted annular ring antenna resulting in a significant reduction of element’s footprint. If the inner radius is selected to obtain a given outer radius, a smaller outer radius can be obtained once the edge loading technique is added to the design. A traditional shorted annular ring antenna was designed and modeled using the full-wave analysis method of Finite Integration Technique (FIT), implemented in CST Microwave Studio [42]. Shorted annular ring antennas with and without the proposed capacitive loading technique were simulated, built, and tested to show the size reduction using this technique.

This element can also be used for applications requiring circular polarization. Maintaining axial symmetry is an important factor in improving polarization characteristics [66]. Subsequently, the circular symmetry of this element makes it ideal for applications requiring circular (or dual-linear) polarization. A sequential phase quadrature feeding of the element has been seen to produce circular polarizations with low axial ratio.

The transcendental equation governing the modes in the shorted annular ring antenna can be solved by viewing the region beneath the radiating annulus as a cavity that is shorted at the inner radius. The resulting characteristic equation governing the TM_{n1} modes in the structure is shown in (2-31). A thorough presentation of this derivation accounting for the fringing fields is presented in [5, 67, 68] as well as section 2.2.1. In this equation, J_n and Y_n are Bessel functions of the first and second kind respectively; a and b are the outer and inner radius of the shorted ring antenna respectively. The derivatives can be removed from (2-31) by applying Bessel function identities. The resulting expression shown in (2-32) is simpler to use since no derivatives need to be calculated.

$$J_n(k_{n1}b)Y_n'(k_{n1}a) = Y_n(k_{n1}b)J_n'(k_{n1}a) \quad \textbf{(2-31)}$$

$$\left[k_{n1}J_{n-1}(k_{n1}a) - \frac{n}{a}J_n(k_{n1}a)\right]Y_n(k_{n1}b) - J_n(k_{n1}b)\left[k_{n1}Y_{n-1}(k_{n1}b) - \frac{n}{a}Y_n(k_{n1}b)\right] = 0 \quad \textbf{(2-32)}$$

The proper mode must be selected in this design to achieve a radiation pattern with the desired characteristics and shape. The dominant mode, TM_{01}, radiates with a pattern similar to that of a monopole. The TM_{11} mode radiates with a maximum value at broadside, similar to that of a traditional microstrip patch antenna. Once the desired mode has been determined, the inner and outer radius can be found from solving (2-32).

A limited size reduction can be obtained by reducing the inner radius in (2) and solving for the outer radius. In some instances, a higher frequency antenna is placed within the inner radius of the shorted annular ring antenna to provide dual-band operation [5, 68], thus limiting the minimum value for the inner radius. Additional size reduction can also be achieved by increasing the dielectric constant of the substrate (ε_r). However, high dielectric constant materials have several drawbacks including high cost [69].

In recent years, different capacitive loading schemes have been used to manipulate the resonant frequency of an antenna, and thus reduce its size. Ciais et al showed that the size of a planar inverted-F antenna (PIFA) can be decreased by adding a capacitive loading post at the edge of the device [70]. The size of the device decreases as the capacitance of the loading structure increases. A similar technique is used in [71] to reduce the size of a cellular handset antenna. However, this size reduction is not obtained without a drawback. It has been shown that the quality factor of the structure increases with load capacitance [72]. The techniques described in [70-72] make use of a capacitive conductor in a plane perpendicular to the radiating conductor to achieve size reduction. The gap between the capacitive conductor and the ground plane determines the capacitance of the load structure. One feature of these methods is that a single substrate is present beneath the radiator and the capacitive loading structure. A higher dielectric constant material would lead to an increased capacitance, resulting in greater size reduction. However, this would also result in a high dielectric constant beneath the entire radiating

structure. The use of high dielectric constant beneath the radiating structure of a patch antenna has been shown to produce narrow bandwidth, low efficiency, and a poor radiation pattern [69, 73].

A capacitive loading technique that reduces the size of a shorted annular ring antenna is illustrated in Figure 2-72 in section view. This structure has several key features that control the capacitive loading. In this antenna, there are two separate substrates. The larger substrate is called the *radiator substrate*, and this material is made of a RF substrate with a low dielectric constant and low loss tangent. The smaller substrate, contained beneath the *capacitive patch*, can be a high dielectric constant material and is referred to as the *capacitive substrate*. The *capacitive patch* is connected to the radiating SAR antenna through a capacitive loading ring which is a cylindrical structure located at the outer radius and perpendicular to the radiating and capacitive patches. In printed circuit designs, it is often easier to realize the capacitive loading ring with a series of plated through holes present at the outer radius of the structure. The three-dimensional section provided in Figure 2-73 illustrates the use of these *capacitive vias*. The structure makes use of a capacitive loading structure in a plane perpendicular to the radiator similar to the techniques described in [70, 71]. However, in this design, the capacitive load structure is circularly symmetric to maintain the symmetry of the shorted annular ring antenna. This allows for an orthogonal feed to be inserted where it sees the exact same boundary conditions as neighboring feeds, thus permitting the addition of multiple feeds for circular, or dual-linear, polarization.

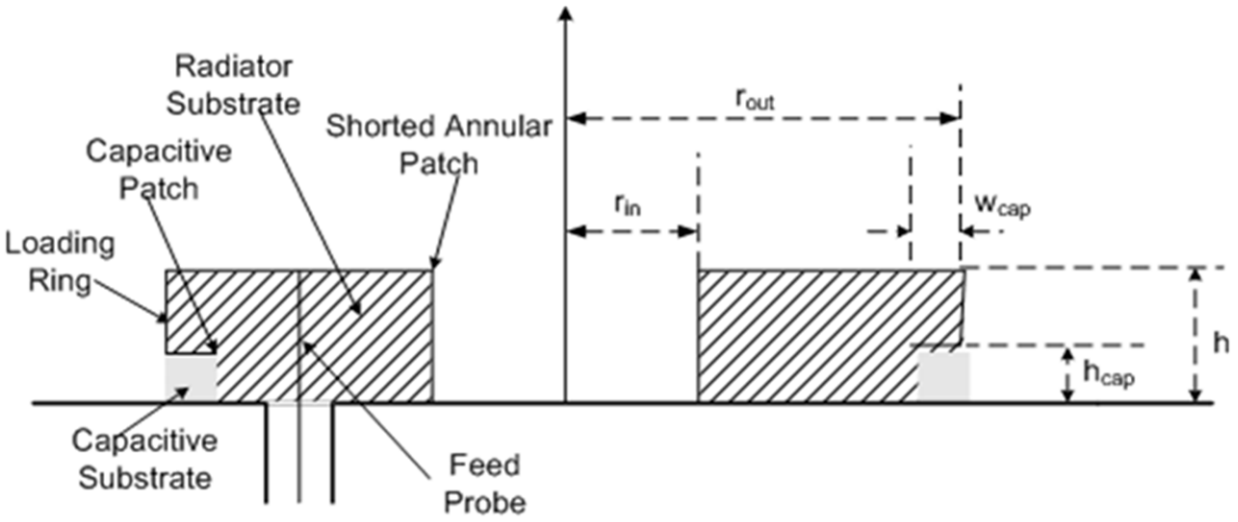

Figure 2-72: 2D Cross-Section of a shorted annular ring antenna with dual-substrate capacitive loading

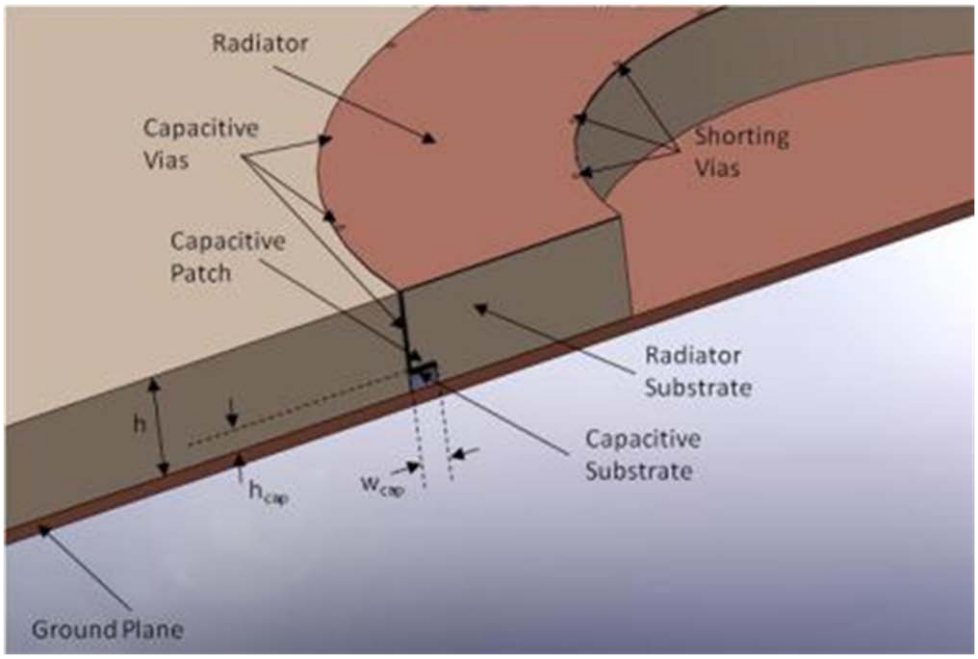

Figure 2-73: Cross-section of an edge-loaded shorted annular ring antenna with a capacitive patch for increased loading effect

The distance between the bottom of the *loading ring* and the ground plane is a key parameter in controlling the capacitance of the load. The inner radius of the *capacitive patch* and the dielectric constant of the *capacitor substrate* are the other two parameters that also impact the loading. In a parallel plate capacitor, the capacitance is determined by three variables: 1) *S* is the surface area of the plate, (2) *d* is the separation between the plate, and (3) ε is the dielectric constant of the substrate. The capacitance of this loading technique behaves in a similar manner; it can be increased by increasing the dielectric constant beneath the patch, decreasing the inner radius of the *capacitive patch* (i.e. increasing the surface area of the *capacitive patch*), and/or decreasing the distance between the ground plane and the *capacitive patch*. This provides the antenna engineer several design variables to use to control the size and performance of the antenna.

Two assembly processes were considered for this element. In the first approach, a single dielectric substrate of full element height would be used as the *radiator substrate*. The radiating patch would be printed on the top of this material, the ground plane is present on the bottom, and the center of the patch is shorted to the ground plane. A groove would then be machined into this substrate with a height and width equal to those of the *capacitive substrate*. The *capacitive patch* would be printed on the top side of the high dielectric constant substrate, and it would be inserted into the groove in the *radiator substrate*. Finally, a conducting ring would be added at the outer radius of the device to provide electrical continuity between the *radiator* and the *capacitive patch*.

A second assembly process was then considered that did not involve the machining of the thin groove for the *capacitive substrate*. In this process, the element was divided vertically in a plane containing the *capacitive patch*. The upper substrate now has a height equal to the overall element height minus the height of the *capacitor substrate*. The *radiator* is printed on the top of this low dielectric constant substrate, and the *capacitive patch* is printed on the bottom. *Capacitive vias* are present at the outer radius of the ring as shown in Figure 2-72. The bottom dielectric layer consists of concentric rings; the inner ring is constructed of the low dielectric constant material, and the outer ring is a thin ring of the high dielectric constant material. The dielectric layers are held in place with a very thin layer≈(0.008cm) of a silicon -based adhesive. The precise dielectric properties of the adhesive are not known, but typical values ($\varepsilon_r \approx 4.0$, $\tan\delta \approx 0.005$) are used to approximate the performance [74]. A ground plane is placed beneath the dielectric layers, and the inner radius of the radiator is shorted to the ground plane. Finally, a feed probe is inserted through the dielectric layers to feed the antenna element. The ground of the coaxial probe is shorted to the ground plane of the antenna, and the center conductor is shorted to the radiating annular ring.

The two low dielectric constant pieces were constructed on Rogers RT/duroid 5880 high frequency laminate ($\varepsilon_r=2.2$, $\tan\delta=0.0009$@10Ghz). The high dielectric piece was used as the capacitive substrate, and this piece was constructed out of Rogers TMM10 ($\varepsilon_r=9.2$, $\tan\delta=0.0022$@10Ghz), a ceramic loaded plastic microwave substrate. The key dimensions of the design are shown in Table 2-11. This table shows that the outer radius for the radiating element is 1.064 cm (0.419”). This radius is just over 48% of the 2.21cm (0.87”) outer radius calculated from (2) for the radiator in a shorted annular ring antennas with the same inner radius and operational frequency. Therefore, it can be seen that the capacitive loading technique results in a reduction of almost 52% in the outer radius of the radiating element. This reduction in radius corresponds to a radiator that would occupy just over 23% of the surface area compared to the area that would be occupied by the unloaded element. This significant size reduction would allow for the inclusion of an antenna that can operate with linear or circular polarization while saving valuable real estate in an RF device.

The capacitively loaded shorted annular ring element was simulated, fabricated, and tested. On performing the simulation, the adhesive used in the assembly process was included in the model. The adhesive layer decreases the capacitance of the loading structure by increasing the distance between the capacitive patch and the ground plane and decreasing the effective dielectric constant of the capacitive substrate. The decreased capacitance causes an increase in the resonant frequency by limiting the overall effect of the loading structure. The simulation model showed that the TM_{11} mode resonates at 3.4 GHz. As shown in Figure 2-74, this compares favorably to the measured return loss, and excellent agreement between the measurements and simulation is illustrated. The agreement indicates the importance of incorporating the dielectric properties and thickness of any adhesive layers into the modeling. Figure 2-74 shows a narrow

impedance bandwidth of 0.8%; this bandwidth is narrower than the 1.5% bandwidth of the unloaded shorted annular ring antenna.

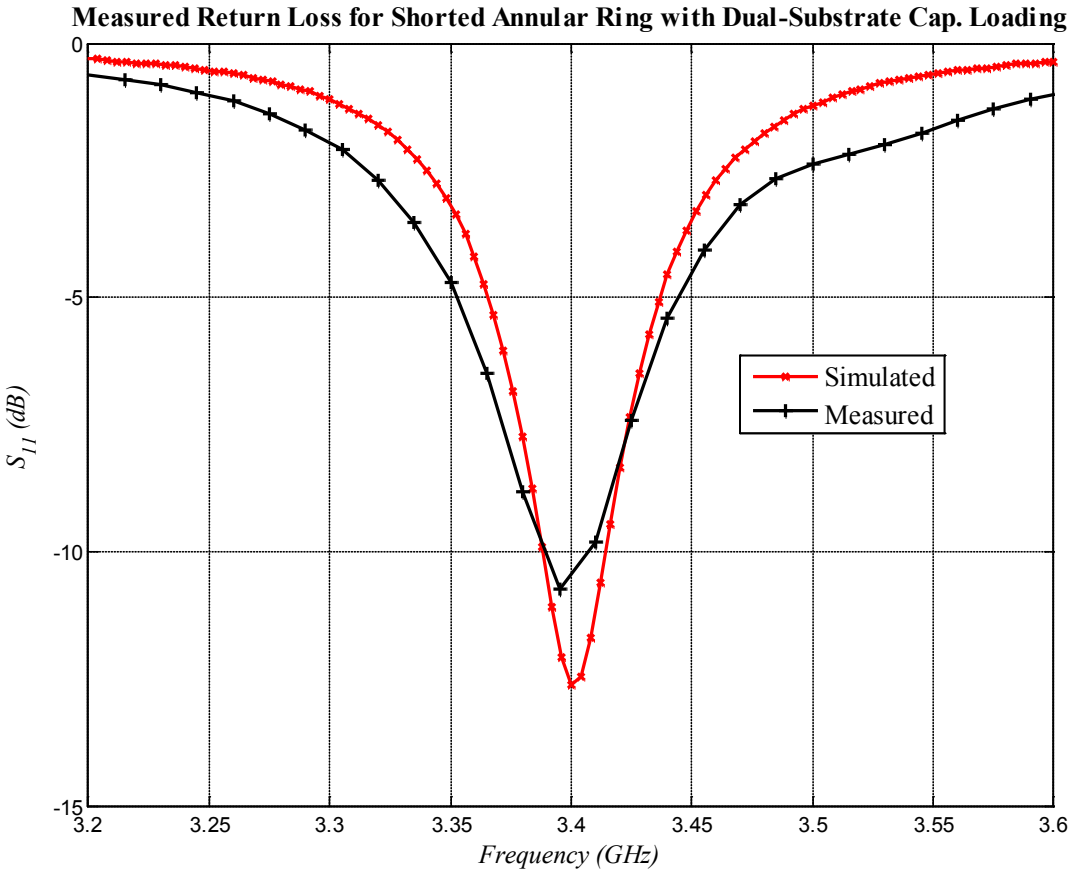

Figure 2-74: Measured Return Loss for Capacitively Loaded Shorted Annular Ring Antenna Element

The radiation patterns of the shorted annular ring antennas, with and without the capacitive loading, were measured in a compact range. The simulated and measured normalized H-plane patterns for the antennas are compared in Figure 2-75. In this figure, the patterns are normalized to 0dB to allow a clear comparison of the radiation pattern shape. The measurements are in excellent agreement with the simulations for both the loaded and unloaded antenna element. The capacitively loaded shorted annular ring antenna shows a broader beam width than the antenna without loading resulting from the smaller aperture size. The capacitively loaded element has a gain of 5.1dBi, which is less than 8.05dBi gain of the unloaded element due to the smaller aperture.

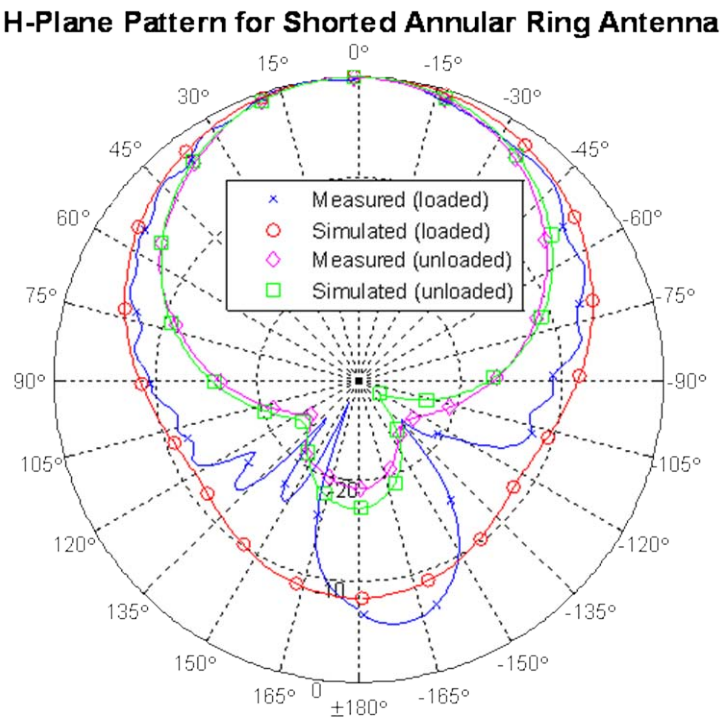

Figure 2-75: H-Plane Pattern for Shorted Annular Ring Antennas

Table 2-11: Dimensions of capacitively loaded shorted 3.4GHz shorted annular ring antenna

ANTENNA SUBSTRATE DIMENSIONS	
Parameter	*Value*
r_{in}	0.635cm (0.25")
r_{out}	1.905cm (0.75")
h	0.183cm (0.072")
CAPACITOR SUBSTRATE DIMENSIONS	
Parameter	*Value*
r_{out}	1.064cm (0.419")
w_{cap}	0.051cm (0.020")
h_{cap}	0.038cm (0.015")
RADIATING ANNULAR RING DIMENSIONS	
Parameter	*Value*
r_{in}	0.635cm (0.25")
r_{out}	1.064cm (0.419")

A multi-substrate capacitive loading technique has been proposed and it provides the antenna engineer with a wide range of variables that can be used to reduce the size of a shorted annular ring antenna. A high dielectric constant material can be used beneath a capacitive loading patch, while the remaining substrate can be made from a low dielectric constant material. The size

reduction is obtained at the expense of decreased impedance bandwidth. An element was built and tested, and the results indicate a reduction in outer radius of greater than 50% when compared to a traditional shorted annular ring of the same inner radius.

CHAPTER 3. LOW PROFILE, DUAL-BAND, DUAL-POLARIZED ANTENNA ELEMENT

A dual-band element has been designed that provides dual-polarized performance in two distinct frequency bands while providing a low profile, printed circuit, lightweight design. The building block for the low band element is the shorted square ring antenna, and the high band radiator is a square ring slot antenna. These elements are inherently linearly polarized, and the sense of the polarization is dependent upon the feed location. If orthogonal feed points are excited, the element can then be operated with dual-linear polarization. Moreover, if opposing corners of these elements are perturbed, the elements can be operated with circular polarization. With perturbations on opposing corners and orthogonal feed lines, dual-CP performance can be obtained. The possible polarization combinations for this element are defined in Table 3-1.

Table 3-1: Possible Polarization States for Dual-Band Dual-Polarization Antenna Element

Low Band Polarization	High Band Polarization
Dual-Circular Pol.	Dual-Circular Pol.
Dual-Circular Pol.	Dual-Linear Pol.
Dual-Linear Pol.	Dual Circular Pol.
Dual-Linear Pol.	Dual-Linear Pol.

The application of two concentric radiators along with the capacitive loading technique provides a unique contribution to the field of antenna engineering. The majority of dual-band antenna elements in the literature operate with a single polarization in each band. The ones that operate with dual-polarization in each band are typically limited to dual-linear polarization. Circular polarization is preferable to linear in many applications because it allows flexible orientation between the transmitting antenna and receiving antenna in a communications system, while also mitigating multipath effects that lead to signal fading. The ability to operate with two orthogonal senses of circular polarization allows a system to reuse frequencies and double system capacity without requiring additional bandwidth. The uniqueness of this element lies in its ability to provide dual-circular polarization in two separate frequency bands for an individual element or an antenna array environment. The arrangement of the two element geometries with the addition of the novel capacitive loading technique is also unique. The performance of this element is achieved while maintaining the light weight, low profile design that is critical for many wireless communications applications. The remainder of this section will discuss simulation results for two polarization combinations. The focus will be placed on a dual-band element that provides

dual-CP operation in two frequency bands because the dual-band, dual-CP antenna element provides the more significant contribution to the antenna engineering community.

3.1 Low Band: Dual-Circular Polarization; High Band: Dual-Circular Polarization

The dual-band, dual-CP element is illustrated in Figure 3-1. An isometric view of the element is shown in Figure 3-1(a). The shorted square ring and square ring slot elements used for the low and high band operation respectively are labeled. The top view shown in Figure 3-1(b) indicates the pertinent parameters for the design. The shorted square ring has an outer side length of L_0 and an inner side length of L_1. The high band square ring slot has outer and inner side lengths of L_1 and L_2 respectively. The element consists of a microwave substrate with a ground plane on the bottom side and conductor on the top. The square ring slot acts as a slotted stripline circuit that forms the high band radiator. The portion of the conductor outside of the slot is treated as the low band shorted square ring. The low band radiator is shorted to the ground plane with plated through holes located at the inner perimeter of the shorted square ring. The top view of Figure 3-1(b) also shows the isosceles triangle shaped perturbations at opposing corners of both the high and low band radiator. The triangular perturbations have side lengths of Δ_{LB} and Δ_{HB} for the low and high band respectively. The use of these perturbations creates two, near-degenerate modes that provides CP polarization with a single feed point. The location of the feed point with respect to the truncated corners determines the sense of CP. Therefore, by having two orthogonal feed points for each band, this dual-band element is capable of generating simultaneous dual-CP operation for each frequency range.

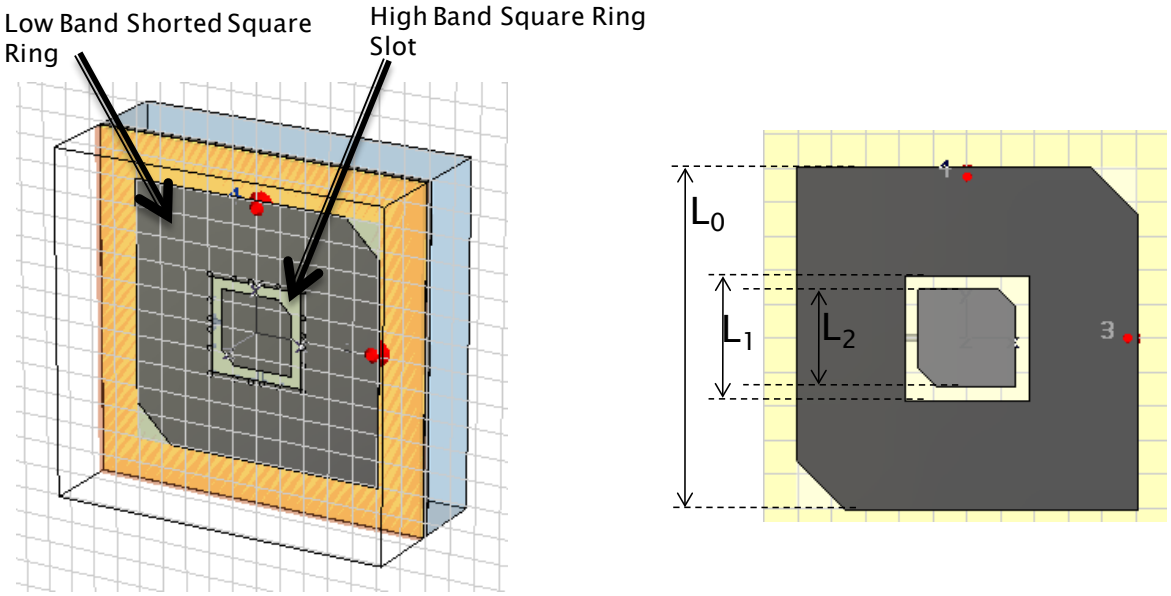

(a) Isometric view of dual-band dual-CP element

(b) Top view of dual-band dual-CP element

Figure 3-1: Illustration of Dual-Band Dual-CP Antenna Element

The high band square ring slot element is fed with orthogonal feed lines as shown in Figure 3-2. These stripline transmission line feeds pass underneath of the square ring slot, and they are terminated in open circuited stubs. In many instances, the ideal stub length for achieving the best axial ratio and impedance match requires the feed to extend beyond the center of the element. If the orthogonal feed lines were present in the same vertical plane, they would physically intersect as they passed this center point. In order to eliminate this problem, a thin substrate (referred to as the *feed substrate*) is placed at the center of the dielectric profile. The two feed lines are printed on opposing sides of the *feed substrate*. The *feed substrate* is then sandwiched between two other substrate layers and conductors are present on the top and bottom of the sandwiched dielectric profile.

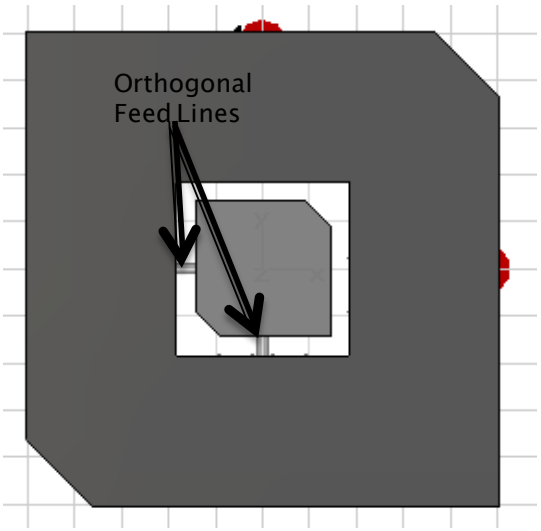

Figure 3-2: Top view of the location of the orthogonal feed lines for the high band radiator

The stripline feeds for exciting the high band element must pass through the plated through holes that provide the shorting mechanism for the low band element. An illustration of the orthogonal feed lines passing through the plated through holes (vias) is shown in Figure 3-3. These plated through holes serve multiple purposes. As previously mentioned, they are used as the shorting mechanism for the low band element. Additionally, they act as mode suppressors for the parallel plate mode that can be generated from the slotted stripline element used for the high band radiator. Slotted stripline designs can be subject to power loss, low efficiency, and degraded pattern shape as a result of the parallel plate mode [52]. Work by Bhattacharyya, Fordham, and Liu [53] has shown that vias can be used to suppress the parallel plate mode in slot-coupled patch antennas fed by stripline feed networks. Their design contains vias surrounding the slot. They show that the presence of the vias improves the gain by increasing the available power for radiation. In this element design, the shorting vias for the low band element will also assist the efficiency of the high band element by working to eliminate the propagation of the parallel plate mode.

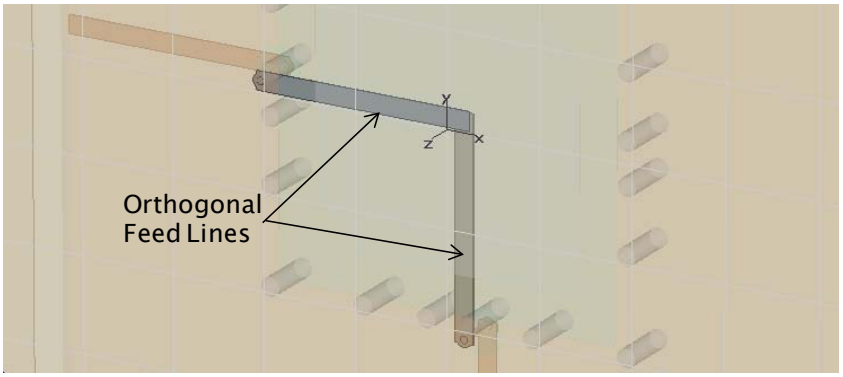

Figure 3-3: Location of the orthogonal high band feeds with respect to the shorting plated through holes for the low band element

Simulations indicated that the presence of high band feed lines beneath the low band radiator had a negative effect on the polarization purity for the low band element. In order to avoid this, the stripline feeds for the high band are transitioned to a microstrip layer present beneath the antenna ground plane. Figure 3-4 shows this transition in section view. The transition occurs just outside of the square ring slot, and it uses a plated through hole that provides electrical continuity between the stripline and a microstrip transmission. The plated through hole passes through a hole in the ground plane, and the two transmission lines have matched impedance. A detailed view of this transition is provided in Figure 3-5. The presence of the microstrip layer beneath the antenna ground plane also provides a convenient location for integrating active components into the antenna design if necessary as well as providing a convenient location for the installation of connectors.

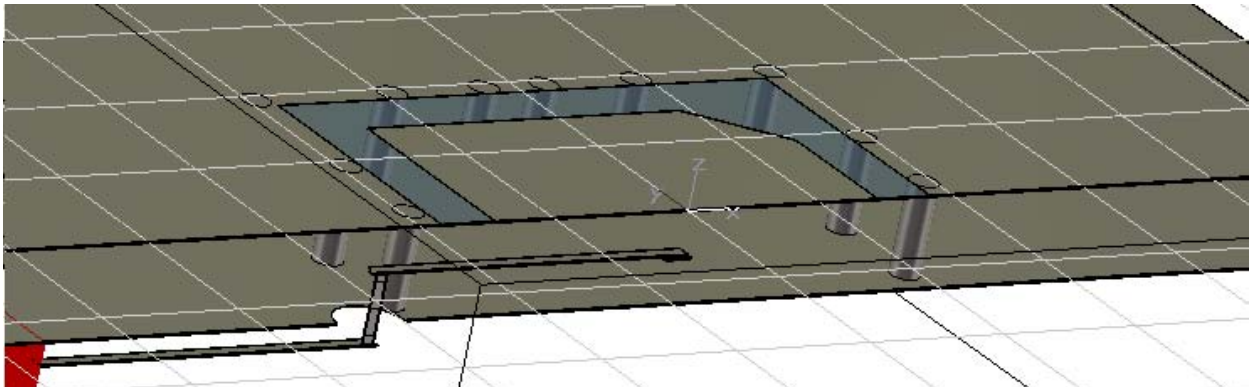

Figure 3-4: Section view of Stripline-to-microstrip transitions

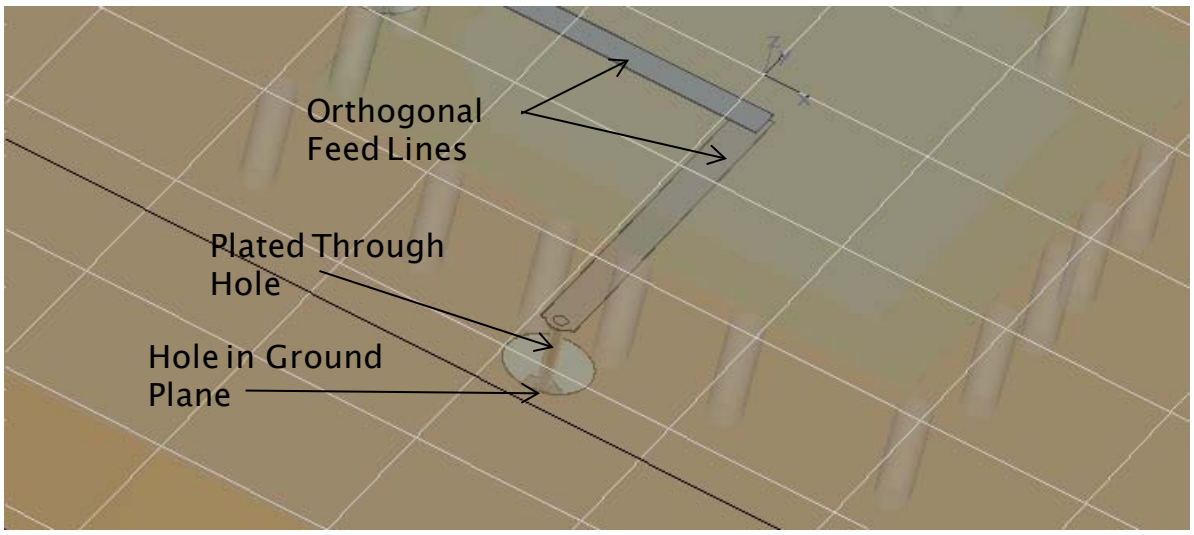

Figure 3-5: Detailed view of Stripline-to-microstrip transitions

The low band element is fed by orthogonal feed probes as shown in Figure 3-6. These feed probes can be realized as coaxial probe feeds or plated through holes from transmission lines present on the microstrip layer that contains the feeding microstrip lines for the high band element.

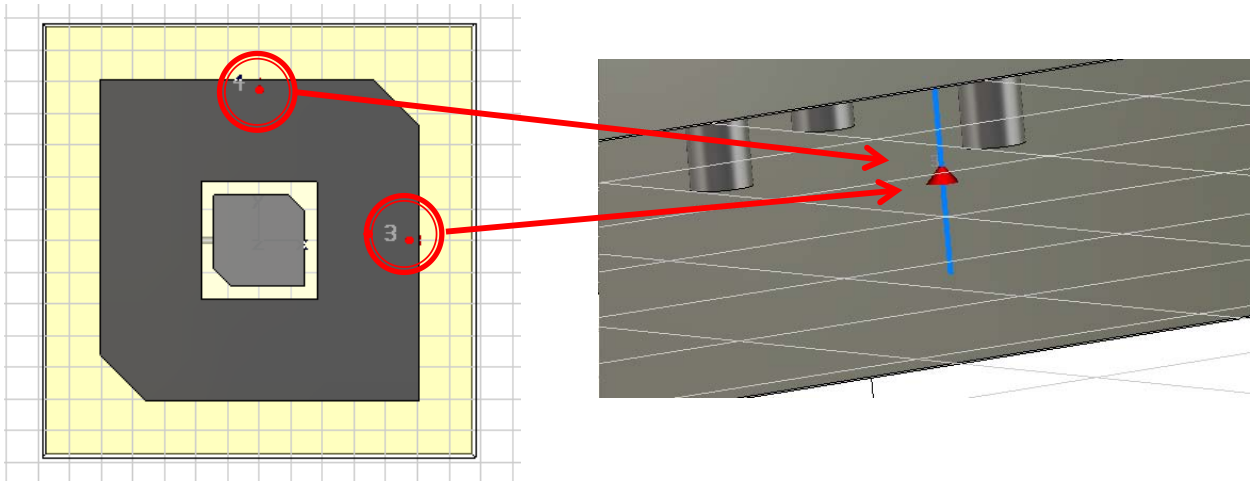

Figure 3-6: Location of low band feed points

3.1.1 Simulated Results

An element using this technique was designed with the goal to cover the 2.45 GHz and 5.8 GHz ISM bands with dual-CP operation in each band. The element used a *feed substrate* of thickness 0.004" with a dielectric constant of 2.33 (Rogers RT5880 material). The *feed substrate* was sandwiched between 0.060" thick dielectric layers with the same properties as the *feed substrate*. The microstrip layer beneath the antenna ground plane was a 0.030" thick layer of the same dielectric material used on for the remaining layers.

A design process was established to show how the simulated element discussed in this chapter could be transitioned to a printed circuit design. The assembly of the element involves a complex process due to the multilayered design of the antenna element. Each of the layers must be etched, and selected layers must be bonded together with precise alignment. The layers can be bonded together with a dielectric-matched epoxy having an overall thickness of approximately 0.001". In addition, plated through holes are present beneath several layers. The plated through holes require a specific order to be followed when assembling the layers. The layout of the layers are defined in *.GBR files. The assembly process is outlined in Appendix A to define the order of operations required for properly assembling this antenna.

The simulations for this element were carried out using CST Microwave Studio [42], a computational electromagnetic tool using the Finite Integration Technique (FIT). The simulated impedance match was seen to provide excellent results in both polarizations for each band. The simulated VSWR is shown in Figure 3-7. The four ports all show a VSWR < 2.0:1 in the given frequency band.

The dual-band dual-CP antenna element can be viewed as a four port microwave network. The band and polarization for the four ports are defined in Table 3-2. A more detailed look into the s-parameters of the four-port antenna is provided in Figure 3-8(a)-(d). This figure plots s_{ij} for each of the four ports. The results indicate that each port has a return loss greater than 10dB (i.e. $|s_{ii}|$<-10 dB) in its operational band; this corresponds to a VSWR <2.0:1 as shown in Figure 3-7. The plots also show that there is isolation greater than 25dB between the high and low band ports. The two high band port-to-port isolation parameters ($|s_{21}|$,$|$ $s_{12}|$) have a maximum value greater than 40dB at the center of the band. The port-to-port isolation between the low band ports ($|s_{43}|$,$|$ $s_{34}|$) is lower than that of the high band ports. This finding is similar to that in the literature for dual-polarized microstrip patch antennas. When a square patch radiator operates with dual-linear polarizations, an isolation exceeding 20dB is typically feasible. However, when the corners of the patch are perturbed to achieve dual-CP operation, the orthogonal modes couple strongly to each other [75]. It has also been shown that this port-to-port isolation can be increased at the expense of impedance match and axial ratio [29, 75]. In this design, the isolation between the two low band ports is between 7 and 10dB across the frequency band. The coupling between the low band ports and high band ports (s_{42}, s_{32}, s_{41}, s_{31}, s_{24}, s_{14}, s_{13}, s_{23}) all have magnitudes below -25dB indicating that there is high isolation between the two frequency bands.

Table 3-2: Port Definition Used in Simulations of Dual-Band Dual-CP Antenna Element

Port	Frequency Band	Polarization
1	5.8 GHz ISM Band	RHCP
2	5.8 GHz ISM Band	LHCP
3	2.45 GHz ISM Band	LHCP
4	2.45 GHz ISM Band	RHCP

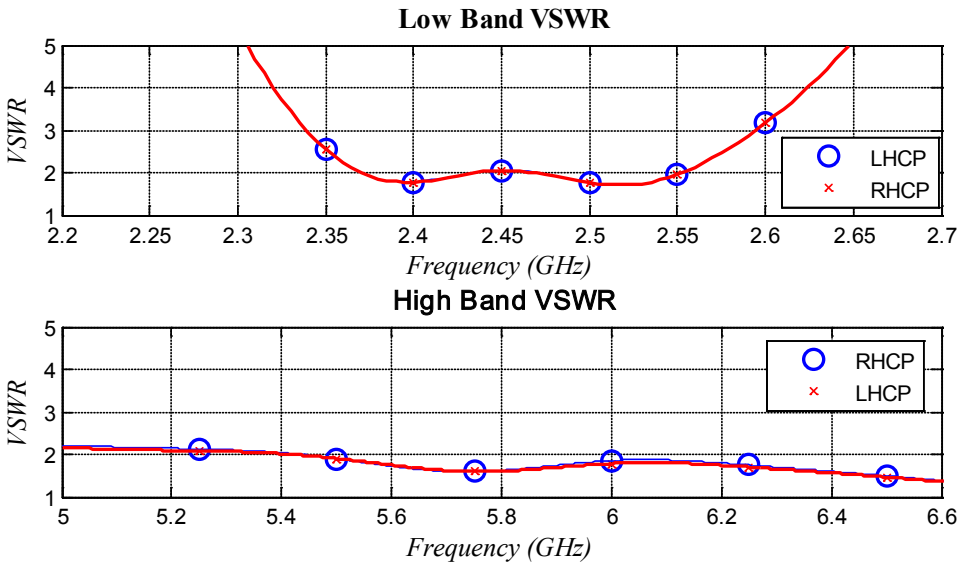

Figure 3-7: Simulated VSWR for Dual-Band Dual-CP Element

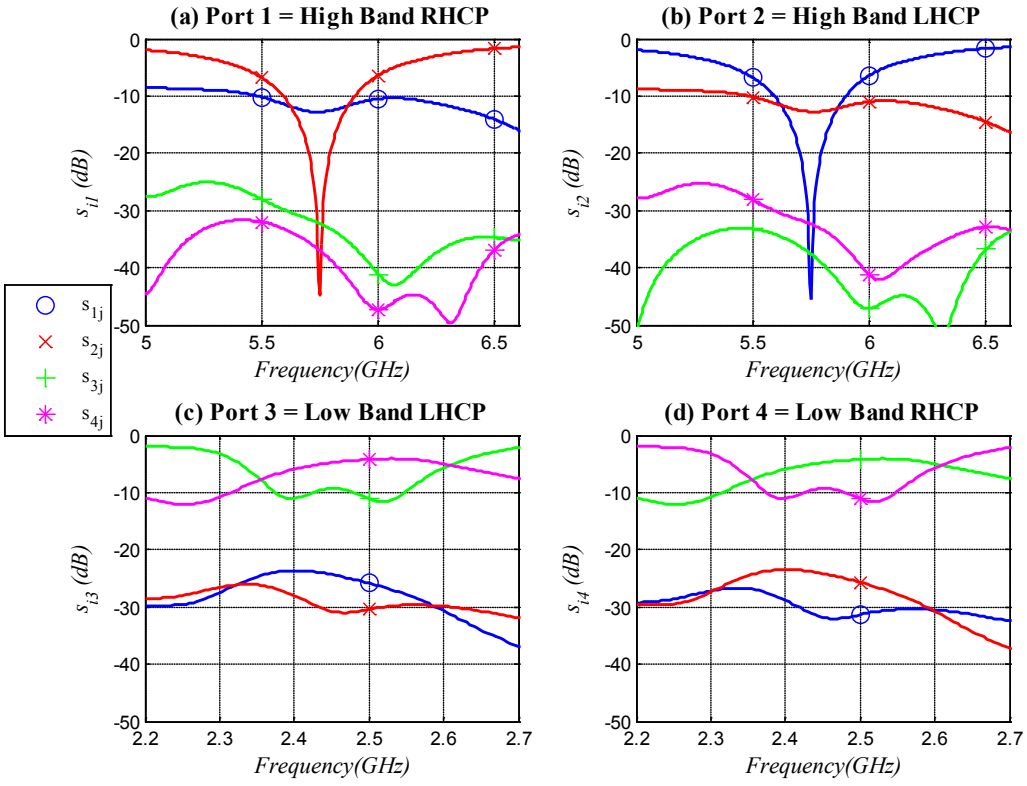

Figure 3-8: Simulated s-parameters for Dual-Band Dual-CP Antenna Element

In addition to showing good impedance match and isolation performance, this element also shows excellent circular polarization purity (axial ratio) for all polarization states. The axial ratio for the low and high band ports is plotted in Figure 3-9. The low band has a minimum axial ratio of 0.33dB occurring at 2.44 GHz, and the axial ratio is below 3dB over the majority of the 2.45 GHz ISM band. The high band element has a much broader CP bandwidth, which is typical of slot elements compared to microstrip radiators. The high band element has a minimum axial ratio of 0.32dB for RHCP and 0.89dB for LHCP. In both cases, the minimum axial ratio occurs at 5.9 GHz. The high band element has an axial ratio better than 3dB from 5.6 – 6.1 GHz, a bandwidth of 8.5%. For both frequency bands, the axial ratio and impedance match are better than typical figures of merit (i.e. VSWR < 2.0:1 and AR < 3.0dB) in the given band.

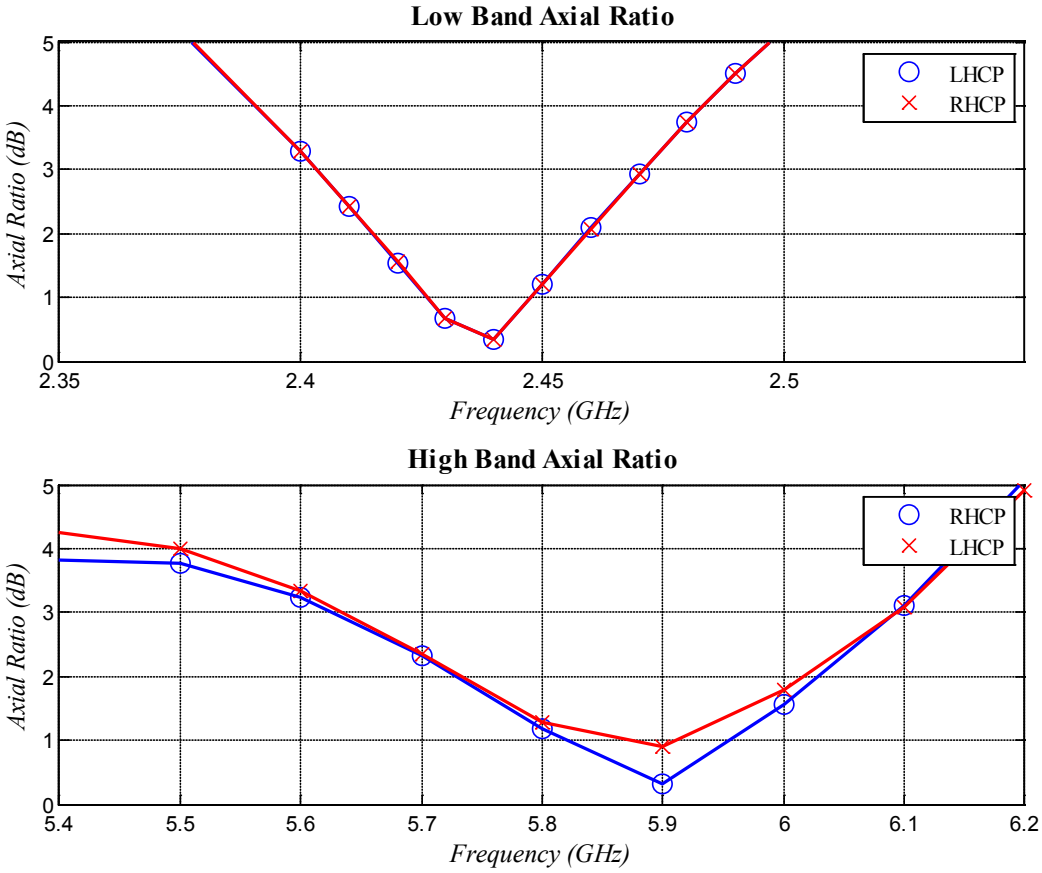

Figure 3-9: Simulated Axial Ratio for Dual-Band Dual-CP Antenna Element

The radiation patterns for each of the CP states are plotted in Figure 3-10 for the low band and 3-11 for the high band. These plots show the co- and cross-polarized plots for two orthogonal planes (φ=0°, 90°). These patterns show broadside co-polarized patterns in all cases with low cross-pol levels indicating excellent cross-polarization discrimination (XPD) in both frequency bands. The high XPD levels are reflective of the excellent axial ratio performance in this element as shown in Figure 1-3.

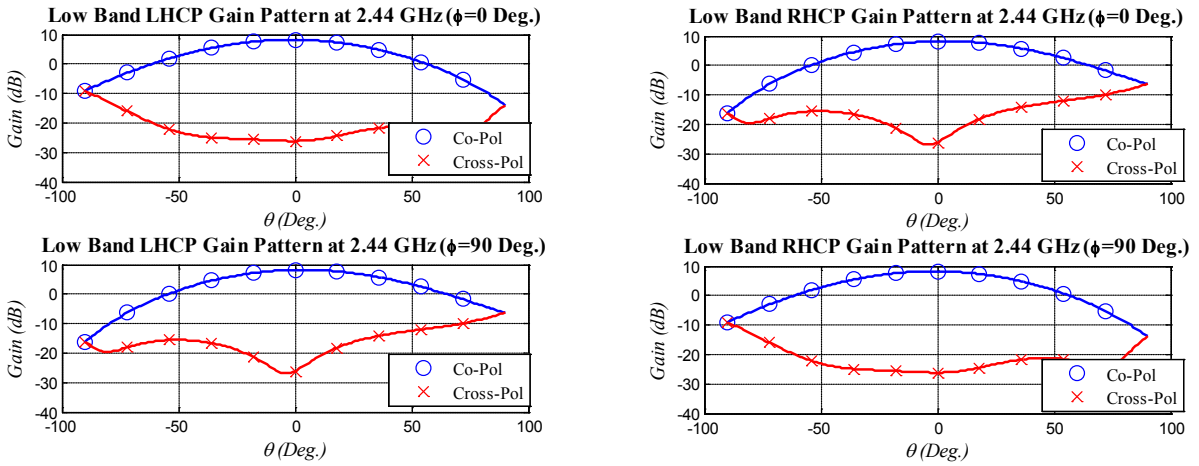

Figure 3-10: Simulated Low Band Radiation Patterns for Dual-Band Dual-CP Antenna Element

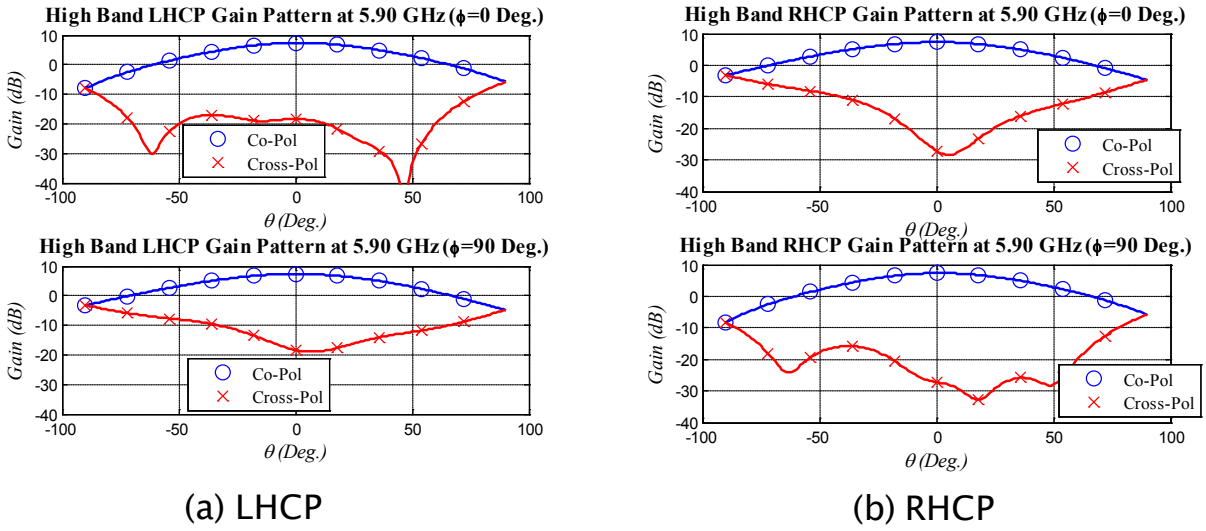

Figure 3-11: Simulated High Band Radiation Patterns for Dual-Band Dual-CP Antenna Element

If the element will be used in an antenna array or in an application requiring a broad beamwidth, it is important that the axial ratio remains near unity over a wide range of angles. The contour plots in figures 3-12 and 3-13 provide a look at the axial ratio vs. frequency vs. theta for the high and low band respectively. In these plots, theta represents the angle measured from broadside. The high band plot shows that the axial ratio is less than 3dB over a theta region of ±60° within the 5.8GHz ISM frequency band. At 5.85GHz, the axial ratio is below 1dB over for $|\theta|<30°$. The axial ratio holds up well for frequencies outside of the 5.8GHz ISM band. The contour plot of Figure 3-12 shows that the axial ratio is less than 3dB over $|\theta|<30°$ from 5.65 – 6.05 GHz, a fractional bandwidth of 6.8%. The low band plot shown in Figure 3-13 indicates excellent axial

ratio over the 2.45GHz ISM frequency band. The axial ratio stays below 1dB for |θ|<40° between the frequencies of 2.43 and 2.45GHz. Over the remainder of the 2.45GHz ISM band, the axial ratio is less than 3dB for |θ|<60°.

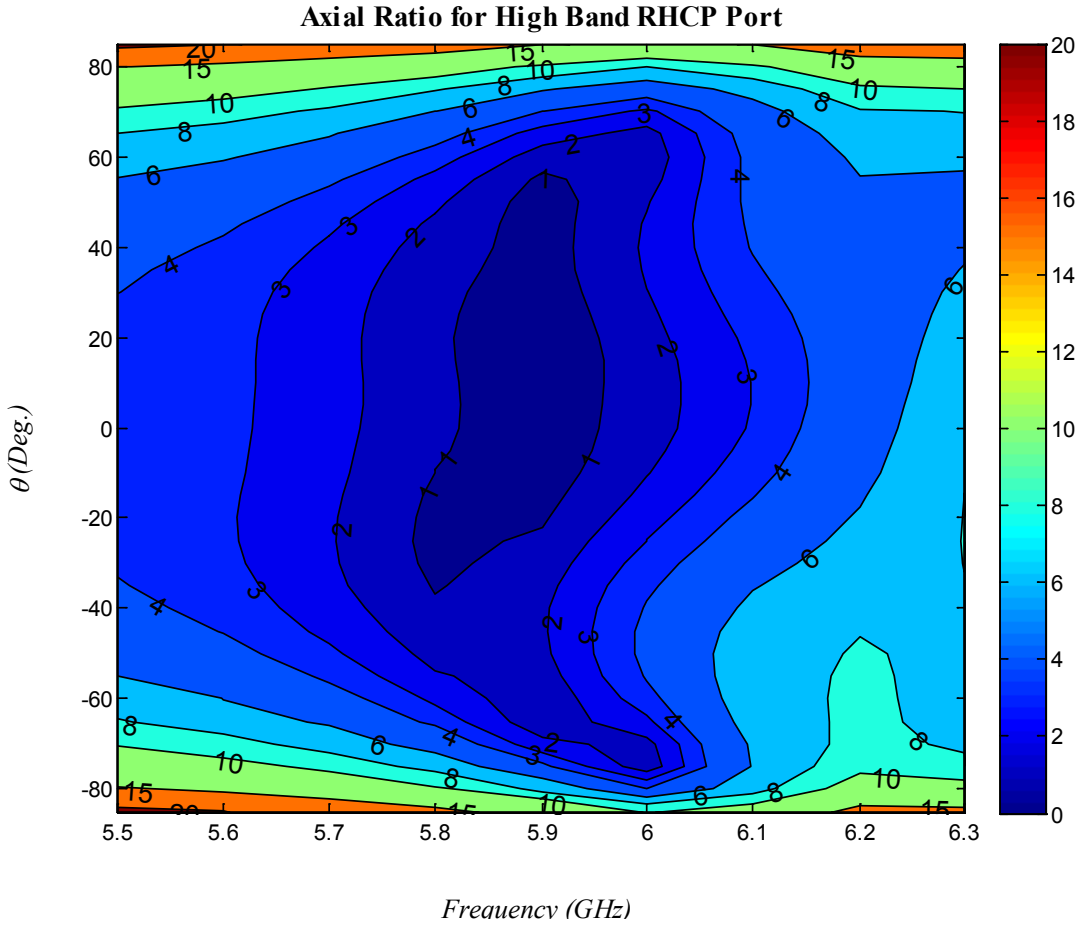

Figure 3-12: Axial Ratio vs. Frequency vs. Theta for High Band RHCP Port

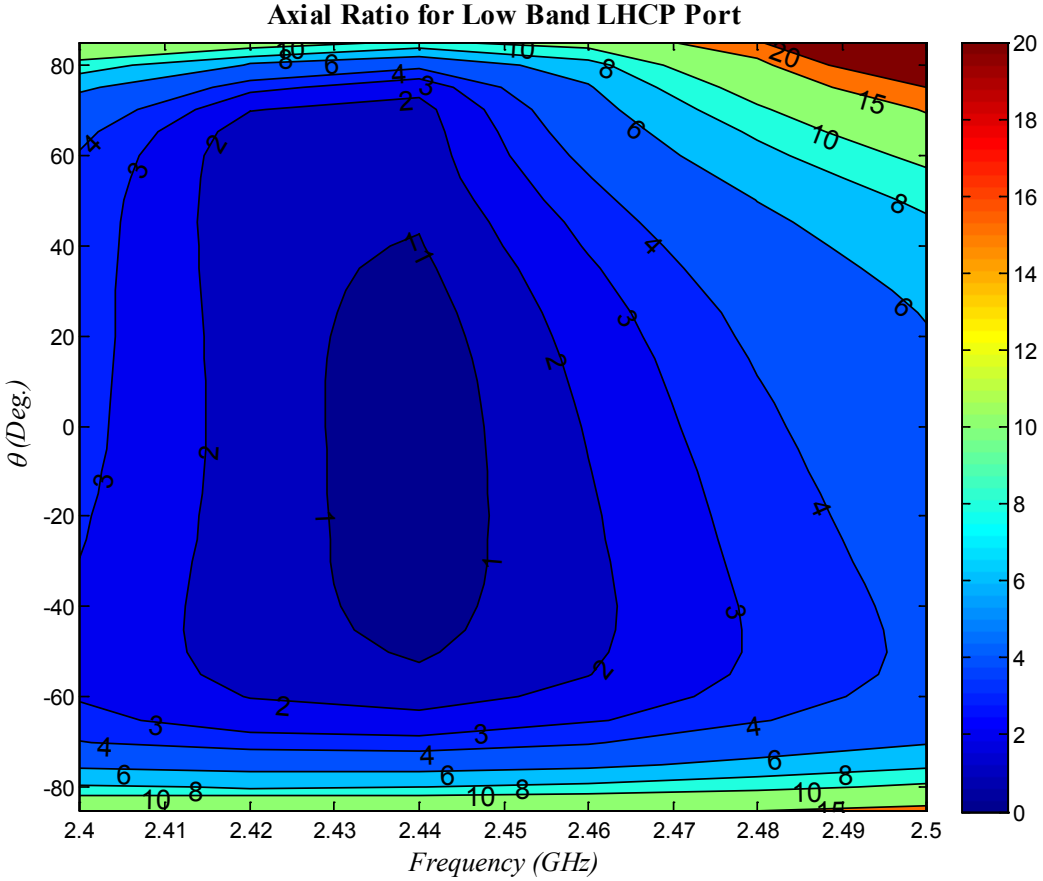

Figure 3-13: Axial Ratio vs. Frequency vs. Theta for Low Band LHCP Port

3.1.2 Measured Results

The element simulated in section 3.1.1 was built and tested to verify the operation of the concept and the proposed manufacturing process. The assembly of the element involves a complex process due to the multilayered layout of the antenna element. Each of the layers must be etched, and selected layers must be bonded together with precise alignment. The layers are bonded together with a dielectric-matched epoxy having an overall thickness of approximately 0.001". In addition, plated through holes are present beneath several layers. The plated through holes require a specific order to be followed when assembling the layers. The layout of the layers are defined in *.GBR files. These files were delivered to Capital ElectroCircuits, a printed circuit board shop in Gaithersburg, MD. The files were accompanied by the assembly process outlined in Appendix A to define the order of operations required for properly assembling this antenna.

A photograph of the assembled element is provided in Figure 3-14 showing the top view (left) and bottom view of the multilayer board. The top view shows the two radiators. The shorted square ring element for the low band operation is the outermost conductor visible in this picture, and the square ring slot for the high frequency radiation is also visible. The plated through holes

used as shorting vias are visible at the center of the multilayer board. The bottom view shown in Figure 3-14 reveals the locations of the feed points. This view shows the substrate layer of the feeding microstrip layer that is present beneath the antenna ground plane layer. Two microstrip feedlines are visible for exciting the RHCP and LHCP polarizations in the 5.8 GHz ISM band. Close inspection of these layers indicates that the high band microstrip feeds have an impedance transformer present to convert the optimized 80Ω impedance of the dual-polarized slot antenna to the 50Ω impedance of the top mount coaxial connector that is used. Four conducting pads are present around each of the microstrip feed lines. There are plated through holes providing electrical continuity between the antenna ground plane and these pads. Top mount connectors are used for the high band excitation. The ground tabs of these connectors are soldered to the ground pads, and the center conductor is soldered to the trace. Two apertures are opened in this layer to expose the antenna ground plane. This is needed for installation of the two coaxial probe feeds that are used for exciting the two low band polarization states. A photograph of the bottom view of the antenna element with the connectors installed is provided in Figure 3-15.

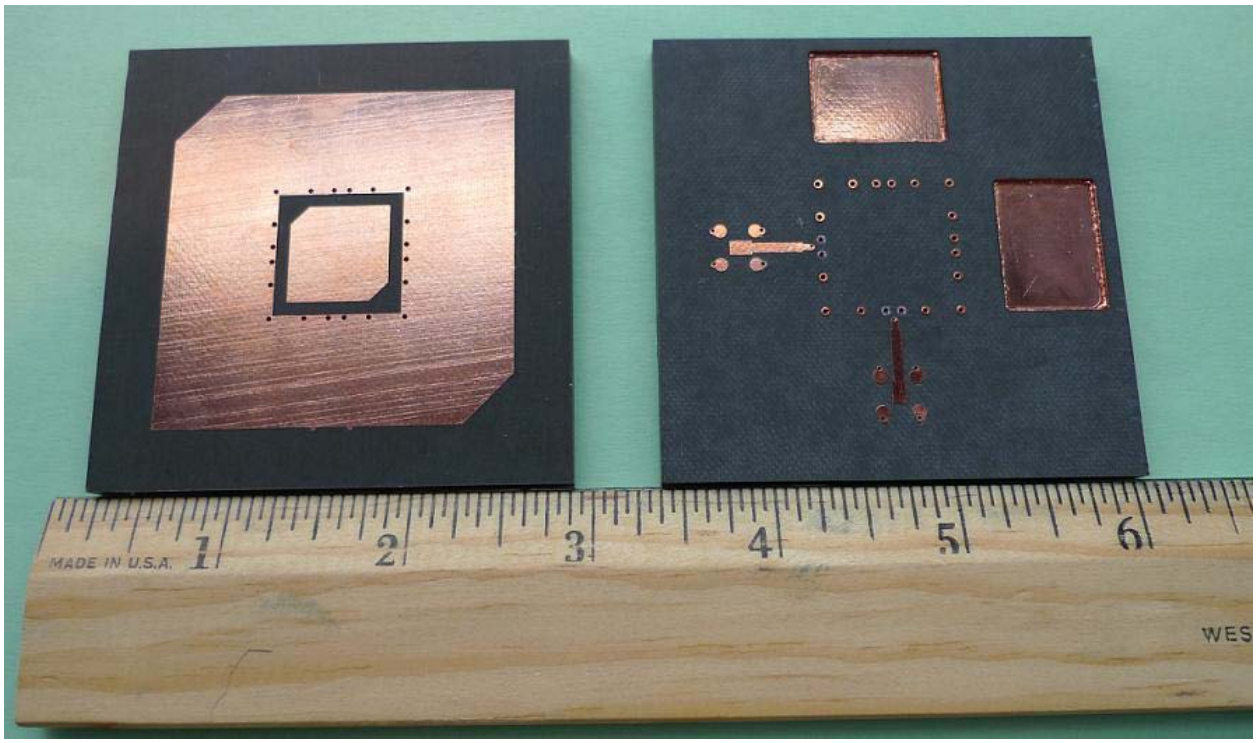

Figure 3-14: Photograph of constructed dual-band, dual-CP antenna element

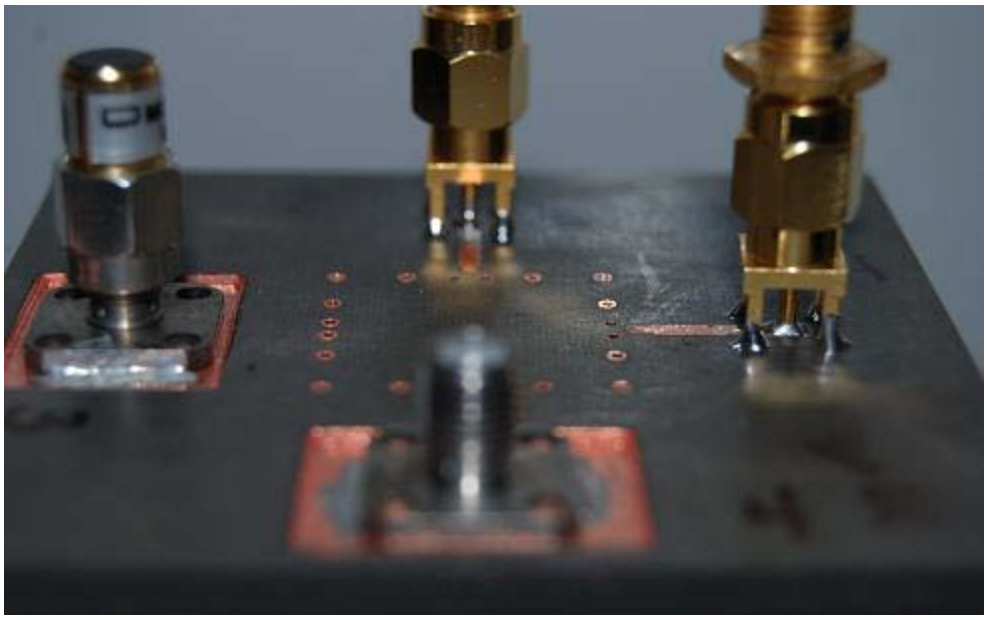

Figure 3-15: Bottom view of the constructed dual-band, dual-CP antenna element showing connector installation

The measured s-parameters are compared to the simulated s-parameters in Figures 3-16 through 3-19. Each of these figures shows the magnitude of the s_{ij} for a fixed 'j' value. These measurements were performed using an Agilent 8722ES Network Analyzer. A full two-port calibration was completed before beginning the measurements to fully characterize the system and cables that were used in the measurements. Additionally, all measurements were performed in an anechoic chamber to minimize the effects of room reflections that can alter the accuracy of the measurements.

The measured s-parameters for the high band polarization states are compared to the CST Microwave Studio simulations in Figures 3-16 (RHCP) and 3-17 (LHCP). The results show good agreement between the measurements and simulations. For the RHCP state, all four s-parameters match very well with the simulated results. The return loss (s_{11}) shows a value exceeding 10dB across the band of operation. The biggest discrepancy between measurements and simulations for the high band RHCP is seen in the s_{21} parameter. This parameter defines the coupling between the high band LHCP and RHCP ports. The simulations showed a null with minimum value of -42dB located at 5.75 GHz, while the measurements showed a slightly narrower null (minimum value of -29dB located at 5.675 GHz. Comparison of the frequency location of the s_{21} null indicates a 1.3% discrepancy between measurements and simulations. The coupling between the high band RHCP port and the two low band ports (s_{31}, s_{41}) show good agreement.

The measured results for the high band LHCP port show good agreement with the simulations, but not quite as good as the high band RHCP. The return loss for the high band LHCP operation (Figure 3-16(b)) shows very good agreement over the 5.8 GHz ISM band, but there are discrepancies above this frequency band (around 6.15 GHz). The high band ports were excited

with a top mount connector. It can be difficult to maintain good contact using top mount connectors. Additionally, it is difficult to place the connector in exactly the designed location without precision soldering equipment. It is hypothesized that subtle differences in connector location and connection are responsible for the slight differences in performance between the two high band polarizations. However, it should be reiterated that these discrepancies are small and occur outside of the operational band of the antenna. Inside of the 5.8 GHz ISM band, the measured s-parameter results show excellent agreement with the simulations.

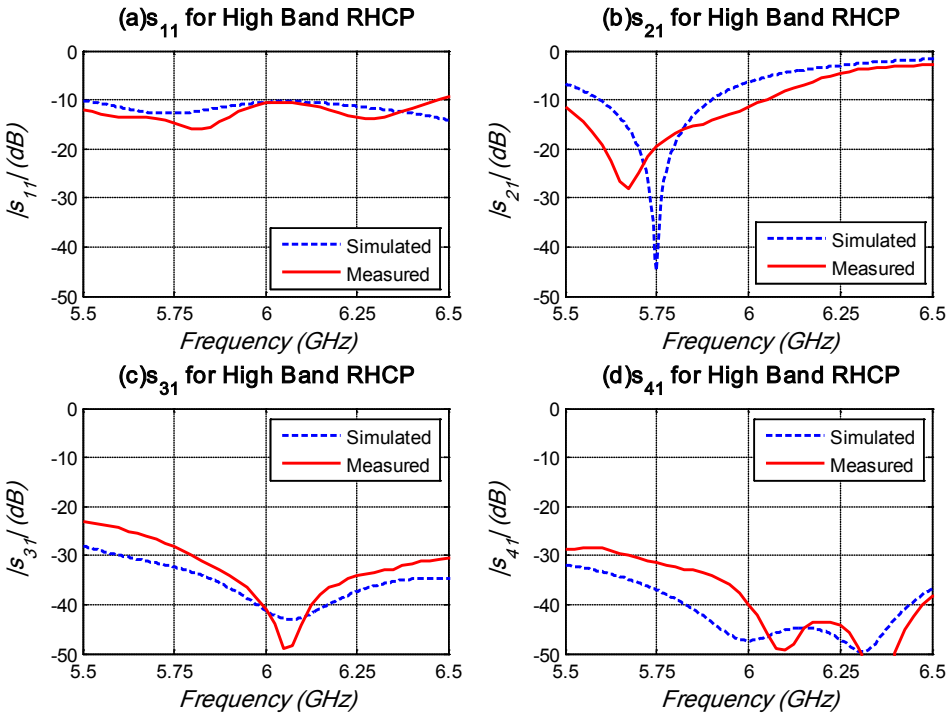

Figure 3-16: Measured s-parameters for High Band RHCP Port (j=1)

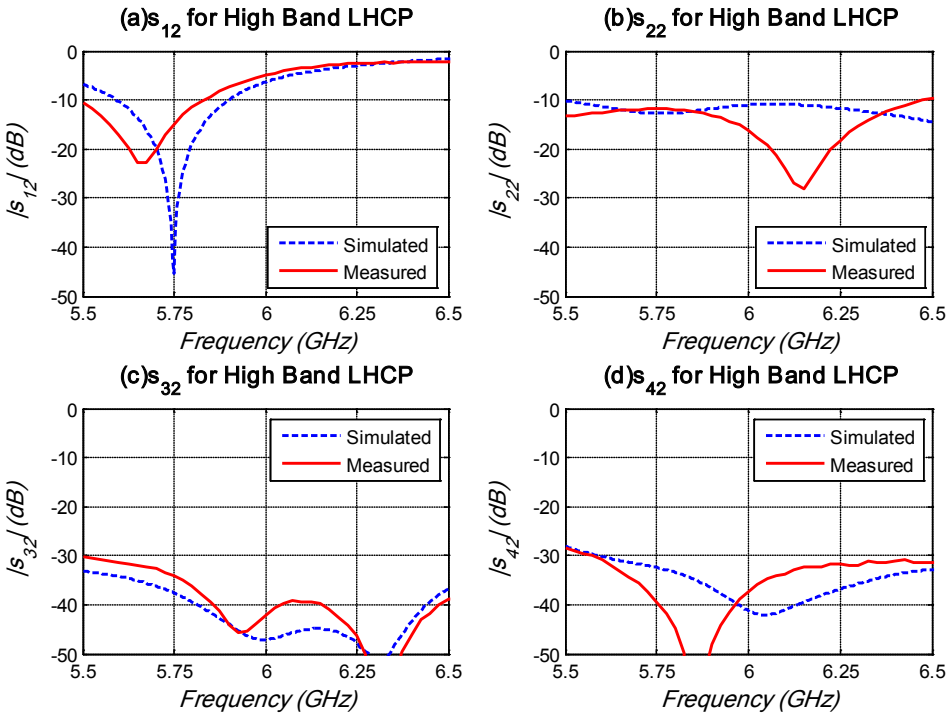

Figure 3-17: Measured s-parameters for High Band LHCP Port (j=2)

The only discrepancies between the measured and simulated s-parameters for the low band ports are seen in the two return loss curves (s_{33} and s_{44}). These differences are partially attributed to the loss present in the coaxial connector. The simulation models utilized a discrete port to excite the low band polarizations. A discrete port is a simplified, ideal version of a coaxial probe that negates the circuit parameters and physical size of the connector. Closer inspection of the antenna element revealed a problem in manufacturing that also could lead to degraded performance. A close-up view of one edge of the low band radiator is provided in Figure 3-20. Inspection of this figure reveals two, small conducting pads present at the outer perimeter of the element. These conducting pads are the top side of two of the vias that provide electric continuity between the antenna ground plane and the ground pads on the bottom side of the board. These vias were not intended to go through all of the layers of the board. These holes can be seen along one other edge of the low band radiator as well. In drilling these holes too deep, the low band radiator has effectively been shorted at two of the four edges. Subsequently, the low band performance of the element has been compromised.

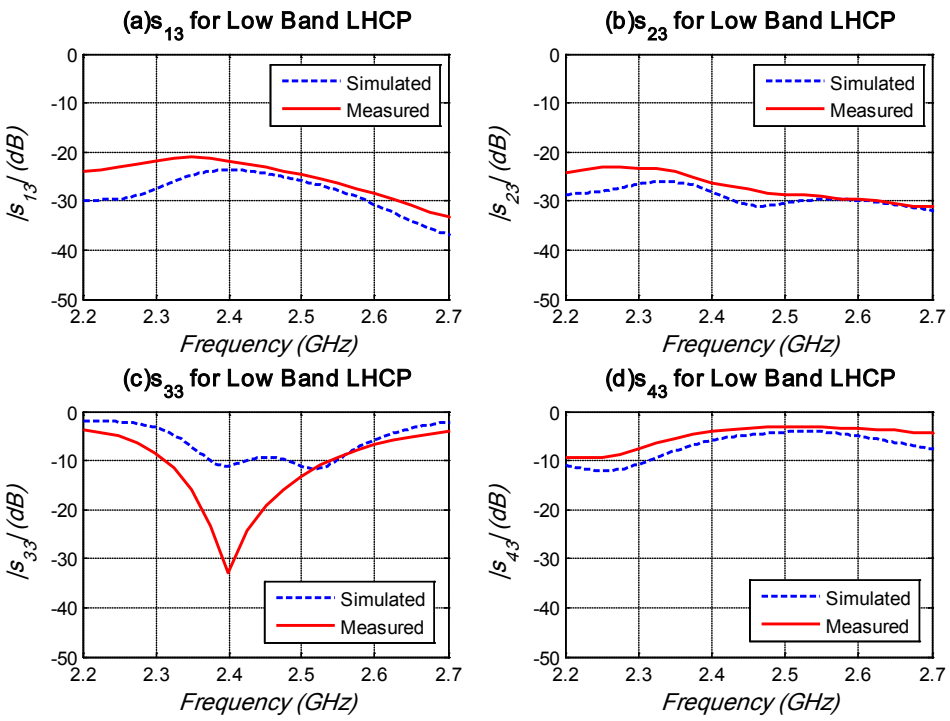

Figure 3-18: Measured s-parameters for Low Band LHCP Port (j=3)

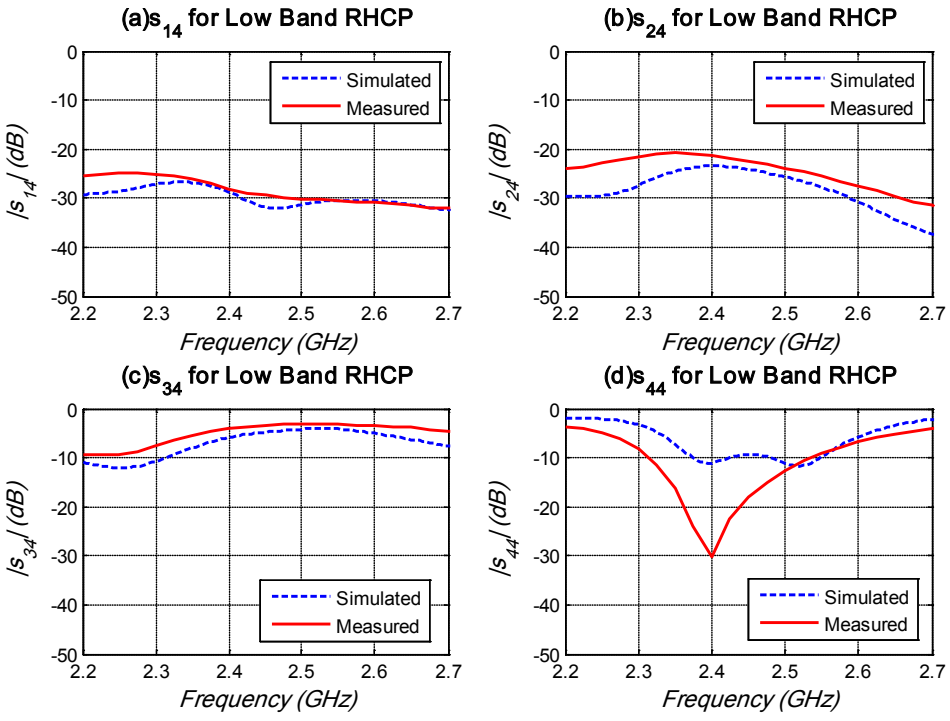

Figure 3-19: Measured s-parameters for Low Band LHCP Port (j=4)

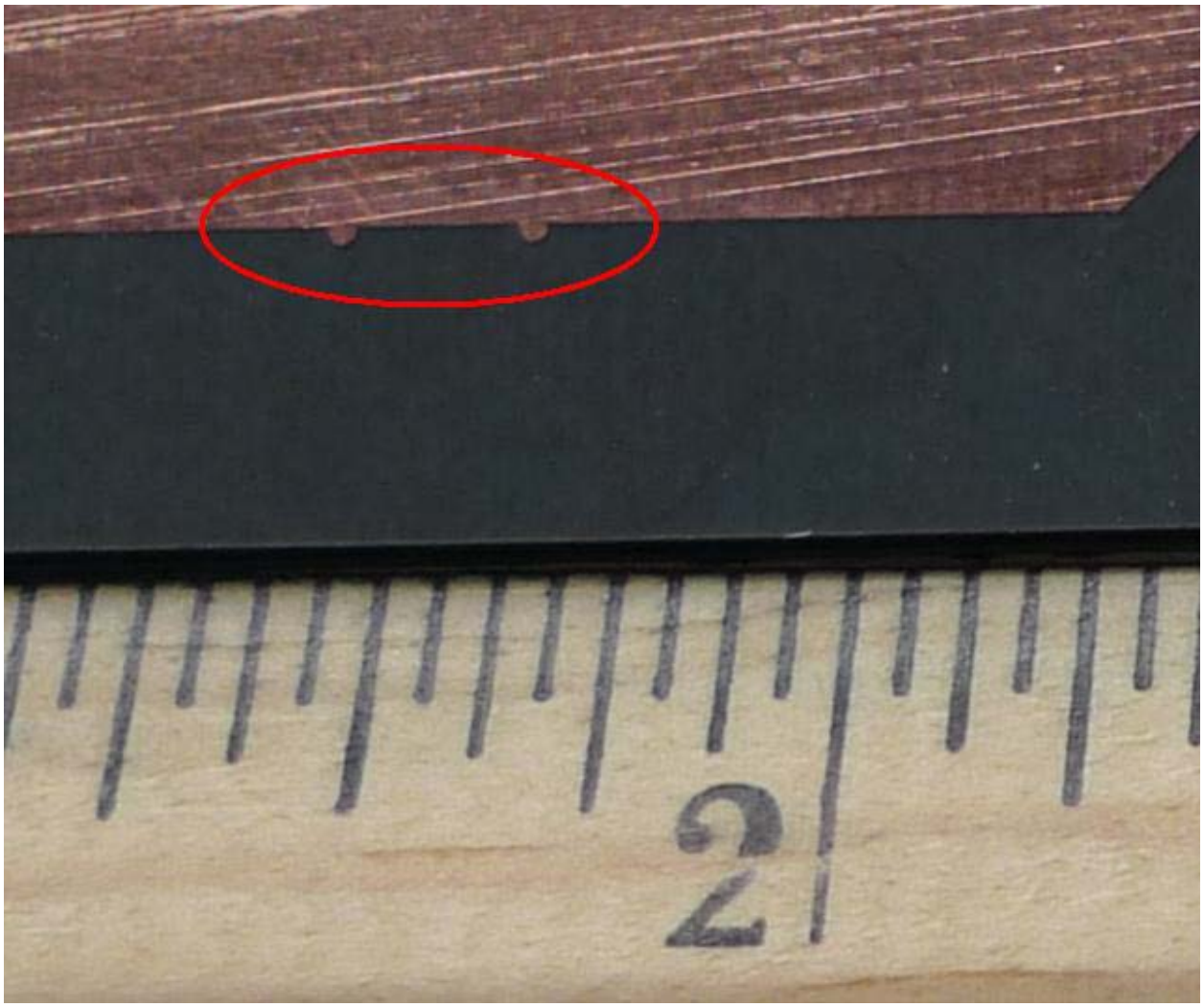

Figure 3-20: Close-up view of one edge of the low band radiator showing the presence of two shorting vias that degrade the low band performance

The axial ratio performance for the four ports was measured in a compact range. All four measurements were taken in a compact range. The feed horn to the range was horizontally polarized. The antenna was mounted in the range, and the antenna was rotated about its axis. The antenna was rotated instead of the feed horn to the range due to subtle differences in the characteristics of the large reflector that exist as a function of polarization. The measured axial ratio is compared to simulations in Figure 3-21. The results show a good agreement between measurements and simulations considering the error in production indicated in Figure 3-20. By shorting two of the four outer edges of the element, it is not surprising that the polarization performance of the element is degraded. Moreover, since the shorting has a larger impact on the low band radiator than the high band radiator, it is expected that the impact would be more severe on the low band performance. The measured polarization patterns are shown in Figures 3-22 and 3-23 for the high and low band respectively. The polarization patterns show an

elliptical polarization with a larger axial ratio than desired, which is reflected in the previously discussed axial ratio performance.

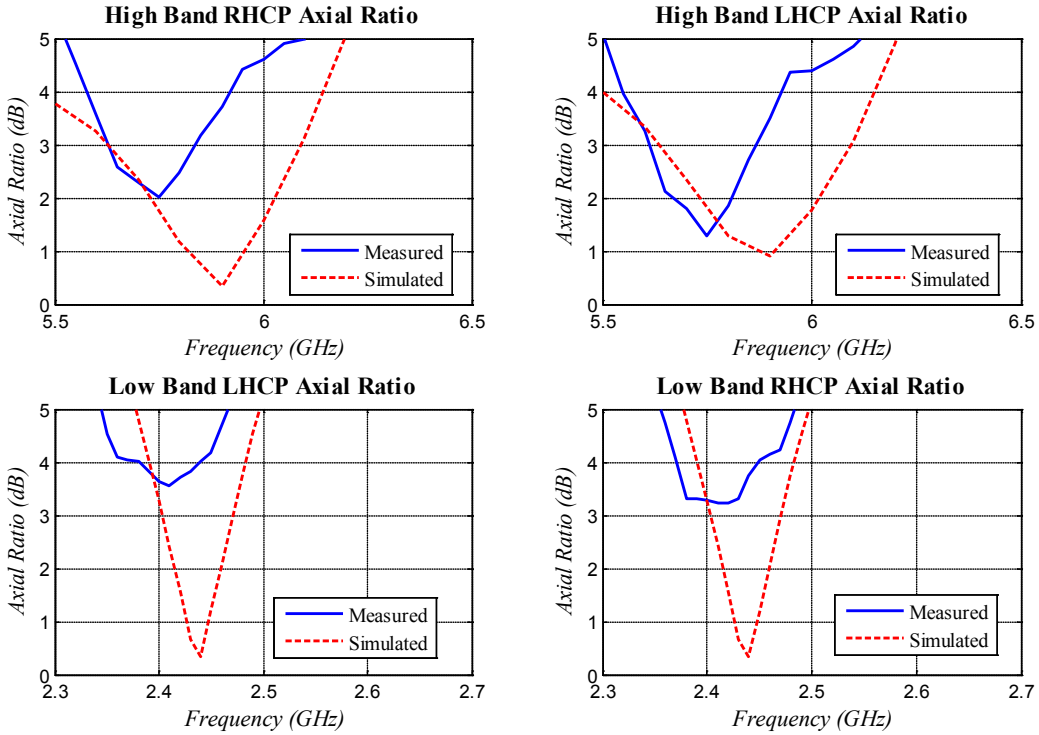

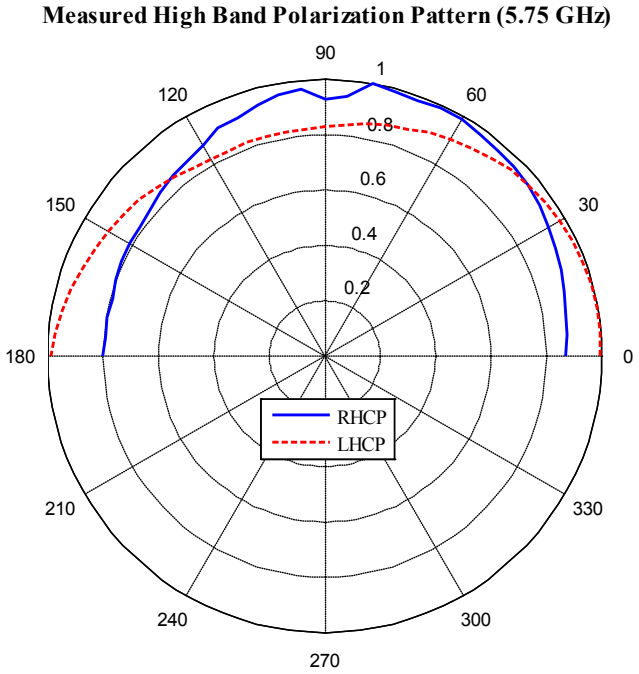

Figure 3-21: Measured high band polarization pattern (5.75 GHz)

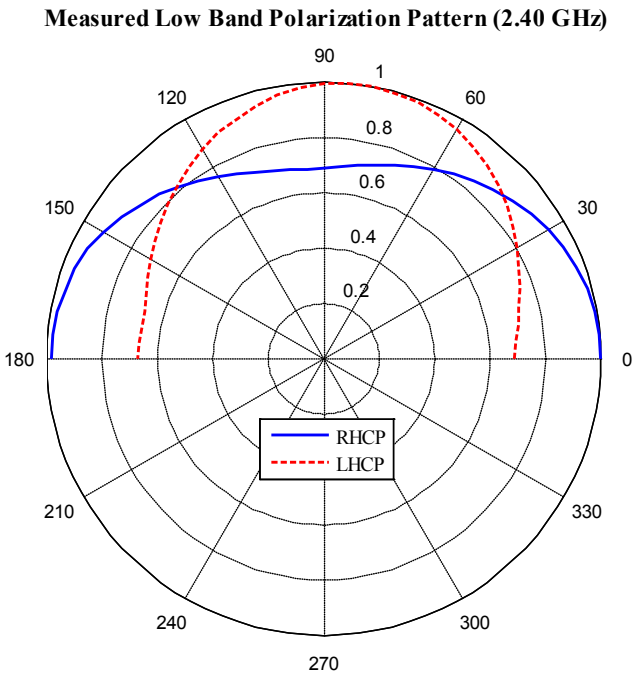

Figure 3-22: Measured low band radiation pattern (2.4 GHz)

The measured results for the dual-band, dual-CP antenna element show good agreement with the simulated results. The s-parameters for all four ports of the antenna are in excellent agreement with the simulations. The most notable differences are in the return loss of the low band elements. These differences are attributed to two misplaced plated through holes that effectively shorted the two outer edges of this element, and this degrade the performance. This performance degradation is seen in both the return loss and axial ratio performance of the low band polarization states. It is also hypothesized that these vias had an impact on the polarization performance of the high band polarization states, but the impact was not as pronounced as in the low band.

The assembly process of this element involves a complex series of steps involving etching of copper layers, alignment and bonding of layers, and drilling and plating a series of holes. The tolerances of the alignment and bonding process is essential to the overall performance of the element, and careful attention must be placed on the locations and depths of the plated through holes.

3.2 Low Band: Dual-Linear Polarization; High Band: Dual-Circular Polarization

The previously described element provides each band with dual-CP polarization. However, this element is not restricted to circularly polarized applications. As an example, an element was designed that operates with dual-linear polarization at the low band and dual-circular polarization at the high band. An isometric top view of this element is shown in Figure 3-23. The low band element does not include the perturbations at the corners, resulting in a perfectly square radiating

aperture. The high frequency radiator still uses the perturbations to create dual-CP performance. The s-parameters for this element are plotted in Figure 3-24. This element uses the 2.45 GHz ISM band for the low band and the 5.8 GHz ISM band for the high band. The dual-linear low band and dual-circular high band radiators exhibit excellent port-to-port isolation. The dual-linear polarized low band element shows much better port-to-port isolation than the dual-CP element. The isolation now ranges from 15-30 dB across the 2.45 GHz ISM band. This finding is not surprising since it has been shown that dual-CP microstrip radiators inherently have degraded isolation compared to dual-LP microstrip radiators [75]. Additional polarization combinations can be designed following Table 3-1.

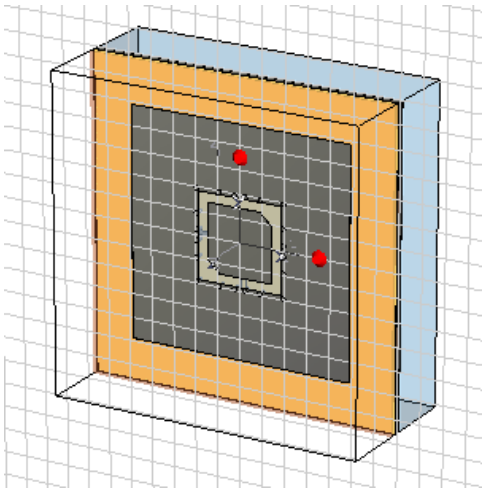

Figure 3-23: Low Band: Dual-LP, High Band: Dual-CP

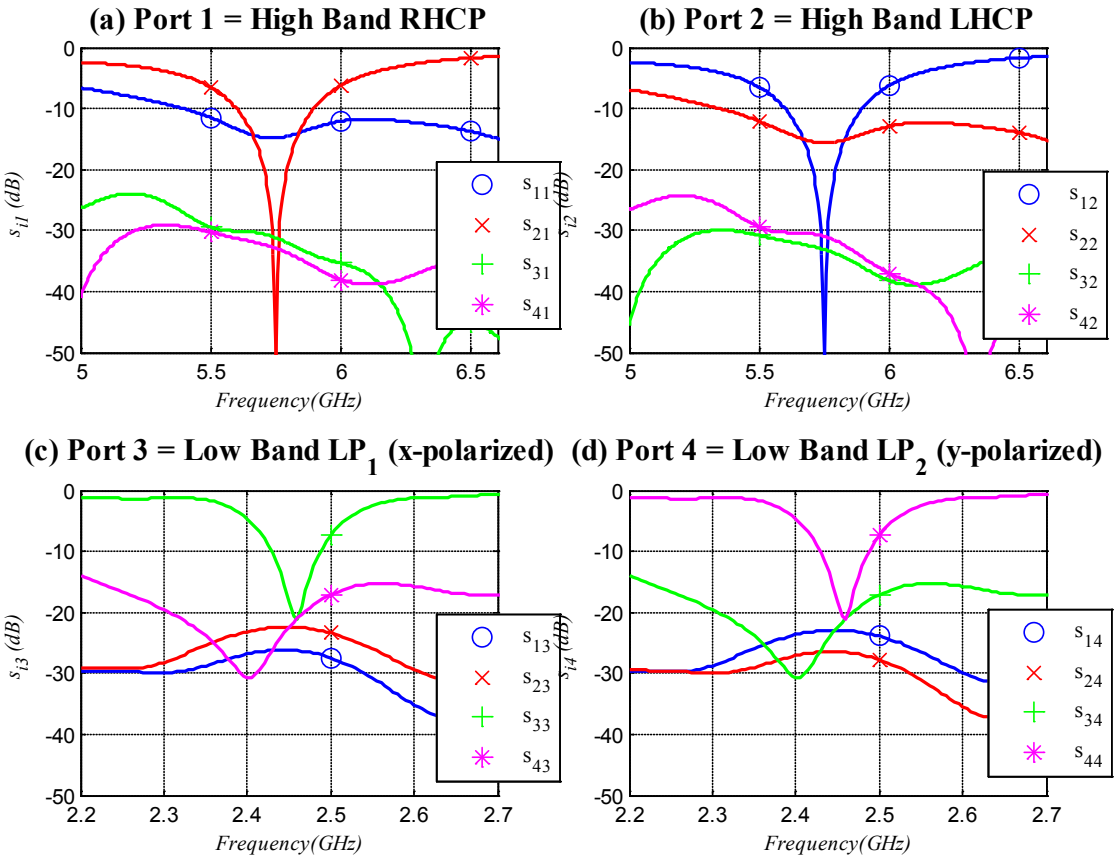

Figure 3-24: Simulated s-parameters for Dual-Band, Dual-Polarized Antenna Element (Low Band: Dual-linear, High Band: Dual-circular)

A parametric study was performed on this element to highlight its flexibility. The initial step in the design process for the dual-band element is to select the high band frequency range and polarization. This design sets two of the main parameters for the element: L_1, and L_2. Once the high band element has been designed, the inner side length for the low band shorted square ring is set. However, this element still can operate over a wide range of frequency bands giving the dual-band element flexibility over the ratio between the two frequency bands.

The dual-band, dual-polarized element in discussed in this section had a high frequency band centered at 5.85 GHz. This element operated with dual-circular polarization. This high frequency element used an outer side length (L_1) of 0.735" and an inner side length (L_2) of 0.575". The final parameter for this element was the determination of L_0, the outer side length for the shorted square ring antenna that serves as the low band radiator. Figure 3-25 shows the results of a parametric study in which the outer side length was varied from 1.2" to 3.0".

The results show that the resonant frequency for the TM_{11} mode of the shorted square ring can be tuned between 4.66 GHz and 1.40 GHz by tuning L_0 from 1.2" to 3.0". The resonant frequency

could be dropped lower if L_0 was increased further. Modifying L_0 left the operation of the high frequency element unchanged with a center frequency of 5.85 GHz. Therefore, the ratio of the high band frequency to the low band frequency varied from 4.18:1 to 1.26:1. This gives the element the flexibility to operate in many applications requiring multiple frequency bands.

The dual-frequency elements described in [18, 20, 76] operate at L- and C-band frequencies to provide coverage for synthetic aperture radar (SAR). They operate with a relatively large frequency ratio of just over 4.0:1. Conversely, the element designed by Shun-Yun Lin and Kuang-Chih Huang in [77] operates with a small frequency ratio of 1.2:1 to cover the frequency ranges needed for applications in the global position system (GPS) and digital communication systems (DCS). The dual-band, dual-polarized element in discussed in this dissertation shows the ability to handle either of those frequency ratios, as well as any frequency ratio in between.

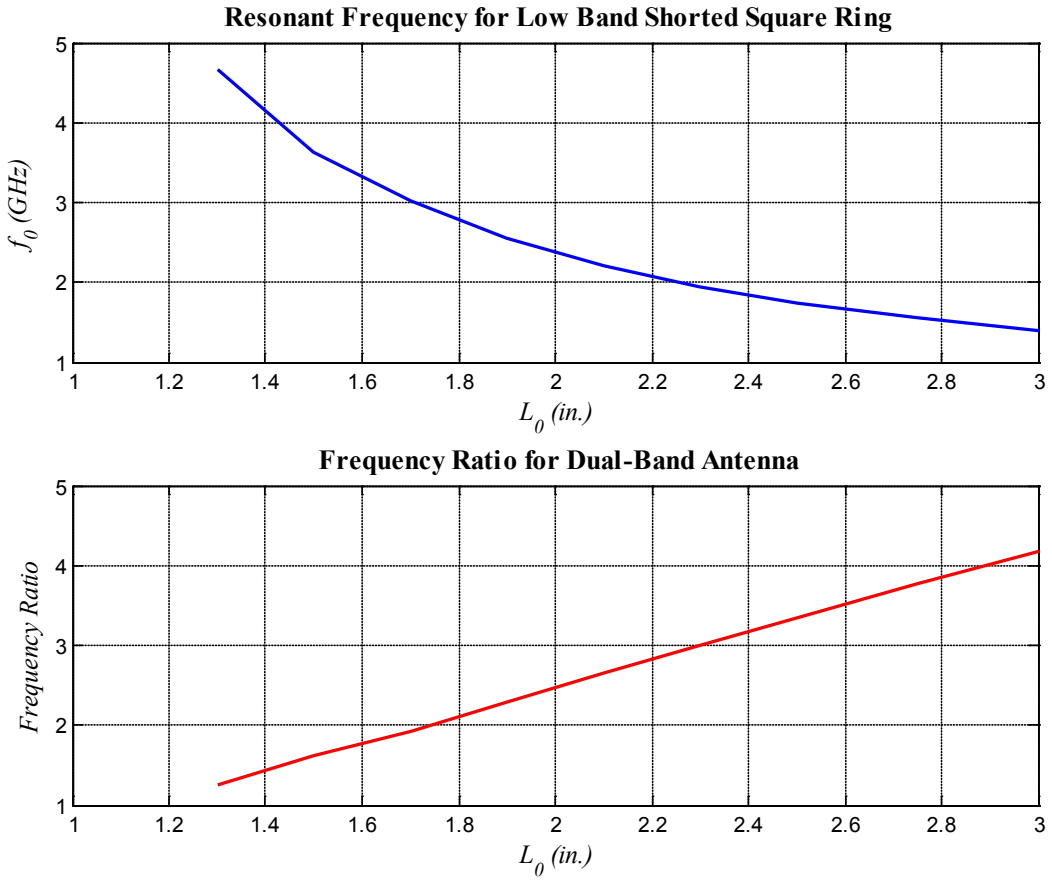

Figure 3-25: Results of parametric study showing the resonant frequency of the low band shorted square ring as a function of the outer side length

The dual-band element designed in this section showed the ability of to operate with dual-polarization in two separate frequency bands. The dual-polarization can be orthogonal senses of either linear or circular polarization. In this case, the low frequency element operated with dual-

linear while the high frequency band operated with dual-circular polarization. The element layout has many variables that provide great flexibility for the ratio between the high and low frequency bands.

3.3 Size reduction using dual-substrate capacitive loading

The size of the low band radiating element is the limiting factor in the array lattice spacing for this dual-band, dual-polarized element. In cases with large separation between the two bands, the low band element will force a large element spacing that will lead to poor scanning performance and the early introduction of grating lobes at the high frequency. The dual-substrate capacitive loading technique described in [7, 8] can be used to reduce the size of the low band element, and thus reduce the overall footprint of the dual-band element. In [7, 8], the dual-substrate capacitive loading technique was applied to a linearly polarized antenna element. In order to maintain the dual-CP performance of this element, the capacitive loading technique will need to be modified.

The top view of the element is provided in Figure 3-26. The radiating elements are described in 3-26(a). The low band radiating element is a shorted square ring with outer side length L_0 and inner side length L_1. The high band radiating element is a square ring slot with outer side length L_1 and inner side length L_2. The radiating apertures use isosceles triangle perturbations at opposing corners to achieve single feed CP operation. The equal sides of the isosceles triangles are of length Δ_{LB} and Δ_{HB} for the low and high band elements respectively. Figure 3-26(b) shows the top view of the capacitive patch. In order to allow the CP operation, the outer perimeter of the capacitive patch is modified to follow the outer perimeter of the low band shorted square ring radiator. The capacitive patch width (w_{CAP}) can be changed to control the capacitance of the loading structure. The width and shape of the capacitive substrate are identical to that of the capacitive patch.

The location of the vias is shown in Figure 3-26(c). The shorting vias provide electrical continuity between the low band radiator and the ground plane. These vias provide the shorting mechanism for the low band shorted square ring while also suppressing the parallel plate mode that can propagate in the slotted stripline structure of the high band radiator. The capacitive vias are located at the outer perimeter of the low band radiator, and they provide electrical continuity between the low band radiating structure and the capacitive patch.

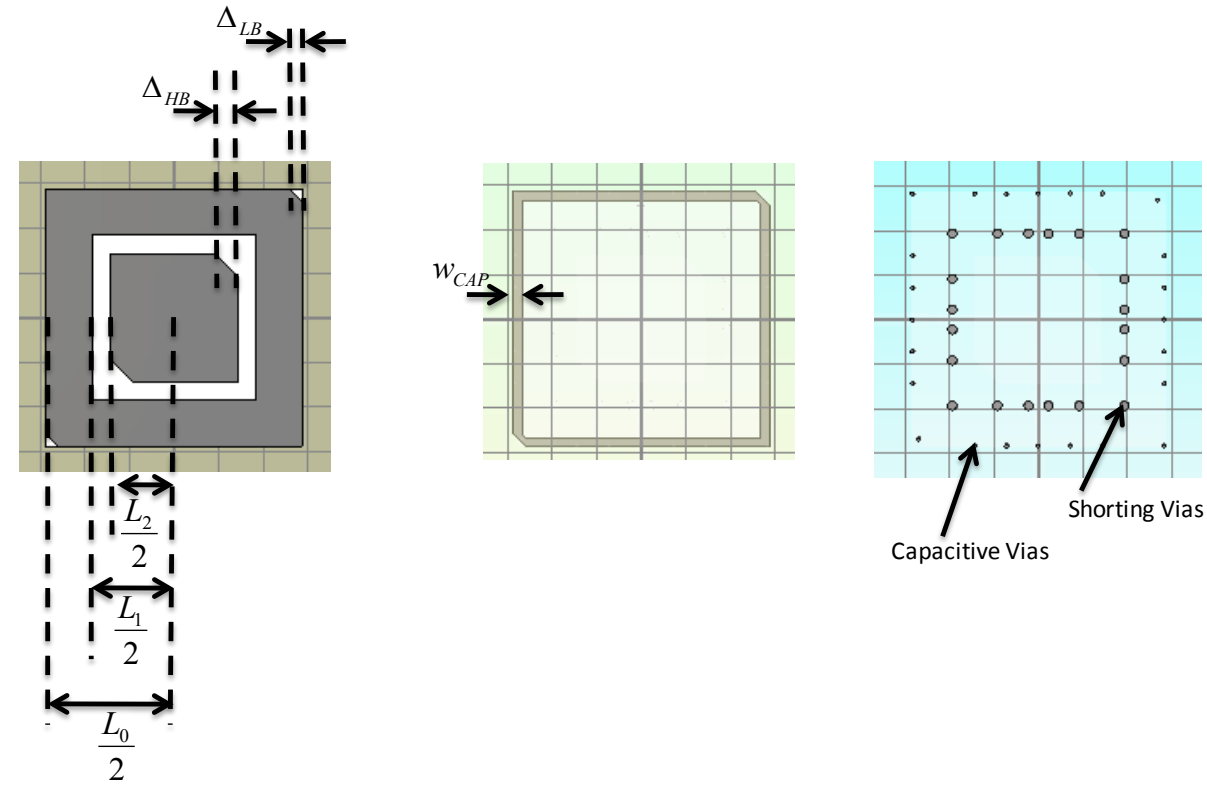

(a) Top view of radiating elements

(b) Top view of capacitive patch

(c) Top view of vias

Figure 3-26: Top view of dual-band, dual-CP antenna element with dual-substrate capacitive loading for size reduction

The dielectric profile of the dual-band, dual-CP element with capacitive loading is similar to that of the element without the loading structure present. The dielectric material between the radiating apertures and the ground plane consists of three layers. The thin feed substrate layer is sandwiched between two dielectric matched substrate layers. These layers use a Rogers RT5880 substrate material with a dielectric constant of 2.33. The feed substrate has a thickness of h_2, while the other two substrate layers have thicknesses of h_1 and h_3. The presence of the capacitive substrate is unique to this element. The high dielectric constant material is present only beneath the capacitive patch, and it is present to increase the capacitive effect of the loading structure. For this simulation, the capacitive substrate has a dielectric constant of 10. This high dielectric constant can be realized through by using Rogers TMM10i, a ceramic-based microwave dielectric. The capacitive substrate has a height of h_{CAP}, where the height represents the distance between the ground plane and the capacitive patch.

The high band feed lines are printed on opposing sides of the feed substrate. Each of the high band slots are excited with a stripline feed terminated in an open-circuit stub. This feed is transitioned to a microstrip layer just prior to the location of the slot. This is done to minimize the impact of the high band feed on the low band radiator. A plated through provides electrical continuity between the stripline feed and an impedance matched microstrip feed line on a

separate layer. This plated through hole passes through an aperture in the ground plane. An isometric view of this transition is provided in Figure 3-27. The dielectric layers are suppressed in this figure to provide a clear view of the transition.

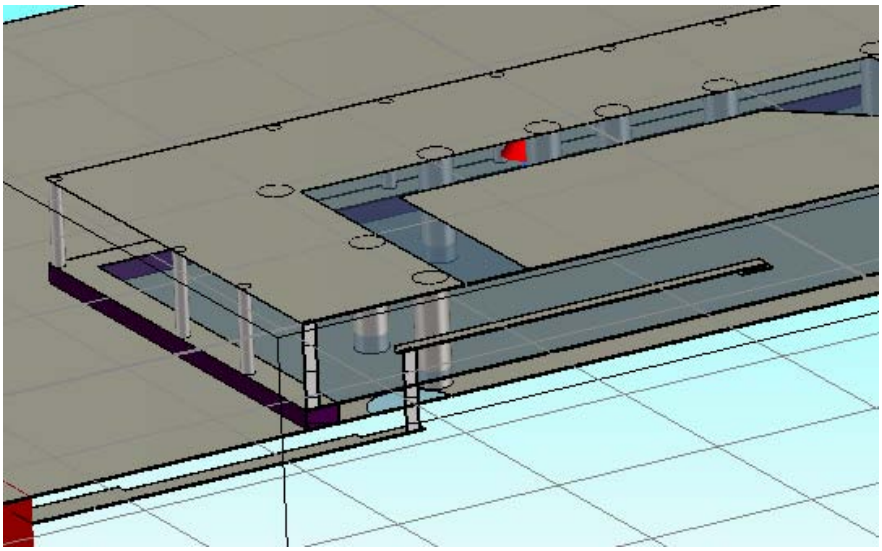

Figure 3-27: Section view of the microstrip-to-stripline feed transition for the high band square ring slot

A dual-band, dual-CP element incorporating the dual-substrate capacitive loading technique for size reduction was designed and simulated. The element covers two distinct ISM frequency bands centered at 2.45 GHz and 5.85 GHz. Each frequency band supports simultaneous dual-CP operation. Table 3-3 provides a comparison between the dimensions of the capacitively loaded element and those for the dual-band, dual-CP element described in Section 3.2. The addition of the loading structure has reduced the outer side length L_0 to 56% of its unloaded value. The outer side length for the loaded element is 1.150", which is 0.56λ at the high frequency band for this dual-band element. That spacing will allow close element spacing in an array environment to allow for wide scanning capabilities. The unloaded element had a value for L_0 that was equal to 0.99λ at the high frequency. That element size would not lead to adequate scanning performance in a phased array environment.

The values for L_1 and L_2 remained unchanged, as did the substrate thickness h_1, h_2, and h_3. The increased element capacitance resulted in a decreased value for Δ_{LB}, while leaving Δ_{HB} unchanged. The capacitive loading structure uses a capacitive patch of width 0.040". The separation between the capacitive patch and the ground plane is 0.022", and the capacitive substrate has a dielectric constant of 10.

Table 3-3: Comparison of parameters for dual-band, dual-polarization antenna elements with and without the inclusion of capacitive loading

Parameter	L_0	L_1	L_2	Δ_{HB}	Δ_{LB}	w_{CAP}	ε_{CAP}	h_{CAP}	h_1	h_2	h_3
Loaded Element	1.150”	0.735”	0.575”	0.105”	0.058”	0.040”	10	0.022”	0.060”	0.060”	0.004”
Unloaded Element	2.020”	0.735”	0.575”	0.105”	0.285”	N/A	N/A	N/A	0.060”	0.060”	0.004”

The s-parameters for the dual-band, dual-CP element with capacitive loading are plotted in Figure 3-28(a)-(d). The high band ports (1 and 2) show performance identical to that of the unloaded element. Each port has a return loss greater than 10 dB (i.e. $|s_{ii}|$<-10dB for i=1,2), indicating a VSWR < 2.0:1. The port-to-port isolation for the high band ports has a maximum value of 30dB at the mid-band frequency of 5.85 GHz. The VSWR plots of Figure 3-29(a)-(b) show that the addition of the capacitive loading structure leaves the impedance match of the high band ports unchanged.

The low band ports have a return loss greater than 10dB over much of the 2.45 GHz ISM band. Figures 3-29(c) and (d) show a decreased bandwidth at the low frequency bands as a result of the capacitive loading structure. The increased capacitance resulting from the loading structure has increased the quality factor of the antenna; subsequently, the bandwidth of the antenna has been reduced. The unloaded element shows a fractional impedance bandwidth of 7.02% compared to the 2.65% fractional bandwidth for the capacitively loaded element.

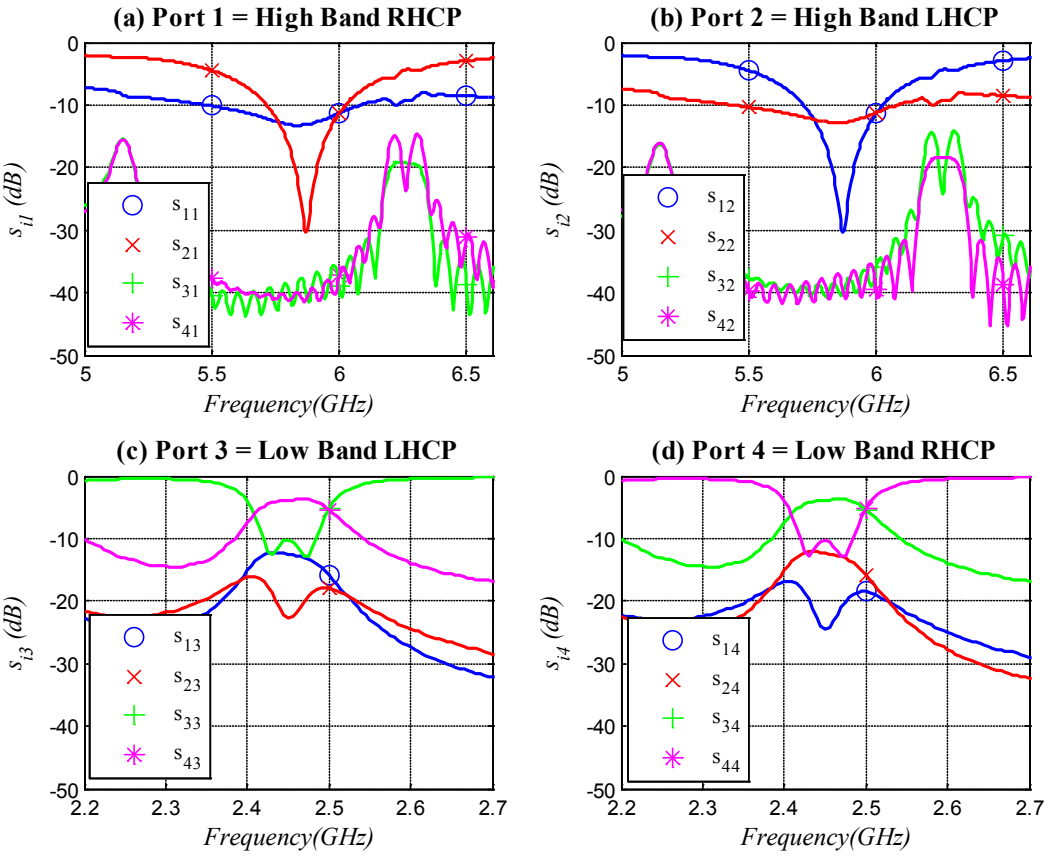

Figure 3-28: Simulated S-parameters for dual-band, dual-CP antenna element with dual-substrate capacitive loading in place

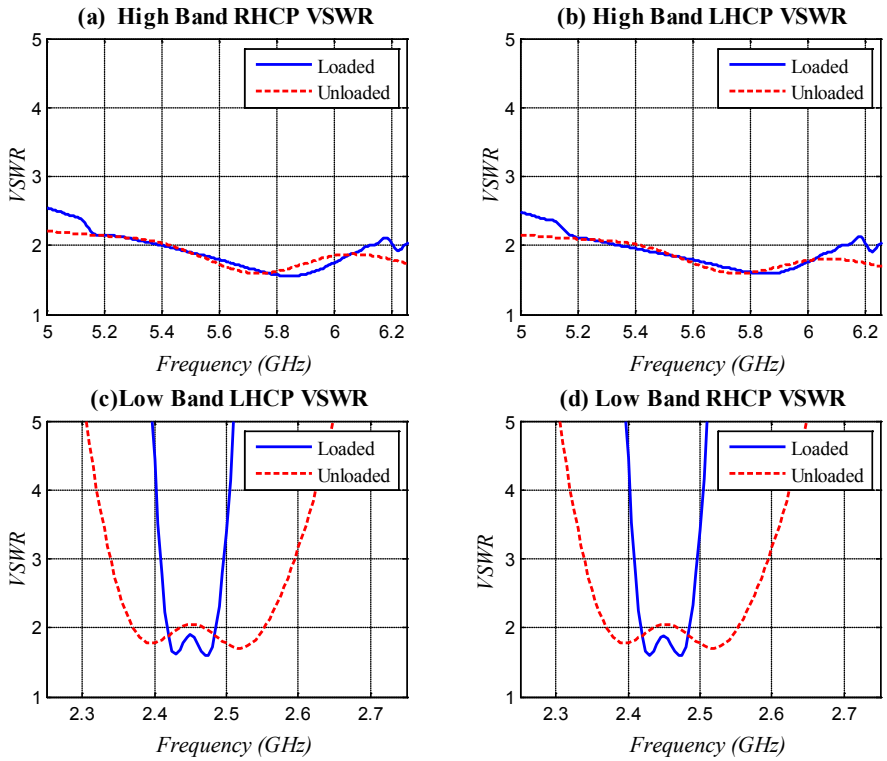

Figure 3-29: Simulated VSWR for the four ports of the dual-band, dual-CP antenna element using capacitive laoding for size reduction

The axial ratio for the loaded element is compared to that of the unloaded element in Figure 3-30(a)-(d) for the four ports of the dual-band dual-CP antenna element. The high band performance is left relatively unchanged when the capacitive loading structure is added. The slight differences are attributed to the reduction of the low band shorted square ring, which corresponds to a reduction in the ground plane size for the square ring slot. In the unloaded element, L_0 is almost three times larger than L_1, resulting in a ground plane that appears near "infinite" to the slot. When the loading structure is added, the size of L_0 is cut almost in half. However, it should be reiterated that any differences in performance at the high frequency band are virtually negligible.

The usable axial ratio region serves as the limiting factor for the overall usable bandwidth of the dual-band, dual-CP element with capacitive loading in the low frequency bands. Figures 3-30(c) and (d) show that the loaded element has a 3dB axial ratio bandwidth of 1.01% compared to the 2.78% bandwidth for the unloaded element. This shows that – while the impedance match bandwidth of the loaded element covers the 2.45 GHz ISM band – the axial ratio performance of the element is limited to a narrow portion at the center of the frequency band. This finding is evident in the axial ratio vs. frequency vs. theta contour plot of Figure 3-31. In this figure, the horizontal axis is frequency (GHz), and the vertical axis represents theta (Deg.). The axial ratio contours in this plot are elliptical in nature with a major axis parallel to the theta axis and a minor

axis parallel to the frequency axis. This indicates that the frequency bandwidth is the limiting factor in the axial ratio coverage. The major axis of the elliptical contours shows that the axial ratio remains below 3dB for $|\theta|<45°$ over the narrow frequency band. This result suggests that the element can be used in an array environment requiring broad scanning, as long as the frequency limitations are acceptable.

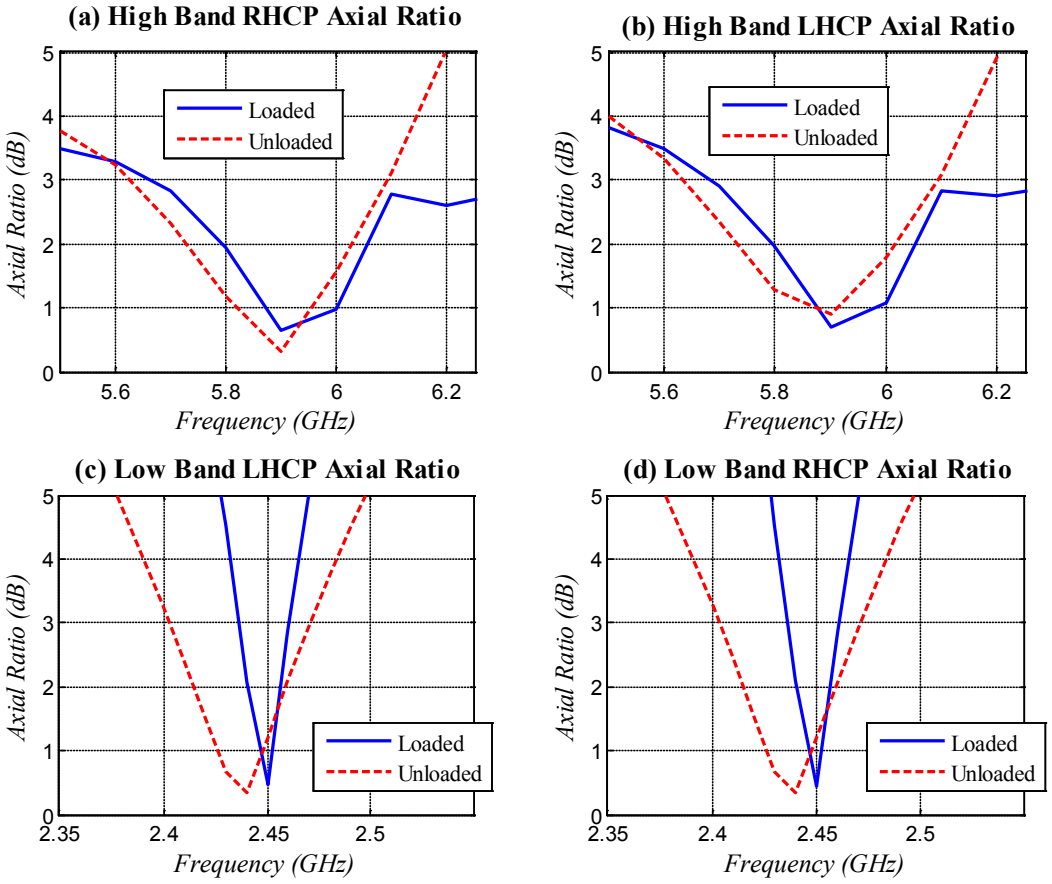

Figure 3-30: Simulated Axial Ratio for the four ports of the dual-band, dual-CP antenna element using capacitive loading for size reduction

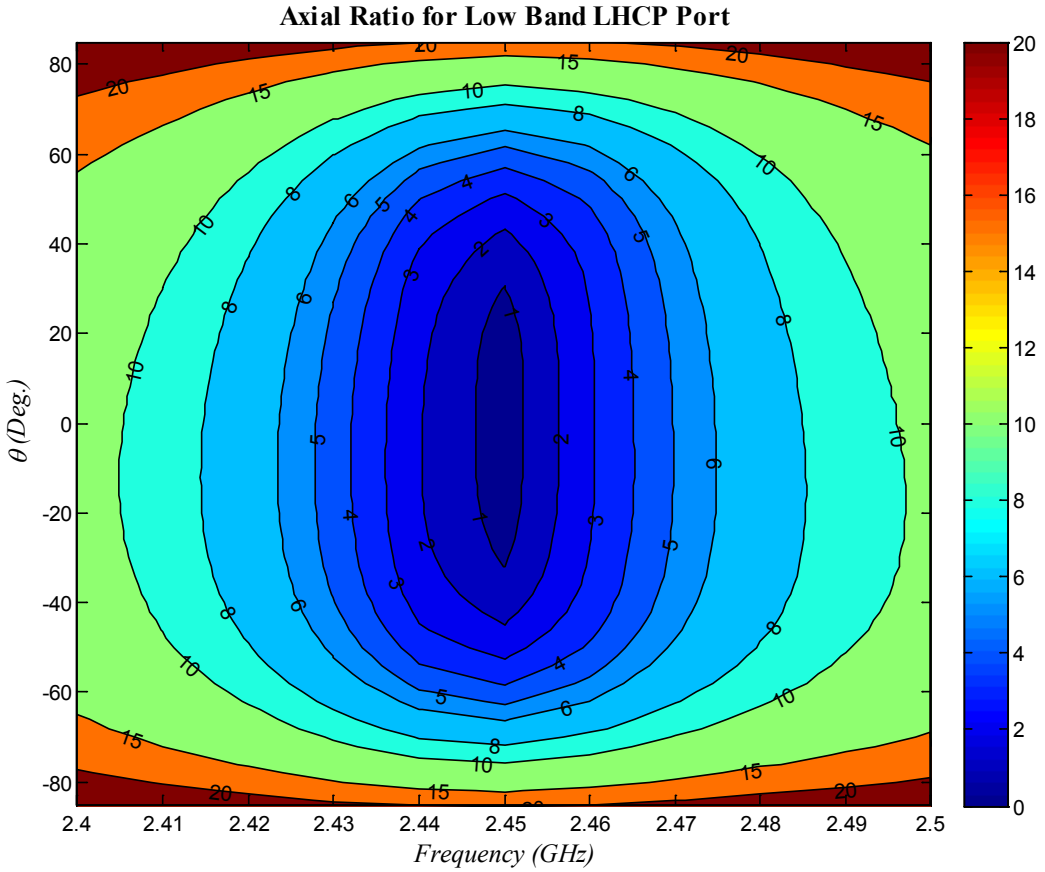

Figure 3-31: Simulated axial ratio vs. frequency vs. theta for the low band LHCP port of the dual-band, dual-CP antenna element using capacitive loading for size reduction

The LHCP and RHCP patterns at 2.44 GHz are plotted in Figures 3-32 and 3-33. These figures provide a comparison between the loaded and unloaded element in the principle planes of the antenna element. The gain patterns show the anticipated pattern changes resulting from a decreased aperture size: reduced gain and increased beamwidth. The cross-polarized component levels are unchanged near broadside, but the XPD decreases at wide values of θ. This will result in a narrower axial ratio pattern. However, the plot in Figure 3-31 shows that – while narrower – the axial ratio still remains below 3dB over a wide range of θ values.

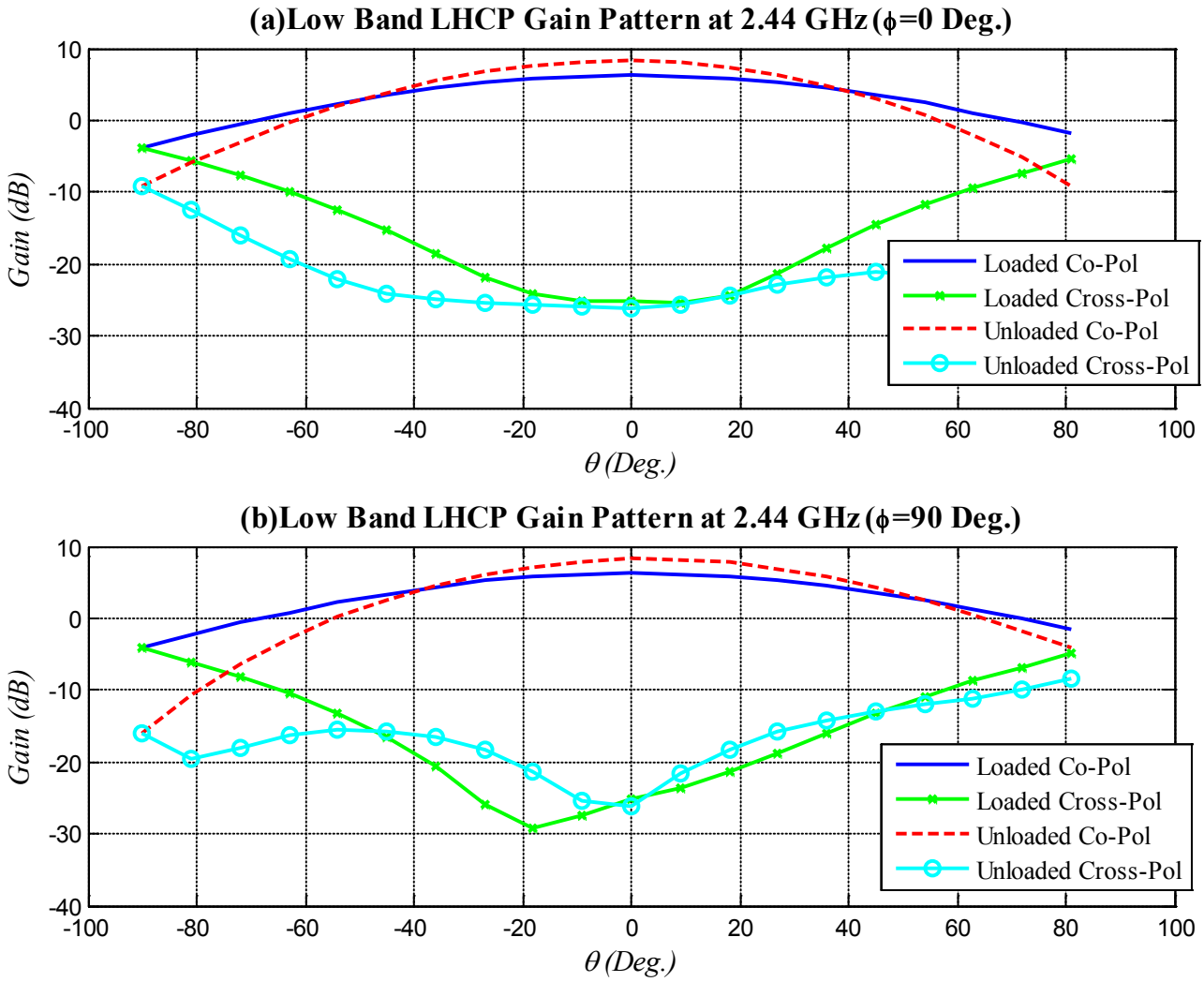

Figure 3-32: Low band LHCP radiation pattern comparison for dual-band, dual-polarized antenna elements with and without capacitive loading

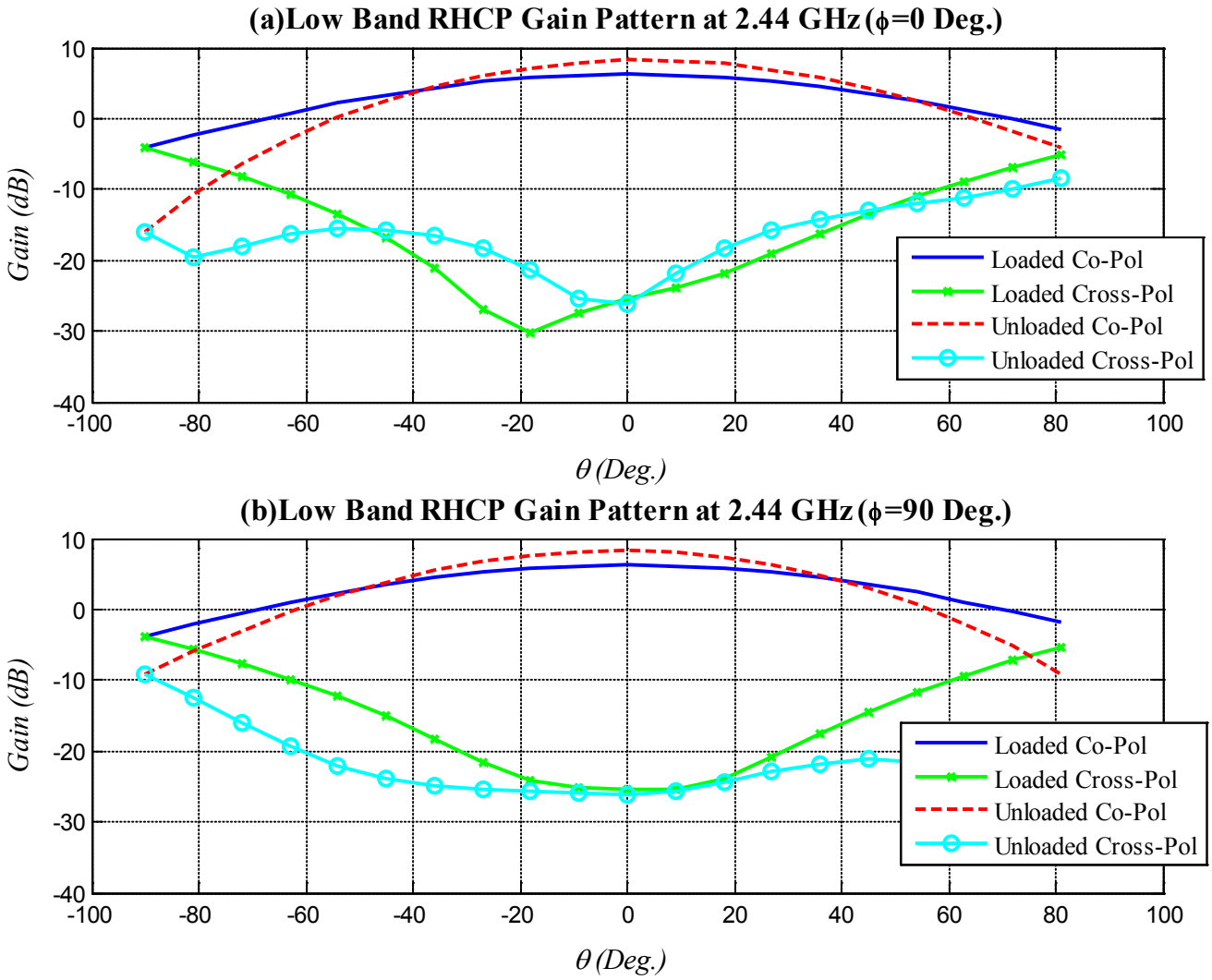

Figure 3-33: Low band RHCP radiation pattern comparison for dual-band, dual-polarized antenna elements with and without capacitive loading

The dual-substrate capacitive loading structure proposed in [7, 8] has effectively been incorporated into the dual-band, dual-polarized antenna element, resulting in an element capable of operating over two distinct frequency bands with orthogonal senses of CP while occupying a small enough footprint for array applications. The small footprint allows for wide scanning coverage in an array environment. The resulting size reduction is not obtained without drawback as outlined in the comparison of Table 3-4. Despite these drawbacks, the addition of the capacitive loading results in a nearly 50% size reduction. The capacitive loading structure had a negligible effect on the performance of the high band performance of the element.

Table 3-4: Performance comparison between dual-band, dual-CP antenna elements with and without capacitive loading

Parameter	Loaded Element	Unloaded Element
Impedance Match Fractional Bandwidth	2.65%	7.02%
Axial Ratio Fractional Bandwidth	1.01%	2.78%
2.45 GHz Realized Gain	2.673 dBi	5.638 dBi
Total Efficiency	43%	52%
2.45 GHz 3dB Bandwidth (φ=0°)	94.9°	71.0°
2.45 GHz 3dB Bandwidth (φ=0°)	95.1°	71.7°
L_0	1.150"	2.020"

3.4 Comparison with existing dual-band, dual-polarized elements from literature

Dual-band elements providing simultaneous dual-polarization in each of the two, distinct frequency bands provide the flexibility needed in applications ranging from space-based synthetic aperture radar to multifunction radar to wireless communications. The advantages of the element designed in this dissertation arise from its ability to radiate dual-circular or dual-linear at each of the two operational frequency bands. This allows the user to utilize maximum polarization diversity in a given system. The four-port feeding allows the polarizations to be used simultaneously. The majority of dual-band elements in the literature are not capable of providing simultaneous dual-CP operation at each polarization bands. Moreover, the design layout provides flexibility over the frequency ratio between the high and low bands.

Several of the dual-band antenna elements seen in the literature use an annular ring radiator. Lin and Huang place a truncated square ring patch inside of an annular ring patch to achieve dual-band performance [77]. The high band square ring patch radiates a single sense of CP, and the low band annular ring element is linearly polarized. In order to fit the high frequency element inside of the annular ring, the square patch is printed on a high dielectric substrate (ε_r=15.5). The element presented in this dissertation has many advantages over this element. The primary advantage is the ability to operate with dual-CP in each frequency band, while the element presented by Lin and Huang has single-polarized performance in each band. In addition, the dual-band, dual-CP element in this dissertation uses a novel capacitive loading technique to reduce the size of the low band radiator. In this approach, a low dielectric constant material is present beneath the majority of the radiating element to minimize the volume of high dielectric material required. Cai, Row, and Wong used an L-shaped feed line to excite circular polarization in the TM_{11} and TM_{21} modes of an annular ring patch [34]. This antenna operates with a single sense of CP in each frequency band, and the frequency ratio is strongly limited by the

dimensions of the annular ring. The element presented in [34] has axial ratio bandwidths of 2.2% and 1.3% in the low and high bands respectively. The element in this dissertation has larger bandwidths when the capacitive loading is not in place. When the loading is in place, the low frequency performance of the Cai, *etl* al element has slightly greater axial ratio bandwidth, but their high band element still has a much narrower performance. In addition, the Cai, *et* al element does not provide dual-CP performance in either band and has a limited frequency ratio.

There are no couplers, hybrids, multiplexers, or active components required in the feed network which makes the circuitry simple and cost effective. This provides an advantage over the feeding techniques used in [36-38]. In this design, the circular polarization is obtained by introducing perturbations into opposing corners of the square radiating apertures: shorted square ring for the low band, and square ring slot for the high band. The introduction of the perturbations leads to circular polarization with only a single feed point. An orthogonal feed point is added to each frequency band resulting in dual-circular polarization. This technique is far simpler than using a hybrid network to generate circular polarization.

Jaworski, *et al* designed a dual-band, dual-linearly polarized antenna element by packaging two circular patches closely together[66]. However, these elements are not concentric making an array environment difficult. Hong, *et al* also packaged two separate antennas together for dual-band performance [78]. In their design, they placed a reactively loaded monopole next to an annular ring antenna. The annular ring antenna operated with circular polarization, while the monopole was linearly polarized. In designs involving two separate antennas packaged together – but not concentrically located – an array environment becomes increasingly difficult.

Owens covers the receiving and transmitting band of a satellite communications system by using square patches [75]. The patches use orthogonal feed lines and perturbed corners to achieve dual-CP performance. The dual-band coverage in this design is only achieved as long as both bands like within the usable bandwidth of the square microstrip patch. Thus, the frequency ratio is extremely limited.

Many designs in the literature for dual-band antenna elements used some type of perforated low band antenna element to provide locations for multiple high frequency band elements. Granholm designed a dual-band, dual-polarized antenna element for synthetic aperture radar (SAR) applications [20]. In this design, the larger low band element is located on a plane above the layer containing the high band elements. The low band element is perforated to allow radiation from the high band element. Both bands in this design operate with dual-linear polarization. The perforated design lends itself nicely to large frequency ratios, but it becomes increasingly difficult to arrange the elements when the frequencies become close. In Granholm's design application, the frequency ratio is greater than 4:1. Shafai, *et al* use a similar perforated design to cover frequencies in L- and C-bands with dual-linear polarization for SAR applications [18]. The design patented by Strickland in [76] uses a low band square ring resonator with nine high

frequency square patches in the center for an SAR array. Similarly to the SAR designs in [18, 20], this element also is limited to large frequency ratios with dual-linear polarization.

The dual-substrate capacitive loading technique used in this dissertation research is itself a novel invention. Subsequently, its inclusion in the design of this dual-band, dual-CP antenna element is also novel. The ability to integrate the dual-substrate capacitive loading technique for size reduction in this element makes the element suitable for integration into a dual-band array with uniform lattice spacing; this makes the element attractive to synthetic aperture radar and multifunction radar applications. To the authors' knowledge, an element of this kind has not been discussed in the literature, and this element marks a significant development in the field of antenna engineering.

The dual-band, dual-polarized element uses a printed circuit design that provides a low profile, light weight, and low cost design that makes is desirable for integration with laptop technology, wireless access points, space born radars, cellular phone handsets, base stations, and many other areas within the ever growing field of wireless communications. The element provides axial ratio bandwidths 2.78% and 8.05% in the low and high band respectively for both sense of circular polarization; when the dual-substrate capacitive loading is incorporated, the low band axial ratio bandwidth decreases to 1.01% while the high band remains unchanged. While it does reduce the bandwidth, the dual-substrate capacitive loading technique provides a novel method for controlling the footprint of the dual-band, dual-polarized antenna element.

The element shown in this dissertation operated at two ISM frequency bands due to their growing popularity, and it had a frequency ratio of 2.4:1. However, this element is not limited to those frequency bands. The design process for this element gives strong flexibility to the frequency ratio. The first step in designing this element is to design the high frequency square ring slot with the desired polarization characteristics. After this is completed, the inner side length of the low band shorted square ring is set. The shorted square ring is then designed to provide suitable operation at the low frequency range. If the element then proves too large for the selected application, the dual-substrate capacitive loading technique can be applied for significant size reduction of the low frequency element. This design process provides unique capability and flexibility to this element that is not seen in the literature. The elements discussed in this section each provide some of the capabilities of this element, but none match the flexibility of this antenna element to cover dual-polarizations in two distinct frequency bands with control of the element's footprint.

CHAPTER 4. LOW PROFILE, DUAL-BAND, DUAL-POLARIZED ANTENNA ARRAY

The introduction of the dual-substrate capacitive loading technique allows the dual-band, dual-polarized antenna element to be placed into an array environment suitable for wide-angle scanning applications. The design focused on in this section used a low band frequency centered at 2.45 GHz, and the high band frequency was centered at 5.85 GHz. In order to properly analyze the array performance including mutual coupling effects, an array analysis technique was developed that uses nine active element patterns to represent all elements in the array. One of the nine active element patterns is assigned to each element in the array based on the element's geometrical location within the array lattice. In this chapter, the array layout is described and followed by an in-depth analysis of several array sizes to show the overall performance of the array.

4.1 Discussion of Hybrid Array Pattern Calculation Technique Using Multiple Active Element Patterns

The dual-band element discussed in the dissertation research has been shown to have advantages over many dual-band elements discussed in current literature. One primary advantage allows this element to be placed in an array without the introduction of grating lobes. When a dual-band element operates with a frequency ratio much greater than unity, the element spacing must be near a half-wavelength at the highest frequency to allow for a suitable scanning range free of grating lobes. Arranging two radiating elements with dissimilar frequency ranges into a small footprint can be challenging. The element used in this research utilizes a dual-substrate capacitive loading scheme [8] on the low frequency element to reduce the size of the element's footprint, this facilitating placement in an array with limited real-estate for low frequency elements.

In order to adequately study the performance of the dual-band element in an array environment, several techniques can be utilized. Typically, the first look at the performance of an element placed in an array comes from the use of periodic boundary conditions. These boundary conditions simulate the infinite periodic extension of the element and make the element appear as if it is surrounded by an infinite number of uniformly excited elements. Once the element pattern is calculated using this approach, it can be multiplied by an array factor to reveal an approximate array pattern. This approach has the advantage of requiring limited computational resources because the computational domain consists of a single unit-cell of the array. However,

this approach assumes that all elements are identical and thus neglects changes in mutual coupling and edge effects that occur for elements near the outer perimeter of the array.

The classical approach for calculation of the radiation pattern for an antenna array involves multiplying the antenna pattern of an isolated element by an array factor accounting for the spatial distribution, amplitude weighting, and phase weighting of the array elements. The shortcomings of the classical approach lie in its inability to account for mutual coupling effects between elements in an array [79]. In order to include mutual coupling effects, active element patterns are used in place of an isolated element pattern to provide a more accurate result using the classical approach. The active element pattern provides the radiation pattern of the entire array when a single element is fed and all other elements are terminated in a conjugately matched termination [79-81]. The active element pattern can be obtained through measurements or simulations. When the active element pattern is multiplied by the proper array factor, the array pattern including mutual coupling effects is obtained.

The work in [82] describes approaches using open-circuited active element patterns and short-circuited active element patterns. In these approaches, the element patterns contain the magnitude and phase information accounting for the spatial phase variation for the given element, and thus the pattern for each individual element is required. It is mentioned that symmetry can be used to reduce the number of patterns that are required, but this is still a large number of elements for large arrays. In this research, a hybrid approach is developed and utilized that requires the calculation of only nine active element patterns. The phase information for each element will be included by taking the phase-adjusted unit-excitation active element pattern and using it as an active element pattern for all elements present in a similar environment. The phase-adjusted unit-excitation active element pattern is discussed in [79], and it is a modified version of the unit-excitation active element pattern in which the spatial phase dependence has been removed. The phase-adjusted patterns will change when the geometry changes. However, if the proper phase-adjusted patterns are selected for the appropriate locations within a large array, the hybrid technique presented can be used to provide an excellent approximation to the overall array pattern. The theory and application of this technique will be described in the remainder of this section, and some example calculations will be performed [9].

4.1.1 Hybrid Array Calculation Theory

The theory describing the use of the active array pattern follows from the work provided by Kelley and Stutzman [79, 82]. This theory is being discussed to show the path to the proposed hybrid array calculation technique. This technique is built upon the simulation of a 3x3 array of elements. These elements will provide sufficient active element pattern information to calculate a close approximation of the array pattern for an MxN array. This saves immense simulation time, and it shifts much of the array calculation work to an algorithm that has been coded in Matlab.

The classical array pattern is calculated using (4-1), where $g_{isol}(\theta,\varphi)$ is the element pattern of one of the array elements in an isolated environment (typically a free-space environment), $\hat{r}$ is a unit vector directed from the origin to the observation point, and $\mathbf{r_q}$ is the vector from the origin to the location of the current element. This approach assumes that the current distribution at each element is identical, and thus it is not impacted by mutual coupling. The classical approach can be sufficient for many array applications where the mutual coupling between elements is insignificant; however, it can be made more accurate if it utilizes the active element pattern.

$$\boldsymbol{E}(\theta,\varphi) = \boldsymbol{g}_{isol}(\theta,\varphi)\sum_{i=1}^{N_{TOT}} I_i e^{jk\hat{r}\cdot\boldsymbol{r}_i} \quad \textbf{(4-1)}$$

The unit-excitation active element pattern, $g_u^q(\theta,\varphi)$, represents the radiation pattern of the entire array when only a single element is excited by a unit voltage with its associated generator impedance (Z_{gq}). All other elements are loaded by their characteristic impedances. The set of unit-excitation element patterns contain all effects of radiative mutual coupling. As a result, (4-2) provides an exact representation of the array pattern. It should be noted that (4-2) does not contain the typical spatial-phase term found in array patterns. This is because the spatial-phase term is already included in the unit-excitation active element pattern. As a result, this pattern is unique to the geometrical location of the given element. In order to use the unit-excitation active element pattern in other geometries, it can be modified to the phase-adjusted, unit-excitation active element pattern using (4-3). The phase-adjusted quantity removes the spatial-phase term from the element. The expression in (4-2) is modified to (4-4) when the phase-adjusted quantity is used. It should be noted that the expression in (4-4) is still an exact representation of the array pattern.

$$\boldsymbol{E}(\theta,\varphi) = \sum_{i=1}^{N_{TOT}} I_i \boldsymbol{g_u^i}(\theta,\varphi) \quad \textbf{(4-2)}$$

$$\boldsymbol{g_p^i}(\theta,\varphi) = \boldsymbol{g_u^i}(\theta,\varphi)e^{-jk\hat{r}\cdot\boldsymbol{r}_i} \quad \textbf{(4-3)}$$

$$\boldsymbol{E}(\theta,\varphi) = \sum_{i=1}^{N_{TOT}} I_i(\theta,\varphi)\,\boldsymbol{g_p^i}(\theta,\varphi)e^{jk\hat{r}\cdot\boldsymbol{r}_i} \quad \textbf{(4-4)}$$

The unit-excitation active element pattern is different for every element within the array due to the unique geometrical location of each element. This requires the measurement, calculation, or simulation of the pattern for every individual element within the array. In order to simplify the process, the average active element pattern can be used to approximate the result. As the size of the array increases, the majority of the elements within the array have nearly identical phase-adjusted, unit-excitation active element patterns. Subsequently, these patterns can be approximated by the average active element pattern. This pattern can be obtained through simulations using periodic boundary conditions to make the element appear as if it is in an infinite array environment. Once the average active element pattern is known, (4-5) can be applied to provide an approximation of the array pattern. This approach is accurate for very large arrays, but it typically fails for smaller arrays due to the significant variation of the active element patterns across the array.

$$\boldsymbol{E}(\theta,\varphi) = \boldsymbol{g_{av}}(\theta,\varphi)\sum_{i=1}^{N_{TOT}} I_i e^{jk\hat{r}\cdot\boldsymbol{r_i}} \quad \textbf{(4-5)}$$

For arrays of small to moderate size, the average active element pattern approach can have shortcomings because of the variation of element performance across the array. An exact solution can be obtained by simulating the entire array using commercial software, but this technique can be time consuming and taxing to typical computational resources. Another method to obtain an exact solution is to construct the entire array, measure the unit-excitation active element pattern of each element, and add the contributions analytically. While this technique requires a large time commitment to measuring many element patterns, it is not without benefit. After all of the element patterns are measured, they can be combined analytically to provide the antenna array pattern for any scanned pattern by introducing the proper amplitude and phase weighting. This eliminates the need to design, build, and test many beamformiung networks for characterizing the array. However, it would be nice to have access to a close approximation of the array pattern without the potentially costly – both in time and money – process of constructing a large array. In order to accomplish this, an approach is presented that utilizes different average active element patterns depending on the location of the element within the array. In the discussion presented here, the necessary set of average active element patterns is obtained by simulating – or measuring – a 3x3 array. Higher levels of accuracy can be obtained by simulating larger arrays at the expense of time and/or cost.

A small finite array of dual-band linearly polarized elements was simulated to investigate the mutual coupling between elements. For this example, the low band was centered at 6 GHz while the high band was centered at 10 GHz. These simulations revealed that the majority of mutual coupling at a given element is generated from the elements immediately surrounding the given element. Figures 4-1 and 4-2 illustrate this finding. Each of these figures contains a diagram of a 4x4 array of dual-band elements. The locations of the elements are located on a rectangular grid, with the lower left-hand element being identified as (1, 1). Each figure also contains a plot of the inter-element coupling when the element located at (3, 3) is excited. For the low band case in Figure 4-1, the elements immediately surrounding the driven element see a mutual coupling signal in the range of -10 to -15dB. Elements located outside of the immediate perimeter see a significantly lower mutual coupling, with a maximum value being in the neighborhood of -25dB. The high band results show similar trends. The elements outside of the immediately surrounding perimeter in the high band elements have a maximum coupling on the order of -30dB. The high band coupling drops off faster than the low band coupling as a function of distance. Intuitively, this makes sense as the elements are separated by a larger electrical distance at the high band frequencies. From these simulations, it became evident that the majority of the mutual coupling effects in the dual-band array could be accounted for if only the immediately surrounding elements were considered. This finding leads to the primary assumption that drives the hybrid calculation approach used in this study.

Transmitting element is located at (3,3).

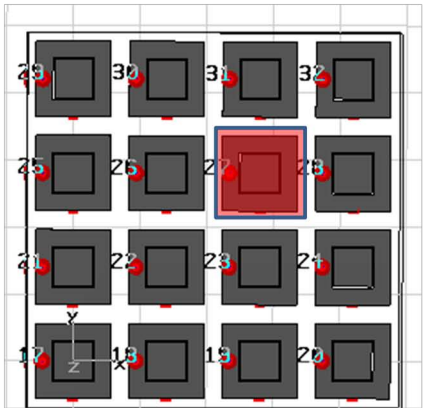

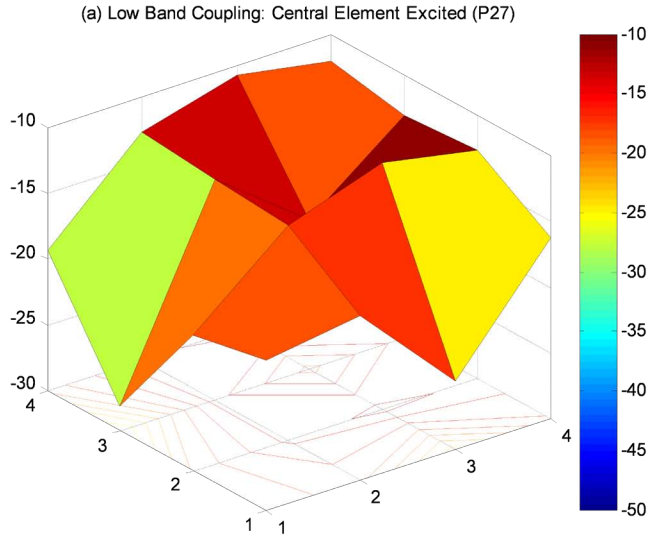

Figure 4-1: Low Band Mutual Coupling Results

Transmitting element is located at (3,3).

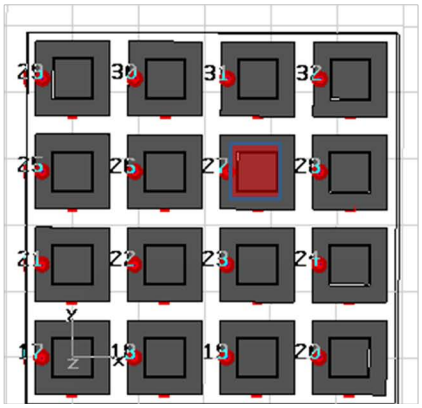

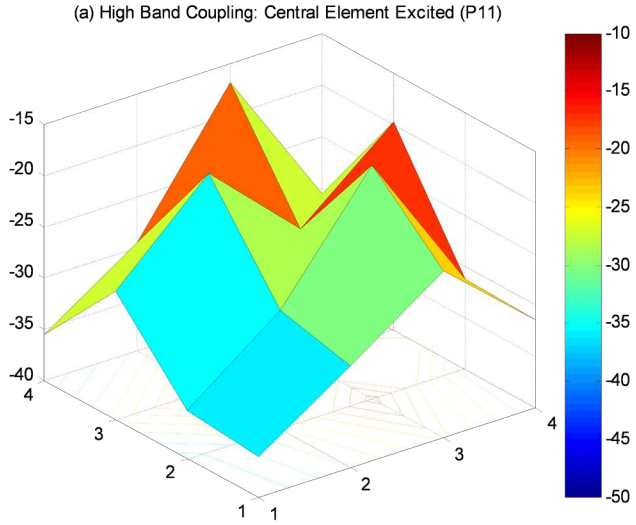

Figure 4-2: High Band Mutual Coupling Results

The hybrid array pattern calculation technique is illustrated in Figure 4-3. The left of this figure shows a 3x3 array, with the elements numbered 1 through 9. The unit-excitation active element pattern for each element in this array is simulated (or measured), and the phase-adjusted unit-excitation active element pattern is calculated by applying (4-3). The phase-adjusted patterns are then used to represent the average active element pattern for the region of the array indicated by the large array illustrated on the right hand side of this figure. This technique utilizes the assumption that the majority of mutual coupling effects come from the elements immediately surrounding the driven element. This approach will not result in the exact pattern that would be obtained using (4-2) or (4-4), but it will have a higher level of accuracy than the approach that assumes an identical active element pattern for all elements within the array. Additionally, the hybrid approach eliminates the need for simulating and/or measuring the active element pattern for every element within in potentially large finite array, thus providing a significant savings in both time and computational resources.

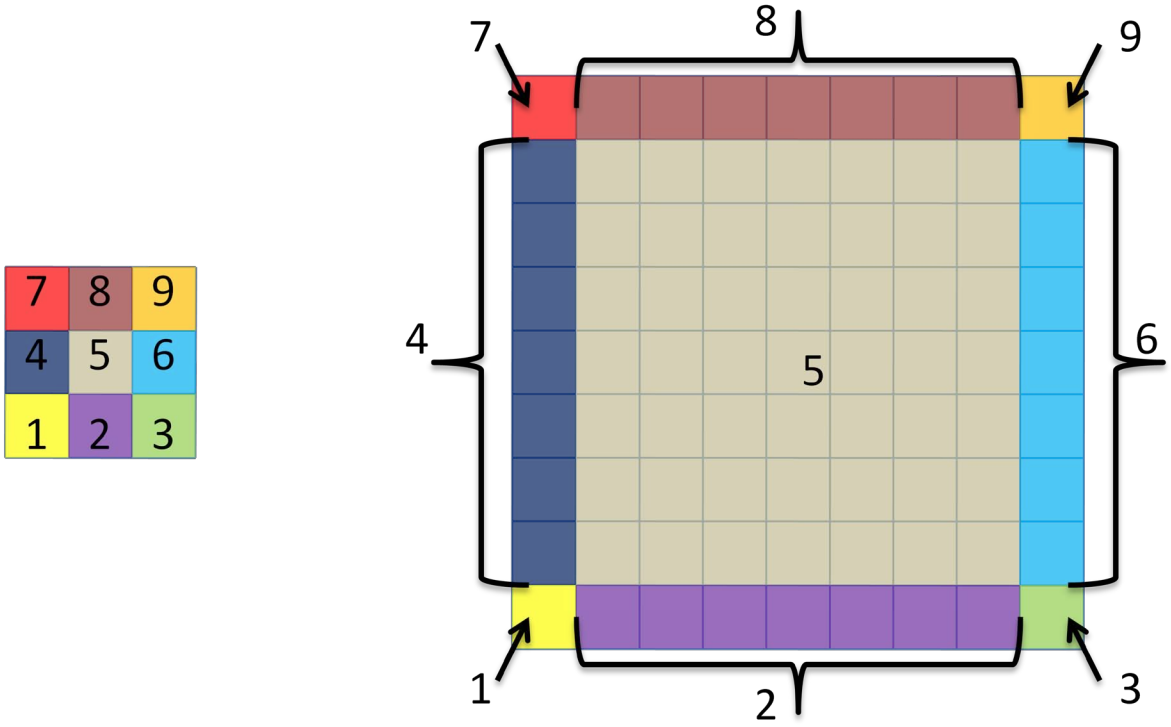

Figure 4-3: Illustration of the Calculation Domain for the Hybrid Array Pattern Approach

After the nine average active element patterns are simulated or measured, they can be summed to provide the array pattern including mutual coupling effects. For example, element 4 has elements 7, 8, 5, 2, and 1 as neighbors. This environment is similar to that of all edge elements excluding corners on the left-hand side of the larger array. Using this approach, the pattern for the moderately sized 10x10 array shown above can be evaluated by completing the simulation of

a small 3x3 array and applying the hybrid calculation technique. This can be extended to any array size larger than 3x3 with no added complexity. The algorithm used for this calculation is shown in (4-6). In this algorithm, $\boldsymbol{g_{av}^{q}}$ is the phase-adjusted unit-excitation element pattern for the given element (and it will be used as the average active element pattern for the corresponding region), N_q is the number of elements in the q_{th} region ($1<q<9$), $\mathbf{r_{i,q}}$ is the vector from the origin to the i^{th} element in the q^{th} region, and $I_{i,q}$ is the complex weight for the i^{th} element in the q^{th} region.

$$\boldsymbol{E}(\theta,\varphi) = \sum_{q=1}^{9}\left\{\boldsymbol{g_{av}^{q}}(\theta,\varphi)\sum_{i=1}^{N_q} I_{i,q}\, e^{jk\hat{r}\cdot\mathbf{r}_{i,q}}\right\} \qquad (4\text{-}6)$$

The dual-band elements used to illustrate the hybrid array analysis were modeled in an infinite array environment to reveal an approximation of the element performance in an array environment. The first element studied was a dual-band element with linear polarization. The model used in this study is shown in Figure 4-4. The low band element was designed to operate at 6 GHz. This element is a shorted annular ring antenna, and it uses the previously mentioned dual-substrate capacitive loading technique to reduce its footprint. The high band portion of the element is a square ring slot element with a stripline realization designed to operate at 10 GHz. The use of the capacitive loading technique allows for the elements to be arranged in a lattice with 0.7" spacing between element centers; this distance corresponds to 0.58λ at the high frequency. This lattice provides the ability to scan the array to wide angles off of broadside at each frequency band. The scan angle where the grating lobes will begin to appear (θ_0) can be calculated using (4-7). At the high band, the 0.58λ spacing suggests that grating lobes will begin to appear at scan angles greater than 43° off of broadside. At the low band, the element spacing is 0.35λ, a spacing that allows scanning to all angles in the visible region without the introduction of grating lobes.

$$\theta_0 = sin^{-1}\left(\frac{\lambda}{d} - 1\right) \qquad \textbf{(4-7)}$$

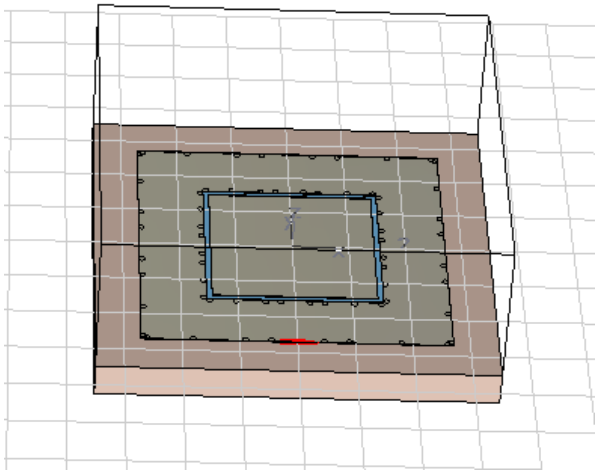

Figure 4-4: Dual-Band Linearly Polarized Infinite Array Model

The infinite array simulations provide the impedance match of the array element when all other elements are excited with the same magnitude and phased. This is important because the mutual coupling from other elements within the array will change the impedance of the elements. The active impedance match results from the infinite array simulations are shown in Figure 4-5. Both elements have a return loss greater than 10dB at the desired frequencies. These return loss values correspond to a VSWR below 2.0:1 which is a commonly used figure of merit in determining an acceptable impedance match in antenna applications. Figure 4-5 also shows the coupling (s_{12}) between the high band element and the low band element of a given unit cell for the array. The two ports have a coupling less below -30dB across the operational frequency bands. However, the coupling between adjacent elements in the array is not available utilizing the infinite array technique.

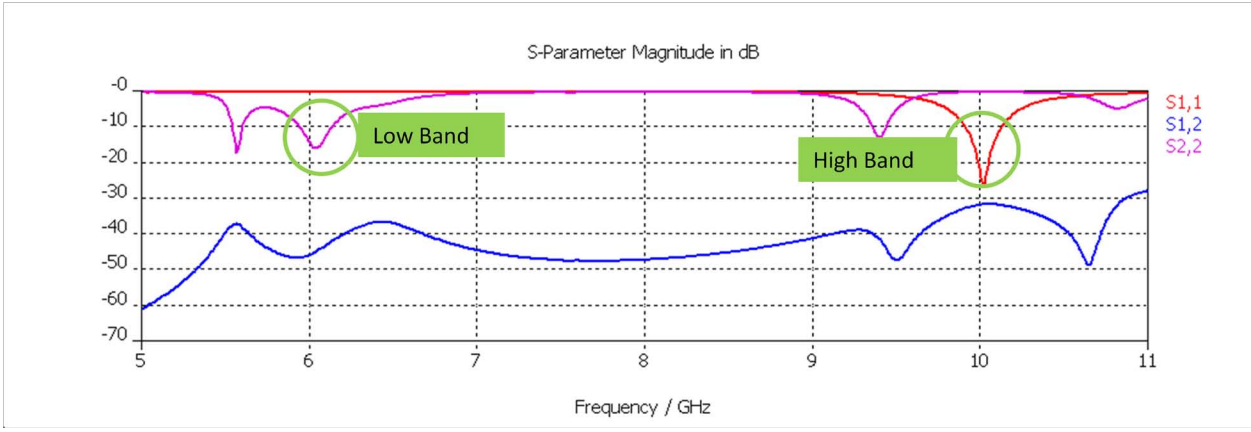

Figure 4-5: Dual-Band Linearly Polarized Active Element Impedance Match

4.1.2 Dual-Band, Linearly Polarized Array Calculations Using the Hybrid Array Technique with Multiple Active Element Patterns

The hybrid technique is based on the simulation of the 3x3 finite antenna array shown in Figure 4-6. This model contains nine dual-band, linearly polarized elements. Each of these elements is based on the design used in the previously mentioned infinite array simulations. The hybrid calculation technique was applied to the results from this finite array simulation, and the patterns of dual-band arrays of arbitrary size were calculated. The linearly polarized, dual-band element consists of a low band element and a high band element. The low band element operates at 6 GHz and is polarized in the x-direction. The high band element operates at 10 GHz and has an electric field parallel to the y-axis.

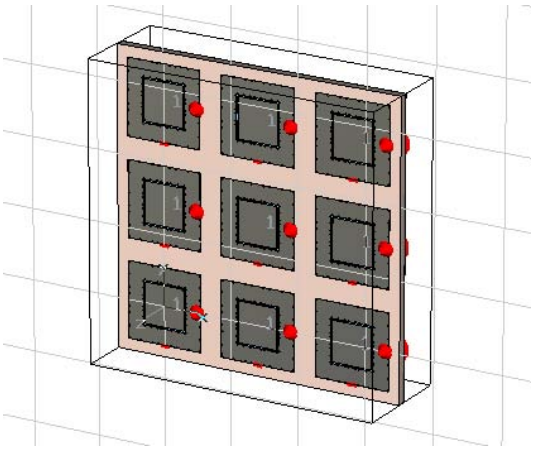

Figure 4-6: 3x3 Finite Array Used in the Hybrid Array Approach for the Dual-Band Linearly Polarized Array Calculations

4.1.2.1 Active Element Patterns

The nine-element approach was adopted to include the fact that elements in different locations within the array exhibit different performance due to contrasting mutual coupling and edge effects stemming from the finite nature of the array. The active element patterns for the low band elements in the φ=0° cut are shown for the center, corner, and edge elements in Figures 4-7 to 4-9 respectively. Each of these figures contains two sets of patterns. The top set is the θ-polarized component, and the bottom set is the φ-polarized component. For the φ=0° cut, the θ-polarized component represents the co-polarized field parallel to the x-axis. These results show that the elements in different portions of the array do in fact exhibit markedly different active element patterns. In approaches neglecting these differences, a result similar to the center element result of Figure 4-7 would be used to represent the performance of all elements within the array.

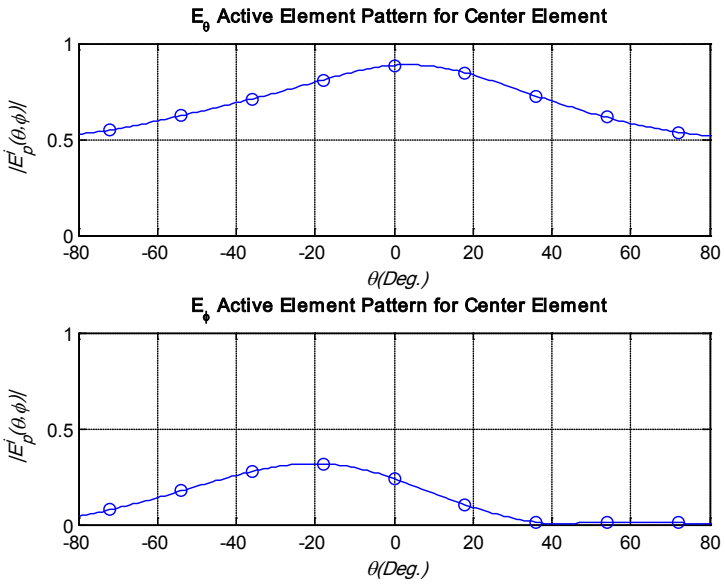

Figure 4-7: Low Band Active Element Pattern: Center Elements, φ=0° cut

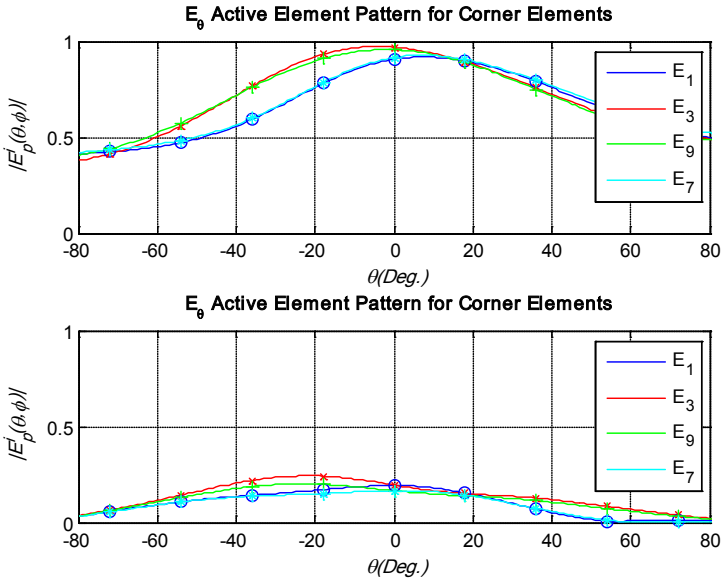

Figure 4-8: Low Band Active Element Pattern: Corner Elements, φ=0° cut

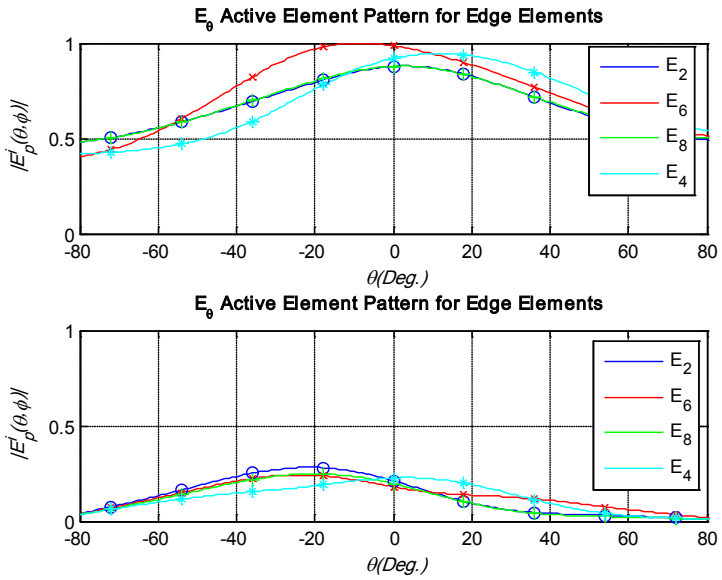

Figure 4-9: Low Band Active Element Pattern: Edge Elements, φ=0° cut

The low band active element patterns for φ=90° are shown in Figures 4-10 to 4-12. For this set of patterns, the φ-polarized component represents the co-polarized field parallel to the x-axis. The corner and edge elements show a squinted beam and increased cross-polarization levels when compared to the center element. The inclusion of these factors leads to a more accurate calculated antenna array pattern then the traditional approach using only a single element to represent all elements within the array.

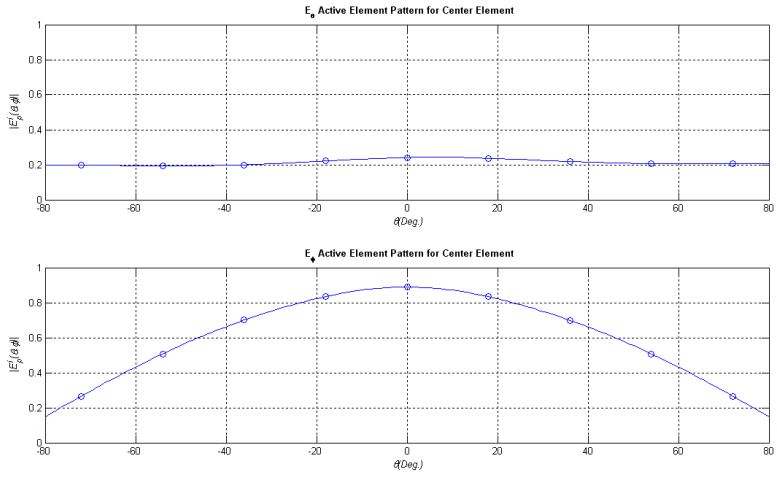

Figure 4-10: Low Band Active Element Pattern: Center Elements, φ=90° cut

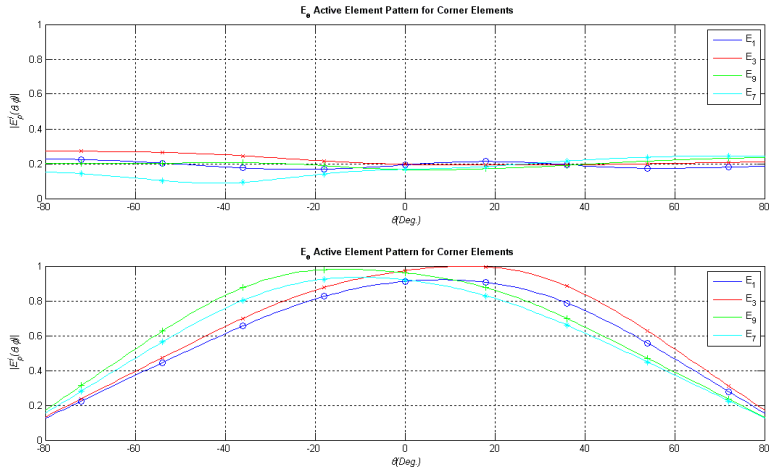

Figure 4-11: Low Band Active Element Pattern: Corner Elements, φ=90° cut

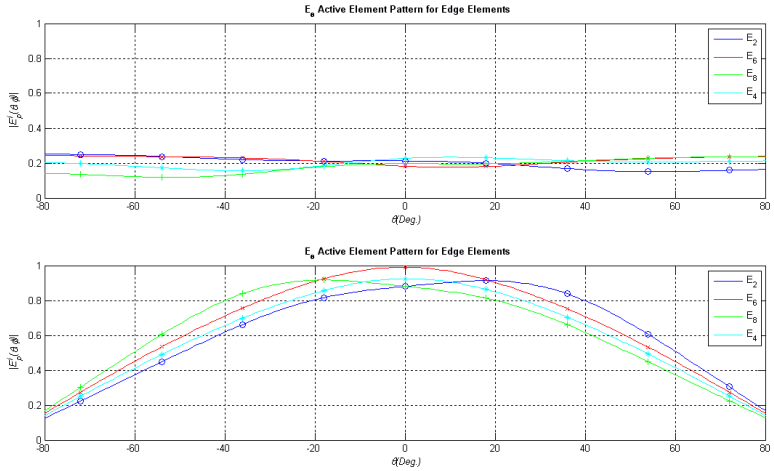

Figure 4-12: Low Band Active Element Pattern: Edge Elements, φ=90° cut

The high band active element patterns for the center, corner, and edge elements are shown in Figures 4-13 to 4-15 for the φ=0° cut and in Figures 4-16 to 4-18 for the φ=90° cut. These active element patterns for the center elements show excellent cross-polarization levels in both cases. The corner and edge elements show a degraded pattern shape and increased cross-polarization levels due to asymmetrical mutual coupling effects and the effects of a finite ground plane.

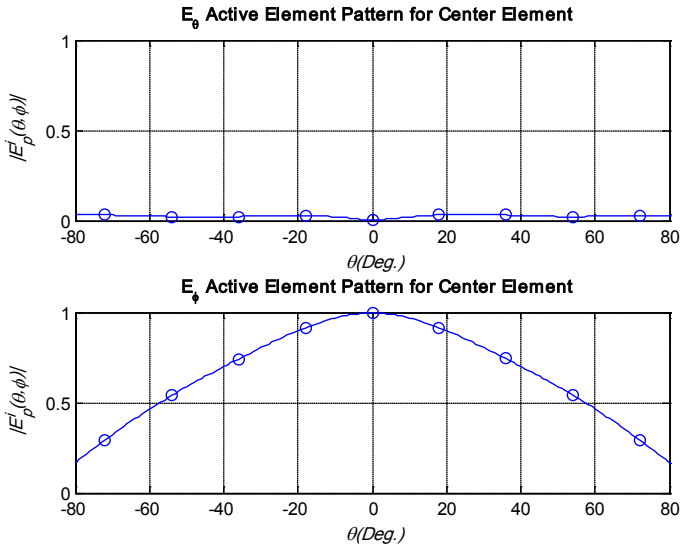

Figure 4-13: High Band Active Element Pattern: Center Elements, φ=0° cut

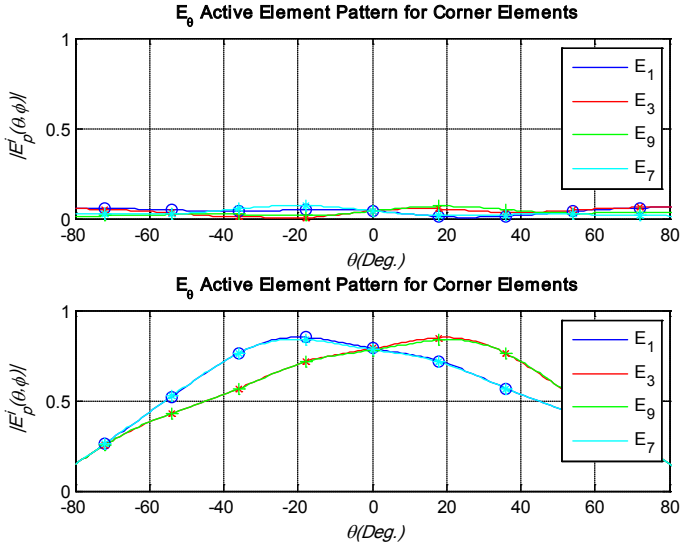

Figure 4-14: High Band Active Element Pattern: Corner Elements, φ=0° cut

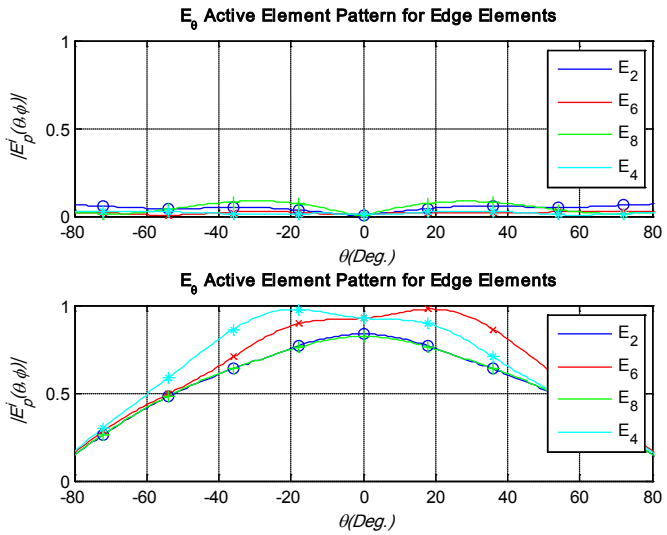

Figure 4-15: High Band Active Element Pattern: Edge Elements, φ=0° cut

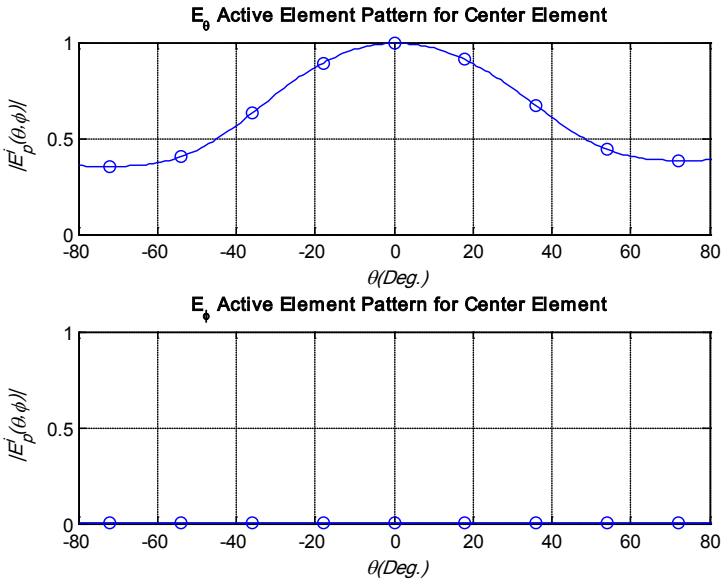

Figure 4-16: High Band Active Element Pattern: Center Elements, φ=90° cut

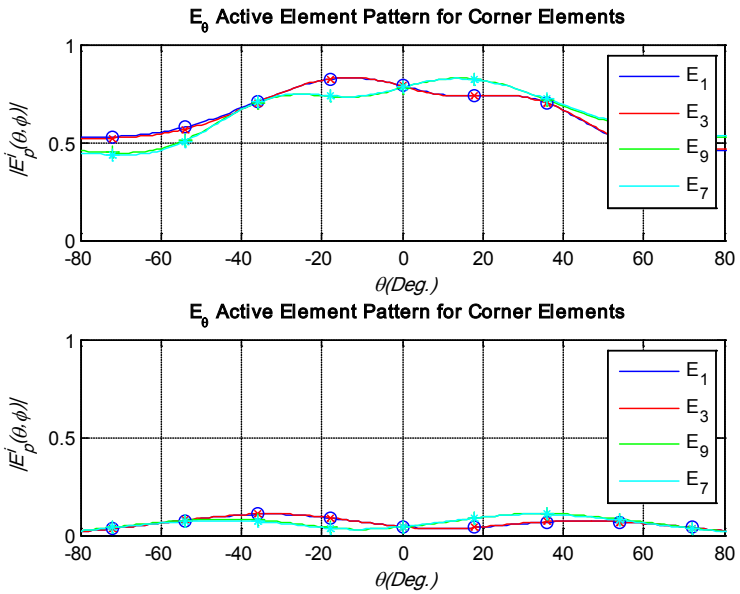

Figure 4-17: High Band Active Element Pattern: Corner Elements, φ=90° cut

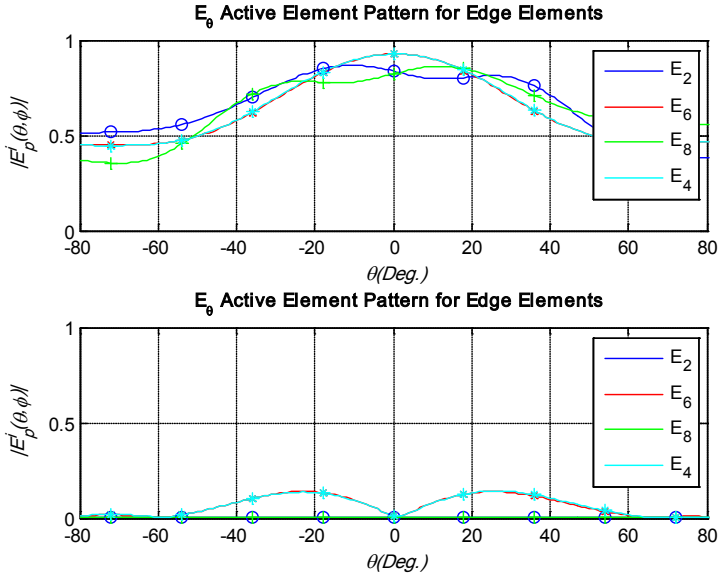

Figure 4-18: High Band Active Element Pattern: Edge Elements, φ=90° cut

4.1.2.2 16x16 Element Antenna Array Patterns

The linearly polarized, dual-band element was designed to be placed in an array with a square unit cell with a side length of 0.7". The scanning limitation on this element is driven by the high frequency, where the spacing is 0.58λ. Theoretically, this spacing limits the scanning to ±43° before the onset of grating lobes. In many applications, this scanning range is sufficient.

However, if the application required wider scanning at the high band frequency, the dual-substrate capacitive loading structure could be modified to provide a smaller element footprint.

The high band scanning performance of a 16x16 element array is shown in Figures 4-19 and 4-20 for the principle planes of the antenna array. Figure 4-19 shows scans of 0°, 15°, 30°, and 45° off of broadside for the φ=0° cut. This figure contains four subplots. Figure 4-19(a) and (b) show the θ- and φ-polarized electric field components calculated using the hybrid approach. In the case of the high band φ=0° cut, the φ-polarized field component is the co-polarized field component. Figure 4-19(c) and (d) show the same two field components calculated using the classical approach to provide a point of comparison. In the classical approach, the resulting pattern from the infinite array simulations was used as the representative active element pattern for all elements in the array. The element pattern is overlaid on each of the four plots as a reference point. Using the classical approach, the amplitude of the scanned patterns at broadside is seen to drop off proportionally to the magnitude of the element pattern. This is the anticipated result because the array pattern is the product of the array factor and the element pattern. However, Figure 4-19(b) suggests that the scanned components drop off faster than the element pattern's magnitude when scanned off of broadside. This additional drop is a result of the degraded element pattern shape and gain for the elements on the outer perimeter of the array. A similar result is seen in the φ=90° cut plots for the high band elements of Figure 4-20 (a)-(d). For the plots in the φ=90° plane, the θ-polarized component represents the co-polarized field.

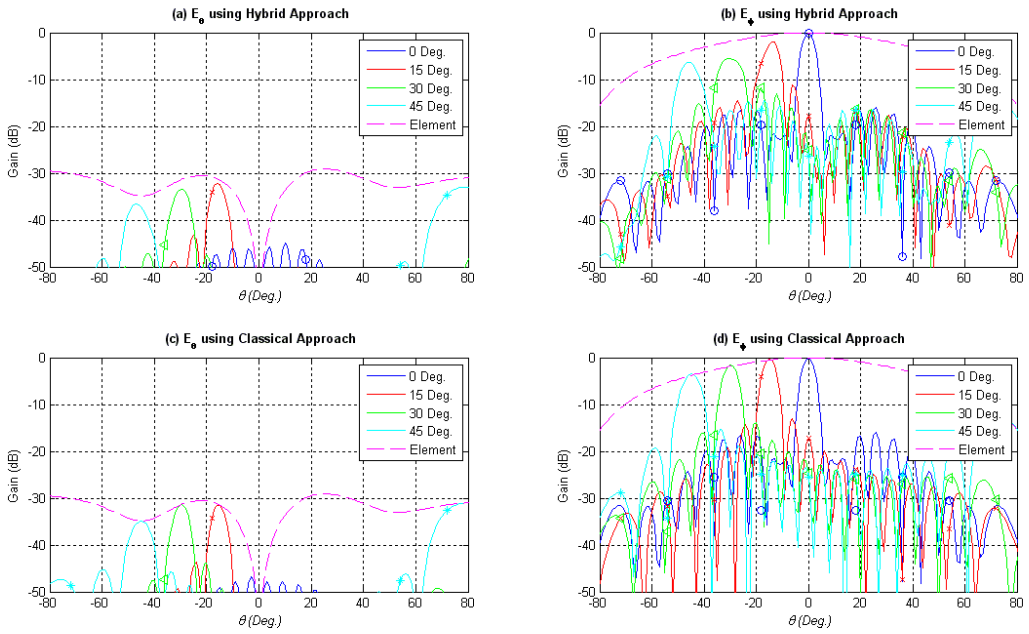

Figure 4-19: Linearly Polarized Dual-Band 16x16 Array Pattern: High Band Elements, φ=0° Cut

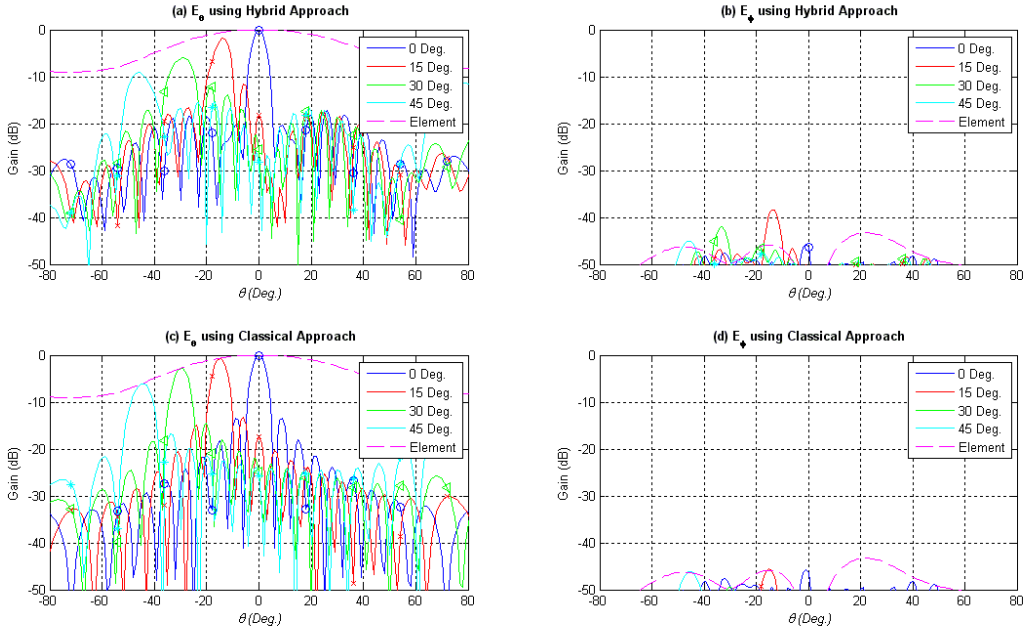

Figure 4-20: Linearly Polarized Dual-Band 16x16 Array Pattern: High Band Elements, φ=90° Cut

Figure 4-19 and 4-20 indicate that the high band elements in the 16x16 dual-band array provide good performance at the desired scanning angles. The magnitude drops off slightly more than the classical approach suggests due to the edge effects and asymmetrical mutual coupling present at the outer perimeter of the array. Figure 4-21 (a)-(d) provides a comparison between the hybrid result and the classical result for the co-polarized field component at the four scan angles. Inspection of the subplot in Figure 4-21(d) reveals the presence of a grating lobe near θ=75°. The magnitude of this lobe is approaching the magnitude of the main beam, thus causing the drop in magnitude of the main beam at this scan angle. If the array were scanned to wider angles, the magnitude of the grating lobe would increase even further as it moved in closer to the scanned main beam. This limits the scanning of the array to angles less than 43°.

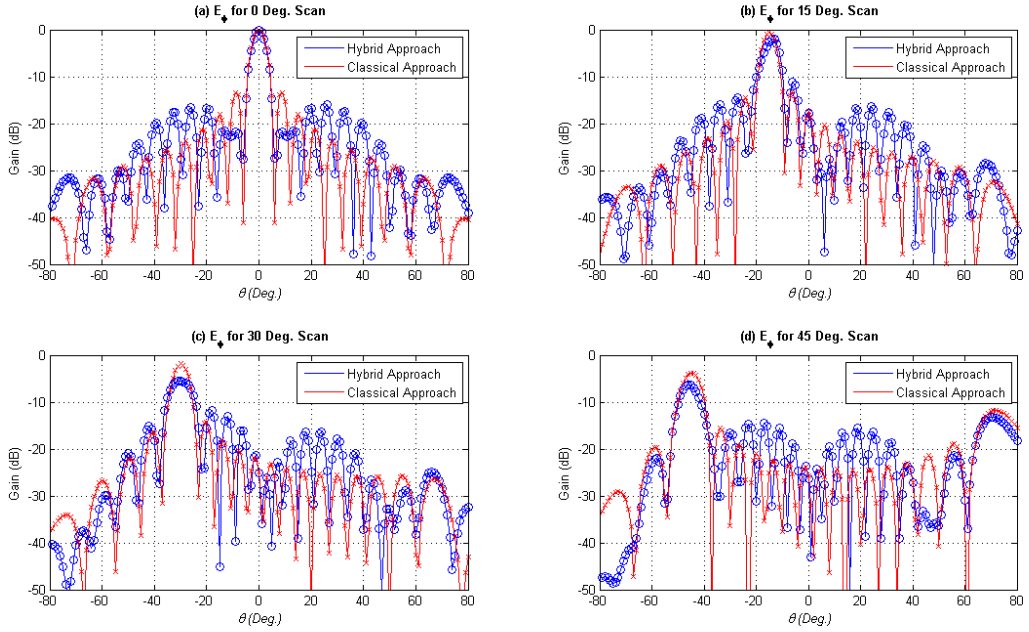

Figure 4-21: Linearly Polarized Dual-Band 16x16 Array Pattern: High Band Elements, φ=90° Cut, Co-Pol

The size reduction used in the low band portion of this dual-band element results in a compact lattice at the low frequency of 6 GHz. Consequently, the low band elements in this array can theoretically be scanned to any angle in the visible region (±180°) without the introduction of grating lobes. The φ=0° cut for the 16x16 low band array is shown in Figure 4-22. The peak magnitude of both the co-polarized field (E_θ) and cross-polarized field (E_φ) drops off closely with the magnitude of the element pattern in the hybrid calculation of Figure 4-22(a). This indicates that the edge effects have less impact on the low band elements in this array. As expected, there is no indication of grating lobes at any of the scan angles. The cross-pol level for the low band portion of the array is significantly higher than at the high band. This trait stems from the higher cross-pol in the low frequency shorted annular ring antenna than in the square ring slot.

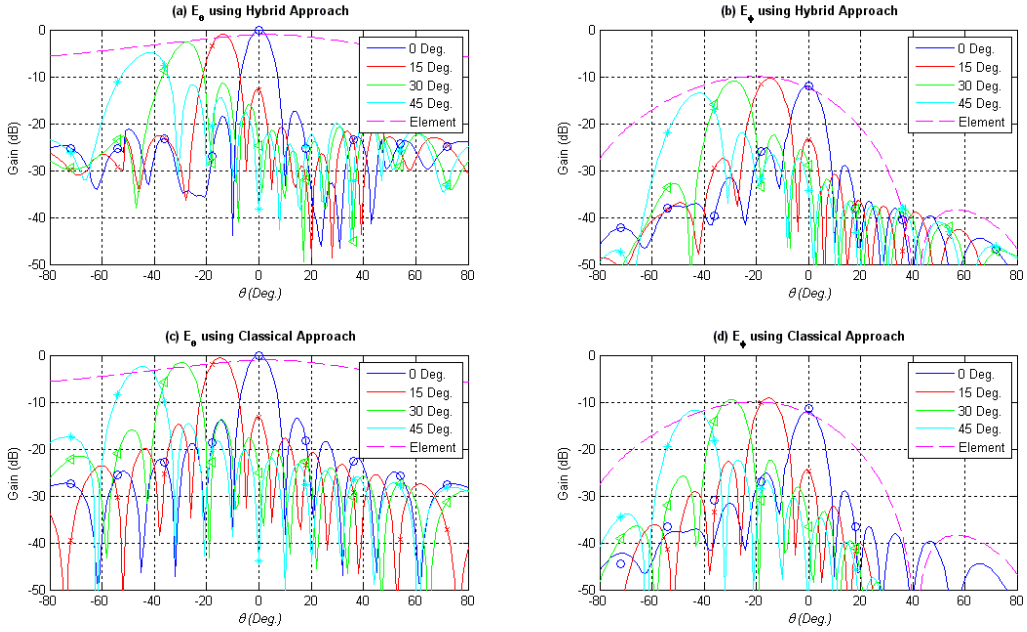

Figure 4-22: Linearly Polarized Dual-Band 16x16 Array Pattern: Low Band Elements, φ=0° Cut

4.1.2.3 48x48 Element Antenna Array Patterns

For higher gain applications, a larger array becomes necessary. To investigate the performance of the proposed dual-band element in a larger array, a 48x48 element array has been chosen. These calculations further illustrate the benefit of the hybrid calculation approach. The classical approach neglects the changes in mutual coupling and the impact of the edges in the array, but the simulation and/or measurement of the entire array would require a significant investment of time, money, and/or computational resources. The simulation of a 48x48 element array is not practically feasible with most commercial software packages. Conversely, the hybrid approach requires only the simulation of a 3x3 array; this calculation domain can be solved on most desktop PCs with virtually any commercial available software package.

The scanned patterns for the high band elements in the 48x48 array are shown in Figures 4-23 and 4-24. These plots show a much better agreement between the hybrid approach and the classical approach which suggests the significance of the edge effects is decreasing. Intuitively, this result makes sense. As the number of elements in the array increases, the percentage of elements that can be accurately represented by the infinite array element increases, thus negating the overall effect of the edge elements. The magnitude of the main beam in this case drops off much more closely to the magnitude of the element pattern than in the smaller 16x16 element case. Grating lobes still appear at the 45° scan in both cases, a fact seen more clearly in the patterns shown in Figure 4-25.

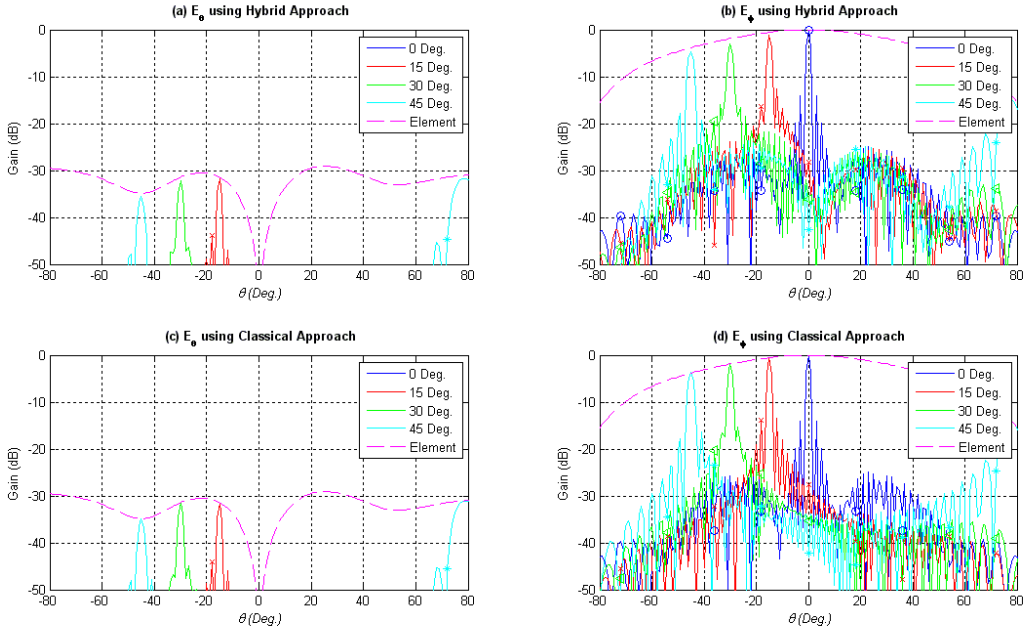

Figure 4-23: Linearly Polarized Dual-Band 48x48 Array Pattern: High Band Elements, φ=0° Cut

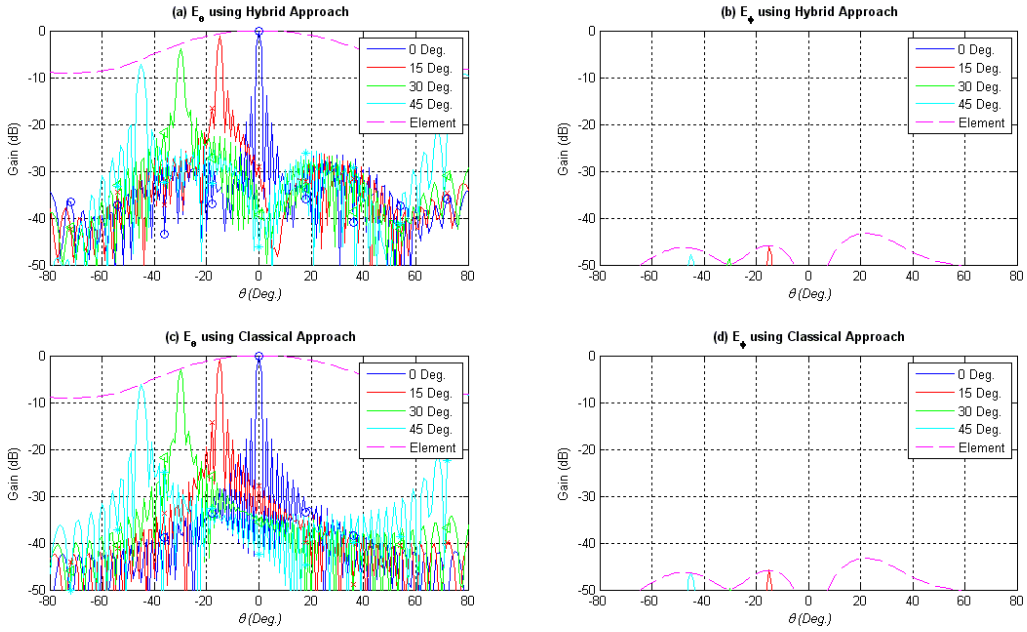

Figure 4-24: Linearly Polarized Dual-Band 48x48 Array Pattern: High Band Elements, φ=90° Cut

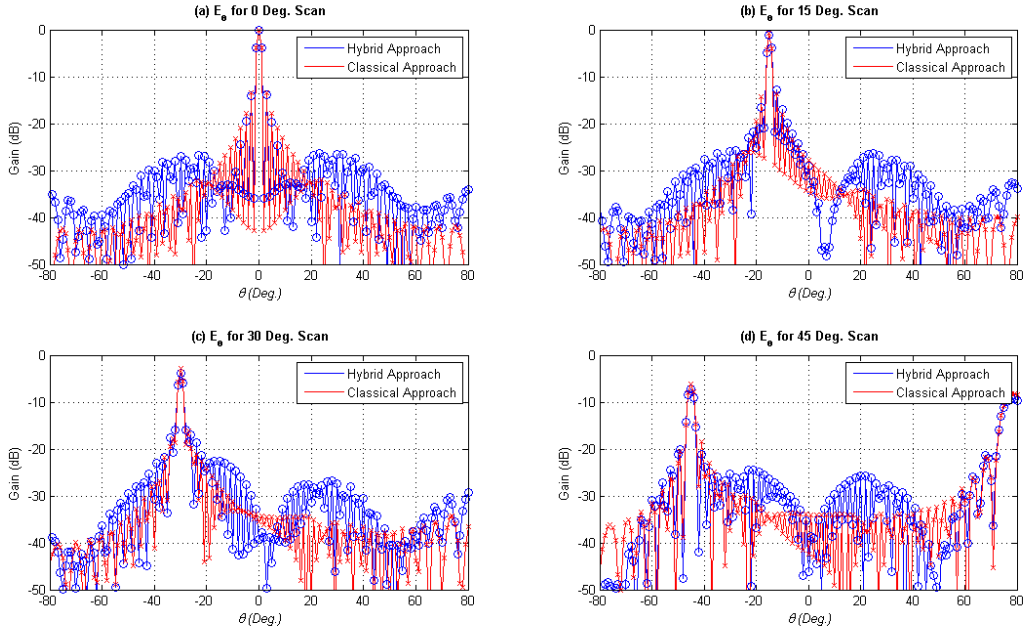

Figure 4-25: Linearly Polarized Dual-Band 48x48 Array Pattern: High Band Elements, φ=90° Cut, Co-Pol

The low band of the larger array posses the same characteristics as the smaller array: higher cross-pol levels than the high band array, good agreement between the hybrid approach and classical approach, and the absence of grating lobes. These characteristics are reflected in the φ=0° principle plane pattern shown in Figure 4-26.

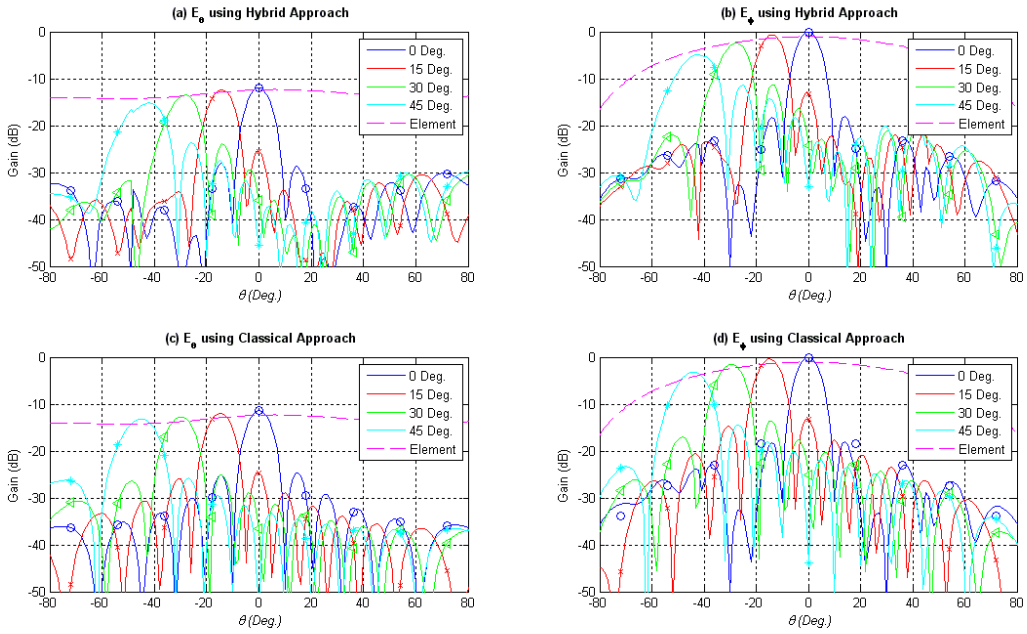

Figure 4-26: Linearly Polarized Dual-Band 48x48 Array Pattern: Low Band Elements, φ=0° Cut

4.2 Dual-Band, Dual-CP Array Analysis

A dual-band antenna array was investigated using the multiple active element pattern hybrid technique. The array element spacing is 3.15 cm (1.204"). This spacing is equivalent to 0.609λ in the high frequency band and 0.257λ in the low band. The maximum scan, θ_0, angle before the onset of grating lobes can be determined from (4-16). The array lattice provides grating-lobe free scanning at the high frequency to angles less than 40° off of broadside. At the low frequency, the fine element spacing will not produce grating lobes at any angles in the visible region.

$$\theta_0 = sin^{-1}\left(\frac{\lambda}{d} - 1\right) \qquad \textbf{(4-16)}$$

In the following sections, the array pattern, F(φ, θ), will be characterized for multiple scan angles. As the beam is scanned, the *half power beamwidth* (BW_{3dB}) will broaden as the effective area for the array decreases. The half power beamwidth will be compared to the theoretical value calculated from (4-17); the expression in (4-17) is valid for scan angles near broadside. The *normalized maximum* value for each case will be investigated. This value, defined in (4-18), will show how the gain of the array decreases as the main beam is scanned. The *cross-polarization discrimination* (XPD) will be calculated for each scan angle. The XPD will be used to calculate the axial ratio at θ_0 for each scan angle.

$$BW_{3dB}^{approx} = 0.886\frac{\lambda}{Nd}csc(\theta_0 - \pi) \qquad \textbf{(4-17)}$$

$$F_{\theta_0}^{norm} = \frac{F_{\theta_0}(\theta_0)}{F_{\theta_0=0}(0)} \quad \textbf{(4-18)}$$

The remainder of this section will discuss the array performance for each band, polarization, and array size. Some array patterns will be shown in the discussion, and a complete set of array patterns is provided in Appendix B.

4.2.1 Dual-Band, Dual-CP Infinite Array Analysis

The initial step of the dual-band, dual-CP array design is to model the dual-band, dual-CP element in an infinite array environment. The use of periodic boundary conditions allows the antenna element to be modeled with the inclusion of the near-field influence of neighboring elements in an infinite expansion of elements (i.e. an infinite array). The infinite array conditions provide a close approximation of the element performance in most large array environments. The simulations described in this section were performed using CST Microwave Studio. Microwave Studio is a commercially available computational electromagnetic software package that employs the Finite Integration Technique (FIT), a variation of the commonly used finite difference time domain (FDTD) method. A top view of the element showing the selected boundary conditions is provided in Figure 4-27.

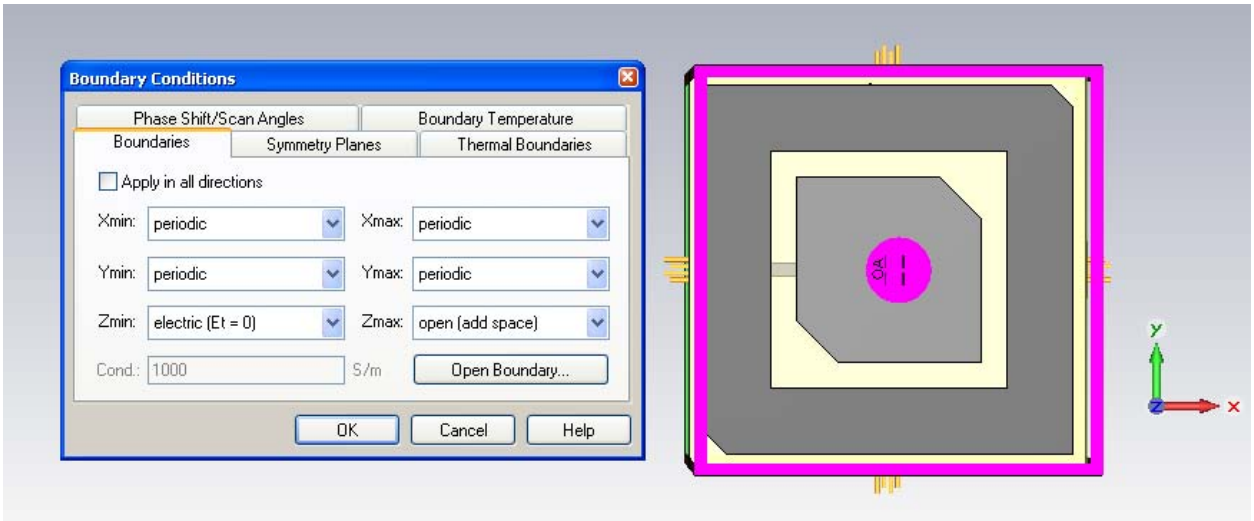

Figure 4-27: Top view of the unit cell used in the infinite array simulations including boundary condition definition

The infinite array simulations provide a look at the active element impedance match. This parameter shows the input match to a given port when all other ports in the array are excited with the same amplitude and phase. The resulting VSWR is plotted in Figure 4-28. The low band ports exhibit a VSWR < 2.0:1 over the majority of the 2.45 GHz ISM frequency band. The high band element operates with a broad impedance bandwidth that more than covers the entire 5.8 GHz ISM band. The high frequency ports exhibit a broader bandwidth than the low frequency element for two main reasons. First of all, the high band square ring slot element inherently

operates over a broader frequency band than the shorted square ring low band element. Secondly, the low band element uses a dual-substrate capacitive loading structure to reduce the element size; the capacitive loading results in a decreased impedance bandwidth.

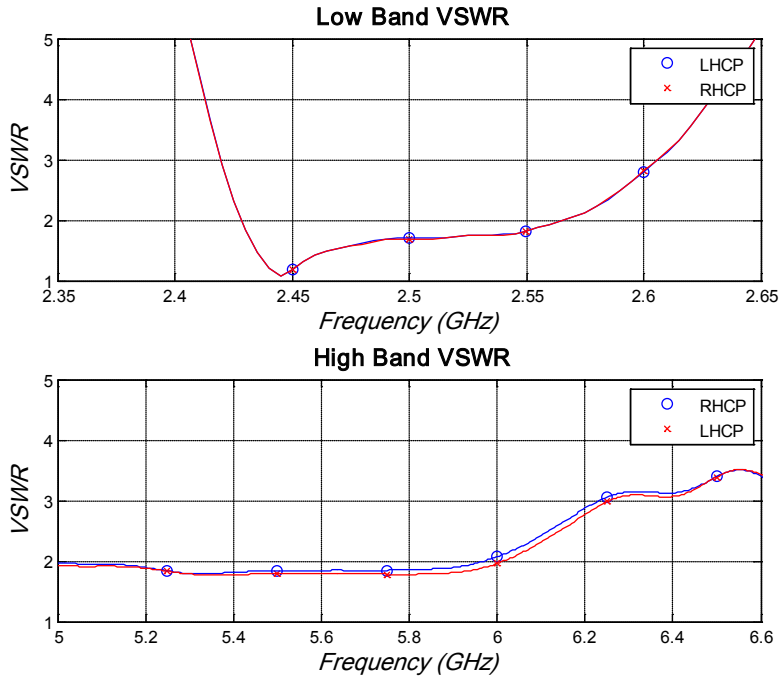

Figure 4-28: Active element VSWR obtained from infinite array simulations in CST Microwave Studio

The active element axial ratio is plotted in Figure 4-29. The low band ports (RHCP and LHCP) have an axial ratio < 3.0dB from 2.44 – 2.52 GHz (3.2% bandwidth). The minimum axial ratio occurs at 2.45GHz for each polarization (AR_{min} = 0.4dB). The high band ports have broad axial ratio coverage. The LHCP polarization has an axial ratio < 3dB from 5.25 – 6.08 GHz with a minimum axial ratio of 0.5dB at 5.9 GHz , and the RHCP polarization covers 4.82 – 6.08 GHz with a minimum axial ratio of 0.18dB at 5.9GHz. The two polarizations exhibit slightly different axial ratio performance due to the slightly asymmetric feeding. One of the two feed lines crosses over the other near the center of the element because they are printed on opposing sides of the thin feed substrate layer; the feed line on the bottom (LHCP) exhibits slightly degraded axial ratio bandwidth compared to the other port. However, both ports have an axial ratio <1.5dB over the entire 5.8 GHz ISM band. The active element axial ratio is plotted as a function of frequency and angle for the low and high frequency bands in Figures 4-30 and 4-31 respectively. The contour plots show that the dual-band dual-CP element maintains good axial ratio performance well off of broadside in both frequency bands, a result that is critical in allowing the dual-band dual-CP array to maintain good axial ratio at scanned conditions.

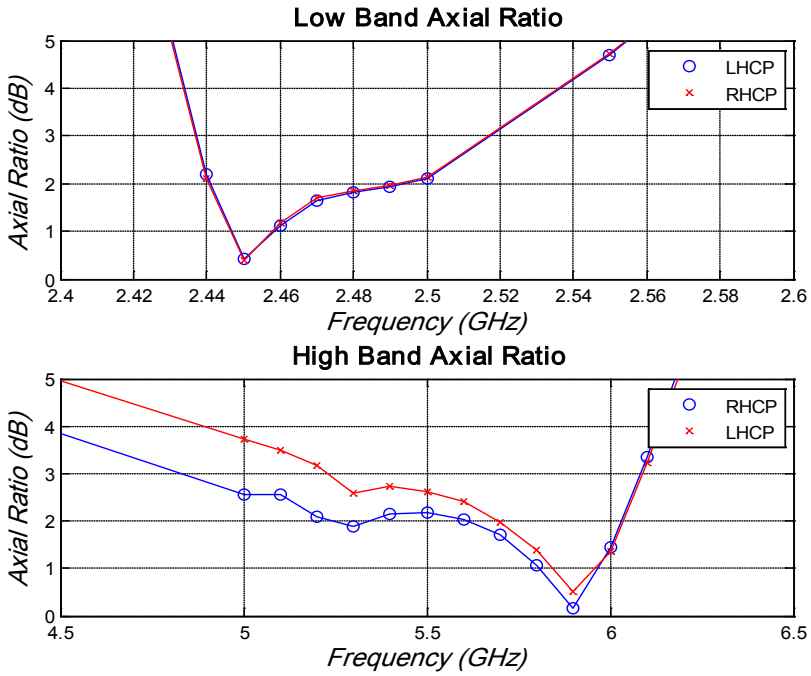

Figure 4-29: Active element Axial Ratio obtained from infinite array simulations in CST Microwave Studio

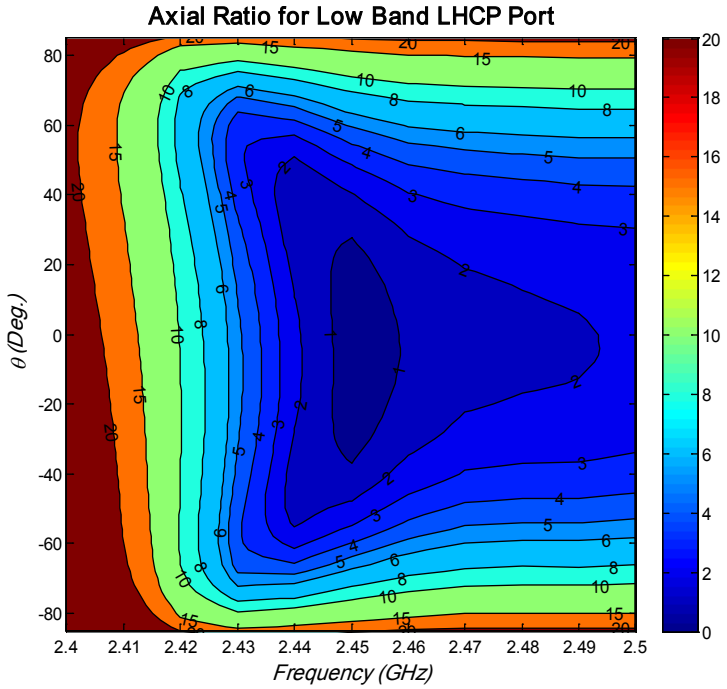

Figure 4-30: Active element Axial Ratio vs. Frequency vs. Theta (low band LHCP port)

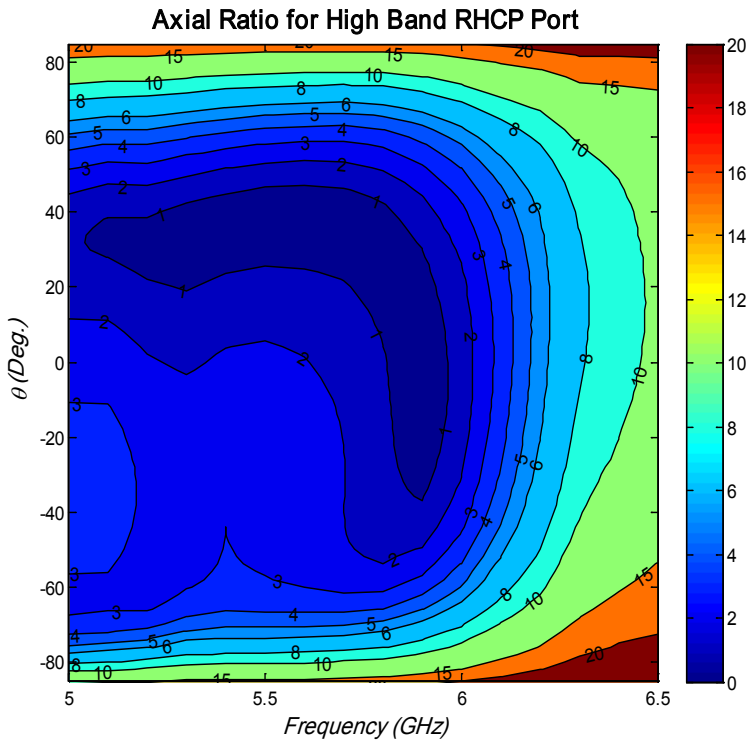

Figure 4-31: Active element Axial Ratio vs. Frequency vs. Theta (high band RHCP port)

The element used in the dual-band, dual-CP array can be viewed as a four port microwave network: Port 1 = high band RHCP, Port 2 = high band LHCP, Port 3 = low band LHCP, Port 4 = low band RHCP. When defined in this way, the full s-matrix, $[s_{ij}]$, provides insight into the inter-polarization coupling and the inter-frequency band coupling. Figure 4-32(a)-(d) provides plots of s_{ij}, with *j* held constant in each plot.

The high band inter-polarization coupling (s_{21}, s_{12}) has a maximum value just below -7dB at the low end of the 5.8 GHz ISM band, and this value drops to below -10dB above 5.9GHz. The low band inter-polarization coupling (s_{43}, s_{34}) is below -10dB over most of the 2.45GHz ISM band with a minimum value nearing -30dB at 2.47GHz. For the most part, the inter-frequency ports have negligible coupling at, or below, -30dB. The one exception occurs in the low band, where the two low band ports (ports 1 and 2) couple to the high band port with orthogonal polarization (ports 3 and 4 respectively) with a magnitude ranging from -11 to -20dB across the 2.45 GHz ISM band.

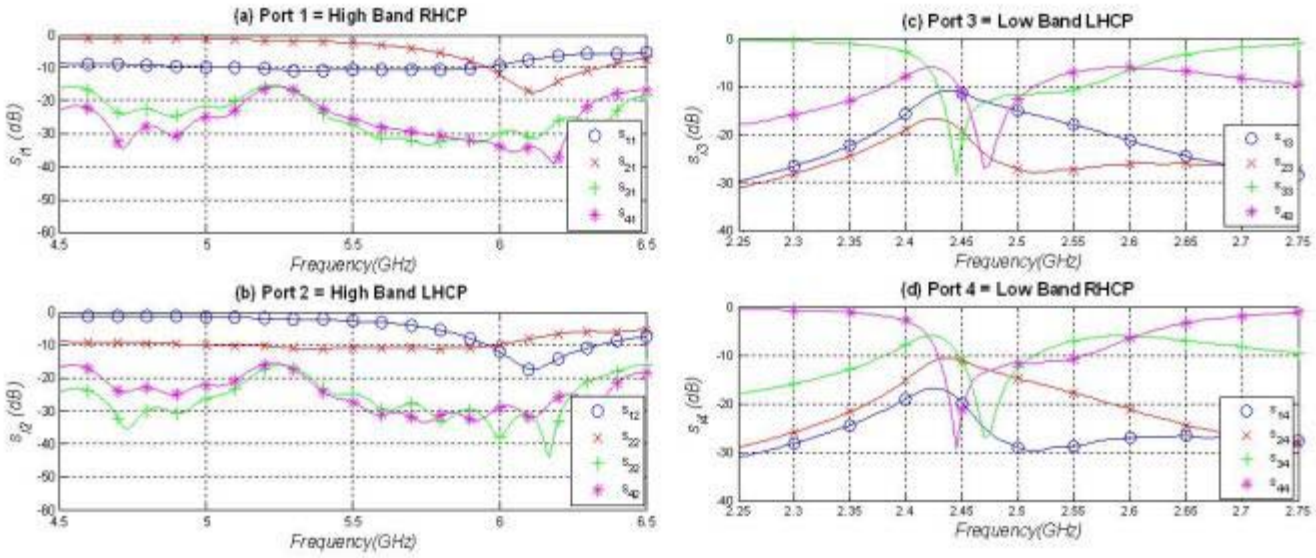

Figure 4-32: Active element s-matrix

The *copolarized* and *cross-polarized* volumetric active element patterns are plotted for ports 1-4 in Figures 4-33 to 4-36 respectively. The results show a broad, symmetric pattern for the copolarized component. In each case, the cross-polarized component is well below the copolarized component. This represents a high cross-polarized discrimination (XPD) which is reflective of an axial ratio near unity according to (1-28) and (1-29).

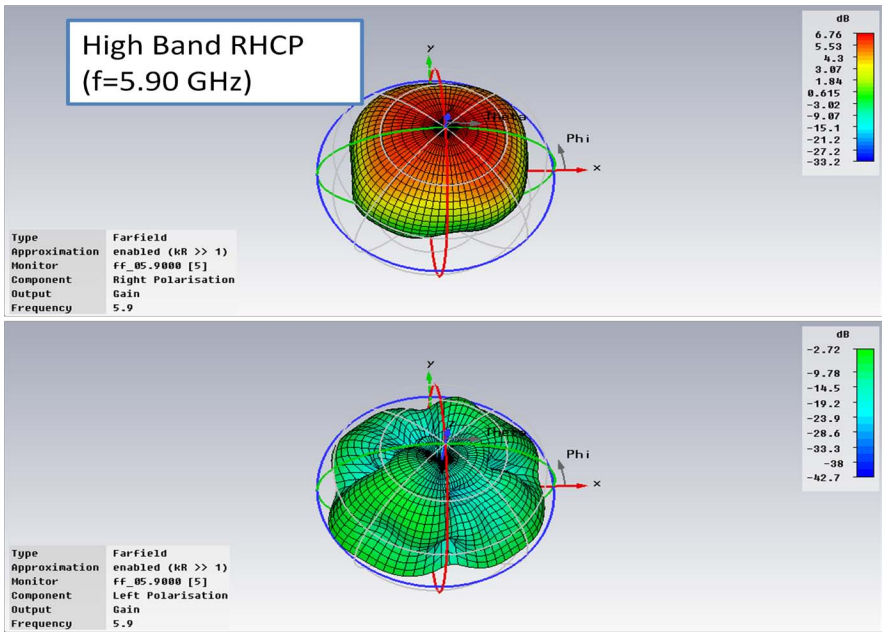

Figure 4-33: Volumetric active element pattern (High Band RHCP)

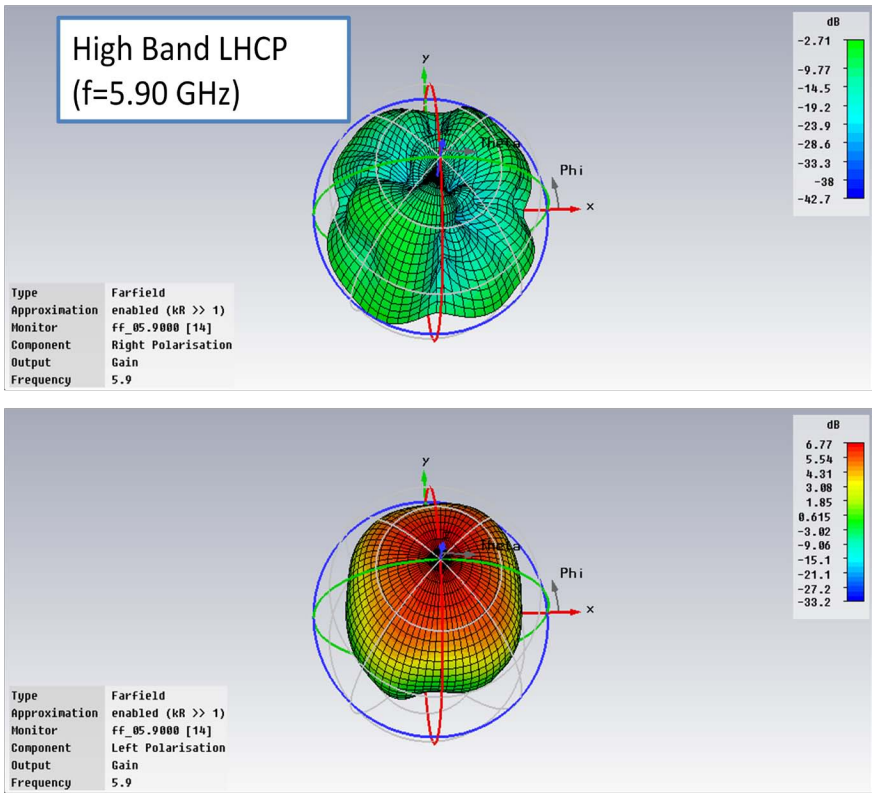

Figure 4-34: Volumetric active element pattern (High Band LHCP)

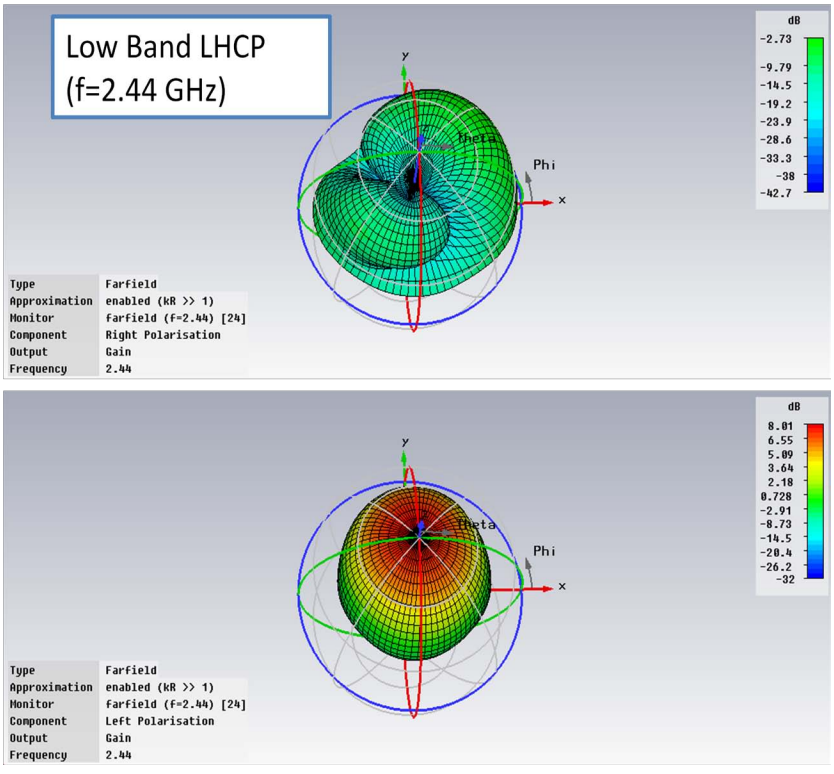

Figure 4-35: Volumetric active element pattern (Low Band LHCP)

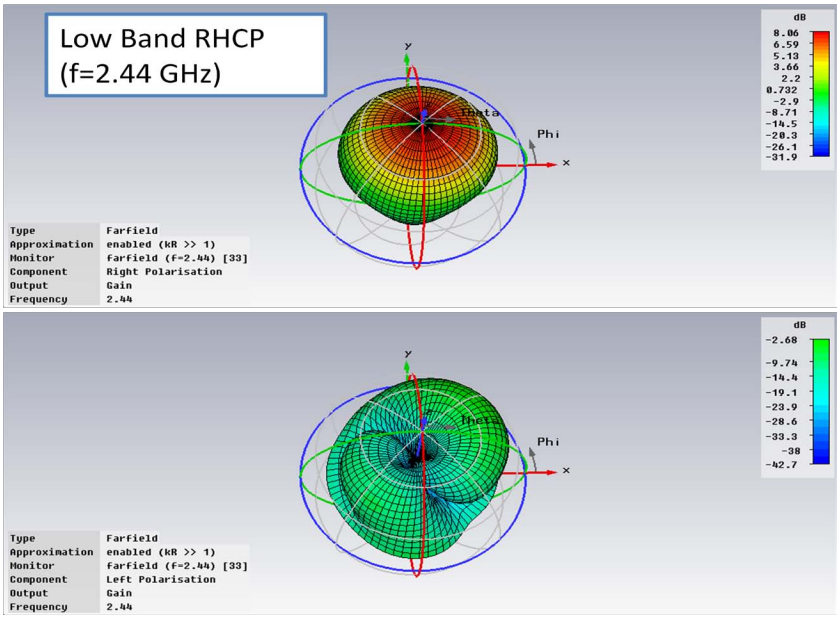

Figure 4-36: Volumetric active element pattern (Low Band RHCP)

4.2.2 3x3 Dual-Band, Dual-CP Array Analysis Used for Hybrid Technique Calculations

The previously discussed infinite array analysis provides insight into the operation of the dual-band, dual-CP element in an array environment. The infinite array analysis includes the near-field influence of neighboring elements when the element is present in an infinite array environment. As a result, it can be seen that the impedance match, radiation pattern, and axial ratio of the dual-band, dual-CP element provides excellent performance in an array. In order to provide a more detailed analysis of the radiation pattern, the hybrid calculation technique described in Section 4.1 will be applied.

The first step in the hybrid array analysis is the simulation of a 3x3 finite array. This analysis provides the active element pattern for the nine elements that are used as the representative patterns for element in their given region according to the technique illustrated in Figure 4-3. The model used in the 3x3 array simulations for the dual-band, dual-CP element is provided in Figure 4-37. This model was simulated in CST Microwave Studio. The 3x3 array model consisted of nine dual-band, dual-CP elements, and thus it required 36 total ports. The high band ports were fed with waveguide ports used to excite the microstrip feed line contained beneath the antenna's ground plane. The low band ports were discrete ports that simulated a 50Ω probe feed.

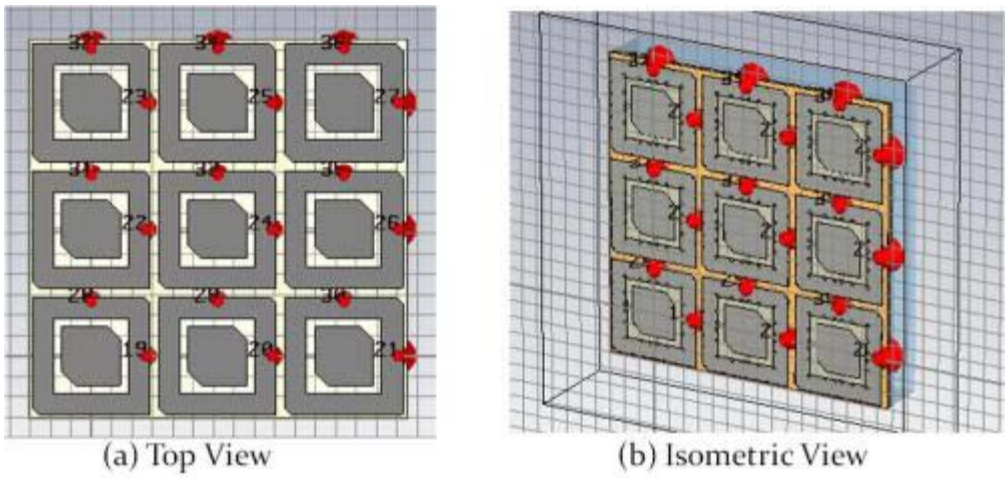

Figure 4-37: 3x3 Array Model for CST Microwave Studio Simulation of Dual-Band Dual-CP Array

The results of the finite array simulation revealed the importance of using the hybrid method for array analysis. The active element patterns for the low band RHCP port are plotted in Figures 4-38 to 4-40; each plot shows the constituent linearly polarized components in (a) and the circularly polarized components in (b). The frequency for these plots is 2.44 GHz. These radiation patterns are for the $\varphi=0°$ plane (x-z plane). Figure 4-38 shows the pattern for the center element (element 5 in the hybrid technique). This element is used to represent all elements in the core region of the antenna. This active element pattern exhibits a maximum value at broadside ($\theta=0°$) and extremely high XPD. The active element patterns for the corner elements (elements 1, 3, 7, 9 in the hybrid technique) are shown in Figure 4-39. These patterns are normalized to the maximum value of the center element case. The results show degraded performance in many aspects of the pattern. The maximum value is reduced significantly, the pattern becomes squinted off of broadside, and the *cross-polarized* component is increased. Similar active element pattern performance is seen in the edge elements (elements 2, 4, 6, and 8 in the hybrid technique).

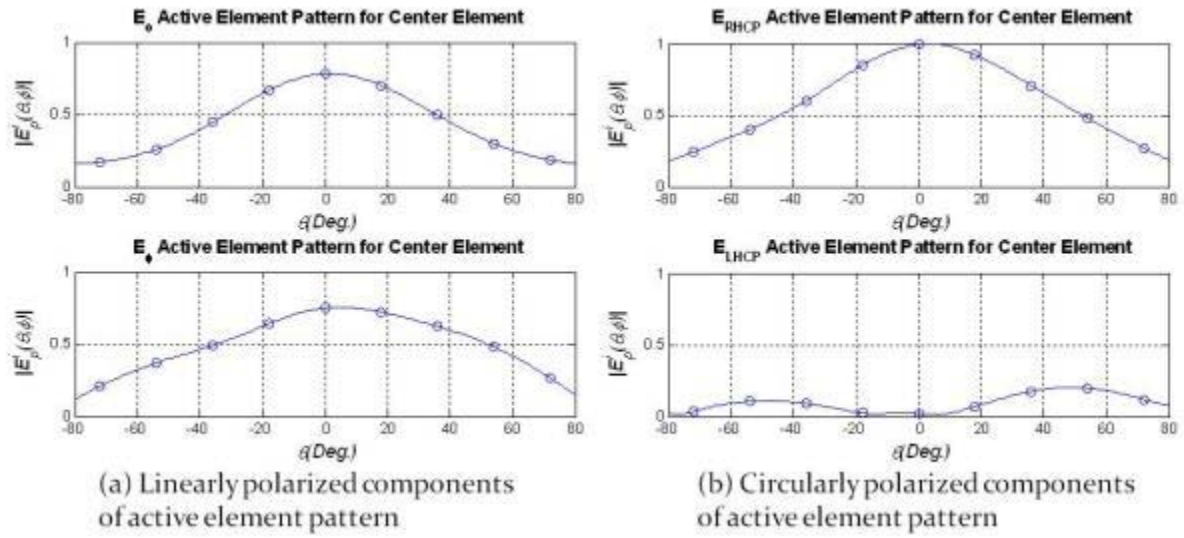

Figure 4-38: Active element pattern for center element (5) for low band RHCP port in the φ=0° plane (2.44 GHz)

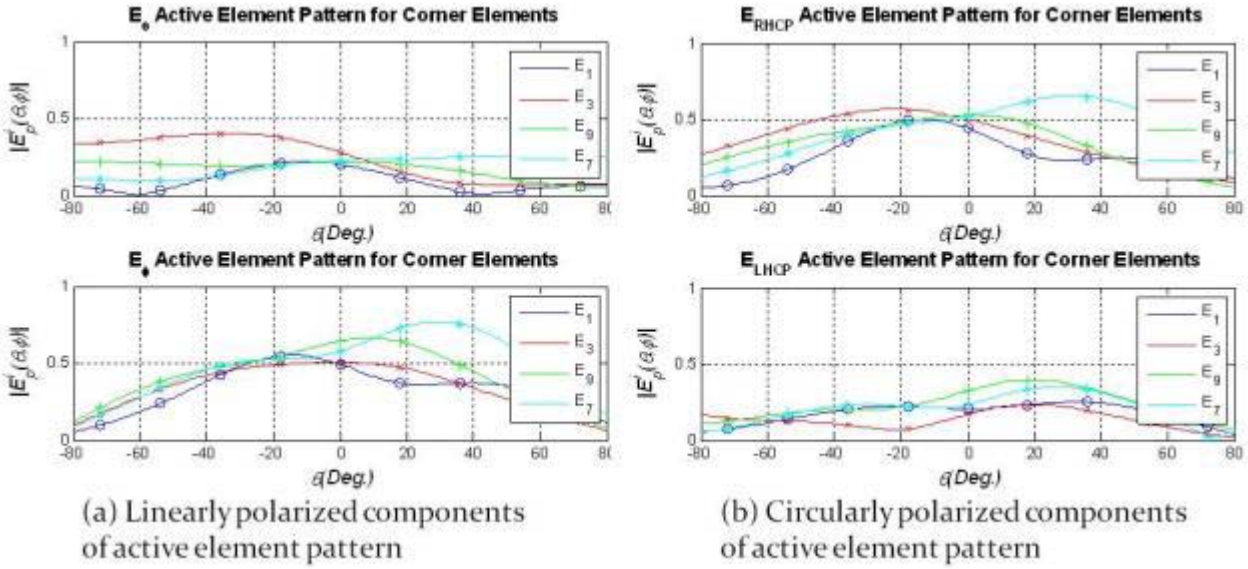

Figure 4-39: Active element pattern for corner elements (1, 3, 7, 9) for low band RHCP port in the φ=0° plane (2.44 GHz)

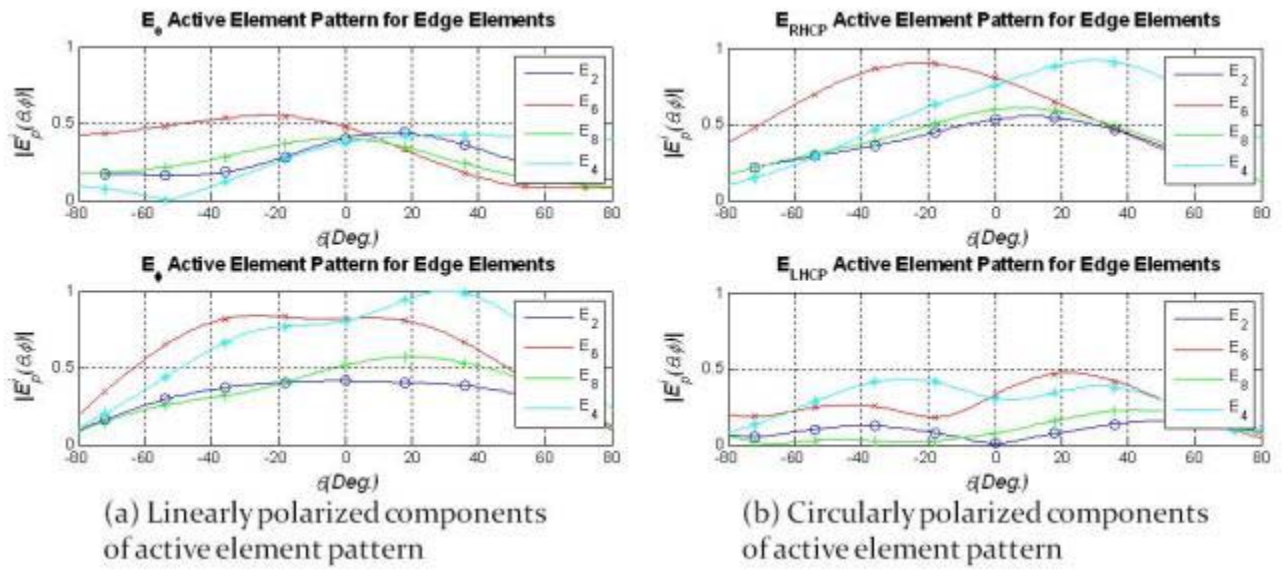

Figure 4-40: Active element pattern for corner elements (2, 4, 6, 8) for low band RHCP port in the φ=0° plane (2.44 GHz)

The active element pattern for the remaining principle plane cuts, frequency bands, and polarizations are provided in Appendix C. In summary, the results for the center element closely resemble the patterns obtained via infinite array analysis. Conversely, the elements around the outer perimeter of the 3x3 array exhibit asymmetries, increased cross-polarization levels, and decreased gain. The active element patterns show that the edge effects and asymmetrical mutual coupling provide distortions in pattern performance that would be ignored if the infinite array pattern was used to approximate the performance of all elements in the array.

The infinite array simulations take into account the mutual coupling between neighboring elements, but the levels of the mutual coupling are not revealed. The finite 3x3 array simulation provides a look at the magnitude of the mutual coupling between elements in an array environment. This is important because high mutual coupling can result in decreased array efficiency by reducing the amount of power available for radiation. Each polarization of each band of the 3x3 simulation can be viewed as a 9-port network with numbering outlined in Figure 4-3. For each band, the s_{i5} network parameter provides the coupling from element 5 to the surrounding element *'i'*. The network parameter s_{i5} is defined in (4-19). The results are plotted in Figures 4-41 and 4-42 for the low band and high band respectively.

$$|S_{i5}| \equiv \left|\frac{b_i}{a_5}\right| \qquad \textbf{(4-19)}$$

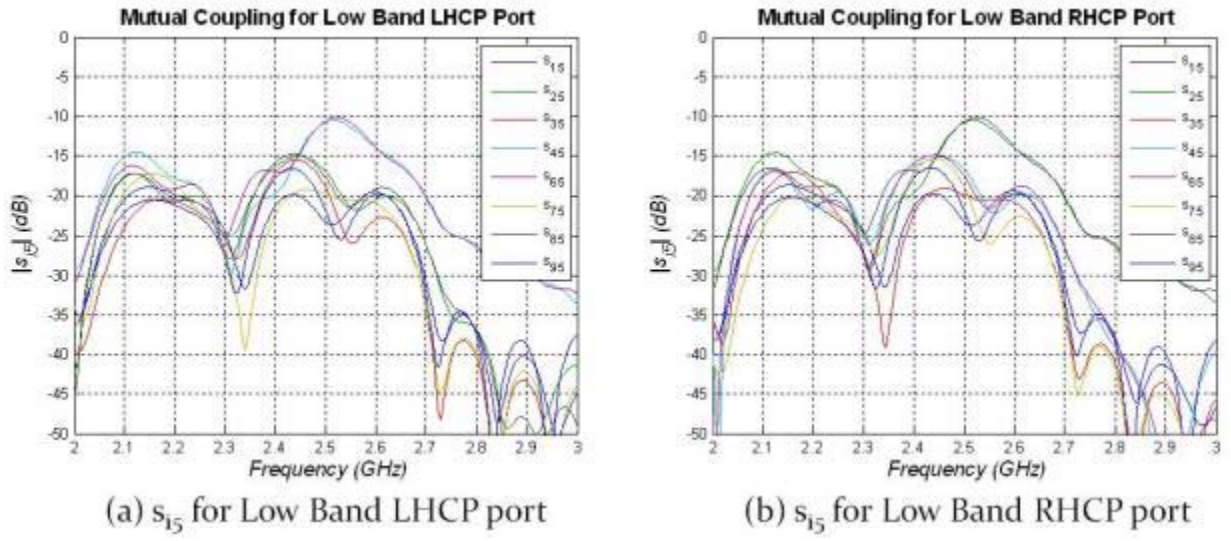

Figure 4-41: Mutual coupling plot for low band ports obtained in the 3x3 array simulation

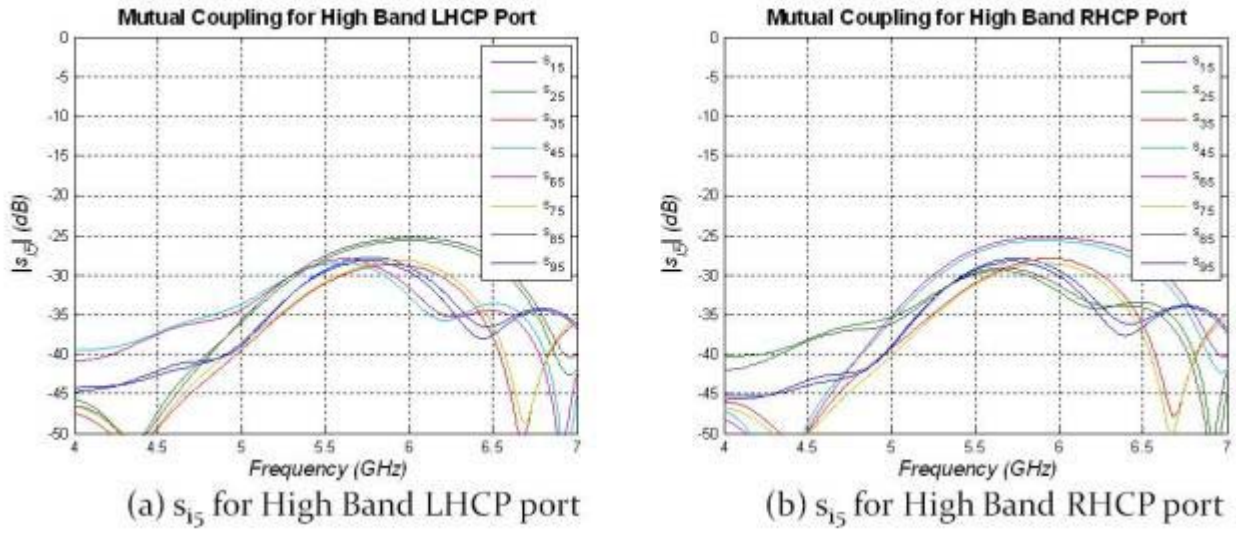

Figure 4-42: Mutual coupling plot for high band ports obtained in the 3x3 array simulation

The s_{45} and s_{65} parameters show the highest level of mutual coupling in low band LHCP operation, and s_{25} and s_{85} are the highest in low band RHCP operation. These coupling levels have a maximum value just below -10dB at the high end of the 2.45GHz ISM band. Ports 4 and 6 are the neighbors to port 5 offset in the x-direction. The low band LHCP ports are offset from the center of the element in the x-direction. This shows that the highest coupling is seen in the plane containing the feeds. The same trend is seen for the low band RHCP case, where the ports neighboring element 5 in the y-direction see the highest level of mutual coupling. The remaining coupling parameters at the low frequency are below -15dB across the frequency band.

The high band elements are separated by a larger electrical distance. Subsequently, they experience lower levels of mutual coupling. All of the coupling parameters in Figure 4-42 have

magnitudes below -25dB. The lower mutual coupling levels result in a smaller impact seen at the edge and corner elements.

The asymmetric mutual coupling helps explain the active element patterns for the low band RHCP edge elements from Figure 4-40. These patterns show that element 2 and 8 are the most significantly impacted in the low band RHCP case. These edge elements have neighboring elements in the x-direction, but they are missing one of the surrounding elements in the y-direction. Since the most significant contribution to their coupling comes from elements offset from them in the y-direction, they are impacted more than elements 4 and 6 who are missing neighboring elements in the x-direction.

4.2.3 Low Band Array Performance

The radiation pattern for the dual-band dual-CP antenna array was calculated using the multiple active element hybrid technique for three array sizes (12 elements x 12 elements, 24x24, and 48x48). The three sizes were intended to show the results for a small, moderate and large antenna array. For the low band radiators, the antenna patterns were calculated using the individual feeding technique and a quad-element technique that will be described in the following section. The remainder of this section will show the calculated array patterns, the performance analysis, and a comparison between the two feeding techniques. Selected patterns are provided in the text of this chapter to illustrate the array performance. Additional array patterns are provided in Appendix B.

4.2.3.1 Discussion of Quad-Element Feeding Technique

The size of the low band radiator was reduced to allow for spacing at the high frequency suitable for grating lobe-free scanning. This size reduction resulted in a small footprint at the low frequency, and thus the low frequency aperture is oversampled. The size reduction results in a larger than necessary number of potentially expensive and lossy components (such as attenuators and/or phase shifters).

If the spacing at the low frequency were doubled, the elements would then be separated by 0.514λ, a spacing allowing scanning to 70.7° before the onset of grating lobes. This element spacing can be accomplished by feeding groups of four elements together at the low frequency; this group of four elements will be referred to as the *quad-element*.

The quad-element is illustrated in Figure 4-43. The phase centers of four dual-band, dual-CP elements are indicated as (x_{pi}, y_{pi}), where i = 1, 2, 3, or 4. For the quad-element feeding, these four elements are excited by a simple four-way power splitter. In doing so, these four elements are fed with equal amplitude and phase. The effective phase center of the quad-element is indicated by (x_{eff}, y_{eff}). When the array is scanned, the scanning phase shift is determined using the effective phase center. The use of this feeding technique eliminates 75% of the required phase shifters and attenuators necessary for low frequency operation. The quad-element feeding

is only used for the low frequency elements. In Figure 4-43, the high frequency radiators still have phase centers at (x_{pi}, y_{pi}).

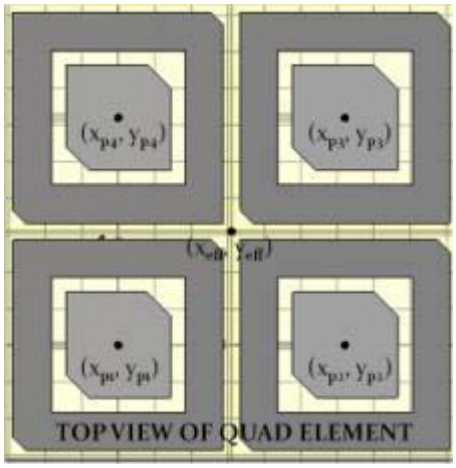

Figure 4-43: Top view of Quad-Element feeding technique

Figure 4-44 shows the phase shift required to scan an 11x11 array to θ=45° in the φ=90° plane. Figure 4-44(a) shows a three-dimensional plot of the required phase shift vs. x(cm) vs. y(cm) for an array in the x-y plane when all elements are excited, and Figure 4-44(b) shows the same plot for the quad-element feeding. The plots in Figure 4-44(c)-(d) overlay the phase shift required for the two feeding techniques in the principle planes of the array. The result shows that the quad-element phase shift is a stair-step approximation of the phase shift when all elements are excited.

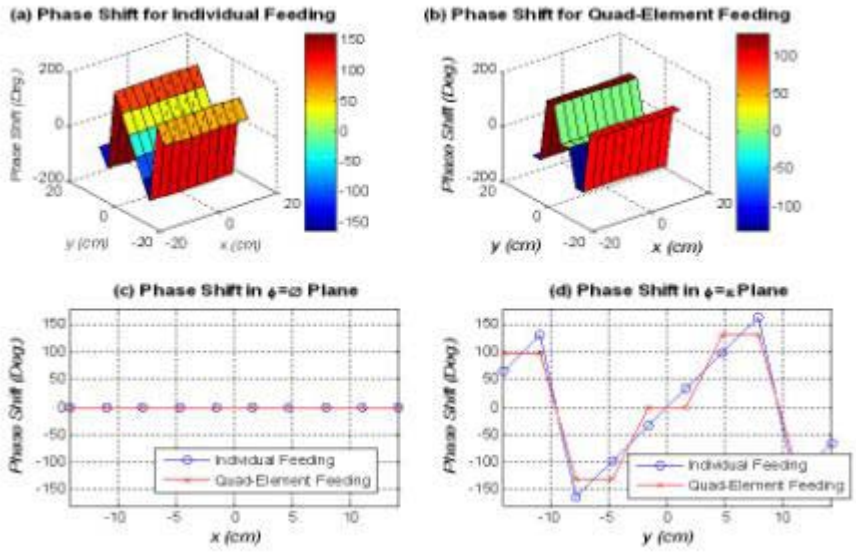

Figure 4-44: Comparison of the phase shift required to scan the array when all elements are excited and when the quad-element feeding is used

4.2.3.2 12x12 Array

The phase centers for the 12x12 antenna array are shown in Figure 4-45. This figure shows the phase centers for two feeding techniques. *Individual Feeding* refers to the case where all elements are fed individually, requiring components at each element. The *Quad-element* feeding technique was previously described. At the low frequency limit, this array is electrically small (3.084λ x 3.084λ).

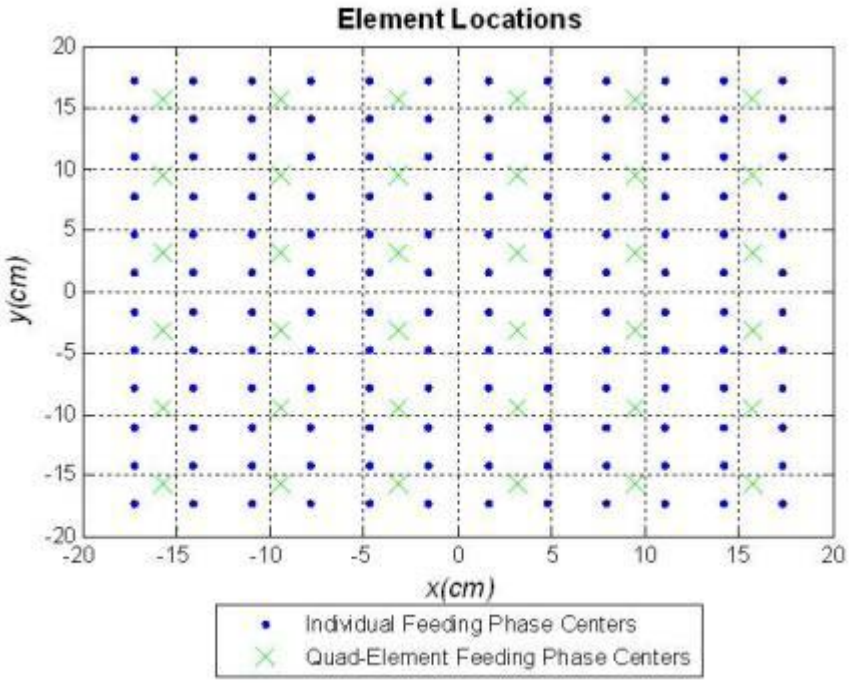

Figure 4-45: Phase center locations for elements in a 12x12 array

The array patterns for θ_0=0°, 15°, 30°, and 45° degrees are plotted in Figure 4-46 for the low band RHCP port in the φ=90° plane using individual element feeding. Figure 4-46(a) shows the *copolarized* components, and Figure 4-46(b) provides the *cross-polarized* components. The element pattern is overlaid on both of these plots to show that the array pattern drops off proportionally to the element pattern at θ_0. The RHCP and LHCP pattern for the quad-element feeding is compared to the individual feeding in Figures 4-47 and 4-48, and the performance for the two feeding techniques is compared in Table 4-1. The beamwidths for the two feeding techniques are identical for the four scan angles. These beamwidths are compared to the theoretical value obtained using (4-17) for scan angles below 30°. In all cases, these results match the approximated value closely. The normalized maximum value drops off faster at wide scan angles for the quad-element feeding, but not drastically. At θ_0=45°, the quad-element case exhibits a maximum value 1.8dB lower than that of the individual element feeding case. The individual feeding technique requires more potentially high loss phase shifters that would most likely decrease the gain of the individual feeding below that of the quad-element feeding. The quad-element feeding showed higher XPD at wide scan angles than the individual element

feeding. The improved XPD leads to an axial ratio value closer to unity, thus improving the performance of the array at wide scan angles for CP operation.

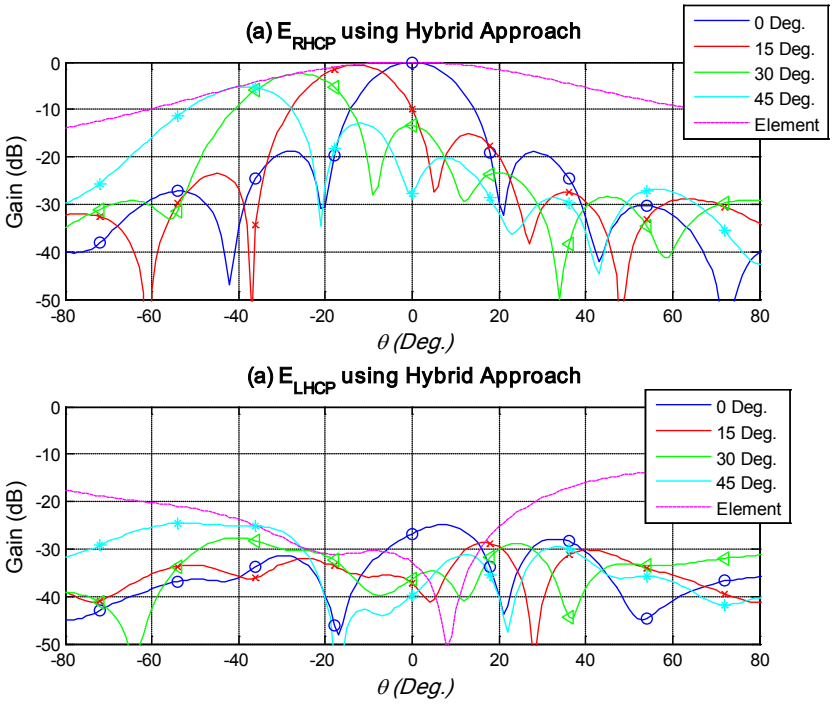

Figure 4-46: Low band RHCP 12x12 array patterns in the φ=90° plane using individual element feeding

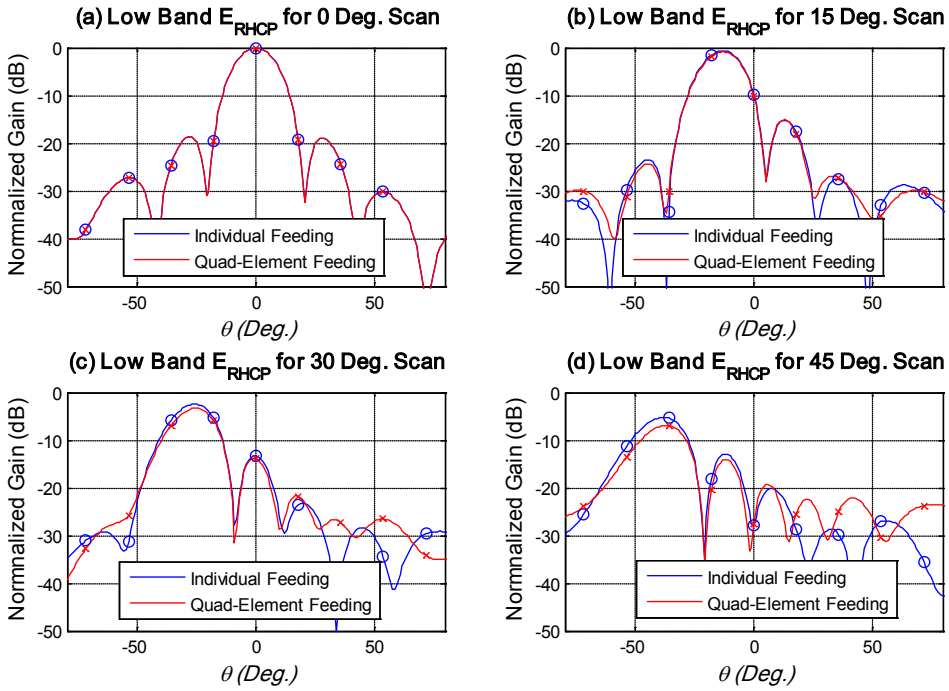

Figure 4-47: Low band RHCP port copolarized pattern in the φ=90° plane, 12x12 array

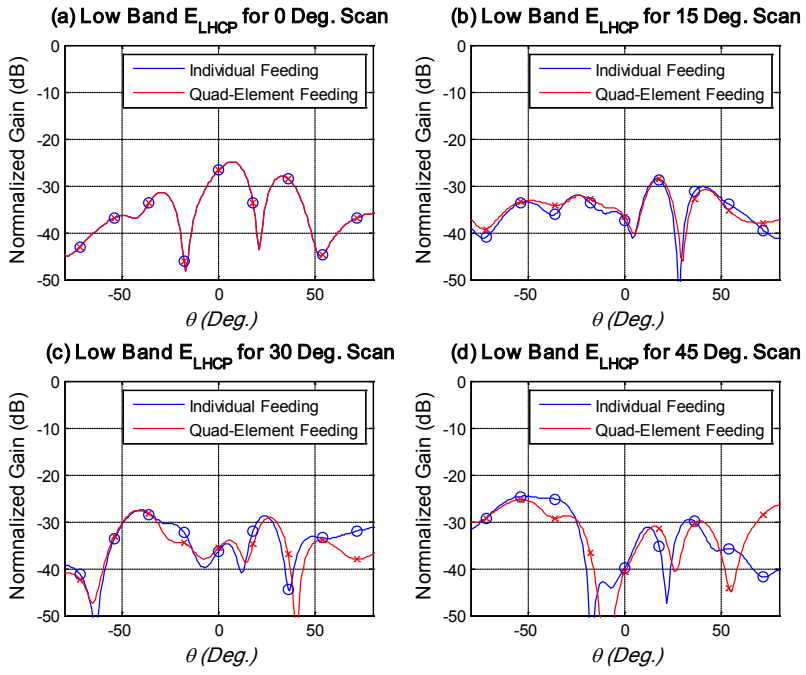

Figure 4-48: Low band RHCP port cross-polarized pattern in the φ=90° plane, 12x12 array

Table 4-1: Performance comparison between the individual element feeding and quad-element feeding: Low band RHCP, φ=90° plane, 12x12 array

		θ_0=0°	θ_0=15°	θ_0=30°	θ_0=45°
3dB Beamwidth (BW_{3dB})	Ind. Feed	17°	16°	18°	19°
	Quad. Feed	17°	17°	18°	19°
	Approx.*	16.4466°	17.0267°	18.9908°	N/A
θ_{MAX}	Ind. Feed	0°	-13°	-26°	-38°
	Quad. Feed	0°	-13°	-25°	-37°
Normalized Maximum Value ($F(\theta_{MAX})_{MAX}$)	Ind. Feed	0dB	-0.5840dB	-2.4677dB	-5.177dB
	Quad. Feed	0dB	-0.8245dB	-3.3461dB	-6.9245dB
Cross-pol. discrimination (XPD)	Ind. Feed	26.7334dB	34.7037dB	27.9628dB	19.9099dB
	Quad. Feed	26.7344dB	33.0733dB	30.6980dB	22.3936dB

The copolarized and cross-polarized components for the low band RHCP port are provided in Figures 4-49 and 4-50 for the φ=0° plane, with the results compared in Table 4-2. The results in Table 4-2 show good agreement between the two feeding techniques. These results show that the φ=90° plane has higher XPD than the φ=0° plane; this result is reflective of the higher XPD in the element pattern for the φ=90° plane.

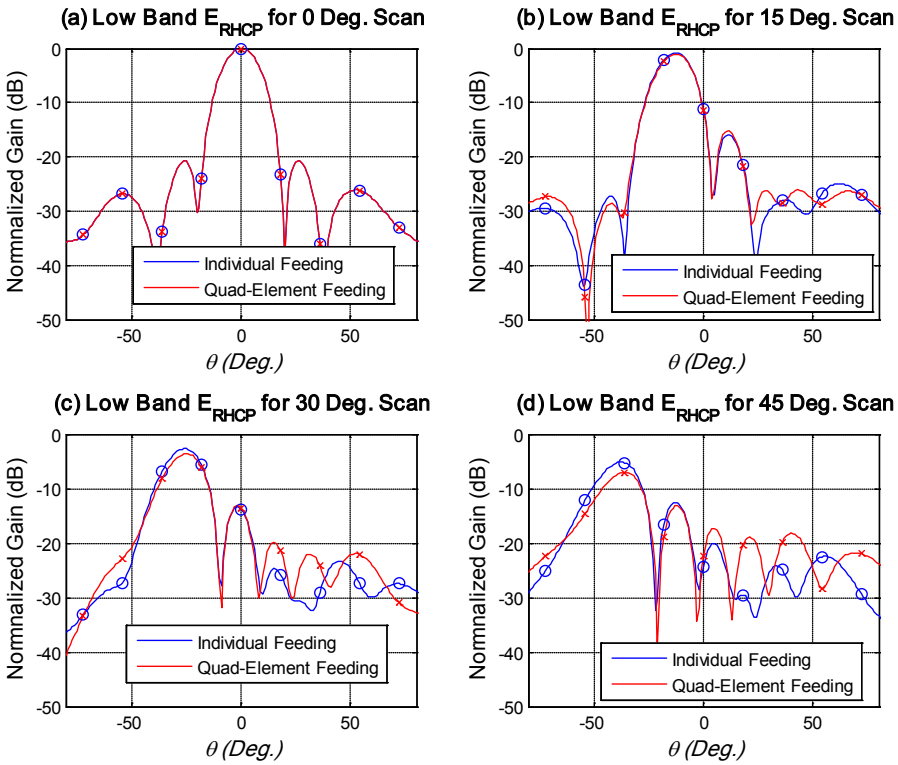

Figure 4-49: Low band RHCP port copolarized pattern in the φ=0° plane, 12x12 array

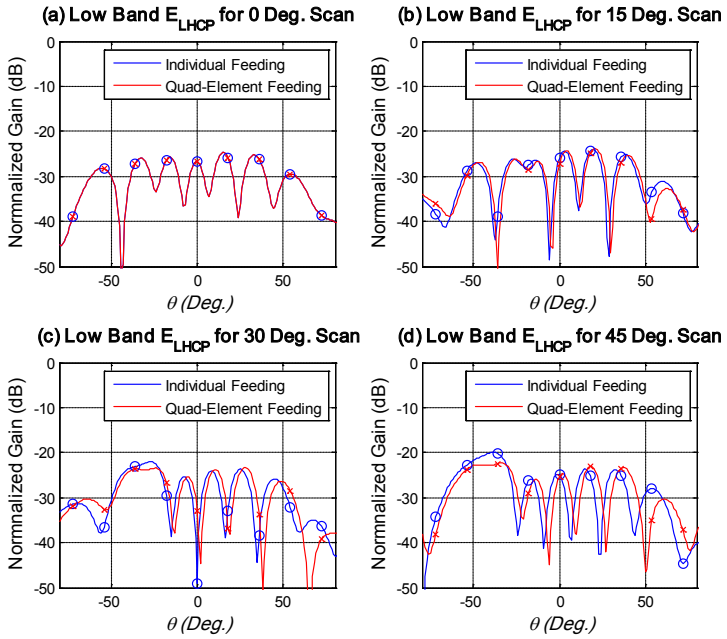

Figure 4-50: Low band RHCP port cross-polarized pattern in the φ=0° plane, 12x12 array

Table 4-2: Performance comparison between the individual element feeding and quad-element feeding: Low band RHCP, φ=0° plane, 12x12 array

		θ_0=0°	θ_0=15°	θ_0=30°	θ_0=45°
3dB Beamwidth (BW_{3dB})	Ind. Feed	15°	16°	17°	18°
	Quad. Feed	15°	15°	16°	18°
	Approx.*	16.4466°	17.0267°	18.9908°	N/A
θ_{MAX}	Ind. Feed	0°	-13°	-26°	-37°
	Quad. Feed	0°	-13°	-25°	-36°
Normalized Maximum Value ($F(\theta_{MAX})_{MAX}$)	Ind. Feed	0dB	-0.8372dB	-2.7278dB	-5.1746dB
	Quad. Feed	0dB	-1.0845dB	-3.6391dB	-7.0435dB
Cross-pol. discrimination (XPD)	Ind. Feed	26.7334dB	25.6602dB	19.3721dB	14.8274dB
	Quad. Feed	26.7344dB	25.6996dB	19.8120dB	15.4344dB

The low band LHCP port showed similar performance to the RHCP port. The performance parameters are shown in Tables 4-3 and 4-4 for the principle planes of the array. These results show that one plane has a distinctly higher XPD than the other. However, for the LHCP polarization, the φ=0° plane shows the higher XPD, whereas the RHCP had higher XPD in the φ=90° plane.

Table 4-3: Performance comparison between the individual element feeding and quad-element feeding: Low band LHCP, φ=90° plane, 12x12 array

		θ_0=0°	θ_0=15°	θ_0=30°	θ_0=45°
3dB Beamwidth (BW_{3dB})	Ind. Feed	15°	16°	17°	18°
	Quad. Feed	15°	15°	16°	18°
	Approx.*	16.4466°	17.0267°	18.9908°	N/A
θ_{MAX}	Ind. Feed	0°	-13°	-26°	-38°
	Quad. Feed	0°	-13°	-25°	-36°
Normalized Maximum Value ($F(\theta_{MAX})_{MAX}$)	Ind. Feed	0dB	-0.8335dB	-2.7162dB	-5.1790dB
	Quad. Feed	0dB	-1.0808dB	-3.6338dB	-7.0490dB
Cross-pol. discrimination (XPD)	Ind. Feed	26.5931dB	25.4063dB	19.1792dB	14.6330dB
	Quad. Feed	26.5931dB	25.4328dB	19.6560dB	15.2886dB

Table 4-4: Performance comparison between the individual element feeding and quad-element feeding: Low band LHCP, φ=0° plane, 12x12 array

		θ_0=0°	θ_0=15°	θ_0=30°	θ_0=45°
3dB Beamwidth (BW_{3dB})	Ind. Feed	17°	16°	18°	19°
	Quad. Feed	17°	17°	18°	19°
	Approx.*	16.4466°	17.0267°	18.9908°	N/A
θ_{MAX}	Ind. Feed	0°	-13°	-26°	-38°
	Quad. Feed	0°	-13°	-26°	-37°
Normalized Maximum Value ($F(\theta_{MAX})_{MAX}$)	Ind. Feed	0dB	-0.5795dB	-2.4495dB	-5.1716dB
	Quad. Feed	0dB	-0.8194dB	-3.3285dB	-6.9175dB
Cross-pol. discrimination (XPD)	Ind. Feed	26.5931dB	34.3800dB	28.5282dB	20.1628dB
	Quad. Feed	26.5931dB	32.7412dB	31.1331dB	22.7729dB

The low band 12x12 array calculations show good performance for a relatively small array. The quad-element feeding reduced the number of components required for the array without compromising performance. Both feeding techniques (individual feeding and quad-element feeding) exhibited half-power beamwidths that agree well with the approximation obtained using (4-17). The array maintains a XPD greater than 15dB over wide scan angles, which corresponds to an axial ratio lower than 3dB according to Figure 1-3. The scanning performance shows some error in θ_0 as the beam is scanned off of broadside. This error is minimized in larger array sizes, and those results will be shown in subsequent sections.

4.2.3.3 24x24 Array

The 24x24 element array consists of 576 dual-band, dual-CP elements, and 144 effective quad-elements for the low band. The phase centers for this array are shown in Figure 4-51. The φ=0° copolarized pattern for the low band LHCP port is shown in Figure 4-52, and the cross-polarized components are provided in Figure 4-53. These patterns show many of the same trends that were present in the smaller, 12x12 array: beamwidth in good agreement with approximation, high XPD, and a normalized maximum value that decreases proportionally to the element pattern. The XPD was higher in one principle plane compared to the other. As in the 12x12 array case,

the φ=0° plane was the better for LHCP, and the φ=90° was the better plane in RHCP. These results are reflected in the tabulated parameters for LHCP low band operation in the φ=0° plane (Table 4-5) and φ=90° plane (Table 4-6).

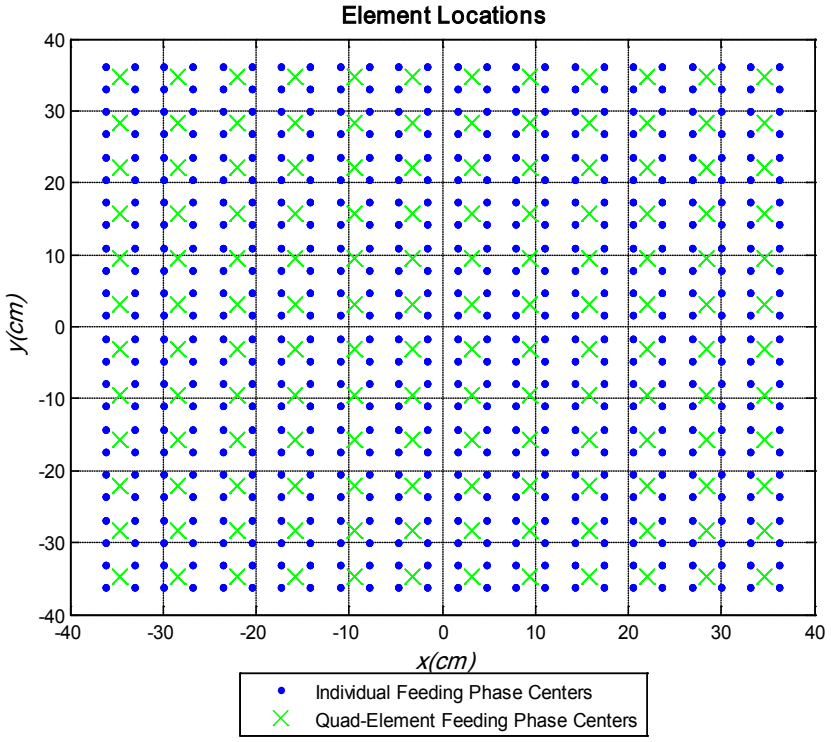

Figure 4-51: Phase center locations for elements in a 24x24 array

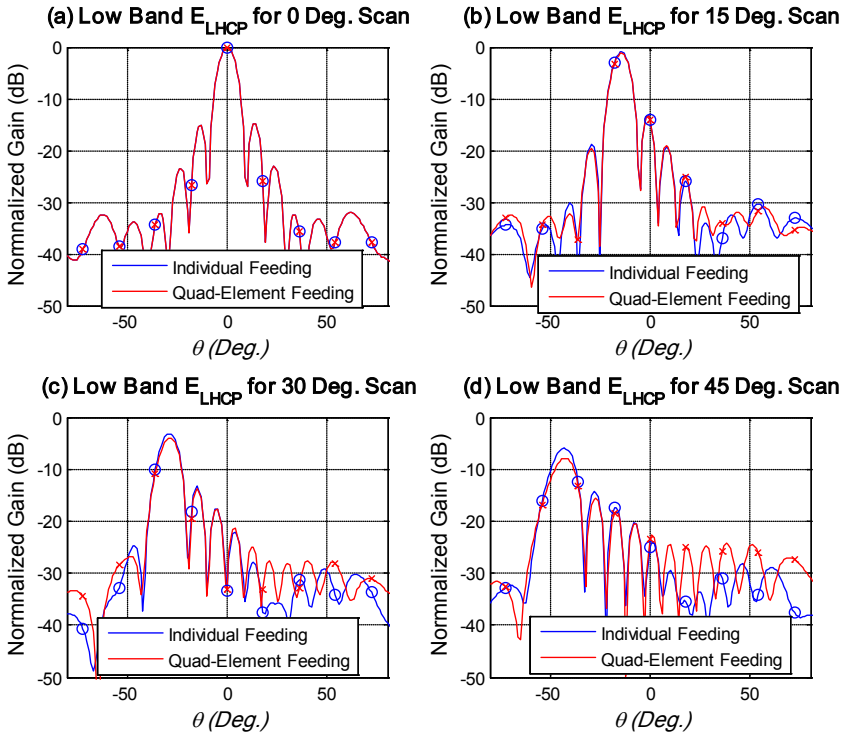

Figure 4-52: Low band LHCP port copolarized pattern in the φ=0° plane, 24x24 array

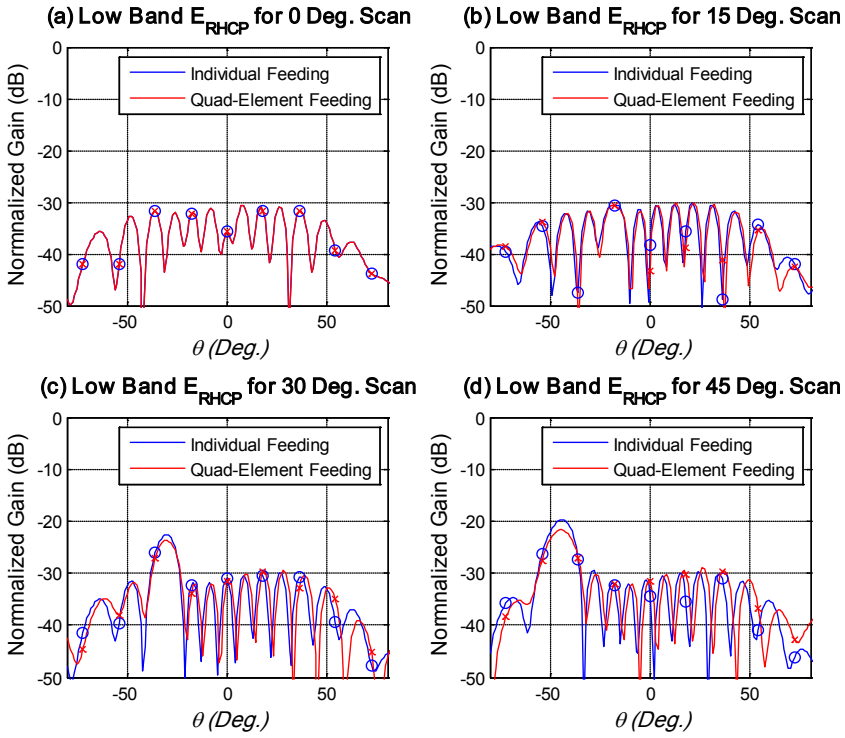

Figure 4-53: Low band LHCP port cross-polarized pattern in the φ=0° plane, 24x24 array

Table 4-5: Performance comparison between the individual element feeding and quad-element feeding: Low band LHCP, φ=0° plane, 24x24 array

		θ_0=0°	θ_0=15°	θ_0=30°	θ_0=45°
3dB Beamwidth (BW_{3dB})	Ind. Feed	9°	8°	9°	11°
	Quad. Feed	9°	8°	9°	11°
	Approx.*	8.2233°	8.5134°	9.4954°	N/A
θ_{MAX}	Ind. Feed	0°	-14°	-29°	-43°
	Quad. Feed	0°	-14°	-28°	-43°
Normalized Maximum Value ($F(\theta_{MAX})_{MAX}$)	Ind. Feed	0dB	-0.7086dB	-2.8243dB	-6.0076dB
	Quad. Feed	0dB	-0.9298dB	-3.6576dB	-7.7473dB
Cross-pol. discrimination (XPD)	Ind. Feed	35.6364dB	44.0116dB	26.5507dB	18.2519dB
	Quad. Feed	35.6364dB	44.6704dB	27.5578dB	18.6276dB

Table 4-6: Performance comparison between the individual element feeding and quad-element feeding: Low band LHCP, φ=90° plane, 24x24 array

		θ_0=0°	θ_0=15°	θ_0=30°	θ_0=45°
3dB Beamwidth (BW_{3dB})	Ind. Feed	9°	8°	9°	11°
	Quad. Feed	9°	8°	9°	11°
	Approx.*	8.2233°	8.5134°	9.4954°	N/A
θ_{MAX}	Ind. Feed	0°	-14°	-29°	-43°
	Quad. Feed	0°	-14°	-29°	-42°
Normalized Maximum Value ($F(\theta_{MAX})_{MAX}$)	Ind. Feed	0dB	-0.9900dB	-3.1520dB	-5.9807dB
	Quad. Feed	0dB	-1.2117dB	-4.0649dB	-7.8882dB
Cross-pol. discrimination (XPD)	Ind. Feed	35.6364dB	30.8238dB	19.6092dB	13.8412dB
	Quad. Feed	35.6364dB	30.6369dB	19.8048dB	14.2079dB

The 24x24 array exhibits better scanning performance than the 12x12 array for low band operation. The larger array exhibits less deviation between the desired pointing direction and the actual pointing direction due to the narrower beamwidth in the array factor. The XPD is improved compared to that for the smaller array, presumably because of the decreased impact that edge effects will have on the overall array pattern.

4.2.3.4 48x48 Array

The pattern was also calculated for a 48x48 array to show the performance of the dual-band, dual-CP element in a large array environment. The RHCP patterns for the low band frequency of 2.45 GHz is plotted for the φ=90° plane in Figures 4-55 and 4-56 for the copolarized and cross-polarized components. This large antenna array exhibits excellent performance using both the quad-element and individual feeding technique. The beamwidth agrees well with the approximation, the pointing angles accuracy is high, the XPD remains high at wide scan angles, and the two feeding techniques have main beam maximum values that track well with the element pattern.

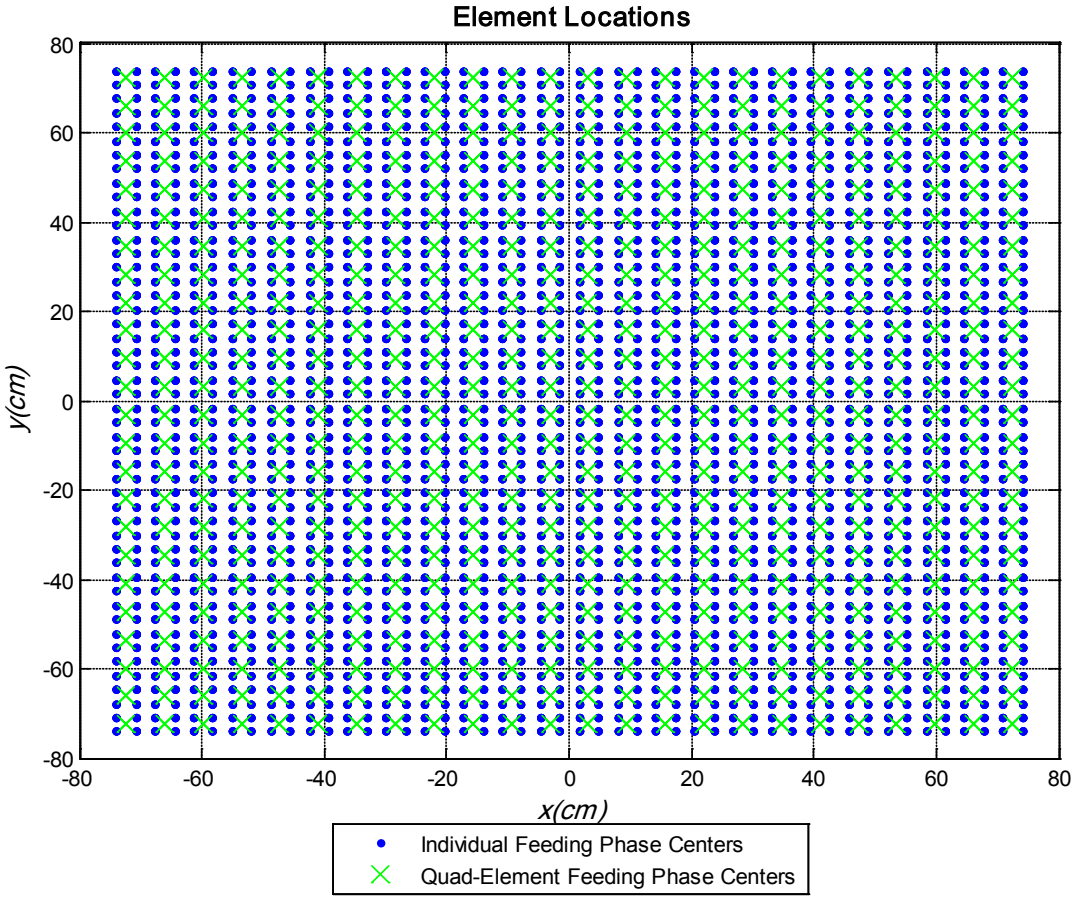

Figure 4-54: Phase center locations for elements in a 48x48 array

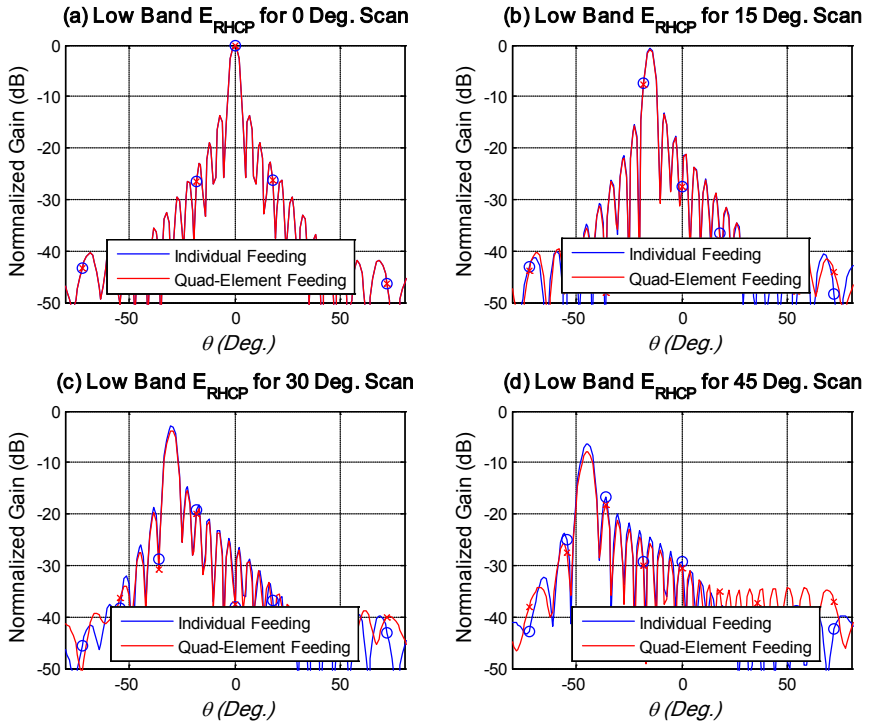

Figure 4-55: Low band RHCP port copolarized pattern in the φ=90° plane, 48x48 array

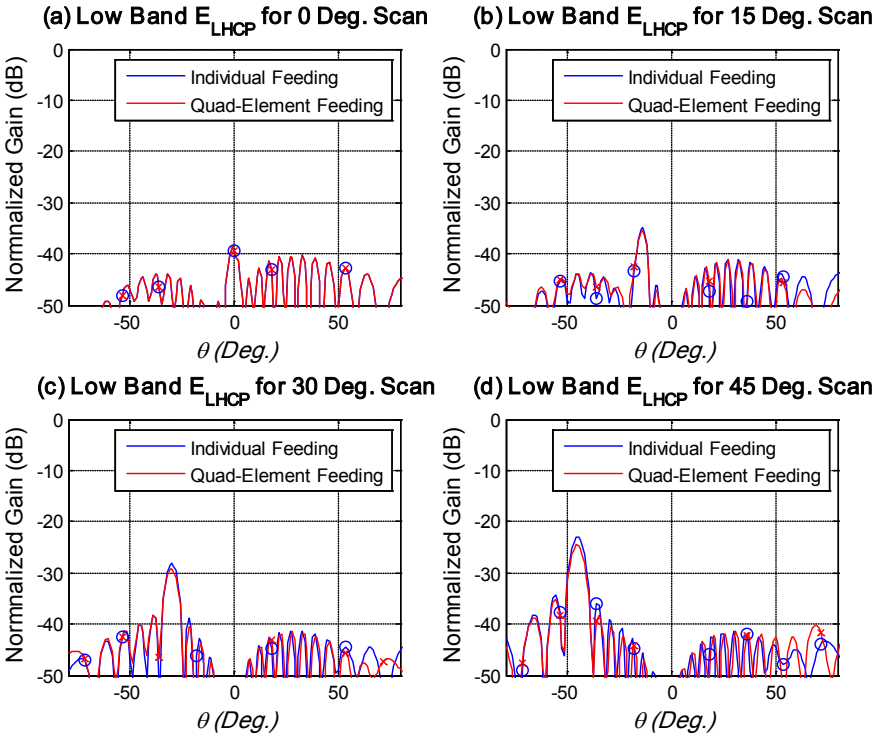

Figure 4-56: Low band RHCP port cross-polarized pattern in the φ=90° plane, 48x48 array

4.2.3.5 Discussion on Cross-Polarization Discrimination and Axial Ratio

The XPD and axial ratio performance for the low band antenna array sizes investigate in this study is provided in Figures 4-57 to 4-60. Each of these figures contains four subplots: XPD for individual feeding, XPD for quad-element feeding, AR for individual feeding and AR for quad-element feeding. Each figure has data points indicating the value for all three array sizes that were discussed. The results show that the low band radiators of the dual-band dual-CP antenna element provide excellent CP performance in an antenna array environment. The low band radiator maintains an axial ratio better than 2.0 dB for scans less than 30°.

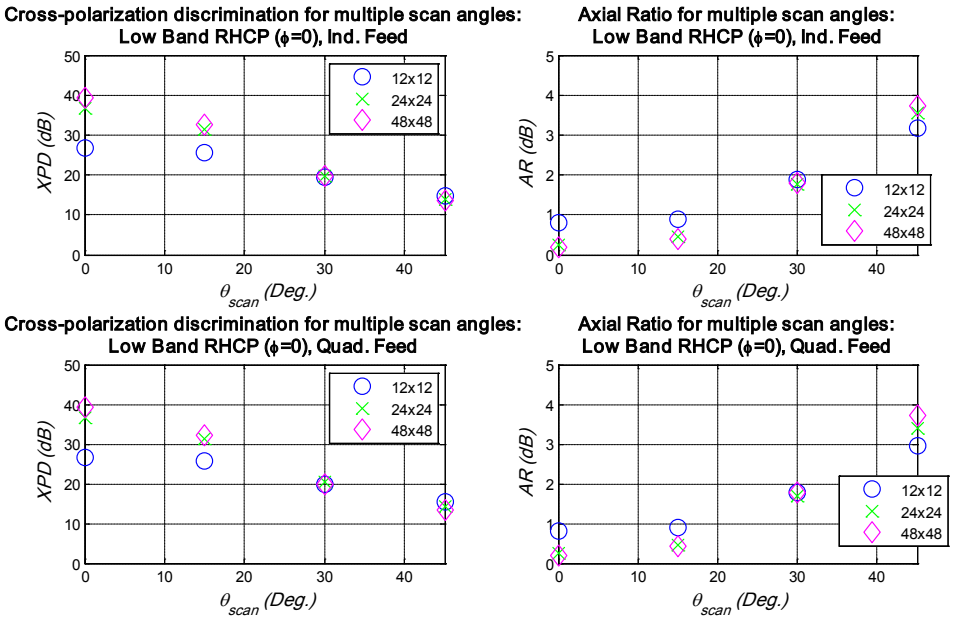

Figure 4-57: Low Band RHCP XPD and AR (φ=0° cut)

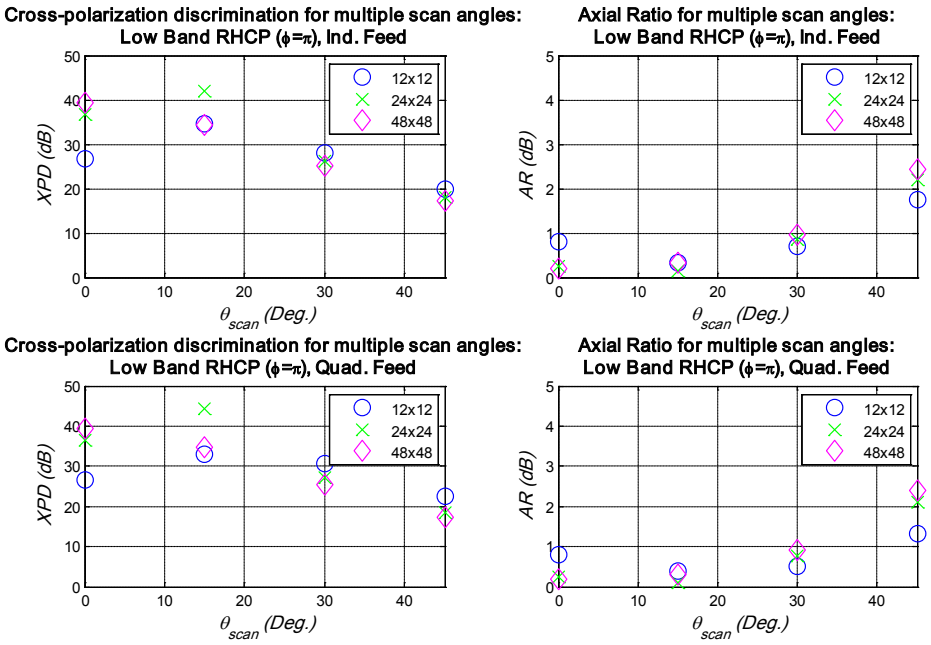

Figure 4-58: Low Band RHCP XPD and AR (φ=90° cut)

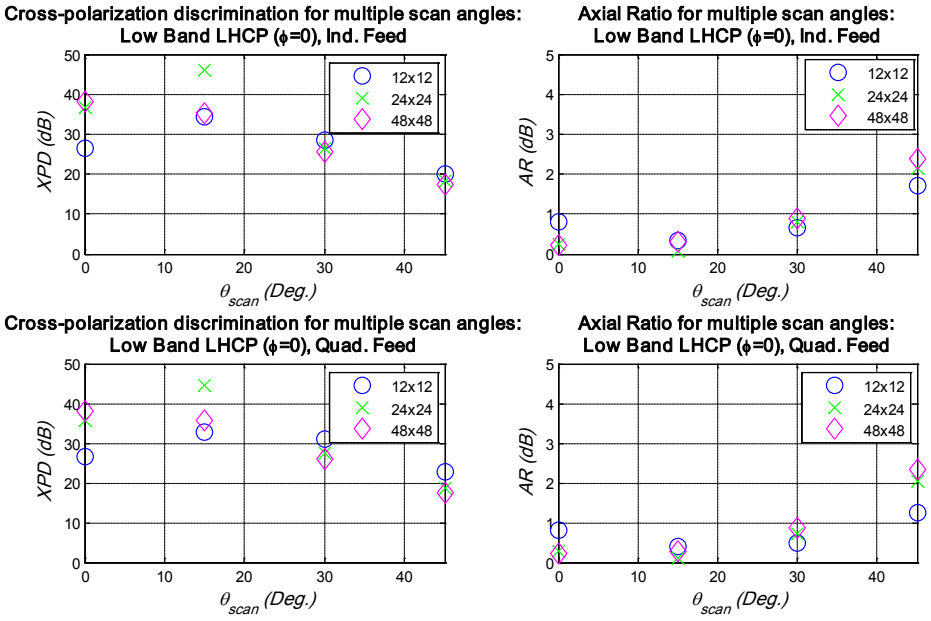

Figure 4-59: Low Band LHCP XPD and AR (φ=0° cut)

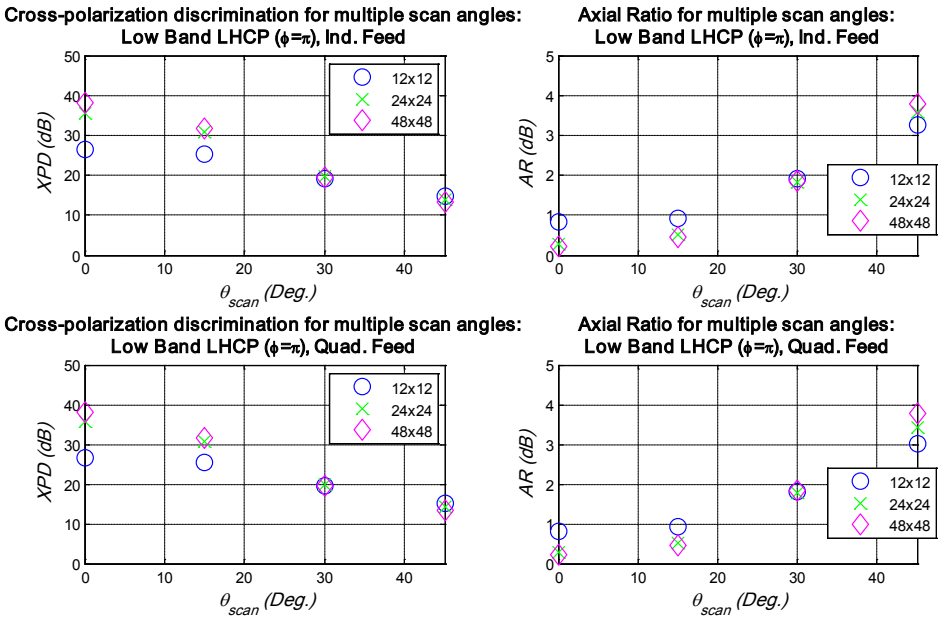

Figure 4-60: Low Band LHCP XPD and AR (φ=90° cut)

4.2.4 High Band Array Performance

The radiation pattern for the dual-band, dual-CP antenna array was calculated using the multiple active element hybrid technique for three array sizes (12x12, 24x24, and 48x48). The three sizes were intended to show the results for a small, moderate and large antenna array. The high band radiators used only the individual element feeding due to the element spacing. The 0.609λ spacing allows scanning of the main beam up to 40° off of broadside before grating lobes appear in the pattern. This section will show the calculated results for the three array sizes at various scan angles accompanied by performance analysis. Selected patterns are provided in the text of this chapter to illustrate the array performance. Additional array patterns are provided in Appendix B.

4.2.4.1 12x12 array

The smallest array size that analyzed in this study was a 12x12 dual-band, dual-CP antenna array. The coincident phase center nature of the dual-band, dual-CP elements results in phase centers for the high band elements being the same as those shown in Figure 4-45 for the individual feeding.

The scanned array patterns for the RHCP high band radiators of the 12x12 array are shown in Figure 4-61. Figure 4-61(a) shows the copolarized patterns normalized to the maximum value of the broadside case; this normalization is done to show the reduction in maximum gain as the array is scanned. The gain reduction is proportional to the overlaid element pattern until grating lobes begin to appear. This is evident in the 45° scan case. The main lobe maximum value has

dropped off much faster than the element pattern, and a grating lobe is visible in the range from 50°<θ<80°. The cross-polarized patterns of Figure 4-61(b) illustrate the excellent XPD for the array. As mentioned before a high XPD corresponds to an axial ratio near unity. The performance parameters of the RHCP high band radiator for the 12x12 array are provided for the φ=0° and φ=90° in Table 4-8 and 4-9 respectively.

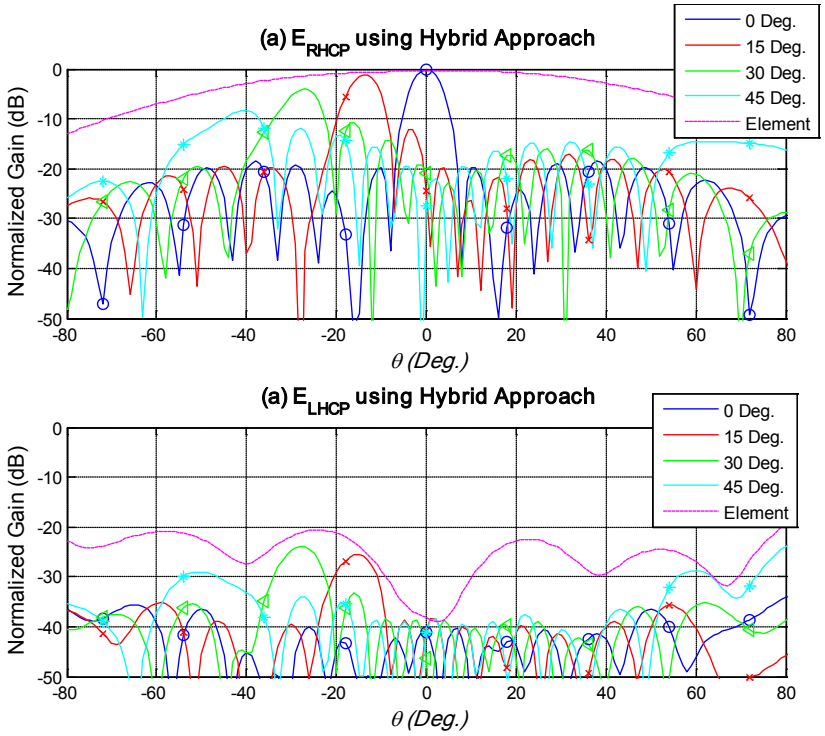

Figure 4-61: High band pattern for RHCP φ=0° plane, 12x12 array

Table 4-7: Performance of High band RHCP, φ=0° plane, 12x12 array

		θ_0=0°	θ_0=15°	θ_0=30°	θ_0=45°
3dB Beamwidth (BW_{3dB})	Calculated	7°	7°	8°	11°
	Approx.*	6.9473°	7.1923°	8.0220°	N/A
θ_{MAX}	Calculated	0°	-14°	-27°	-40°
Normalized Maximum Value ($F(\theta_{MAX})_{MAX}$)	Calculated	0dB	-1.1521dB	-4.0778dB	-8.3121dB
Cross-pol. discrimination (XPD)	Calculated	41.0871dB	24.7663dB	19.9566dB	24.8445dB

Table 4-8: Performance of High band RHCP, φ=90° plane, 12x12 array

		θ_0=0°	θ_0=15°	θ_0=30°	θ_0=45°
3dB Beamwidth (BW_{3dB})	Calculated	7°	7°	8°	11°
	Approx.*	6.9473°	7.1923°	8.0220°	N/A
θ_{MAX}	Calculated	0°	-14°	-27°	-40°
Normalized Maximum Value ($F(\theta_{MAX})_{MAX}$)	Calculated	0dB	-1.1387dB	-4.0797dB	-8.3745dB
Cross-pol. discrimination (XPD)	Calculated	41.0871dB	39.1293dB	26.5732dB	19.8965dB

The performance parameters for the LHCP radiators for the high frequency band of the 12x12 array are tabulated in Tables 4-10 and 4-11 for the φ=0° and φ=90° principle planes. The XPD for the LHCP radiators is slightly lower than that of the RHCP array due to the asymmetry in the stripline feeding network. The two feed lines are printed on opposing sides of a thin microwave substrate layer to avoid physical intersection. The RHCP feed line passes above the LHCP line, and this has been seen to result in improved polarization performance for the RHCP compared to the LHCP. Although the XPD is not as high as for the RHCP port, it is still between 21dB and 32dB across a wide range of scan angles.

Table 4-9: Performance of High band LHCP, φ=0° plane, 12x12 array

		θ_0=0°	θ_0=15°	θ_0=30°	θ_0=45°
3dB Beamwidth (BW_{3dB})	Calculated	7°	7°	8°	11°
	Approx.*	6.9473°	7.1923°	8.0220°	N/A
θ_{MAX}	Calculated	0°	-14°	-27°	-41°
Normalized Maximum Value ($F(\theta_{MAX})_{MAX}$)	Calculated	0dB	-1.1902dB	-4.2171dB	-8.2405dB
Cross-pol. discrimination (XPD)	Calculated	29.6270dB	32.0779dB	26.6203dB	21.4788dB

Table 4-10: Performance of High band LHCP, φ=90° plane, 12x12 array

		θ_0=0°	θ_0=15°	θ_0=30°	θ_0=45°
3dB Beamwidth (BW_{3dB})	Calculated	7°	7°	8°	12°
	Approx.*	6.9473°	7.1923°	8.0220°	N/A
θ_{MAX}	Calculated	0°	-14°	-27°	-41°
Normalized Maximum Value ($F(\theta_{MAX})_{MAX}$)	Calculated	0dB	-1.2597dB	-4.4097dB	-8.4719dB
Cross-pol. discrimination (XPD)	Calculated	29.6270dB	24.7661dB	21.1263dB	26.0551dB

The 12x12 array patterns for the high band radiators show excellent polarization performance even at wide scan angles. As anticipated, grating lobes are introduced into the visible region of the antenna pattern when the scan angle exceeds 40°, but a wide grating lobe-free scan region is still provided. The beamwidths are virtually identical in the two principle planes due to the inherent symmetry in the volumetric pattern of the constituent elements. The maximum gain value for the array falls off proportionally to the element pattern magnitude as the main beam is scanned, and no additional source of loss in the main beam is noticed until the onset of grating lobes.

4.2.4.2 24x24 Array

The 24x24 array was previously analyzed for the low band frequencies. In this section, the high band performance is discussed. The RHCP pattern at 5.9 GHz is plotted in Figure 4-62(a) and (b) for the φ=90° plane. The patterns show similar XPD performance to the smaller, 12x12 array. The maximum gain drops off proportionally to the element pattern until the onset of grating lobes. The grating lobe appears in approximately the same region as in the 12x12 array, but for this larger array the grating lobe is narrower. The performance of the RHCP principle planes (φ=0° and φ=90°) is provided in Tables 4-12 and 4-13, and the LHCP performance is shown in Tables 4-14 and 4-15. The right hand CP patterns exhibits higher XPD than the LHCP polarization as it did in the smaller array. The patterns exhibit symmetry in the principle plane beamwidth, and the beamwidths agree well with the approximated values. There is minimal discrepancy between the desired and actual pointing angles for the wide range of scan angles used.

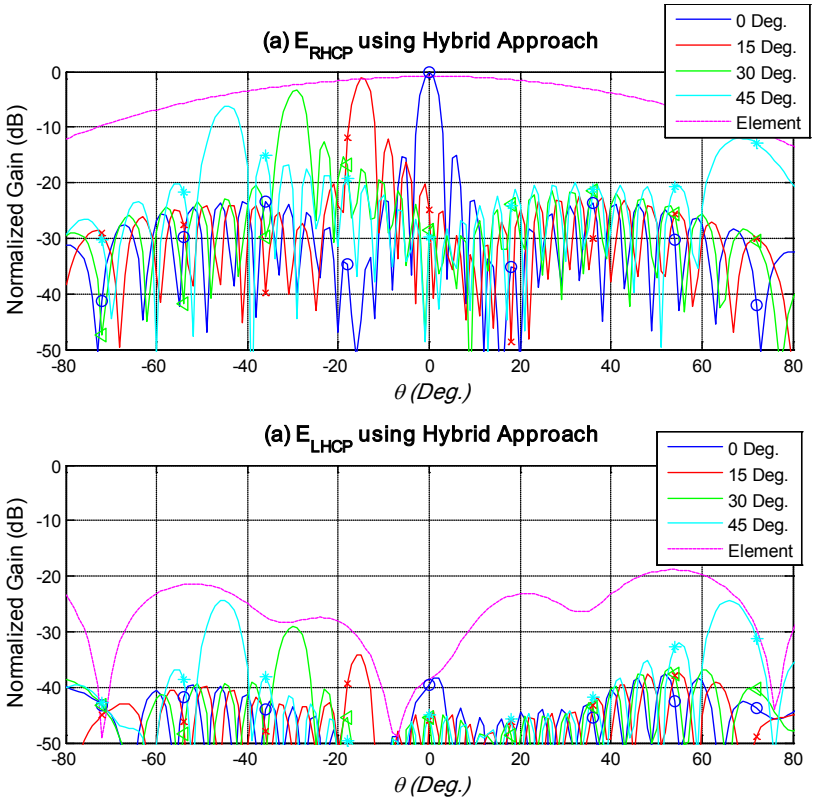

Figure 4-62: High band pattern for RHCP φ=90° plane, 24x24 array

Table 4-11: Performance of High band RHCP, φ=0° plane, 24x24 array

		θ_0=0°	θ_0=15°	θ_0=30°	θ_0=45°
3dB Beamwidth (BW_{3dB})	Calculated	3°	4°	4°	6°
	Approx.*	3.4736°	3.5962°	4.0110°	N/A
θ_{MAX}	Calculated	0°	-15°	-29°	-44°
Normalized Maximum Value ($F(\theta_{MAX})_{MAX}$)	Calculated	0dB	-0.9416dB	-3.0767dB	-6.1817dB
Cross-pol. discrimination (XPD)	Calculated	39.5948dB	23.5188dB	19.9319dB	21.8875dB

Table 4-12: Performance of High band RHCP, φ=90° plane, 24x24 array

		θ_0=0°	θ_0=15°	θ_0=30°	θ_0=45°
3dB Beamwidth (BW_{3dB})	Calculated	3°	4°	4°	6°
	Approx.*	3.4736°	3.5962°	4.0110°	N/A
θ_{MAX}	Calculated	0°	-15°	-29°	-44°
Normalized Maximum Value ($F(\theta_{MAX})_{MAX}$)	Calculated	0dB	-1.0933dB	-3.4253dB	-6.1986dB
Cross-pol. discrimination (XPD)	Calculated	39.5948dB	33.2006dB	25.8047dB	18.6798dB

Table 4-13: Performance of High band LHCP, φ=0° plane, 24x24 array

		θ_0=0°	θ_0=15°	θ_0=30°	θ_0=45°
3dB Beamwidth (BW_{3dB})	Calculated	3°	4°	4°	6°
	Approx.*	3.4736°	3.5962°	4.0110°	N/A
θ_{MAX}	Calculated	0°	-15°	-29°	-44°
Normalized Maximum Value ($F(\theta_{MAX})_{MAX}$)	Calculated	0dB	-1.0090dB	-3.2080dB	-6.0014dB
Cross-pol. discrimination (XPD)	Calculated	28.6096dB	30.3891dB	26.1229dB	19.9702dB

Table 4-14: Performance of High band LHCP, φ=90° plane, 24x24 array

		θ_0=0°	θ_0=15°	θ_0=30°	θ_0=45°
3dB Beamwidth (BW_{3dB})	Calculated	3°	4°	4°	6°
	Approx.*	3.4736°	3.5962°	4.0110°	N/A
θ_{MAX}	Calculated	0°	-15°	-29°	-44°
Normalized Maximum Value ($F(\theta_{MAX})_{MAX}$)	Calculated	0dB	-0.9254dB	-3.0425dB	-6.2363dB
Cross-pol. discrimination (XPD)	Calculated	28.6096dB	23.4678dB	21.1889dB	21.1300dB

4.2.4.3 48x48 Array

The electrically large 48x48 array exhibits excellent performance parameters making it ideal for applications requiring narrow beamwidths. The 5.9 GHz RHCP pattern in for the y-z plane (φ=90°) is shown in Figure 4-63. The pattern has a beamwidth less than 2° for the broadside case. CST Microwave Studio will not export data files with finer resolution than 1°; this results in the rough appearance of the patterns. The pattern characteristics are tabulated in Tables 4-16 and 4-17 for RHCP and LHCP in the y-z plane. The results are consistent with those seen in the analysis of the small and moderate sized arrays.

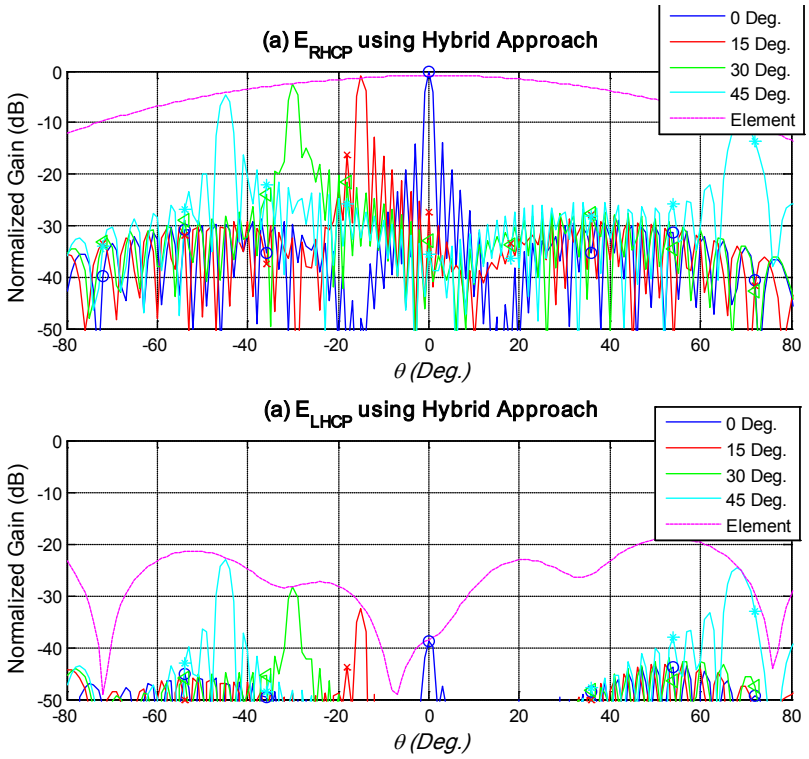

Figure 4-63: High band pattern for RHCP φ=90° plane, 48x48 array

Table 4-15: Performance of High band RHCP, φ=90° plane, 48x48 array

		θ_0=0°	θ_0=15°	θ_0=30°	θ_0=45°
3dB Beamwidth (BW_{3dB})	Calculated	2°	2°	2°	3°
	Approx.*	1.7368°	1.7981°	2.0055°	N/A
θ_{MAX}	Calculated	0°	-15°	-30°	-45°
Normalized Maximum Value ($F(\theta_{MAX})_{MAX}$)	Calculated	0dB	-0.7941dB	-2.5521dB	-4.7473dB
Cross-pol. discrimination (XPD)	Calculated	38.6918dB	31.6850dB	25.6196dB	18.2955dB

Table 4-16: Performance of High band LHCP, φ=90° plane, 48x48 array

		θ_0=0°	θ_0=15°	θ_0=30°	θ_0=45°
3dB Beamwidth (BW_{3dB})	Calculated	2°	2°	2°	3°
	Approx.*	1.7368°	1.7981°	2.0055°	N/A
θ_{MAX}	Calculated	0°	-15°	-30°	-45°
Normalized Maximum Value ($F(\theta_{MAX})_{MAX}$)	Calculated	0dB	-0.6191dB	-2.1533dB	-4.8102dB
Cross-pol. discrimination (XPD)	Calculated	28.1364dB	23.0574dB	21.3860dB	20.4223dB

4.2.4.4 Discussion on Cross-Polarization Discrimination and Axial Ratio

The XPD and axial ratio performance for the high band antenna array sizes investigate in this study is provided in Figures 4-64 to 4-67. Each of these figures contains two subplots: XPD and AR. Each figure has points indicating the value for all three array sizes that were discussed. The results show that the high band radiators of the dual-band dual-CP antenna element provides excellent CP performance in an antenna array environment. The high band radiator maintains an axial ratio better than 2.0 dB for scans less than 45°. The element spacing is slightly over 0.6λ in the high frequency band causing grating lobes to appear in the visible region when the array is scanned past 40°.

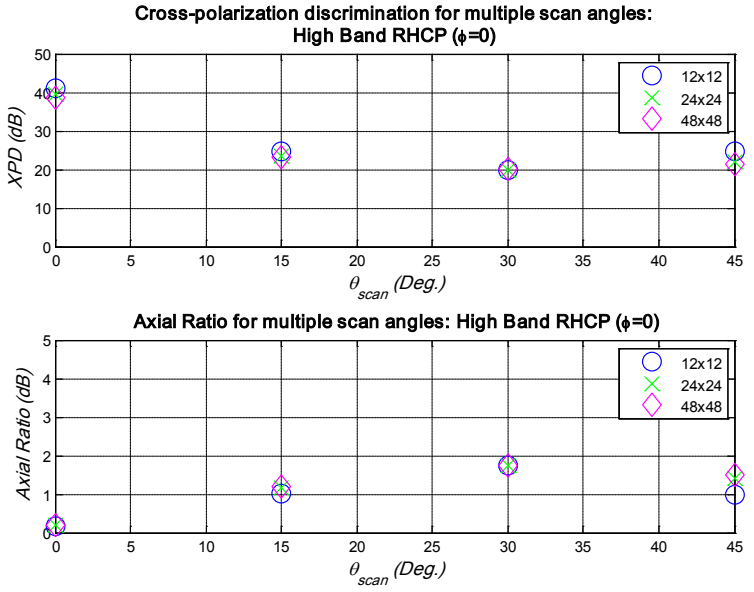

Figure 4-64: High Band RHCP XPD and AR (φ=0° cut)

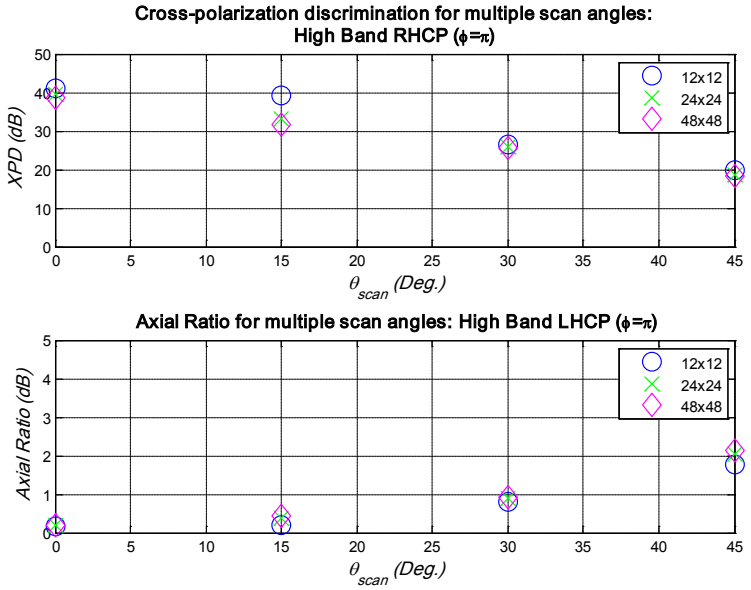

Figure 4-65: High Band RHCP XPD and AR (φ=90° cut)

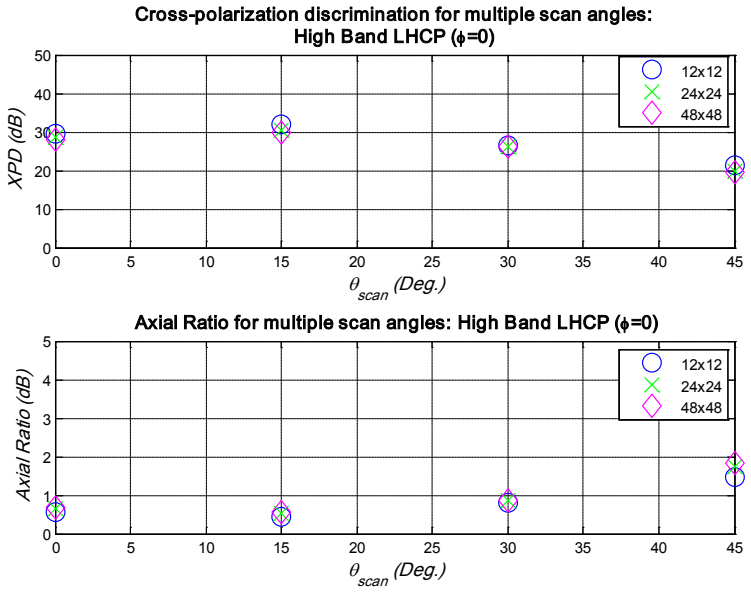

Figure 4-66: High Band LHCP XPD and AR (φ=0° cut)

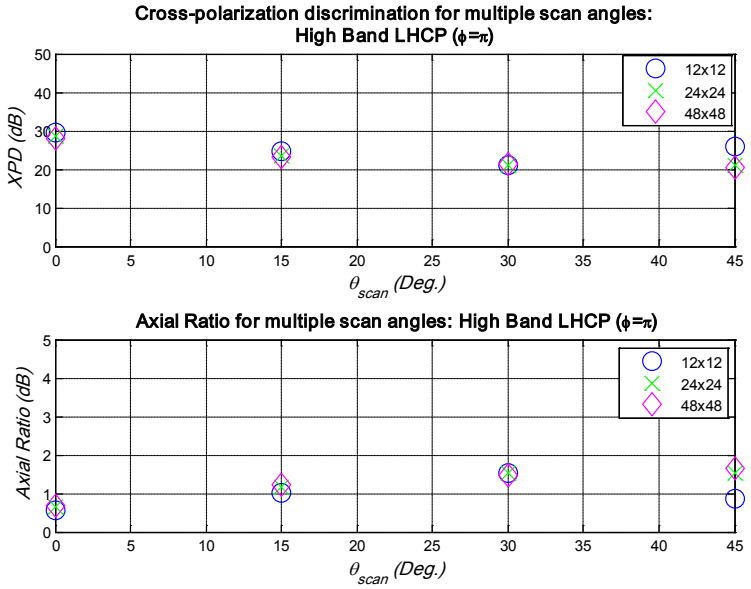

Figure 4-67: High Band LHCP XPD and AR (φ=90° cut)

4.3 Comparison with Existing Dual-Band, Dual-Polarized Array Apertures from the Literature

The ability of this element to be placed in a uniform array lattice is another strong advantage for this element. Many dual-band radiating apertures are created from interleaving arrays of different sizes on different lattice structures [4, 19, 52]. Interleaving elements in this way provides the difficulty of physically arranging the element footprints to avoid overlapping, while at the same time maintaining proper spacing to avoid grating lobes [21]. The element disclosed in this document eliminates the need to interleave elements. Placing the low band elements on the same lattice as the high frequency band elements results in an oversampled aperture at the low band. If all elements in the low band were fed with individual amplitude and phase weighting, more components (including attenuators, low noise amplifiers, and phase shifters) would be used resulting in increased cost and complexity. A quad-element feeding technique is described that alleviates the problem of oversampling without complicating the array layout.

The synthetic aperture radar (SAR) element patented by Strickland in [76] utilized multiple high frequency resonant microstrip antennas placed inside of a low frequency square ring patch. The frequency ratio of this configuration is limited to make sure that the elements can be arranged properly. The Strickland patent deals with dual-linear polarization only, and no mention of scanning is provided.

Mangenot and Lorenzo discuss a dual-band, dual-linear subarray concept for SAR applications in [19]. Their design operates with a frequency ratio of just over 3:1 by using arrays of interlaced radiators. Cavity-backed annular slots are used for both frequency bands. The array provides scanning of up to 15° off of broadside in each of the two frequency bands.

The design proposed by Vallecchi, *et al* for SAR applications uses a perforated low band patch to allow radiation from the high frequency patches printed on a lower level in the design [14]. Each polarization of this device operates with a single sense of polarization that can be either linear or circular depending on the feed network design. The array layout uses a series fed concept with no mention of beam scanning. Granholm's perforated patch design is also for SAR applications, and it shows the ability to provide dual-linear polarization [20]. Similar to [14], the design in [20] is presented without mention of beam scanning.

Shafai, *et al* designed a SAR dual-band array capable of operating with dual-linear polarization. In [18], the authors state that arranging dual-band antenna elements on a lattice suitable for scanning is a challenge that becomes more severe as the scanning window increases. In their design, they were able to achieve a scanning of the main beam up to 25° off of broadside.

The design discussed in this dissertation avoids many of the difficulties commonly faced in dual-band array design. The low band element can be reduced in size to the point where concentric low and high band elements are arranged on the same lattice. The resulting antenna array is oversampled at the low frequency band, but a quad-element feeding is introduced to reduce the number of active components by 75%. The presence of the capacitive loading structure provides the antenna engineer with a wide range of variables to control the frequency ratio and size of the element, thus making it suitable for a wide range of applications.

CHAPTER 5. CONCLUSIONS

A novel dual-band element has been designed that provides dual-CP performance in two distinct frequency bands. The element, consisting of two concentric radiating elements, was built and tested to verify the concept and performance shown in simulations. The measured results show good agreement with the simulations, this establishing a high confidence level in the validity of the simulation models used in this dissertation. Moreover, the measured results confirm the ability of this element to generate dual-circular polarization at two distinct frequency bands while providing a lightweight, low-profile, printed circuit design capable of facilitating system integration.

The high frequency element is a square ring slot element. The element is realized in stripline to restrict the radiation to the upper half plane for a more directive element than in slot line or slotted microstrip designs. Slotted stripline designs often experience inefficiencies and power loss due to the excitation of a parallel plate mode that propagates between the upper and lower ground plane. In this design, the plated through holes are placed around the outer perimeter of the square ring slot to suppress the parallel plate mode. This technique has been used in the literature for aperture coupled antennas, and it is seen to improve the efficiency of the high band radiator. The plated through holes also serve as the shorting mechanism for the low band shorted square ring antenna element. These two concentric elements are printed on the same microwave substrate providing a low-profile, lightweight design that can be manufactured at low cost.

The two constituent elements in this design are the square ring slot and the shorted square ring element. By adding an orthogonal feed point, they can be operated with dual-linear polarization. Dual-linear polarization is commonly used for applications such as synthetic aperture radar. However, many applications prefer circular polarization because it allows flexible orientation between transmitting and receiving antennas while reducing multipath effects that can lead to signal fading. In this research, isosceles triangle perturbations are added to opposing corners of both radiators. These perturbations introduce two near-degenerate modes in the radiating structure. If the feed point is chosen correctly, the modes can be excited in phase quadrature resulting in circular polarization. The sense of circular polarization is determined by the feed placement with respect to the perturbations. If orthogonal feeds are present, both senses of circular polarization can be excited. The ability to operate with both sense of circular polarization provides the ability to reuse frequencies in a communication system and double the system capacity without requiring additional bandwidth.

In many applications, the footprint and/or weight of the antenna is limited by several factors. For instance, in space based applications the cost of the mission is impacted by the overall weight of the platform. In such cases, the weight and size of the antenna should be minimized. In personal

wireless communications, the desired size of the electronic device decreases as the technology and functionality of the device increases. This increases the need for a small antenna capable of supporting multiple frequency bands and functions. In any application requiring an antenna array, the size of the antenna element must be sized correctly to allow for spacing in a suitable lattice structure enabling adequate scanning performance. If the element forces electrically large lattice spacing, the array pattern will experience grating lobes as the main beam is scanned.

In this dissertation, a novel capacitive loading structure was designed that provides significant size reduction in the low band shorted square ring radiator. This substrate adds a capacitive loading patch in a plane parallel to the radiating elements. The patch is a thin, annular ring of width w_{cap}. The radiating structure and the capacitive patch maintain electrical continuity through a series of plated through holes. The structure generates a capacitance between the capacitive patch and the antenna's ground plane to facilitate size reduction. The structure can have a substrate separate from that of the radiating element. This substrate can have a high dielectric constant to maximize the capacitance of the structure. By restricting this substrate to the capacitive loading structure, the radiating element can still be printed on a low loss, low dielectric constant substrate. This is ideal because high dielectric constant substrates have been seen to degrade antenna performance. The performance of this loading structure was verified through measurements. The outer perimeter of the capacitive patch follows the outer perimeter of the shorted square ring. When perturbations are present for circular polarization, the shape of the capacitive patch is modified to allow circular polarized performance in the compact antenna size.

The dual-substrate capacitive loading structure was incorporated into the dual-band, dual-polarized antenna element to reduce the footprint of the element. This allows a dual-band element with a large frequency ratio to be placed in an array environment conducive to scanning the main beam at the high frequency without the introduction of grating lobes. The capacitive loading structure reduces the size of the low frequency element while leaving the high band element performance unchanged. The size reduction, however, is not obtained without drawback. The operational bandwidth of the low band element – in terms of impedance match and axial ratio – is reduced by the increased quality factor of the element generated by the increased element capacitance.

For this dissertation, the design process focused on two ISM bands due to their availability and popularity within the electromagnetic spectrum. These frequency bands are commonly used in low power electronic applications including Bluetooth technology, several 802.11 protocol, and cordless telephones because unlicensed use is permitted. The 2.45 GHz ISM band and the 5.8 GHz ISM band are chosen for the low and high frequency bands respectively. However, operation of this novel antenna element is not restricted to these frequency bands. The antenna element has shown to support a wide range of frequency ratios making it an ideal element for many applications ranging from wireless communications to multifunction radar arrays to space based synthetic aperture radar.

The majority of dual-band antenna elements in the literature have a frequency ratio ranging from just over unity to slightly over 4:1. For small frequency ratios, concentric radiators and multi-mode elements can be used. Concentric radiators prove difficult to use for small frequency ratios because of the comparable size of the radiators. In order to use concentric radiators, the center element has been printed on extremely high dielectric constant material. Concentric radiators become attractive for frequency ratios of moderate size. As the frequency ratio increases to close to 4:1 for applications such as synthetic aperture radar, perforated patches and interlaced radiators are often used. In perforated patches, the low band radiator contains apertures that allow radiation from several smaller high frequency elements printed on lower levels of a multilayer structure. In interlaced radiators, arrays of low band and high band radiators are printed on different layers of a sandwich structure. Both perforated and interlaced designs have the difficulty of arranging the elements to provide adequate array performance while providing elements that are not co-planar.

A parametric study of the element designed in this dissertation shows that it is capable of handling small, moderate, and large frequency ratios while maintaining concentric, co-planar radiators. For large frequency ratios, the outer side length of the element can become too large for array spacing, thus presenting an ideal application of the dual-substrate capacitive loading structure for size reduction of the low frequency element.

For applications requiring directional beams, antenna elements are typically arranged in an array environment. In these applications, the dual-polarized, dual-band antenna element in this dissertation provides the ability to support multiple functions. Multifunction antenna arrays are commonly used to support functions ranging from synthetic aperture radar, to electronic warfare, to target tracking, to communications. Analyzing the performance of large arrays of multifunction element can be a difficult task.

A common first at the array performance is obtained by using infinite array analysis to reveal the average active element performance. These simulations place a single element in boundary conditions mimicking an infinite extension of the element in both principle planes. The near-field influence of neighboring elements is included in these simulations. The pattern obtained through this technique can be multiplied by an array factor to result in an approximate array pattern. This technique provides a good approximation for a large array, but it fails for small arrays.

In small to moderate sized arrays, the elements in the array do not all experience identical surroundings. The previously described infinite array analysis fails to include these differences, and all elements are assumed to be identical. An exact array pattern can be obtained by calculating, simulating, or measuring the active element pattern for each element in the array. This technique includes the radiative mutual coupling effects from neighboring elements, and the active element pattern for each element is unique. This drawback of this technique stems from the uniqueness of the active element patterns.

A hybrid calculation technique using multiple active element patterns is developed and applied to investigate the performance of this element within an array. In this technique, a 3x3 array of elements is simulated to arrive at nine active element patterns. Each element in the array is assigned one of these nine active element patterns to serve as its active element pattern. The pattern is chosen based on the geometrical location and boundary conditions of the given element within the array. This approach presents a compromise between the time-efficient infinite array analysis and the exact result of the active element pattern approach.

The results of the array analysis indicate that the dual-band, dual-CP element provides an attractive option for applications requiring dual-band apertures requiring dual-frequency operation and main beam scanning. The dual-ISM band antenna array permits scanning up to 70° off of broadside at 2.44 GHz before the onset of grating lobes. At the high frequency, grating lobe-free scanning is achieved for angles up to 40° off of broadside. The cross-polarized discrimination (XPD) and axial ratio holds up extremely well for both polarizations and both frequency bands. At 2.44 GHz, the axial ratio remains below 2.0dB for scans less than 30°. The high frequency polarizations experience an axial ratio better than 2dB over the entire grating lobe-free scanning region. The low profile, low cost, and light weight nature of the element used in this array make it advantageous for use in large apertures.

Recent work by White and Rebeiz has shown the ability to dynamically tune the resonant frequency of a ring slot antennas by placing multiple varactor diodes across the slot [83]. Their work published in 2009 showed the ability to tune the resonant frequency over a 1.7:1 ratio by adjusting the capacitance of the varactor diode. This work was completed on single- and dual-linearly polarized antennas. The dual-band, dual-polarized element discussed in this dissertation can be extended to include dynamic tuning of the high frequency element by including the varactor diode design of White and Rebeiz into the high band square ring slot element. This provides a dual-band, dual-CP antenna element with even greater flexilibilty. The frequency ratio can be controlled by the methods shown in earlier Chapters, and this extension provides the ability to dynamically control the operational frequencies to provide the functionality required for applications such as cognitive radio where the operational frequency must be controllable.

This dissertation provides a comprehensive description of an element that serves as a unique contribution to the antenna engineering community. The work presented in this study details a dual-band dual-CP element operating at the previously mentioned two ISM bands. However, nothing about this element limits its use to these specific frequency bands. The element can be redesigned to operate over different frequency bands to meet specific application needs. The arrangement of the square ring slot and shorted square ring elements provides a novel architecture aimed at increasing frequency ratio flexibility and enhancing system performance. A novel capacitive loading structure providing significant size reduction in shorted ring elements was designed and verified through measurements. The size reduction the placement of this element in a phased array environment suitable for wide scanning applications. Subsequently,

this element is suitable for multifunction applications requiring a single element or an array environment.

REFERENCES

[1] P. K. Hughes and J. Y. Choe, "Overview of advanced multifunction RF system (AMRFS)," in *Phased Array Systems and Technology, 2000. Proceedings. 2000 IEEE International Conference on*, 2000, pp. 21-24.

[2] G. C. Tavik, C. L. Hilterbrick, J. B. Evins, J. J. Alter, J. G. Crnkovich, Jr., J. W. de Graaf, W. Habicht, II, G. P. Hrin, S. A. Lessin, D. C. Wu, and S. M. Hagewood, "The advanced multifunction RF concept," *Microwave Theory and Techniques, IEEE Transactions on,* vol. 53, pp. 1009-1020, 2005.

[3] R. M. Sorbello and A. I. Zaghloul, "Wideband, high-efficiency, circularly polarized slot elements," in *Antennas and Propagation Society International Symposium, 1989. AP-S. Digest*, 1989, pp. 1473-1476 vol.3.

[4] R. M. Sorbello and A. I. Zaghloul, "Orhotgonally Polarized Dual-Band Printed Circuit Antenna Employing Radiating Element Capacitively Coupled to Feedlines," U. S. P. Office, Ed.: Comast, 1996.

[5] C. B. Ravipati and A. I. Zaghloul, "A hybrid antenna element for dual-band applications," in *Antennas and Propagation Society International Symposium, 2004. IEEE*, 2004, pp. 4020-4023 Vol.4.

[6] A. I. Zaghloul and W. M. Dorsey, "Dual-Band Reduced-Size Circularly Polarized Co-Planer Printed-Circuit Antenna Element," in *International Union of Radio Science (URSI) Electromagnetic Theory Symposium (EMTS)* Ottawa, ON, Canada, 2007.

[7] W. M. Dorsey, J. A. Valenzi, and A. I. Zaghloul, "Dual-Substrate Capacitive Loading Technique in Linearly and Circularly Polarized Annular Ring Antennas," Monticello, IL, 2007.

[8] W. M. Dorsey and A. I. Zaghloul, "Size reduction and bandwidth enhancement of shorted annular ring (SAR) antenna," in *Antennas and Propagation International Symposium, 2007 IEEE*, 2007, pp. 897-900.

[9] W. M. Dorsey and A. I. Zaghloul, "Dual-Band Array Calculations Using Hybrid Calculation Technique," U.S Naval Research Laboratory, Washington, DC 2009.

[10] R. F. Harrington, *Time-Harmonic Electromagnetic Fields*. New York: John Wiley & Sons, Inc., 2001.

[11] D. Sterc and Z. Sipus, "A Dirac-like inference of Maxwell's equations," in *Antennas and Propagation Society International Symposium, 2001. IEEE*, 2001, pp. 400-403 vol.1.

[12] W. L. Stutzman, *Polarization in Electromagnetic Systems*. Norwood, MA: Artech House, 1993.

[13] V. Ivaska and R. Aleksiejunas, "Polarisation of electromagnetic waves in four-dimensional Euclidean space," in *Microwaves, Radar and Wireless Communications. 2000. MIKON-2000. 13th International Conference on*, 2000, pp. 91-93 vol.1.

[14] A. Vallecchi, G. B. Gentili, and M. Calamia, "Dual-band dual polarization microstrip antenna," in *Antennas and Propagation Society International Symposium, 2003. IEEE*, 2003, pp. 134-137 vol.4.

[15] Z. N. Chen, "Broadband Planar Antennas for High-Speed Wireless Communications," in *Antenna Engineering Handbook (4th Edition)*, 4th ed, J. L. Volakis, Ed. New York: McGraw Hill, 2007.

[16] B. S. Collins, "VHF and UHF Antennas for Communications and Broadcasting," in *Antenna Engineering Handbook (4th Edition)*, 4th ed, J. L. Volakis, Ed. New York: McGraw Hill, 2007.

[17] T. H. Lee, *Planar Microwave Engineering: A Practical Guide to Theory, Measurements and Circuits*. Cambrige: Cambridge University Press, 2004.

[18] L. Shafai, W. Chamma, G. Seguin, and N. A. S. N. Sultan, "Dual-band dual-polarized microstrip antennas for SAR applications," in *Antennas and Propagation Society International Symposium, 1997. IEEE., 1997 Digest*, 1997, pp. 1866-1869 vol.3.

[19] C. Mangenot and J. Lorenzo, "Dual band dual polarized radiating subarray for synthetic aperture radar," in *Antennas and Propagation Society International Symposium, 1999. IEEE*, 1999, pp. 1640-1643 vol.3.

[20] J. Granholm and N. Skou, "Dual-frequency, dual-polarization microstrip antenna development for high-resolution, airborne SAR," in *Microwave Conference, 2000 Asia-Pacific*, 2000, pp. 17-20.

[21] J. C. Eade and J. Whitehurst, "Dual band phased array antenna design for radar applications," in *Antennas and Propagation, 2001. Eleventh International Conference on (IEE Conf. Publ. No. 480)*, 2001, pp. 77-81 vol.1.

[22] B. Lindmark, "A dual polarized dual band microstrip antenna for wireless communications," in *Aerospace Conference, 1998. Proceedings., IEEE*, 1998, pp. 333-338 vol.3.

[23] K. S. Bialkowski and S. Zagriatski, "Investigations into a dual band 2.4/5.2 GHz antenna for WLAN applications," in *Microwaves, Radar and Wireless Communications, 2004. MIKON-2004. 15th International Conference on*, 2004, pp. 660-663 Vol.2.

[24] L. Duxian and B. Gaucher, "A new multiband antenna for WLAN/cellular applications," in *Vehicular Technology Conference, 2004. VTC2004-Fall. 2004 IEEE 60th*, 2004, pp. 243-246 Vol. 1.

[25] M. Bodley, M. Sarcione, F. Beltran, and M. Russell, "Dual band cellular antenna," in *Wireless Applications Digest, 1997., IEEE MTT-S Symposium on Technologies for*, 1997, pp. 93-98.

[26] S. H. Hsu and C. Kai, "A Novel Reconfigurable Microstrip Antenna With Switchable Circular Polarization," *Antennas and Wireless Propagation Letters, IEEE,* vol. 6, pp. 160-162, 2007.

[27] F. Shyh-Tirng, "A novel polarization diversity antenna for WLAN applications," in *Antennas and Propagation Society International Symposium, 2000. IEEE*, 2000, pp. 282-285 vol.1.

[28] Y. J. Sung, T. U. Jang, and Y. S. Kim, "A reconfigurable microstrip antenna for switchable polarization," *Microwave and Wireless Components Letters, IEEE,* vol. 14, pp. 534-536, 2004.

[29] R. L. Jefferson and D. Smith, "Dual circular polarised microstrip antenna design for a passive microwave transponder," in *Antennas and Propagation, 1991. ICAP 91., Seventh International Conference on (IEE)*, 1991, pp. 141-143 vol.1.

[30] A. K. Sharma and A. Mittal, "Diagonal slotted diamond shaped dual circularly polarized microstrip patch antenna with dumbbell aperture coupling," in *Wireless Technology, 2005. The European Conference on*, 2005, pp. 463-465.

[31] A. K. Sharma and A. Mittal, "Diagonal slotted diamond shaped dual circularly polarized microstrip patch antenna with dumbbell aperture coupling," in *Microwave Conference, 2005 European*, 2005, p. 3 pp.

[32] E. Aloni and R. Kastner, "Analysis of a dual circularly polarized microstrip antenna fed by crossed slots," *Antennas and Propagation, IEEE Transactions on,* vol. 42, pp. 1053-1058, 1994.

[33] A. E. Daniel, "Array of dual band RMSAs with bend stub along the radiating edge," in *Antennas and Propagation Society International Symposium, 2003. IEEE*, 2003, pp. 560-563 vol.4.

[34] C. H. Cai, J. S. Row, and K. L. Wong, "Dual-frequency microstrip antenna with dual circular polarisation," *Electronics Letters,* vol. 42, pp. 1261-1262, 2006.

[35] J. Joo-Seong and P. Sang-Hoon, "Wideband antenna for PCS and IMT-2000 service band," in *Vehicular Technology Conference, 2004. VTC2004-Fall. 2004 IEEE 60th*, 2004, pp. 216-219 Vol. 1.

[36] D. L. Helms, J. R. Sherman, and B. B. Pruett, "Integrated Stacked Patch Antenna Polarizer Circularly Polarized Integrated Stacked Dual-Band Patch Antenna," U. S. P. Office, Ed., 1998.

[37] K. M. Lee, A. T. S. Wang, and L. Chau, "Low-profile, Integrated Radiator Tiles for Wideband, Dual-Linear and Circular-Polarized Phased Array Applications," U. S. P. Office, Ed.: Raytheon Company, 2000.

[38] A. Cha and A. Bhattacharyya, "Dual Hybrid-Fed Patch Element for Dual Band Circular Polarization Radiation," U. S. P. Office, Ed.: The Boeing Company, 2002.

[39] W. L. Stutzman and G. A. Thiele, *Antenna Theory and Design* vol. 2. New York: John Wiley & Sons., Inc., 1998.

[40] T. F. Eibert and J. L. Volakis, "Fundamentals of Antennas, Arrays, and Mobile Communications," in *Antenna Engineering Handbook (4th Edition)*, 4th ed, J. L. Volakis, Ed. New York: McGraw Hill, 2007.

[41] L. C. Kempel, "Computational Electromagnetics for Antennas," in *Antenna Engineering Handbook (4th Edition)*, 4th ed, J. L. Volakis, Ed. New York: McGraw Hill, 2007.

[42] "CST Microwave Studio," 2006B ed.

[43] I. Munteanu and F. Hirtenfelder, "Convergence of the Finite Integration Technique on Various Mesh Types," in *German Microwave Conference (GeMiC)*, 2005, pp. 209-212.

[44] A. F. Peterson, S. L. Ray, and R. Mittra, *Computational Methods for Electromagnetics*: IEEE Press, 1998.

[45] I. Munteanu, "RF & Microwave Simulations with Finite Integration Technique - From Component to System," in *Scientific Computing in Electrical Engineering Conference (SCEE)*, 2006.

[46] E. Lerox and L. Sassi, "Finite Integration Technique Applied to a Component Widely Used in Microwave Heating," in *MISA*, 2004.

[47] J. S. Row, "The design of a squarer-ring slot antenna for circular polarization," *Antennas and Propagation, IEEE Transactions on,* vol. 53, pp. 1967-1972, 2005.

[48] K. Chang and L. H. Hsieh, *Microwave Ring Circuits and Related Structures*, 2 ed. Hoboken: John Wiley & Sons, Inc., 2004.

[49] W. Kin-Lu, H. Chien-Chin, and C. Wen-Shan, "Printed ring slot antenna for circular polarization," *Antennas and Propagation, IEEE Transactions on,* vol. 50, pp. 75-77, 2002.

[50] R. Janaswamy and D. H. Schaubert, "Characteristic Impedance of a Wide Slotline on Low-Permittivity Substrates (Short Paper)," *Microwave Theory and Techniques, IEEE Transactions on,* vol. 34, pp. 900-902, 1986.

[51] C. Chen and N. G. Alexopoulos, "Triplate-fed arbitrarily-shaped annular ring slot antennas," in *Antennas and Propagation Society International Symposium, 1995. AP-S. Digest*, 1995, pp. 2070-2073 vol.4.

[52] K. Itoh and M. Yamamoto, "A slot-coupled microstrip array antenna with a triplate line feed where parallel-plate mode is suppressed efficiently," in *Antennas and Propagation Society International Symposium, 1997. IEEE., 1997 Digest*, 1997, pp. 2135-2138 vol.4.

[53] A. Bhattacharyya, O. Fordham, and L. Yaozhong, "Analysis of stripline-fed slot-coupled patch antennas with vias for parallel-plate mode suppression," *Antennas and Propagation, IEEE Transactions on,* vol. 46, pp. 538-545, 1998.

[54] T. Yuasa, T. Nishino, and H. Oh-Hashi, "Simple design formula for parallel plate mode suppression by ground via-holes," in *Microwave Symposium Digest, 2004 IEEE MTT-S International*, 2004, pp. 641-644 Vol.2.

[55] P. Sharma and K. Gupta, "Optimized design of single feed circularly polarized microstrip patch antennas," in *Antennas and Propagation Society International Symposium, 1982*, 1982, pp. 156-159.

[56] P. Sharma and K. Gupta, "Analysis and optimized design of single feed circularly polarized microstrip antennas," *Antennas and Propagation, IEEE Transactions on [legacy, pre - 1988],* vol. 31, pp. 949-955, 1983.

[57] M. Niroojazi and M. N. Azarmanesh, "Practical design of single feed truncated corner microstrip antenna," in *Communication Networks and Services Research, 2004. Proceedings. Second Annual Conference on*, 2004, pp. 25-29.

[58] C. We-Shyang, W. Chun-Kun, and W. Kin-Lu, "Single-feed square-ring microstrip antenna with truncated corners for compact circular polarisation operation," *Electronics Letters,* vol. 34, pp. 1045-1047, 1998.

[59] C. Rui-Hung and J. S. Row, "Single-Fed Microstrip Patch Antenna With Switchable Polarization," *Antennas and Propagation, IEEE Transactions on,* vol. 56, pp. 922-926, 2008.

[60] Y. Fan and Y. Rahmat-Samii, "A reconfigurable patch antenna using switchable slots for circular polarization diversity," *Microwave and Wireless Components Letters, IEEE,* vol. 12, pp. 96-98, 2002.

[61] M. K. Fries, M. Grani, and R. Vahldieck, "A reconfigurable slot antenna with switchable polarization," *Microwave and Wireless Components Letters, IEEE,* vol. 13, pp. 490-492, 2003.

[62] T. Hiraguri, Y. Ojiro, K. Hirasawa, and K. Shouno, "Polarisation control of a loop antenna by PIN diodes," *Microwaves, Antennas & Propagation, IET,* vol. 1, pp. 592-596, 2007.

[63] J. Shuhua, D. R. Jackson, S. A. Long, J. T. A. W. J. T. Williams, and V. B. A. D. V. B. Davis, "Characteristics of the shorted annular-ring patch antenna," in *Antennas and Propagation Society International Symposium, 1994. AP-S. Digest*, 1994, pp. 464-467 vol.1.

[64] W. N. Everitt and H. Kalf, "The Bessel differential equation and the Hankel transform," *Journal of Computational and Applied Mathematics,* vol. 208, pp. 3-19, November 2007 2007.

[65] V. Gonzalez-Posadas, D. Segovia-Vargas, E. Rajo-Iglesias, J. L. A. V.-R. J. L. Vazquez-Roy, and C. A. M.-P. C. Martin-Pascual, "Approximate analysis of short circuited ring patch antenna working at TM/sub 01/ mode," *Antennas and Propagation, IEEE Transactions on,* vol. 54, pp. 1875-1879, 2006.

[66] G. Jaworski, M. Hornik, P. Gorski, T. Maleszka, D. Wydymus, and P. Kabacik, "Highly Integrated Ligthweight Dual Band Antenna with Dual or Quadruple Polarization Agility," in *Wireless Technologies, 2007 European Conference on*, 2007, pp. 114-117.

[67] G. J. K. Moernaut and G. A. E. Vandenbosch, "Simple pen and paper design of shorted annular ring antenna," *Electronics Letters,* vol. 39, pp. 1784-1785, 2003.

[68] H. K. Kan, R. B. Waterhouse, and D. Pavlickovski, "Compact dual concentric ring printed antennas," *Microwaves, Antennas and Propagation, IEE Proceedings -,* vol. 151, pp. 37-42, 2004.

[69] R. R. Ramirez, L. Jofre, and F. De Flaviis, "Reduced size single and dual-band diversity antennas for portable devices," in *Microwave Conference, 2001. APMC 2001. 2001 Asia-Pacific*, 2001, pp. 1155-1158 vol.3.

[70] P. Ciais, R. Staraj, G. Kossiavas, and C. A. L. C. Luxey, "Compact internal multiband antenna for mobile phone and WLAN standards," *Electronics Letters,* vol. 40, pp. 920-921, 2004.

[71] S. C. K. Ko and R. D. Murch, "Compact integrated diversity antenna for wireless communications," *Antennas and Propagation, IEEE Transactions on,* vol. 49, pp. 954-960, 2001.

[72] C. R. Rowell and R. D. Murch, "A capacitively loaded PIFA for compact mobile telephone handsets," *Antennas and Propagation, IEEE Transactions on,* vol. 45, pp. 837-842, 1997.

[73] Y. Fan, K. Chul-Sik, and Y. Rahmat-Samii, "Step-like structure and EBG structure to improve the performance of patch antennas on high dielectric substrate," in *Antennas and Propagation Society International Symposium, 2001. IEEE*, 2001, pp. 482-485 vol.2.

[74] E. Kulhman, "Investigation of high temperature antenna designs for space shuttle," in *Antennas and Propagation Society International Symposium, 1974*, 1974, pp. 210-213.

[75] R. P. Owens and A. C. Smith, "Low-profile dual band, dual polarised array antenna module," *Electronics Letters,* vol. 26, pp. 1433-1434, 1990.

[76] P. C. Strickland, "Polarimetric Dual Band Radiating Element for Synthetic Aperture Radar," U. S. P. Office, Ed. United States: EMS Technologies, 1999.

[77] L. Shun-Yun and H. Kuang-Chih, "A compact microstrip antenna for GPS and DCS application," *Antennas and Propagation, IEEE Transactions on,* vol. 53, pp. 1227-1229, 2005.

[78] H. Young-Pyo, K. Jung-Min, J. Soon-Chul, K. Dong-Hyun, C. Mun-Ho, L. Yongshik, and Y. Jong-Gwan, "S-band dual-path dual-polarized antenna system for satellite digital audio radio service (SDARS) application," *Microwave Theory and Techniques, IEEE Transactions on,* vol. 54, pp. 1569-1575, 2006.

[79] D. F. Kelley and W. L. Stutzman, "Array antenna pattern modeling methods that include mutual coupling effects," *Antennas and Propagation, IEEE Transactions on,* vol. 41, pp. 1625-1632, 1993.

[80] D. M. Pozar, "The active element pattern," *Antennas and Propagation, IEEE Transactions on,* vol. 42, pp. 1176-1178, 1994.

[81] D. M. Pozar, "A relation between the active input impedance and the active element pattern of a phased array," *Antennas and Propagation, IEEE Transactions on,* vol. 51, pp. 2486-2489, 2003.

[82] D. F. Kelley, "Relationships between active element patterns and mutual impedance matrices in phased array antennas," in *Antennas and Propagation Society International Symposium, 2002. IEEE*, 2002, pp. 524-527 vol.1.

[83] C. R. White and G. M. Rebeiz, "Single- and Dual-Polarized Tunable Slot-Ring Antennas," *Antennas and Propagation, IEEE Transactions on,* vol. 57, pp. 19-26, 2009.

APPENDICES

APPENDIX A: Assembly Procedure for Multilayer, Printed Circuit, Dual-Band Dual-CP Antenna Element

This appendix describes the proposed assembly procedure for a dual-band dual-CP antenna element. This circuit board is a multilayer design. The substrate materials, conductor layers, dielectric layer outlines, and via locations are all described in this appendix.

Substrate Materials

- Layer D1 – Rogers RT/Duroid 5870: h = 0.060", $\varepsilon_r = 2.33$
- Layer D2 – Rogers RT/Duroid 5870: h = 0.004", $\varepsilon_r = 2.33$
- Layer D3 – Rogers RT/Duroid 5870: h = 0.060", $\varepsilon_r = 2.33$
- Layer D4 – Rogers RT/Duroid 5870: h = 0.030", $\varepsilon_r = 2.33$
- 0.5 oz. Copper for all conducting layers
- Dielectric adhesive: dielectric constant as close to 2.33 as possible; adhesive layers should have minimal thickness

Assembly Steps

1. Start with dielectric layer *D4*. The outline is described by D4.gbr. The top side of the substrate is bare dielectric, and the conductor on the bottom side of the material is defined by C5.gbr.

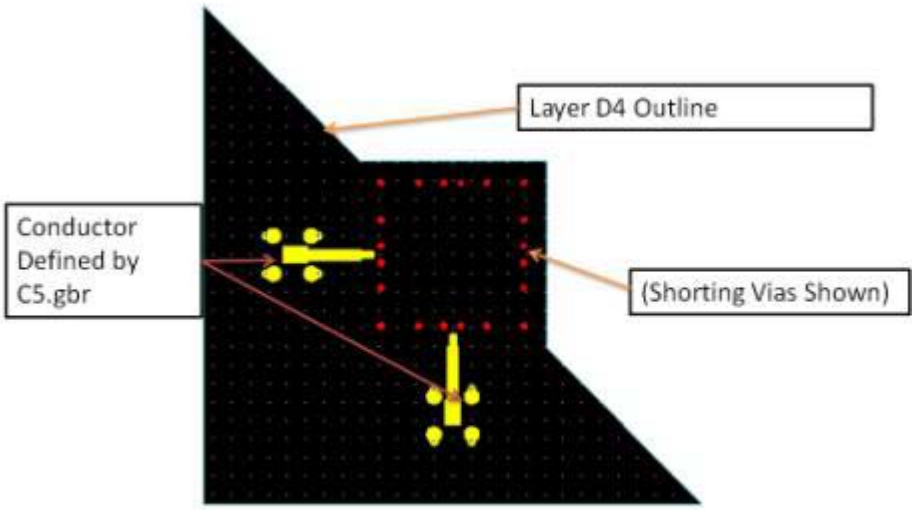

2. The outline for layer *D3* is defined by D3.gbr. The bottom-side conductor of this board is defined by C4.gbr, and the top-side conductor is defined by C3.gbr.

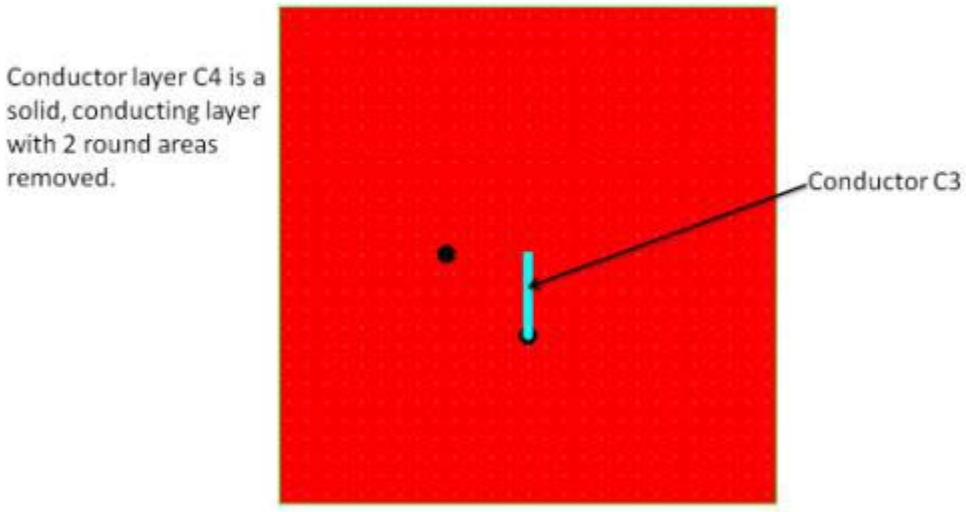

3. Layer *D3* is bonded on top of layer *D4*.

4. Drill and plate the hole defined by Feedvia_1.gbr. This plated through hole provides electrical continuity between *C5* and *C3*.

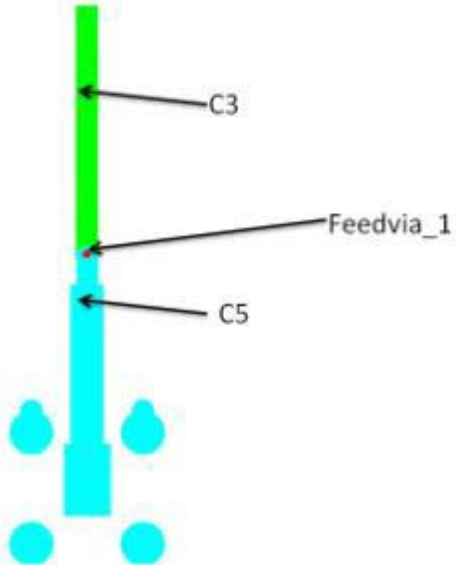

5. Drill and plate holes defined by Gndvia.gbr. These plated through holes provide continuity from layer *C5* to *C4*. These holes may need to be drilled and plated all the way through layer *D3*, and then back drilled (if necessary).

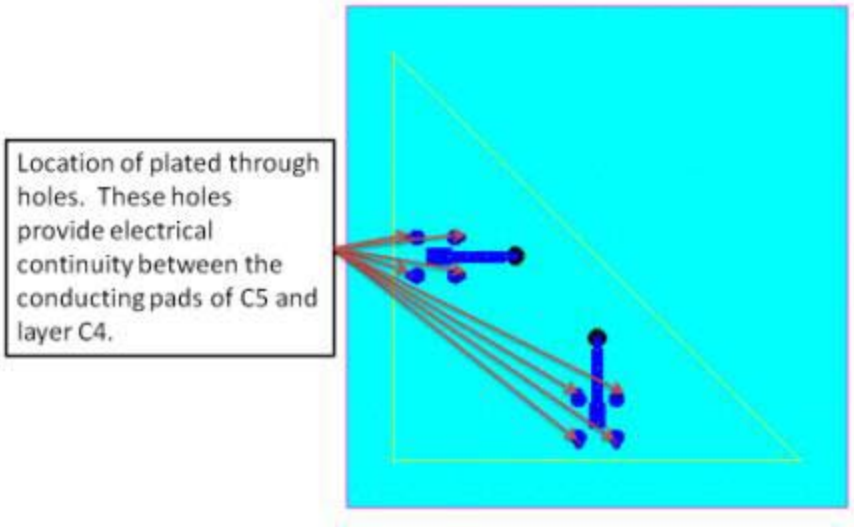

6. Layer *D2* is outlined in D2.gbr. The top-side of this substrate has a conductor defined by C2.gbr, and the bottom-side of this substrate is bare dielectric.

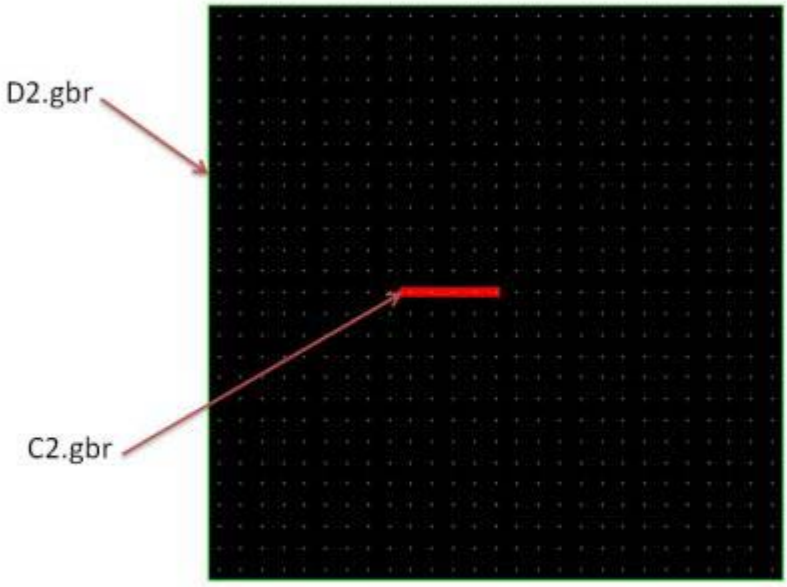

7. Layer *D2* is bonded on top of the previously bonded *D3-D4*.
8. Drill and plate the hole defined by Feedvia_2.gbr. This plated through hole provides electrical continuity between *C5* and *C2*.

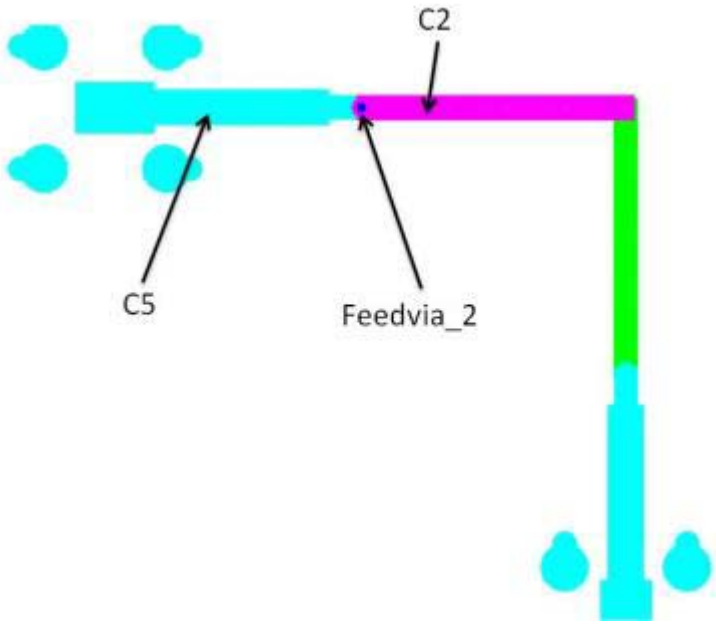

9. Layer *D1* is outlined in D1.gbr. The top-side of this substrate has a conductor defined by C1.gbr, and the bottom-side of this substrate is bare dielectric.

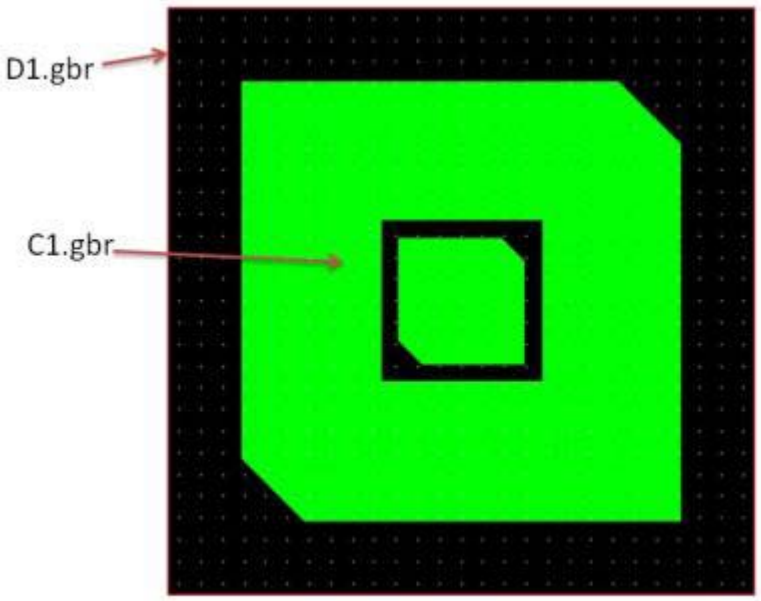

10. Layer *D1* is bonded on top of the previously bonded *D2-D3-D4*.
11. Drill and plate the holes defined by SHORTINGVIAS.gbr. These holes provide electrical continuity between *C1* and C*4*. These holes may need to be drilled all the way through the finished design, plated, and then back drilled to the appropriate depth.

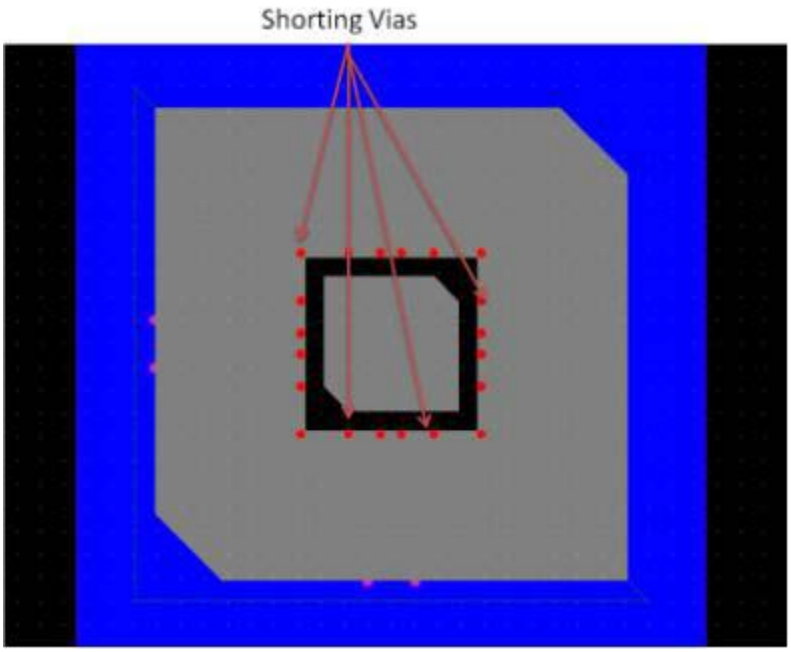

Additional Views

- Dielectric Profile

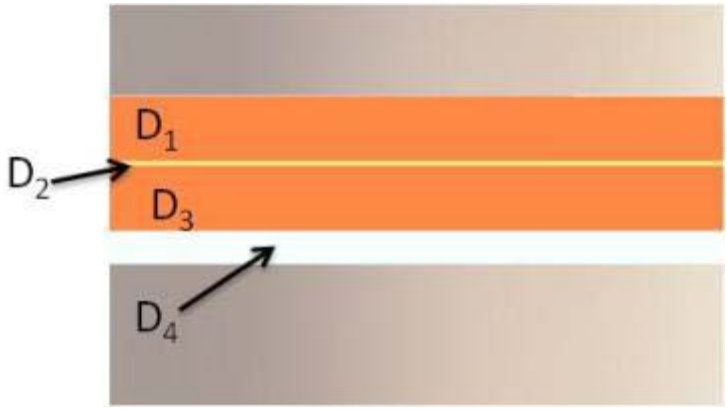

- Conductor Layers: Dielectric layers hidden; section view

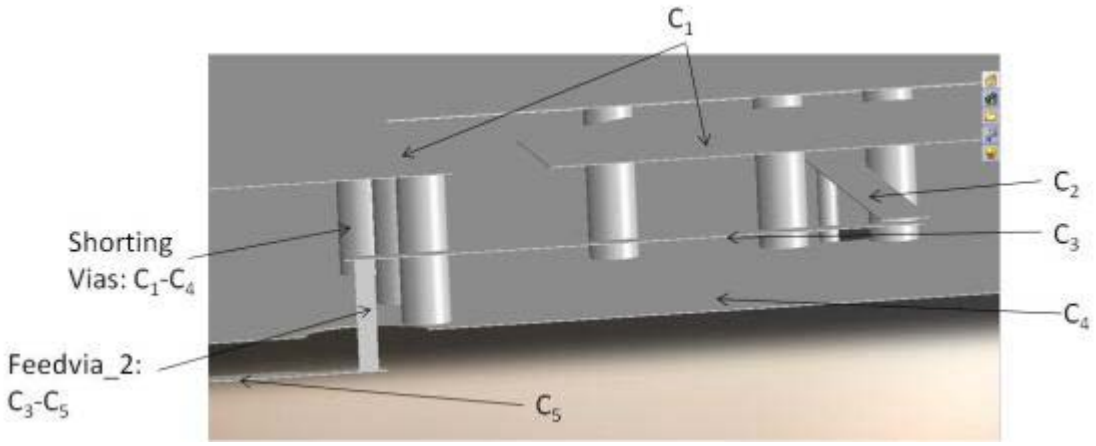

- Isometric View (From Top)

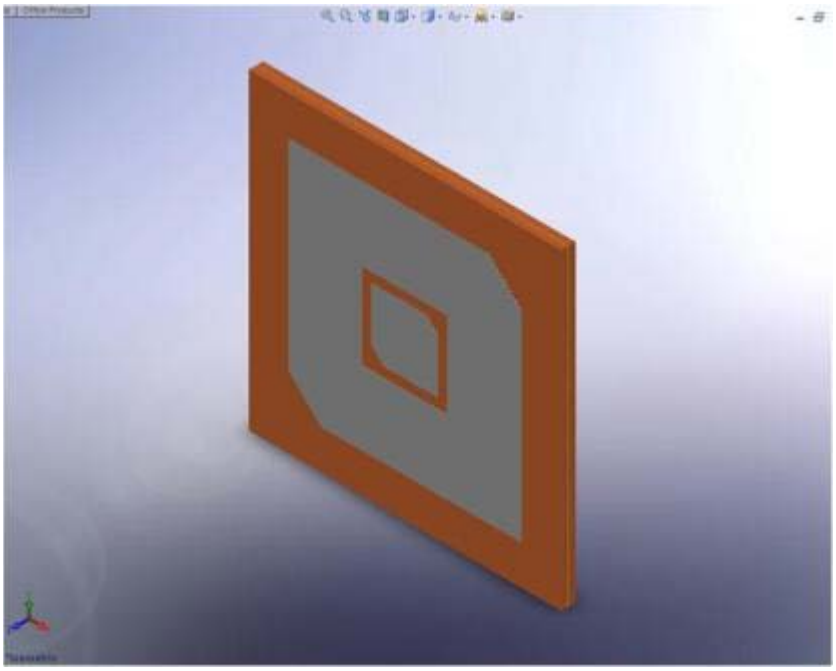

APPENDIX B: Dual-Band Dual-CP Antenna Array Patterns

The patterns for dual-band dual-CP antenna arrays of various sizes were calculated for the work in this dissertation. A selected subsection of the patterns are provided in Chapter 4. For completion, the remainder of the principle plane patterns is provided in this Appendix.

12x12 Array

Low Band LHCP φ=0°

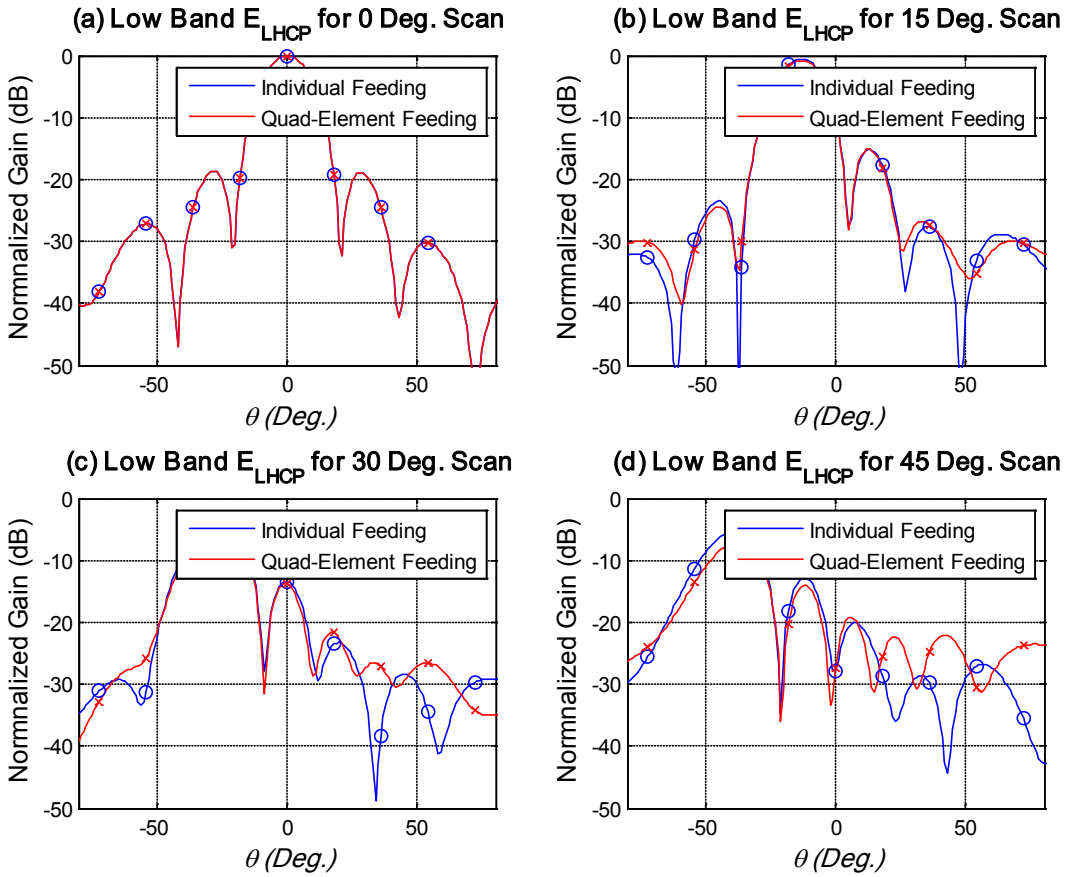

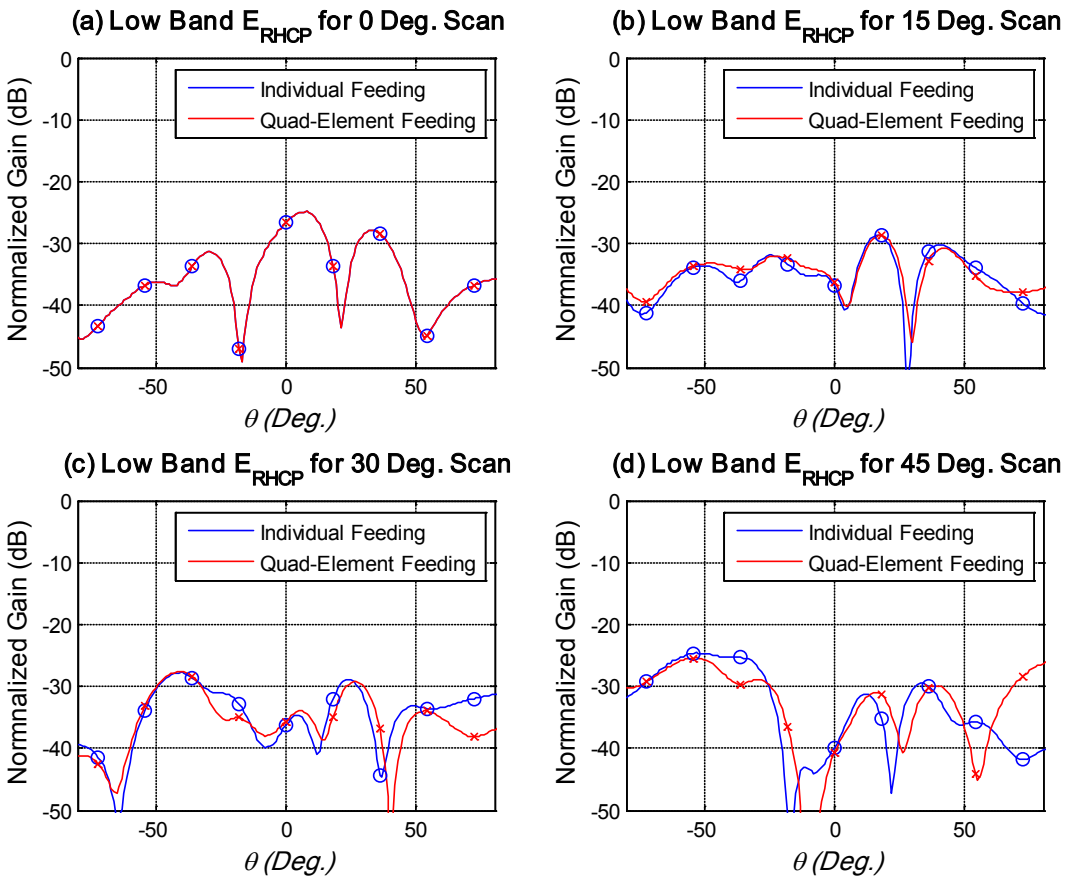
(a) Low Band E RHCP for 0 Deg. Scan
(b) Low Band E RHCP for 15 Deg. Scan
(c) Low Band E RHCP for 30 Deg. Scan
(d) Low Band E RHCP for 45 Deg. Scan
Individual Feeding
Quad-Element Feeding
Normalized Gain (dB)
θ (Deg.)
0
-10
-20
-30
-40
-50
-50
0
50

		θ_0=0°	θ_0=15°	θ_0=30°	θ_0=45°
3dB Beamwidth (BW_{3dB})	Ind. Feed	17°	16°	18°	19°
	Quad. Feed	17°	17°	18°	19°
	Approx.*	16.4466°	17.0267°	18.9908°	N/A
θ_{MAX}	Ind. Feed	0°	-13°	-26°	-38°
	Quad. Feed	0°	-13°	-26°	-37°
Normalized Maximum Value ($F(\theta_{MAX})_{MAX}$)	Ind. Feed	0dB	-0.5795dB	-2.4495dB	-5.1716dB
	Quad. Feed	0dB	-0.8194dB	-3.3285dB	-6.9175dB
Cross-pol. discrimination (XPD)	Ind. Feed	26.5931dB	34.3800dB	28.5282dB	20.1628dB
	Quad. Feed	26.5931dB	32.7412dB	31.1331dB	22.7729dB

Low Band LHCP φ=90°

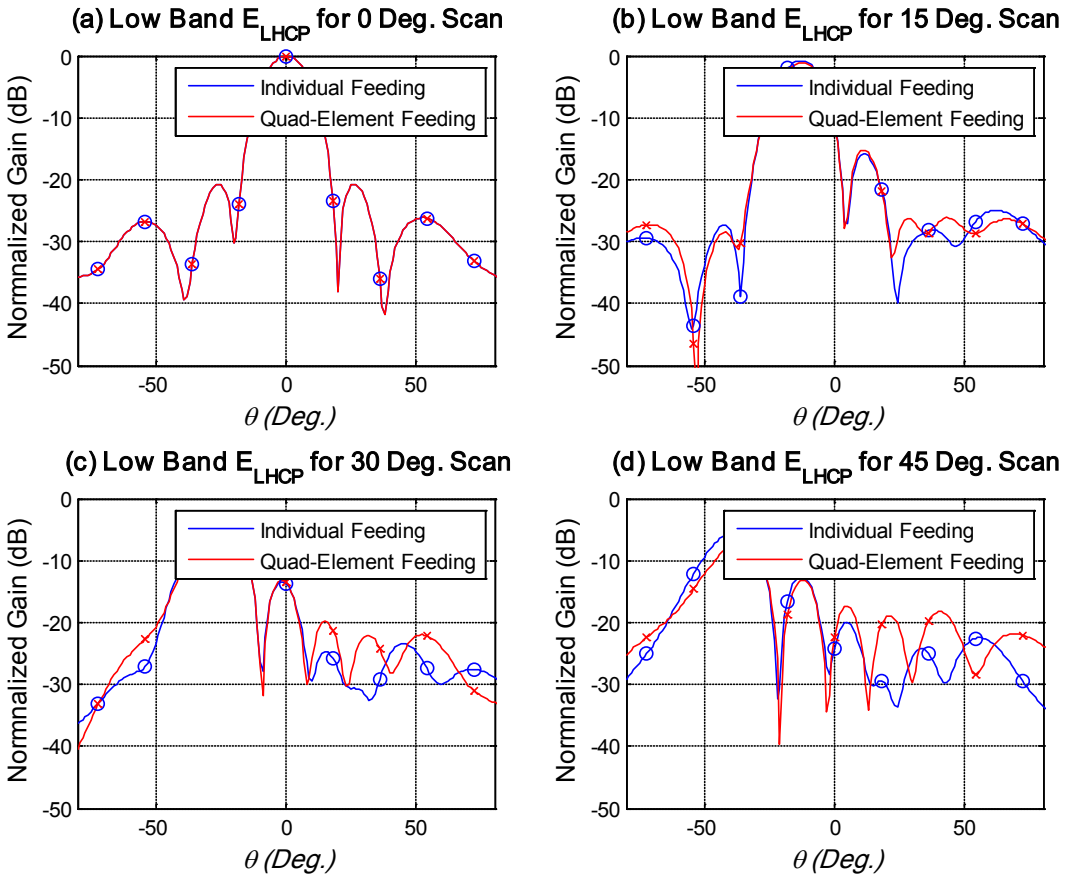

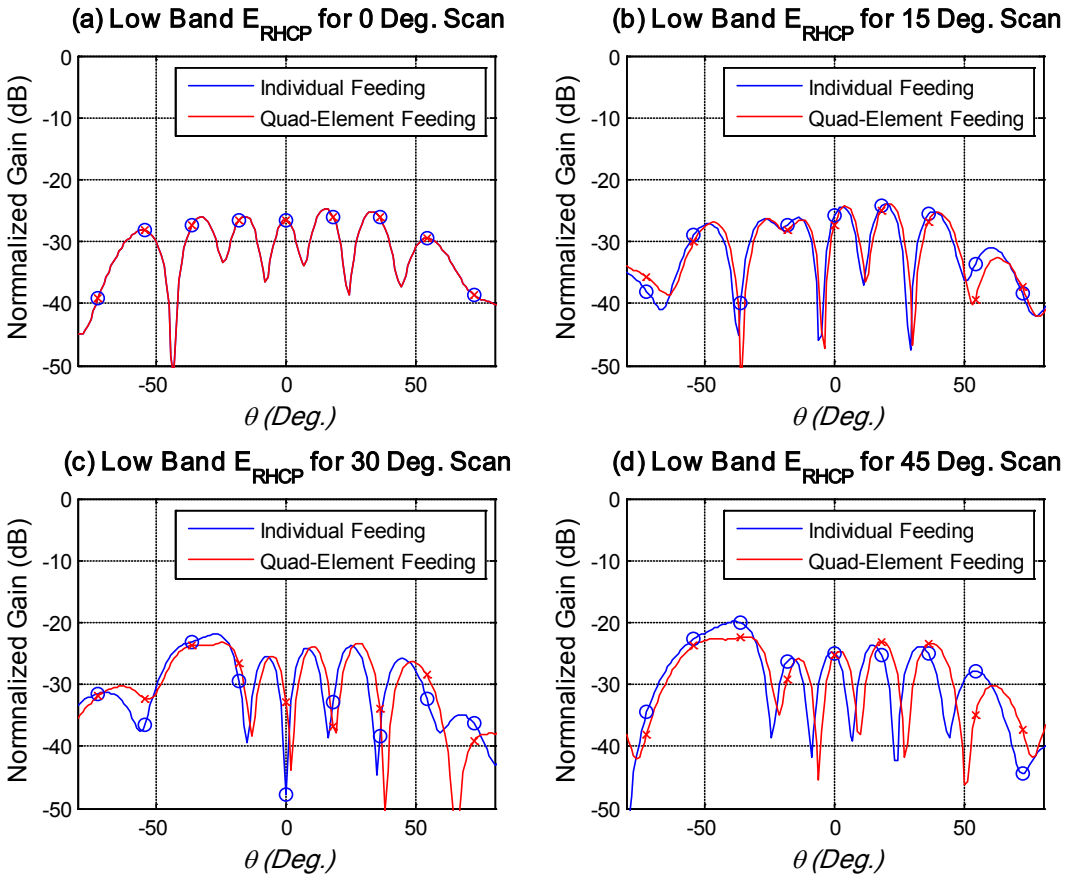
(a) Low Band E RHCP for 0 Deg. Scan
(b) Low Band E RHCP for 15 Deg. Scan
(c) Low Band E RHCP for 30 Deg. Scan
(d) Low Band E RHCP for 45 Deg. Scan
Individual Feeding
Quad-Element Feeding
Normalized Gain (dB)
θ (Deg.)
0
-10
-20
-30
-40
-50
-50
0
50

		θ_0=0°	θ_0=15°	θ_0=30°	θ_0=45°
3dB Beamwidth (BW_{3dB})	Ind. Feed	15°	16°	17°	18°
	Quad. Feed	15°	15°	16°	18°
	Approx.*	16.4466°	17.0267°	18.9908°	N/A
θ_{MAX}	Ind. Feed	0°	-13°	-26°	-38°
	Quad. Feed	0°	-13°	-25°	-36°
Normalized Maximum Value ($F(\theta_{MAX})_{MAX}$)	Ind. Feed	0dB	-0.8335dB	-2.7162dB	-5.1790dB
	Quad. Feed	0dB	-1.0808dB	-3.6338dB	-7.0490dB
Cross-pol. discrimination (XPD)	Ind. Feed	26.5931dB	25.4063dB	19.1792dB	14.6330dB
	Quad. Feed	26.5931dB	25.4328dB	19.6560dB	15.2886dB

Low Band RHCP φ=0°

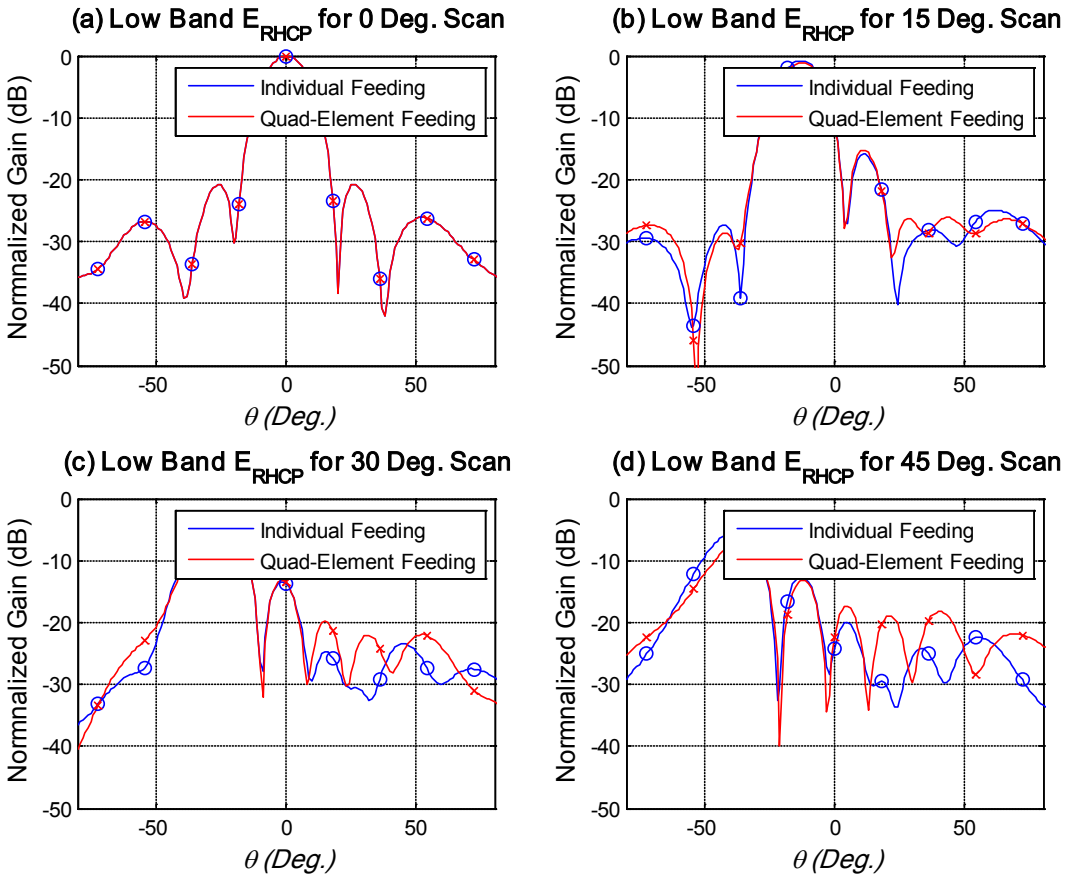

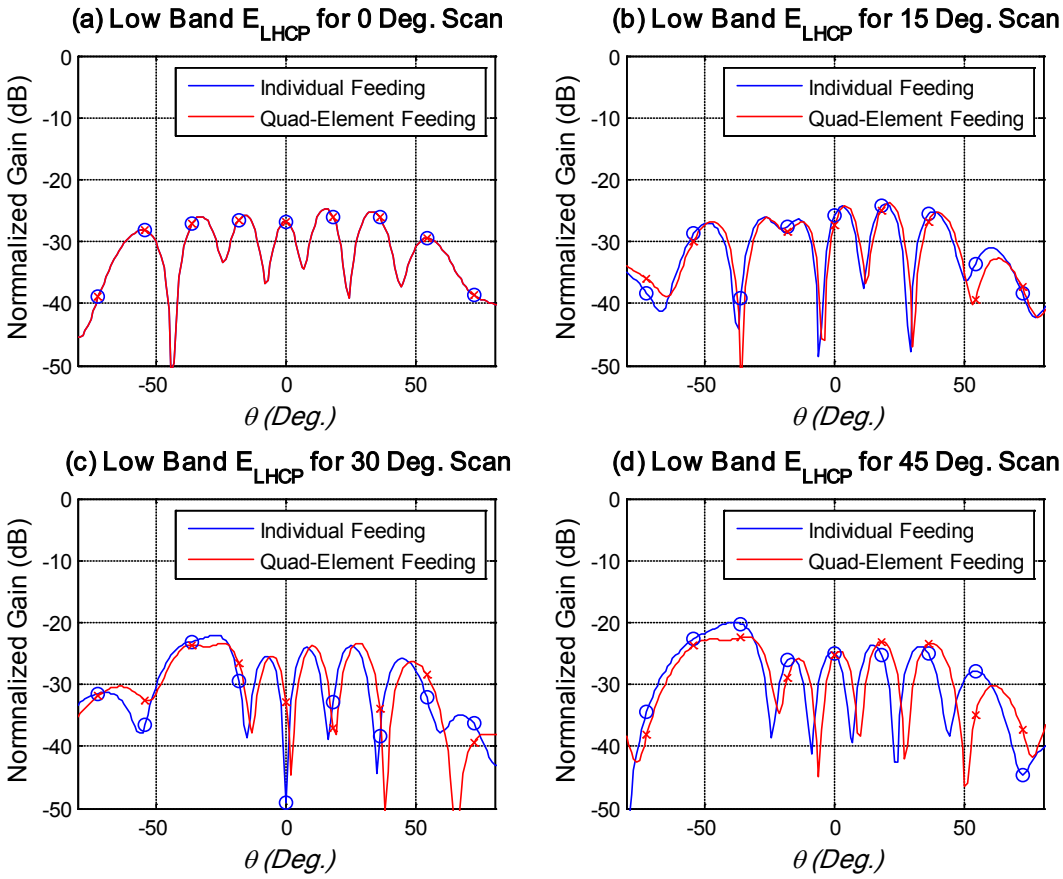
(a) Low Band E_LHCP for 0 Deg. Scan
(b) Low Band E_LHCP for 15 Deg. Scan
(c) Low Band E_LHCP for 30 Deg. Scan
(d) Low Band E_LHCP for 45 Deg. Scan
Individual Feeding
Quad-Element Feeding
Normalized Gain (dB)
θ (Deg.)
0
-10
-20
-30
-40
-50
-50
0
50

		θ_0=0°	θ_0=15°	θ_0=30°	θ_0=45°
3dB Beamwidth (BW_{3dB})	Ind. Feed	15°	16°	17°	18°
	Quad. Feed	15°	15°	16°	18°
	Approx.*	16.4466°	17.0267°	18.9908°	N/A
θ_{MAX}	Ind. Feed	0°	-13°	-26°	-37°
	Quad. Feed	0°	-13°	-25°	-36°
Normalized Maximum Value ($F(\theta_{MAX})_{MAX}$)	Ind. Feed	0dB	-0.8372dB	-2.7278dB	-5.1746dB
	Quad. Feed	0dB	-1.0845dB	-3.6391dB	-7.0435dB
Cross-pol. discrimination (XPD)	Ind. Feed	26.7334dB	25.6602dB	19.3721dB	14.8274dB
	Quad. Feed	26.7344dB	25.6996dB	19.8120dB	15.4344dB

Low Band RHCP φ=90°

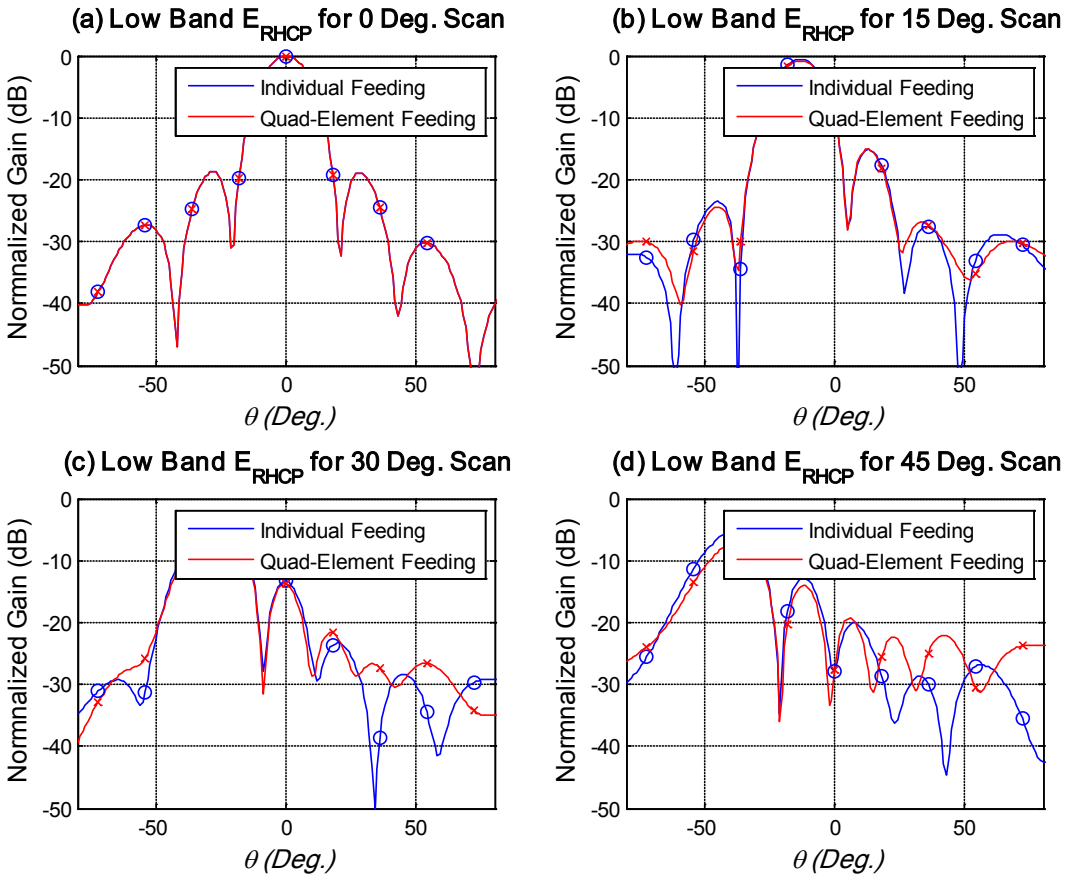

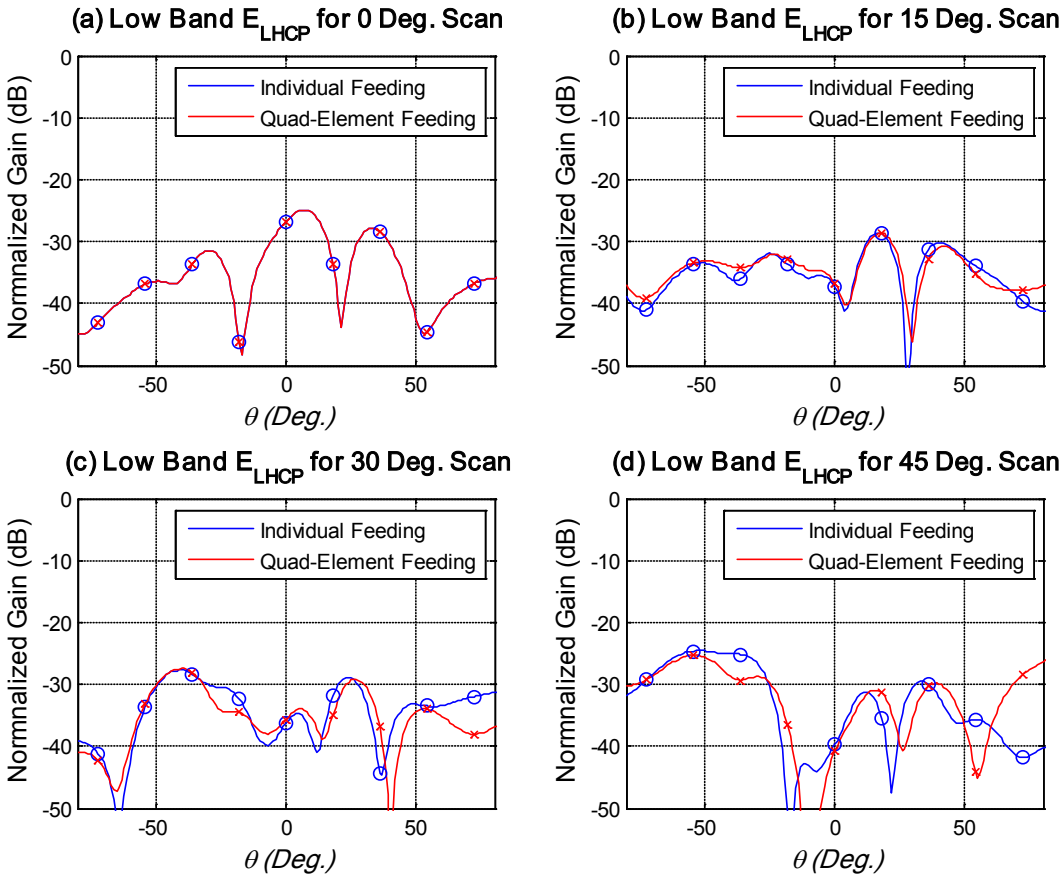
(a) Low Band E_LHCP for 0 Deg. Scan
(b) Low Band E_LHCP for 15 Deg. Scan
(c) Low Band E_LHCP for 30 Deg. Scan
(d) Low Band E_LHCP for 45 Deg. Scan
Individual Feeding
Quad-Element Feeding
Normalized Gain (dB)
θ (Deg.)
0
-10
-20
-30
-40
-50
-50
0
50

		θ_0=0°	θ_0=15°	θ_0=30°	θ_0=45°
3dB Beamwidth (BW_{3dB})	Ind. Feed	17°	16°	18°	19°
	Quad. Feed	17°	17°	18°	19°
	Approx.*	16.4466°	17.0267°	18.9908°	N/A
θ_{MAX}	Ind. Feed	0°	-13°	-26°	-38°
	Quad. Feed	0°	-13°	-25°	-37°
Normalized Maximum Value ($F(\theta_{MAX})_{MAX}$)	Ind. Feed	0dB	-0.5840dB	-2.4677dB	-5.177dB
	Quad. Feed	0dB	-0.8245dB	-3.3461dB	-6.9245dB
Cross-pol. discrimination (XPD)	Ind. Feed	26.7334dB	34.7037dB	27.9628dB	19.9099dB
	Quad. Feed	26.7344dB	33.0733dB	30.6980dB	22.3936dB

High Band LHCP φ=0°

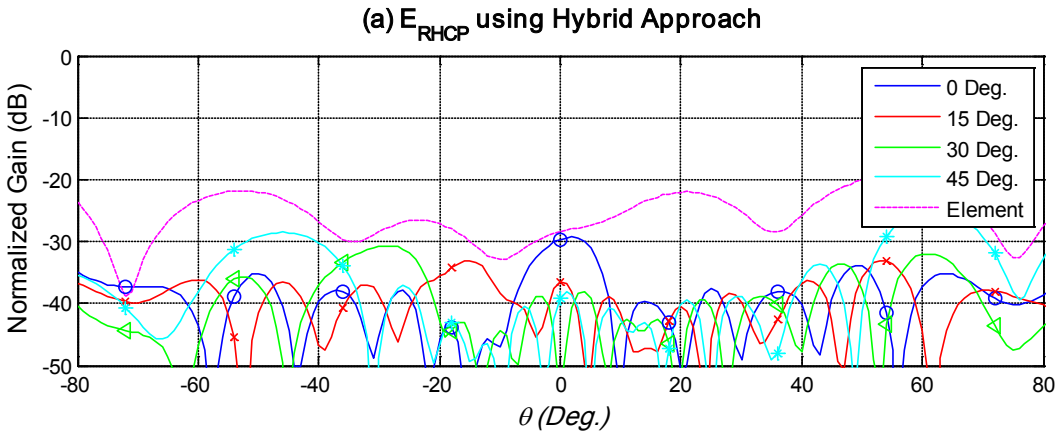

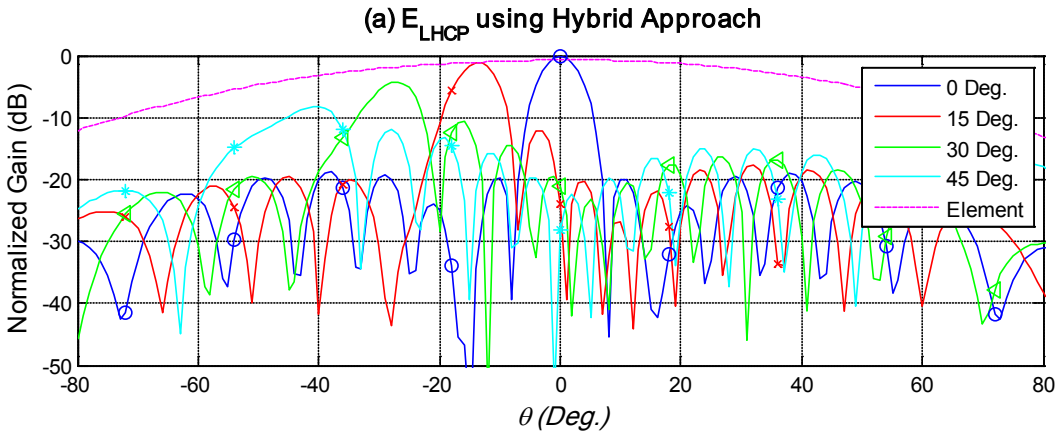

		θ_0=0°	θ_0=15°	θ_0=30°	θ_0=45°
3dB Beamwidth (BW_{3dB})	Calculated	7°	7°	8°	11°
	Approx.*	6.9473°	7.1923°	8.0220°	N/A
θ_{MAX}	Calculated	0°	-14°	-27°	-41°
Normalized Maximum Value ($F(\theta_{MAX})_{MAX}$)	Calculated	0dB	-1.1902dB	-4.2171dB	-8.2405dB
Cross-pol. discrimination (XPD)	Calculated	29.6270dB	32.0779dB	26.6203dB	21.4788dB

High Band LHCP φ=90°

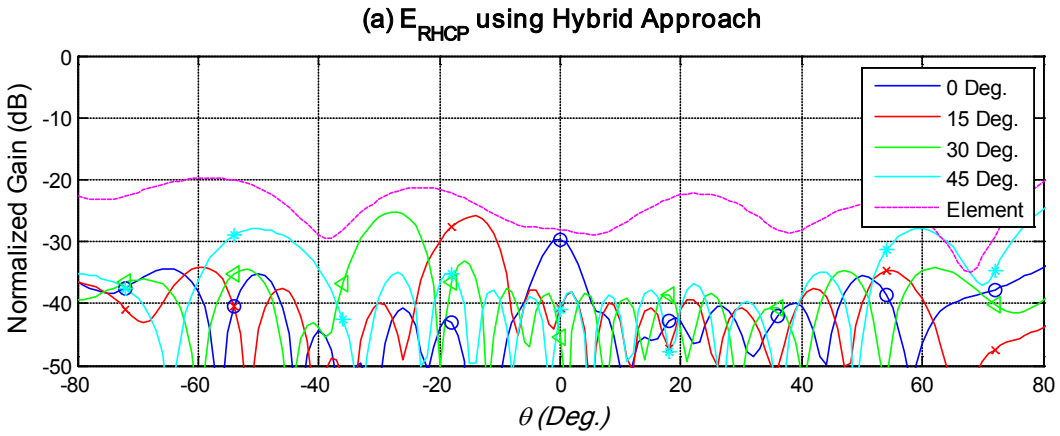

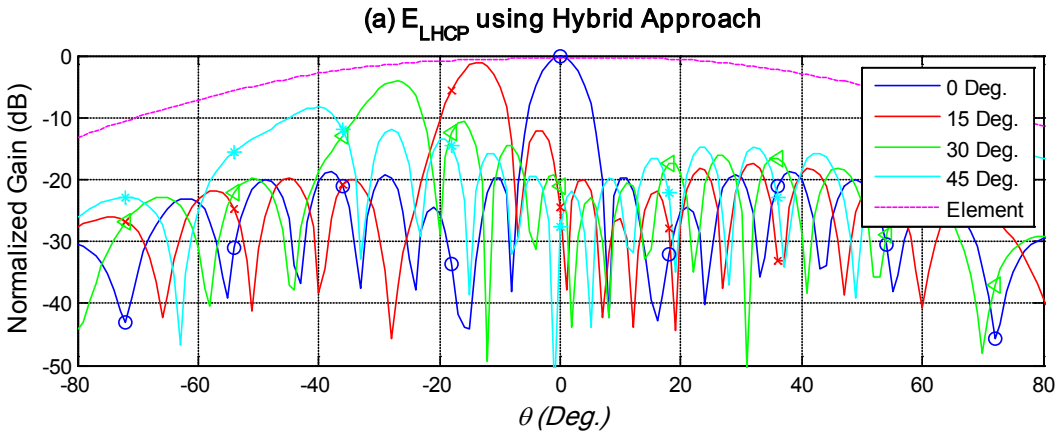

		θ_0=0°	θ_0=15°	θ_0=30°	θ_0=45°
3dB Beamwidth (BW_{3dB})	Calculated	7°	7°	8°	12°
	Approx.*	6.9473°	7.1923°	8.0220°	N/A
θ_{MAX}	Calculated	0°	-14°	-27°	-41°
Normalized Maximum Value ($F(\theta_{MAX})_{MAX}$)	Calculated	0dB	-1.2597dB	-4.4097dB	-8.4719dB
Cross-pol. discrimination (XPD)	Calculated	29.6270dB	24.7661dB	21.1263dB	26.0551dB

High Band RHCP φ=0°

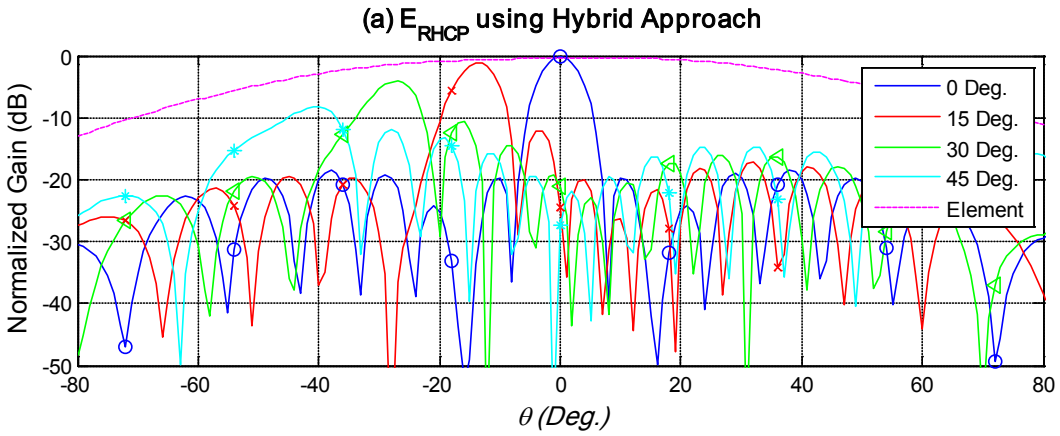

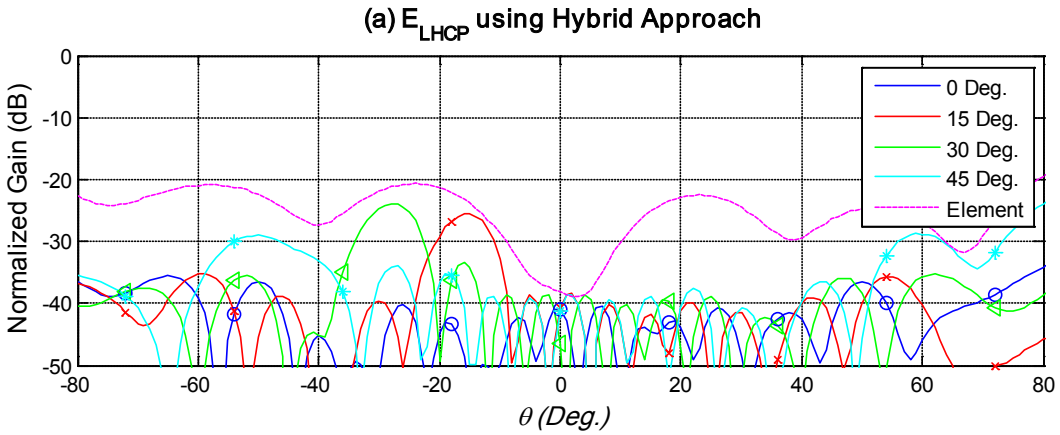

		θ_0=0°	θ_0=15°	θ_0=30°	θ_0=45°
3dB Beamwidth (BW_{3dB})	Calculated	7°	7°	8°	11°
	Approx.*	6.9473°	7.1923°	8.0220°	N/A
θ_{MAX}	Calculated	0°	-14°	-27°	-40°
Normalized Maximum Value ($F(\theta_{MAX})_{MAX}$)	Calculated	0dB	-1.1521dB	-4.0778dB	-8.3121dB
Cross-pol. discrimination (XPD)	Calculated	41.0871dB	24.7663dB	19.9566dB	24.8445dB

High Band RHCP φ=90°

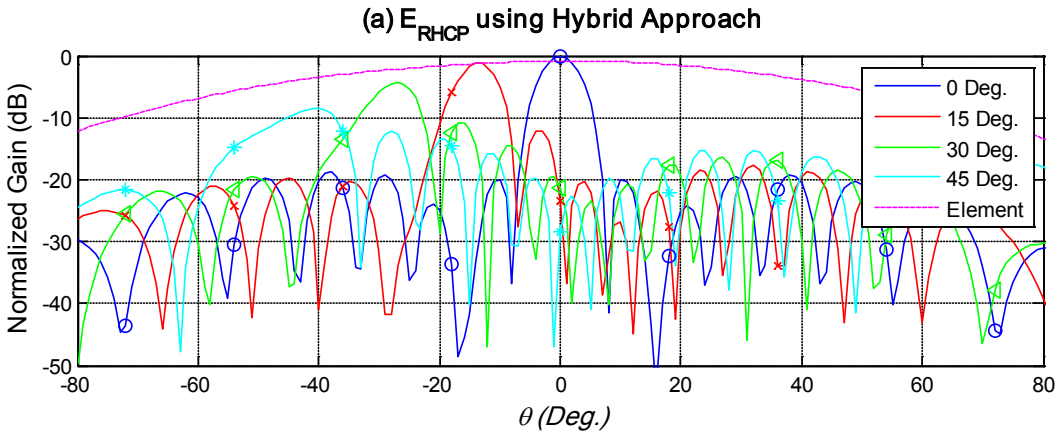

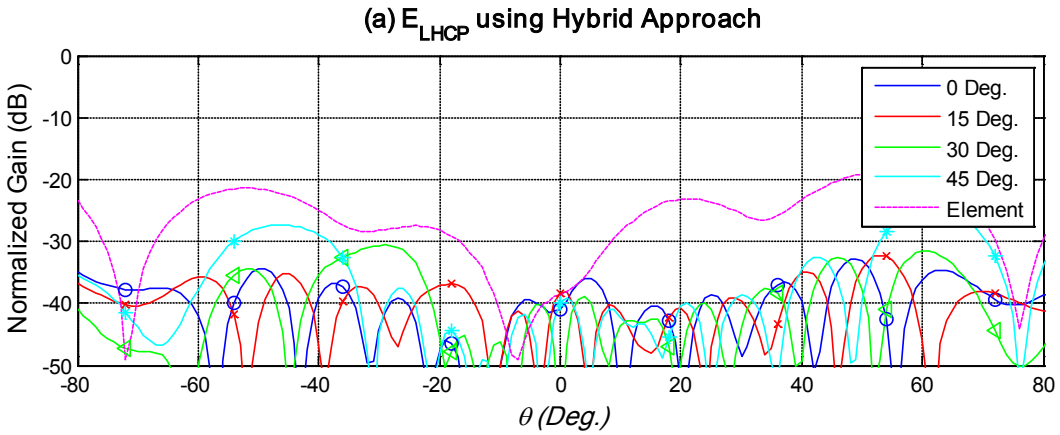

		θ_0=0°	θ_0=15°	θ_0=30°	θ_0=45°
3dB Beamwidth (BW_{3dB})	Calculated	7°	7°	8°	11°
	Approx.*	6.9473°	7.1923°	8.0220°	N/A
θ_{MAX}	Calculated	0°	-14°	-27°	-40°
Normalized Maximum Value ($F(\theta_{MAX})_{MAX}$)	Calculated	0dB	-1.1387dB	-4.0797dB	-8.3745dB
Cross-pol. discrimination (XPD)	Calculated	41.0871dB	39.1293dB	26.5732dB	19.8965dB

24x24 Array

Low Band LHCP φ=0°

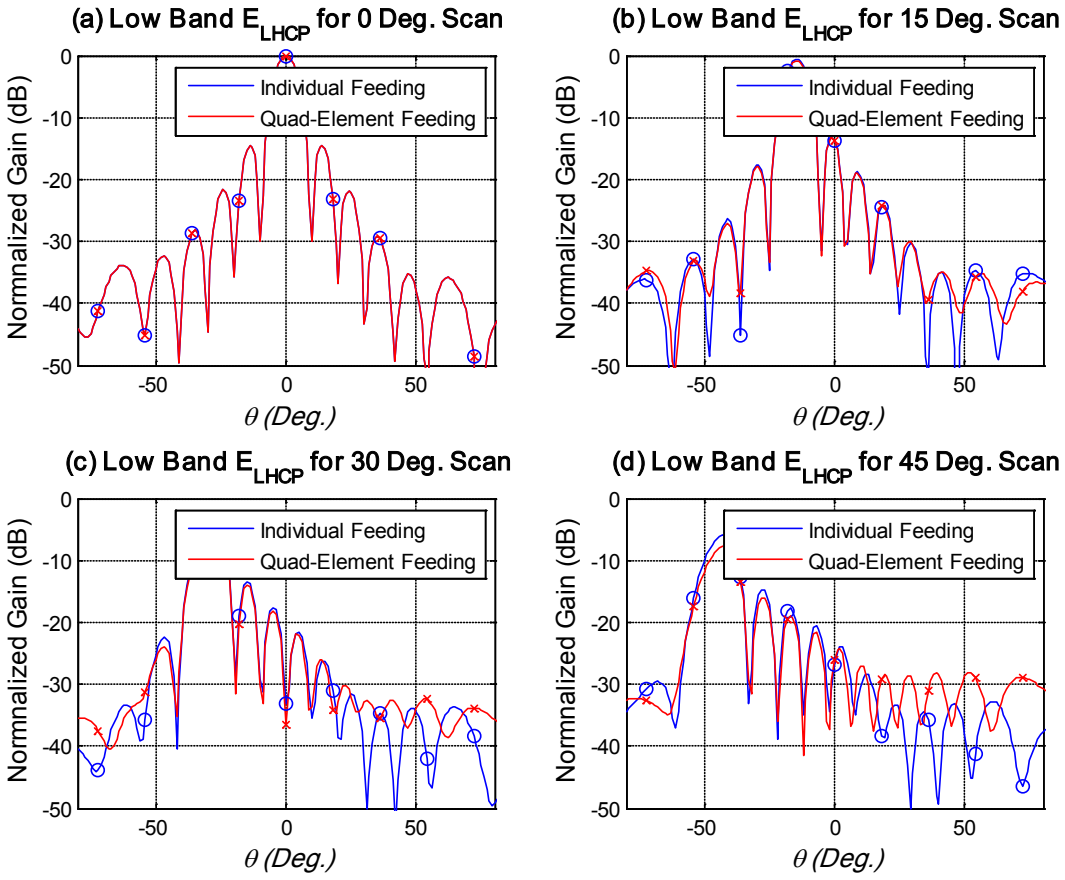

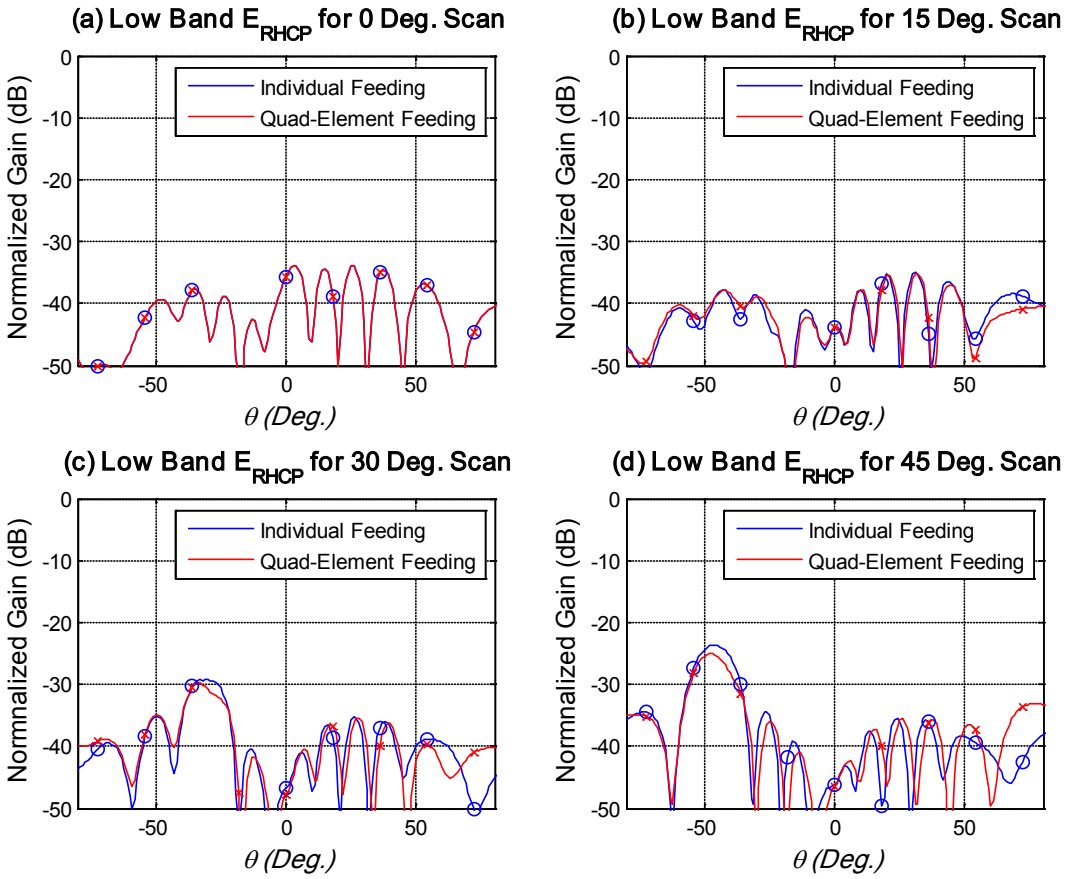
(a) Low Band E RHCP for 0 Deg. Scan
(b) Low Band E RHCP for 15 Deg. Scan
(c) Low Band E RHCP for 30 Deg. Scan
(d) Low Band E RHCP for 45 Deg. Scan
Individual Feeding
Quad-Element Feeding
Normalized Gain (dB)
θ (Deg.)
0
-10
-20
-30
-40
-50
-50
0
50

		θ_0=0°	θ_0=15°	θ_0=30°	θ_0=45°
3dB Beamwidth (BW_{3dB})	Ind. Feed	9°	8°	9°	11°
	Quad. Feed	9°	8°	9°	11°
	Approx.*	8.2233°	8.5134°	9.4954°	N/A
θ_{MAX}	Ind. Feed	0°	-14°	-29°	-43°
	Quad. Feed	0°	-14°	-28°	-43°
Normalized Maximum Value ($F(\theta_{MAX})_{MAX}$)	Ind. Feed	0dB	-0.7086dB	-2.8243dB	-6.0076dB
	Quad. Feed	0dB	-0.9298dB	-3.6576dB	-7.7473dB
Cross-pol. discrimination (XPD)	Ind. Feed	35.6364dB	44.0116dB	26.5507dB	18.2519dB
	Quad. Feed	35.6364dB	44.6704dB	27.5578dB	18.6276dB

Low Band LHCP φ=90°

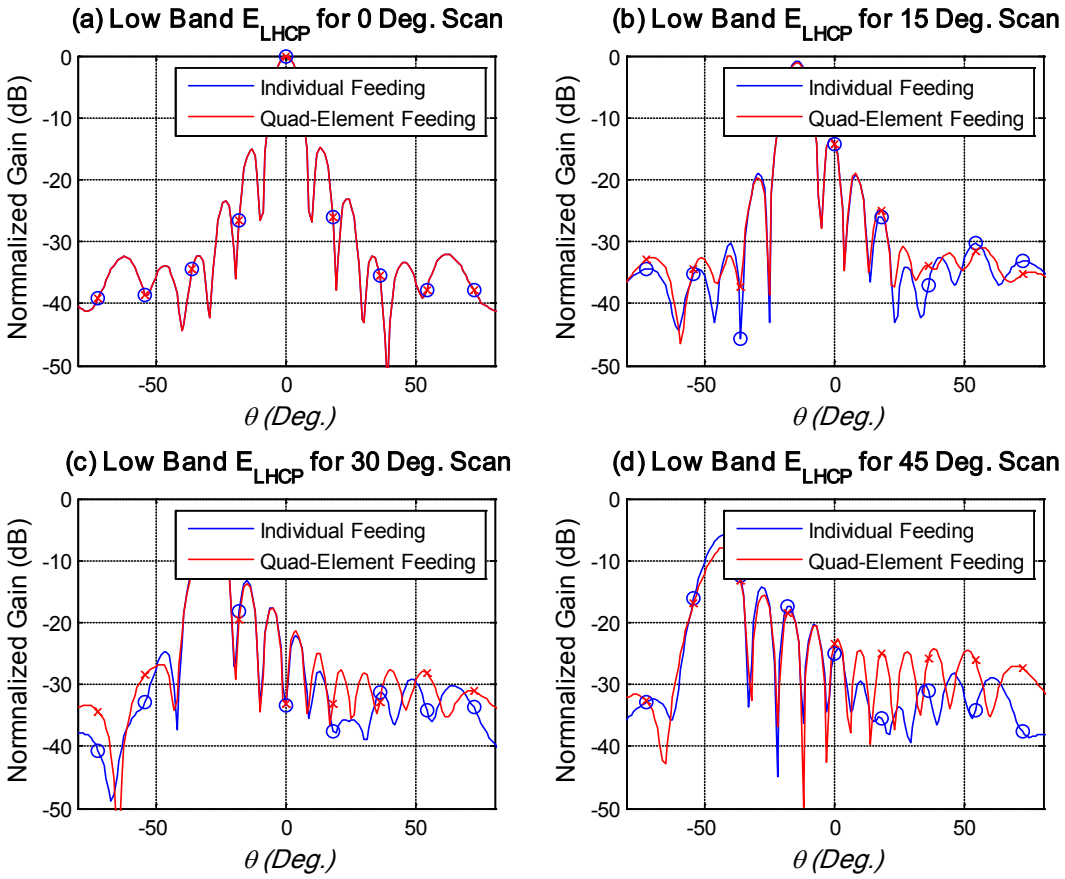

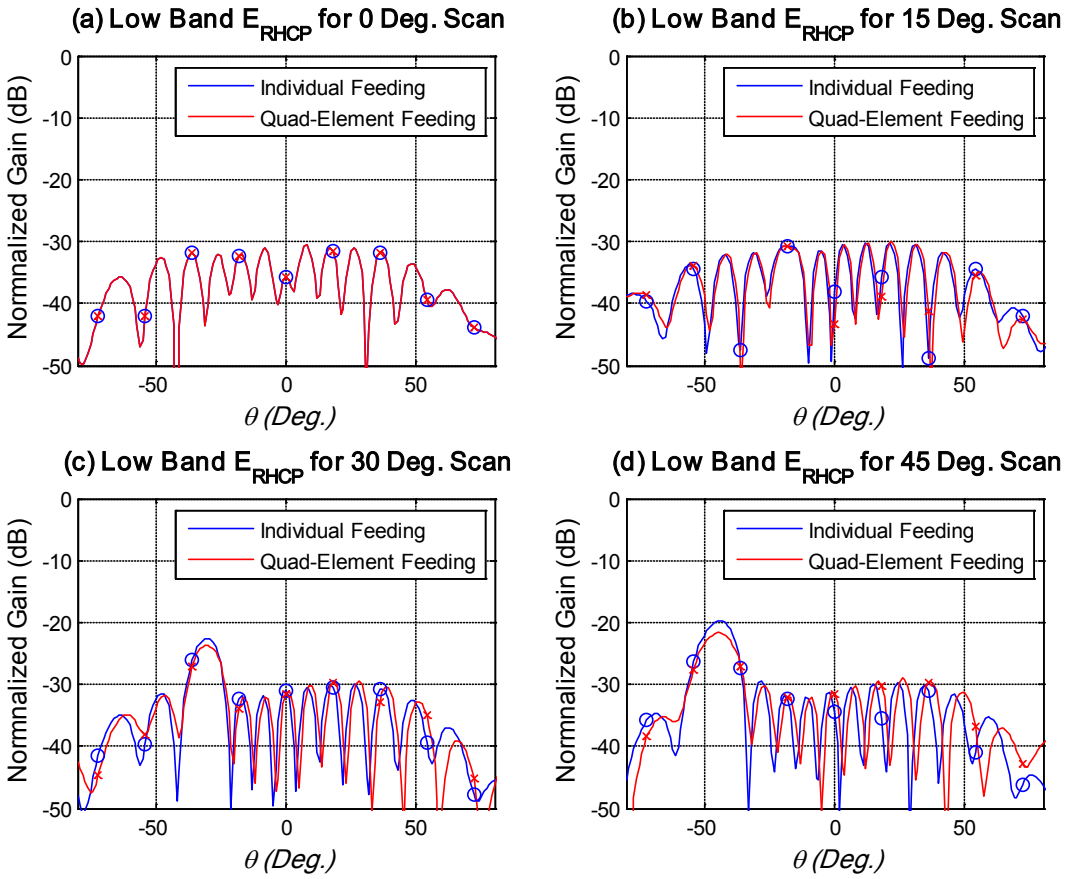
(a) Low Band E RHCP for 0 Deg. Scan
(b) Low Band E RHCP for 15 Deg. Scan
(c) Low Band E RHCP for 30 Deg. Scan
(d) Low Band E RHCP for 45 Deg. Scan
Individual Feeding
Quad-Element Feeding
Normalized Gain (dB)
θ (Deg.)
0
-10
-20
-30
-40
-50
-50
0
50

		θ_0=0°	θ_0=15°	θ_0=30°	θ_0=45°
3dB Beamwidth (BW_{3dB})	Ind. Feed	9°	8°	9°	11°
	Quad. Feed	9°	8°	9°	11°
	Approx.*	8.2233°	8.5134°	9.4954°	N/A
θ_{MAX}	Ind. Feed	0°	-14°	-29°	-43°
	Quad. Feed	0°	-14°	-29°	-42°
Normalized Maximum Value ($F(\theta_{MAX})_{MAX}$)	Ind. Feed	0dB	-0.9900dB	-3.1520dB	-5.9807dB
	Quad. Feed	0dB	-1.2117dB	-4.0649dB	-7.8882dB
Cross-pol. discrimination (XPD)	Ind. Feed	35.6364dB	30.8238dB	19.6092dB	13.8412dB
	Quad. Feed	35.6364dB	30.6369dB	19.8048dB	14.2079dB

Low Band RHCP φ=0°

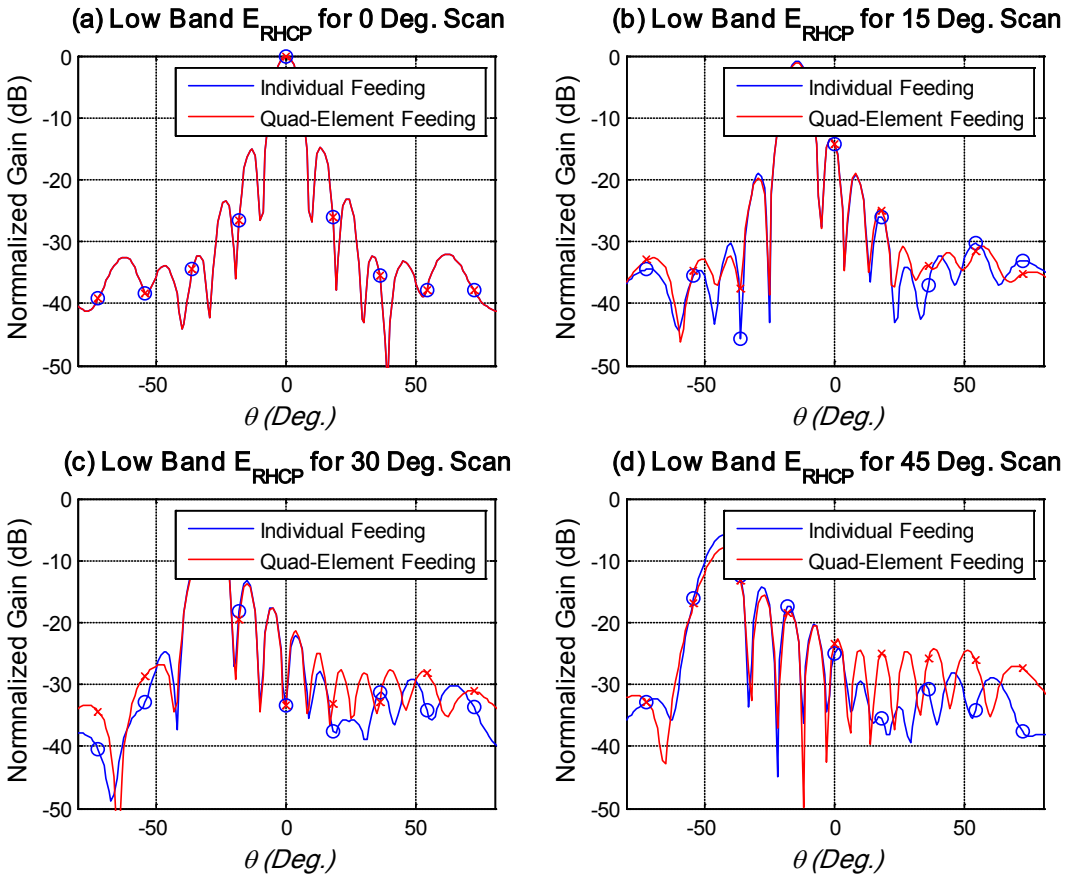

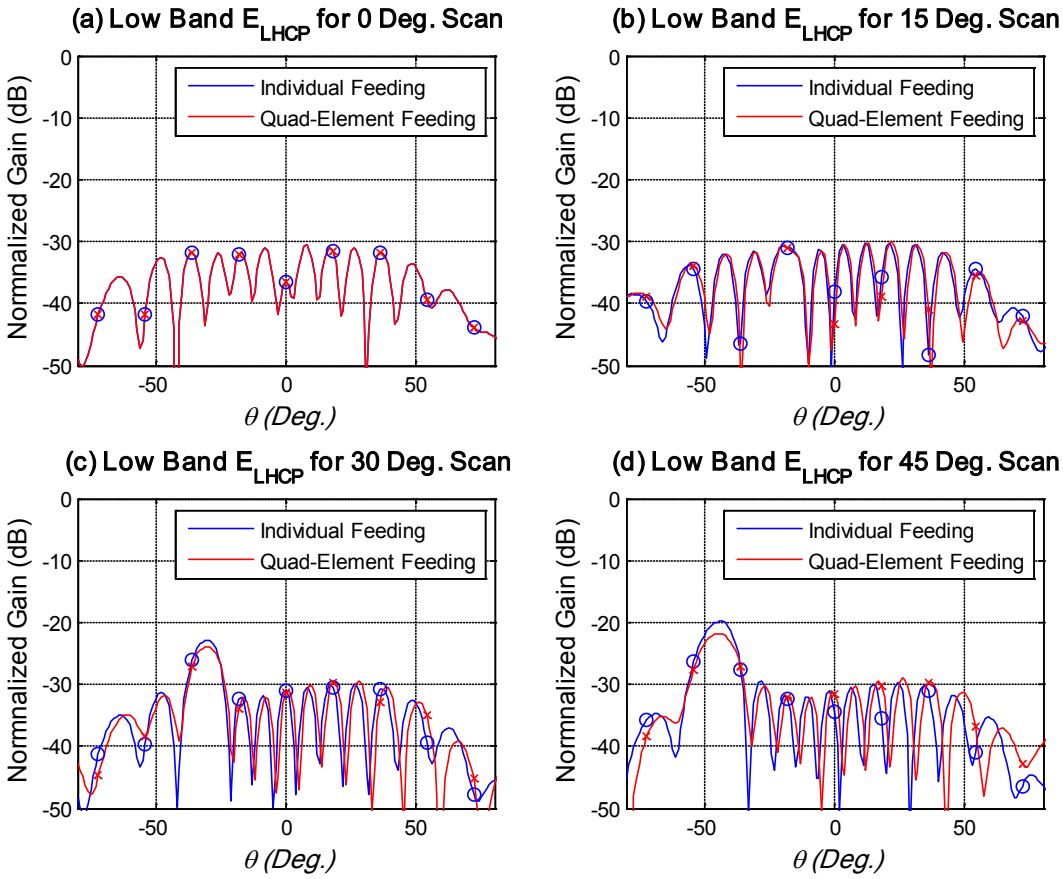
(a) Low Band E_LHCP for 0 Deg. Scan
(b) Low Band E_LHCP for 15 Deg. Scan
(c) Low Band E_LHCP for 30 Deg. Scan
(d) Low Band E_LHCP for 45 Deg. Scan
Individual Feeding
Quad-Element Feeding
Normalized Gain (dB)
θ (Deg.)
0
-10
-20
-30
-40
-50
-50
0
50

		θ_0=0°	θ_0=15°	θ_0=30°	θ_0=45°
3dB Beamwidth (BW_{3dB})	Ind. Feed	9°	8°	9°	11°
	Quad. Feed	9°	8°	9°	11°
	Approx.*	8.2233°	8.5134°	9.4954°	N/A
θ_{MAX}	Ind. Feed	0°	-14°	-29°	-43°
	Quad. Feed	0°	-14°	-28°	-42°
Normalized Maximum Value ($F(\theta_{MAX})_{MAX}$)	Ind. Feed	0dB	-0.9950dB	-3.1594dB	-5.9823dB
	Quad. Feed	0dB	-1.2167dB	-4.0663dB	-7.8900dB
Cross-pol. discrimination (XPD)	Ind. Feed	36.5918dB	31.5555dB	19.8053dB	13.9058dB
	Quad. Feed	36.5918dB	31.3464dB	20.3257dB	14.2702dB

Low Band RHCP φ=90°

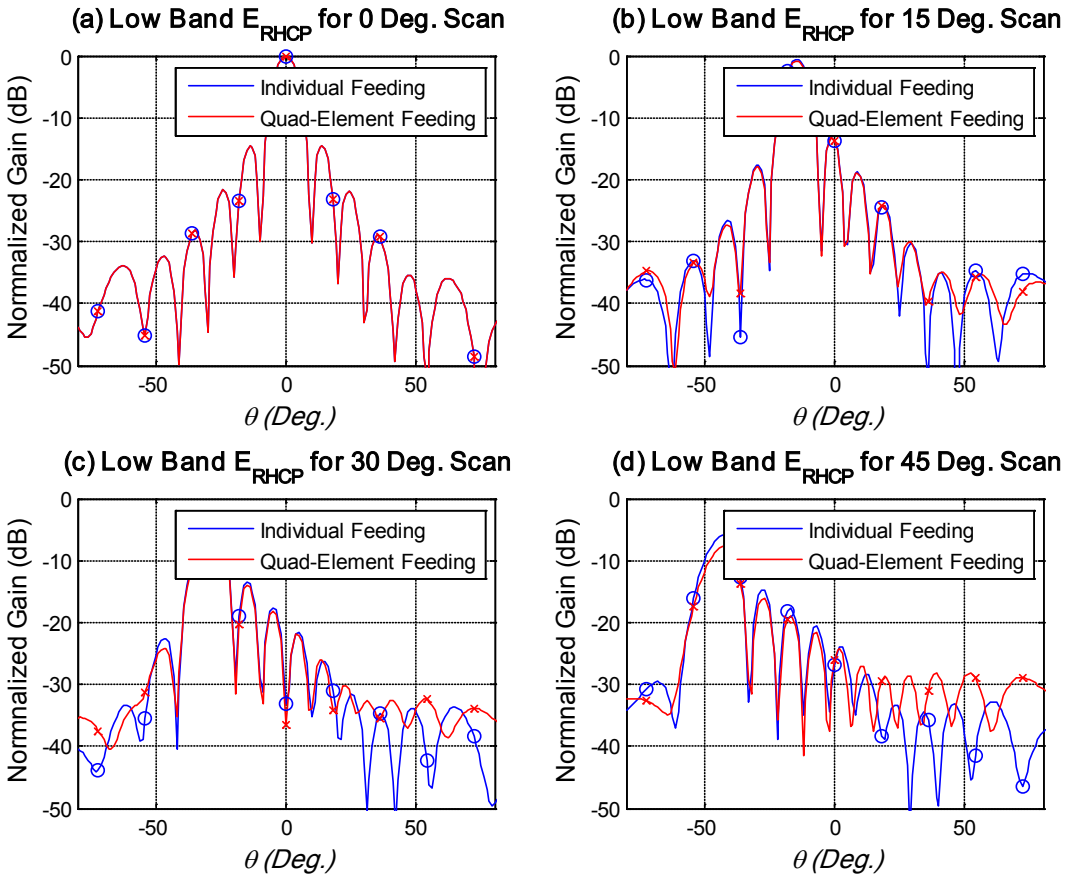

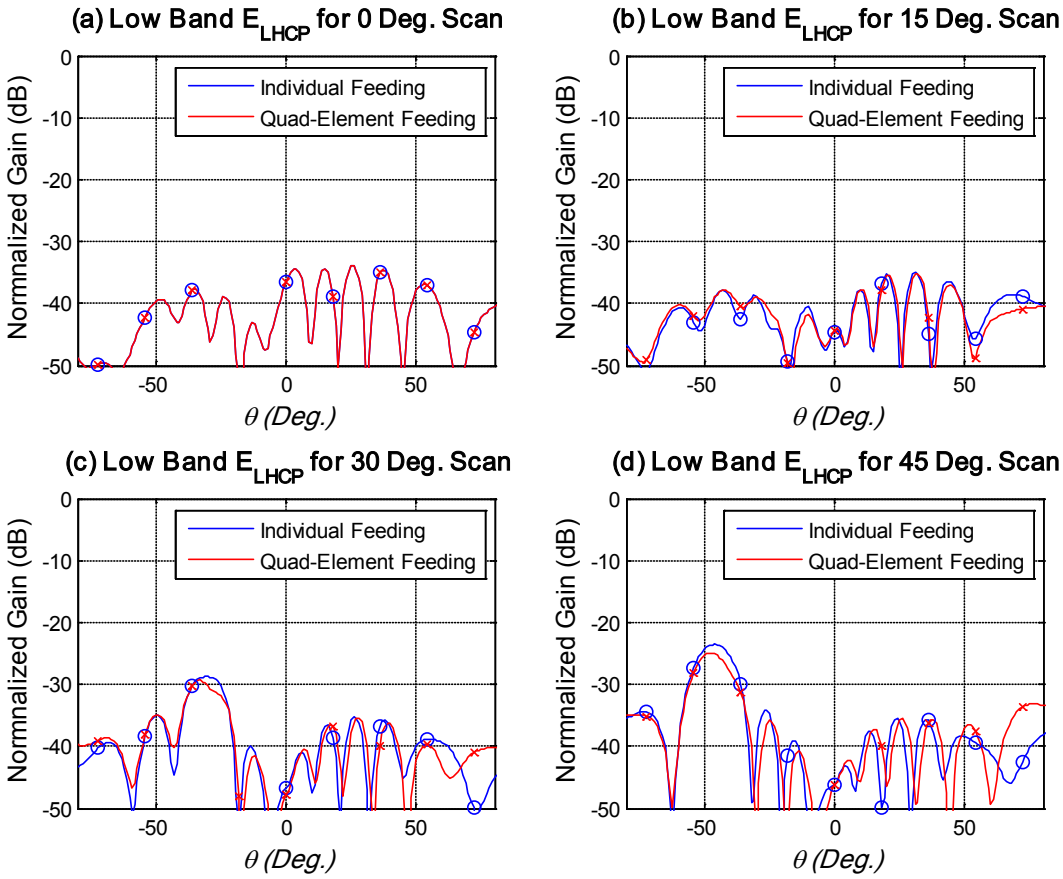
(a) Low Band E_LHCP for 0 Deg. Scan
(b) Low Band E_LHCP for 15 Deg. Scan
(c) Low Band E_LHCP for 30 Deg. Scan
(d) Low Band E_LHCP for 45 Deg. Scan
Individual Feeding
Quad-Element Feeding
Normalized Gain (dB)
θ (Deg.)
0
-10
-20
-30
-40
-50
-50
0
50

		θ_0=0°	θ_0=15°	θ_0=30°	θ_0=45°
3dB Beamwidth (BW_{3dB})	Ind. Feed	9°	8°	9°	11°
	Quad. Feed	9°	8°	9°	11°
	Approx.*	8.2233°	8.5134°	9.4954°	N/A
θ_{MAX}	Ind. Feed	0°	-14°	-29°	-44°
	Quad. Feed	0°	-14°	-29°	-44°
Normalized Maximum Value ($F(\theta_{MAX})_{MAX}$)	Ind. Feed	0dB	-0.7103dB	-2.8472dB	-6.0163dB
	Quad. Feed	0dB	-0.9271dB	-3.6814dB	-7.7576dB
Cross-pol. discrimination (XPD)	Ind. Feed	36.5918dB	42.0005dB	26.0924dB	18.0325dB
	Quad. Feed	36.5918dB	44.2489dB	27.0765dB	18.3827dB

High Band LHCP φ=0°

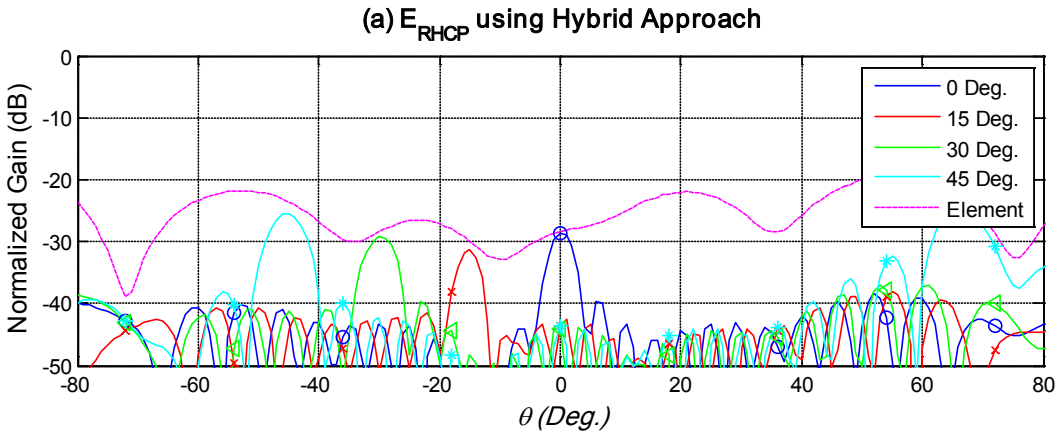

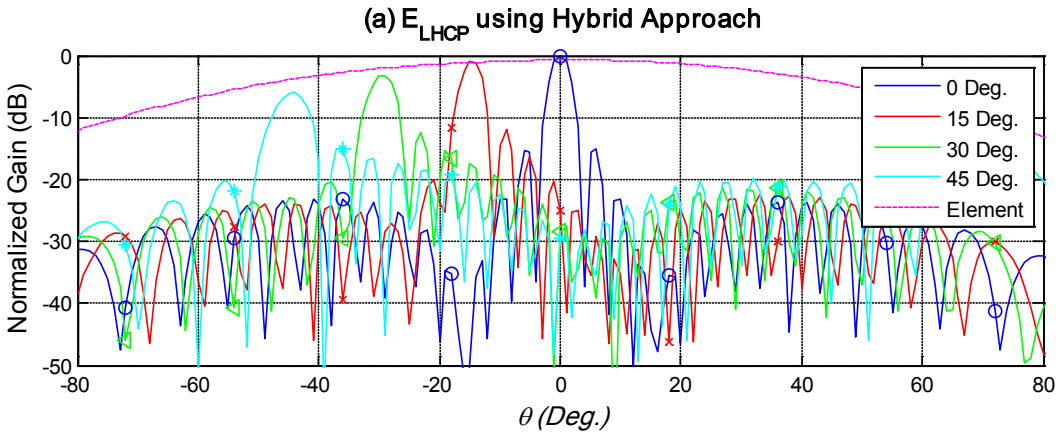

		θ_0=0°	θ_0=15°	θ_0=30°	θ_0=45°
3dB Beamwidth (BW_{3dB})	Calculated	3°	4°	4°	6°
	Approx.*	3.4736°	3.5962°	4.0110°	N/A
θ_{MAX}	Calculated	0°	-15°	-29°	-44°
Normalized Maximum Value ($F(\theta_{MAX})_{MAX}$)	Calculated	0dB	-1.0090dB	-3.2080dB	-6.0014dB
Cross-pol. discrimination (XPD)	Calculated	28.6096dB	30.3891dB	26.1229dB	19.9702dB

High Band LHCP φ=90°

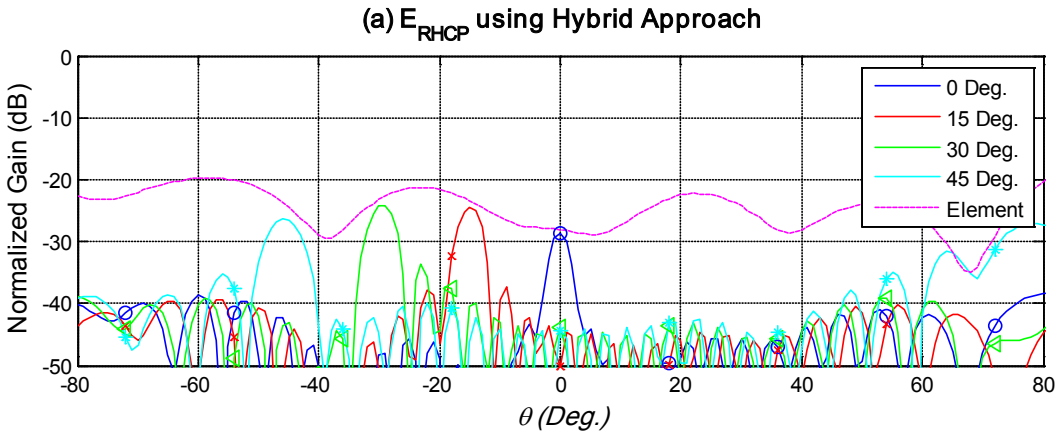

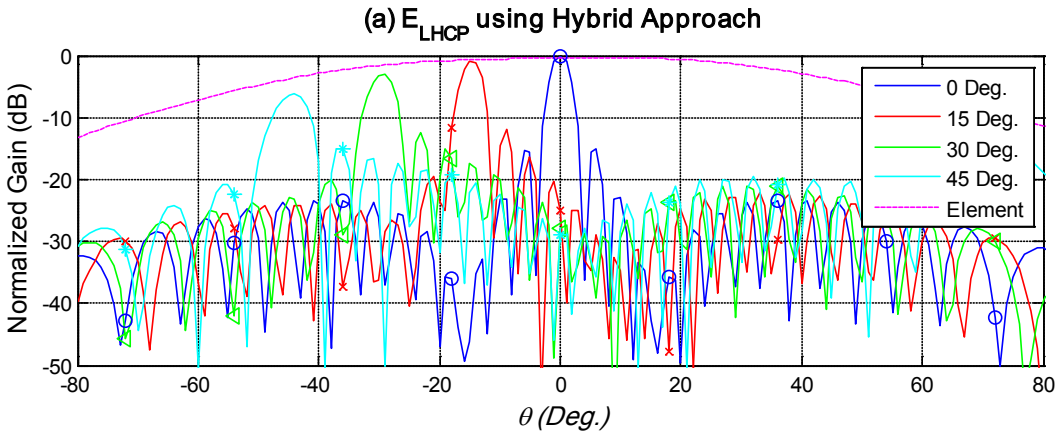

		θ_0=0°	θ_0=15°	θ_0=30°	θ_0=45°
3dB Beamwidth (BW_{3dB})	Calculated	3°	4°	4°	6°
	Approx.*	3.4736°	3.5962°	4.0110°	N/A
θ_{MAX}	Calculated	0°	-15°	-29°	-44°
Normalized Maximum Value ($F(\theta_{MAX})_{MAX}$)	Calculated	0dB	-0.9254dB	-3.0425dB	-6.2363dB
Cross-pol. discrimination (XPD)	Calculated	28.6096dB	23.4678dB	21.1889dB	21.1300dB

High Band RHCP φ=0°

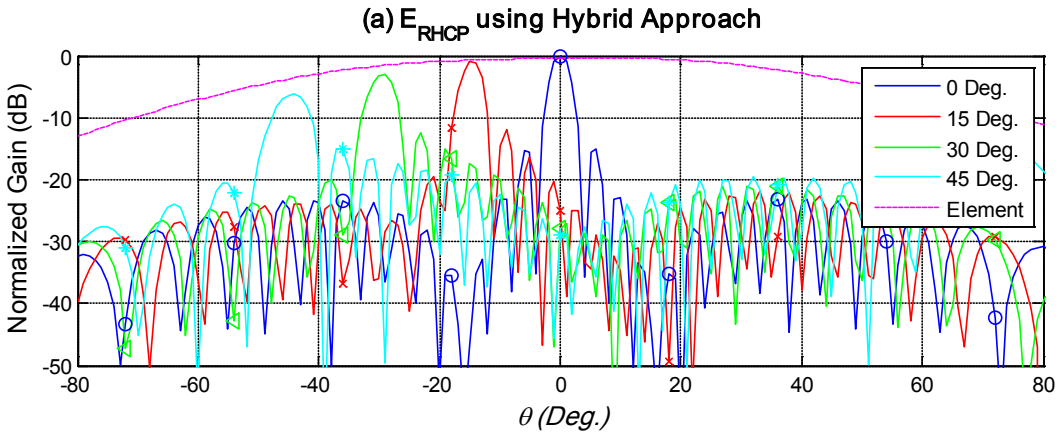

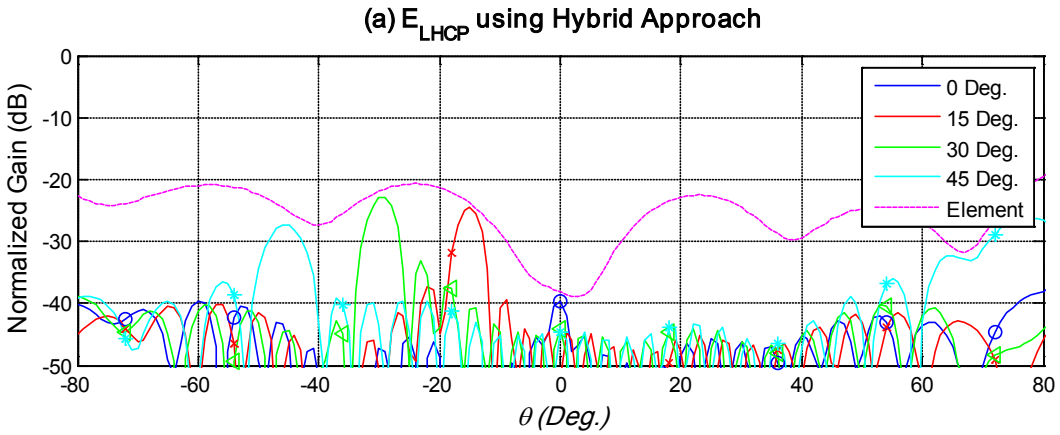

		θ_0=0°	θ_0=15°	θ_0=30°	θ_0=45°
3dB Beamwidth (BW_{3dB})	Calculated	3°	4°	4°	6°
	Approx.*	3.4736°	3.5962°	4.0110°	N/A
θ_{MAX}	Calculated	0°	-15°	-29°	-44°
Normalized Maximum Value ($F(\theta_{MAX})_{MAX}$)	Calculated	0dB	-0.9416dB	-3.0767dB	-6.1817dB
Cross-pol. discrimination (XPD)	Calculated	39.5948dB	23.5188dB	19.9319dB	21.8875dB

High Band RHCP φ=90°

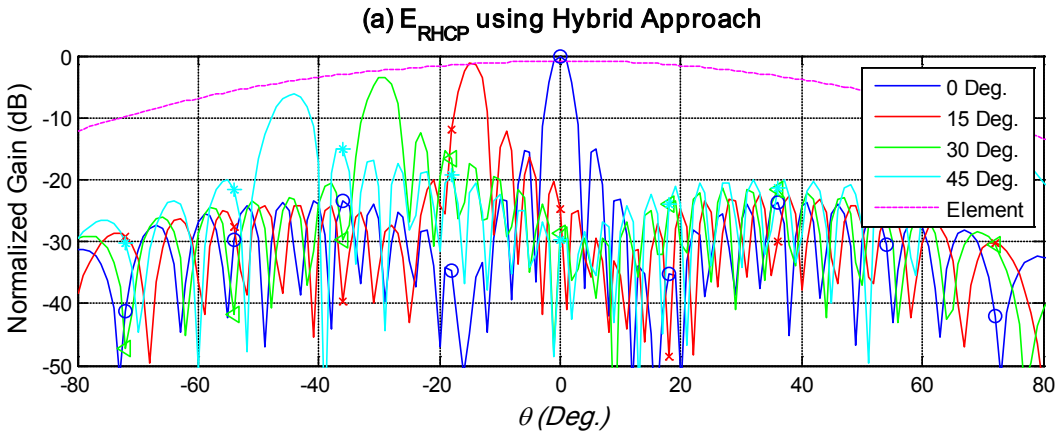

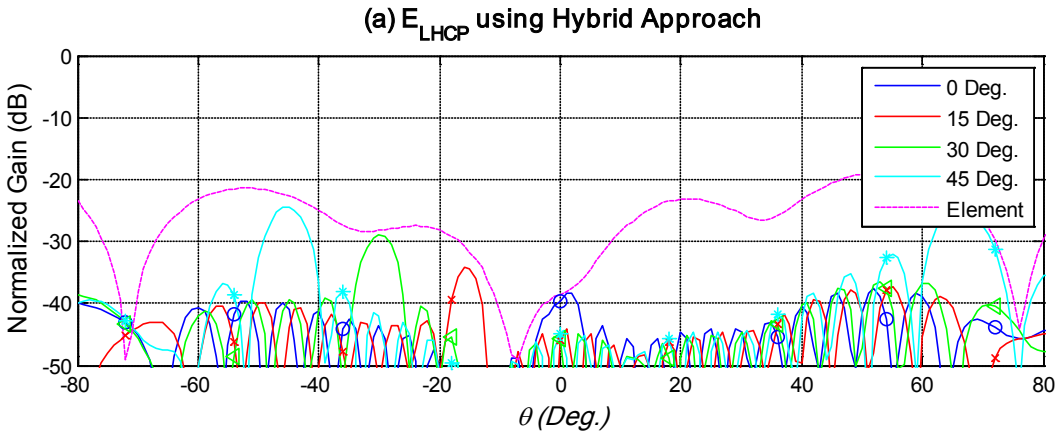

		θ_0=0°	θ_0=15°	θ_0=30°	θ_0=45°
3dB Beamwidth (BW_{3dB})	Calculated	3°	4°	4°	6°
	Approx.*	3.4736°	3.5962°	4.0110°	N/A
θ_{MAX}	Calculated	0°	-15°	-29°	-44°
Normalized Maximum Value ($F(\theta_{MAX})_{MAX}$)	Calculated	0dB	-1.0933dB	-3.4253dB	-6.1986dB
Cross-pol. discrimination (XPD)	Calculated	39.5948dB	33.2006dB	25.8047dB	18.6798dB

48x48 Array

Low Band LHCP φ=0°

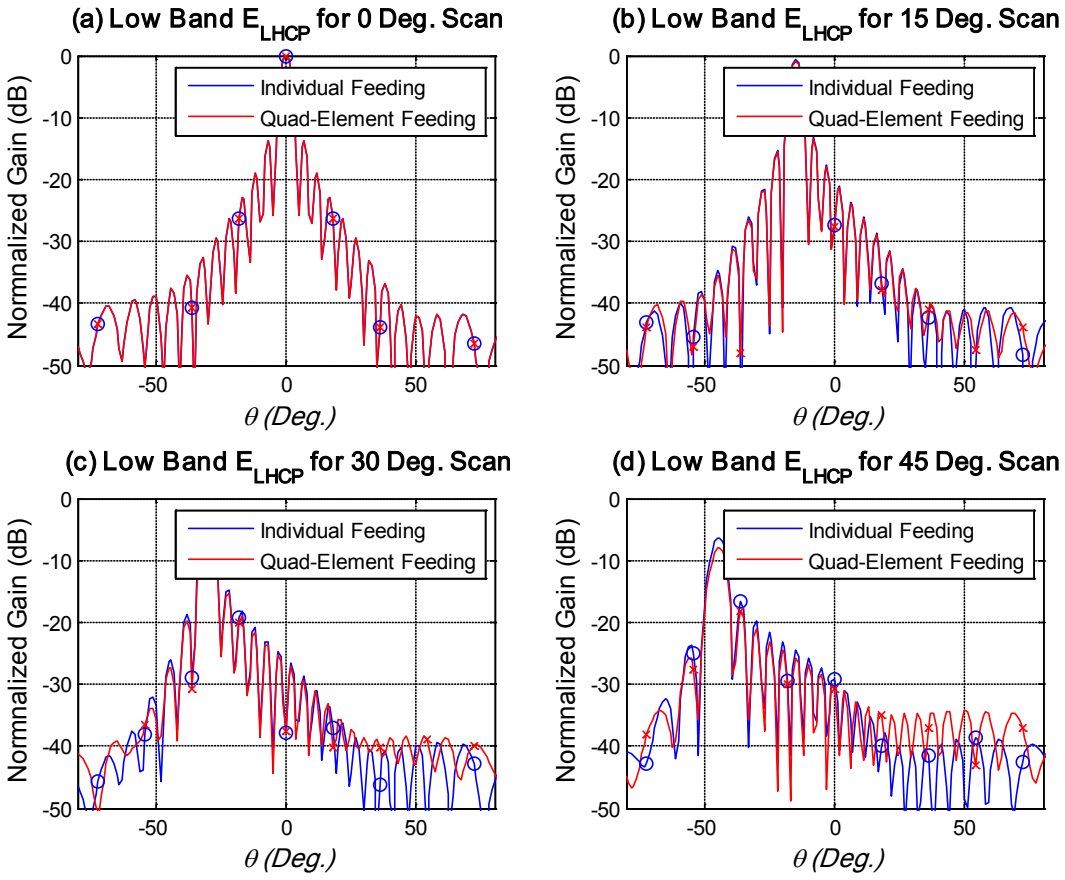

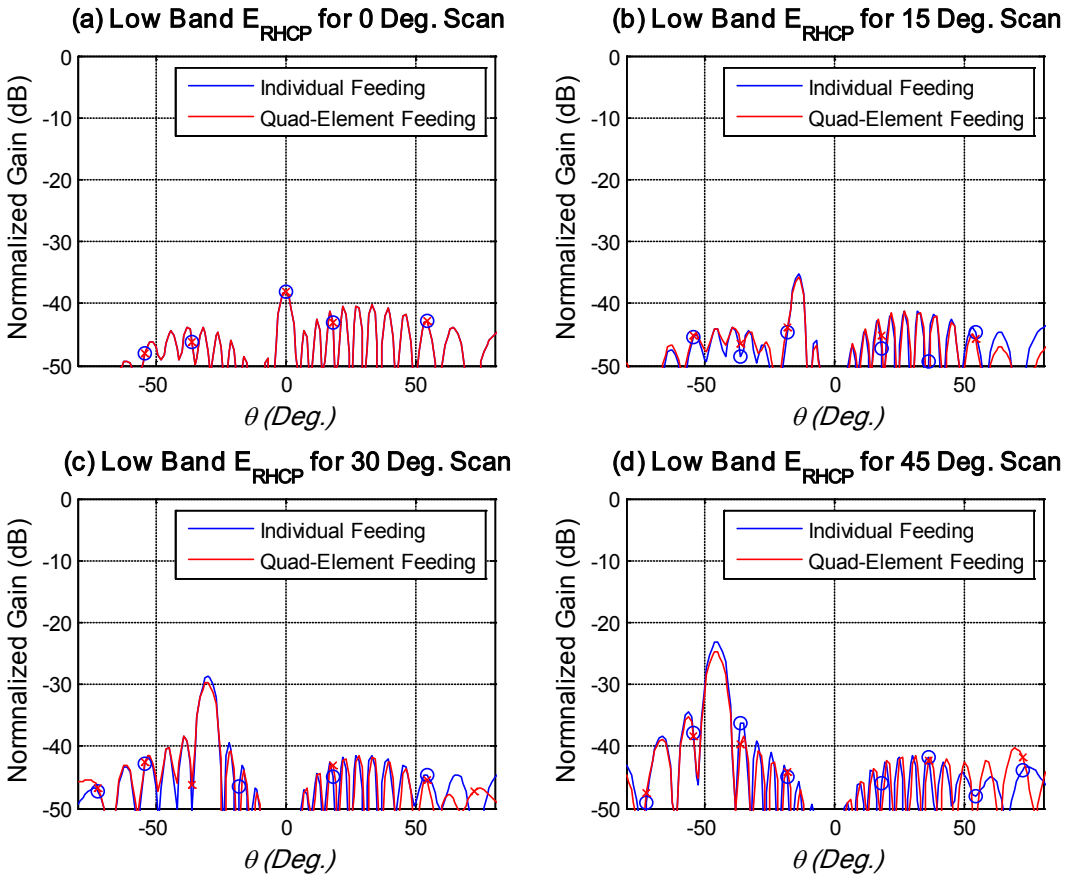
(a) Low Band E RHCP for 0 Deg. Scan
(b) Low Band E RHCP for 15 Deg. Scan
(c) Low Band E RHCP for 30 Deg. Scan
(d) Low Band E RHCP for 45 Deg. Scan
Individual Feeding
Quad-Element Feeding
Normalized Gain (dB)
θ (Deg.)
0
-10
-20
-30
-40
-50
-50
0
50

		θ_0=0°	θ_0=15°	θ_0=30°	θ_0=45°
3dB Beamwidth (BW_{3dB})	Ind. Feed	5°	5°	5°	6°
	Quad. Feed	5°	5°	5°	6°
	Approx.*	4.1116°	4.2567°	4.7477°	N/A
θ_{MAX}	Ind. Feed	0°	-15°	-30°	-44°
	Quad. Feed	0°	-15°	-30°	-44°
Normalized Maximum Value ($F(\theta_{MAX})_{MAX}$)	Ind. Feed	0dB	-0.7025dB	-2.9774dB	-6.3232dB
	Quad. Feed	0dB	-0.9093dB	-3.7675dB	-7.9491dB
Cross-pol. discrimination (XPD)	Ind. Feed	38.1352dB	35.2256dB	25.6745dB	17.3319dB
	Quad. Feed	38.1352dB	35.6180dB	26.0330dB	17.4581dB

Low Band LHCP φ=90°

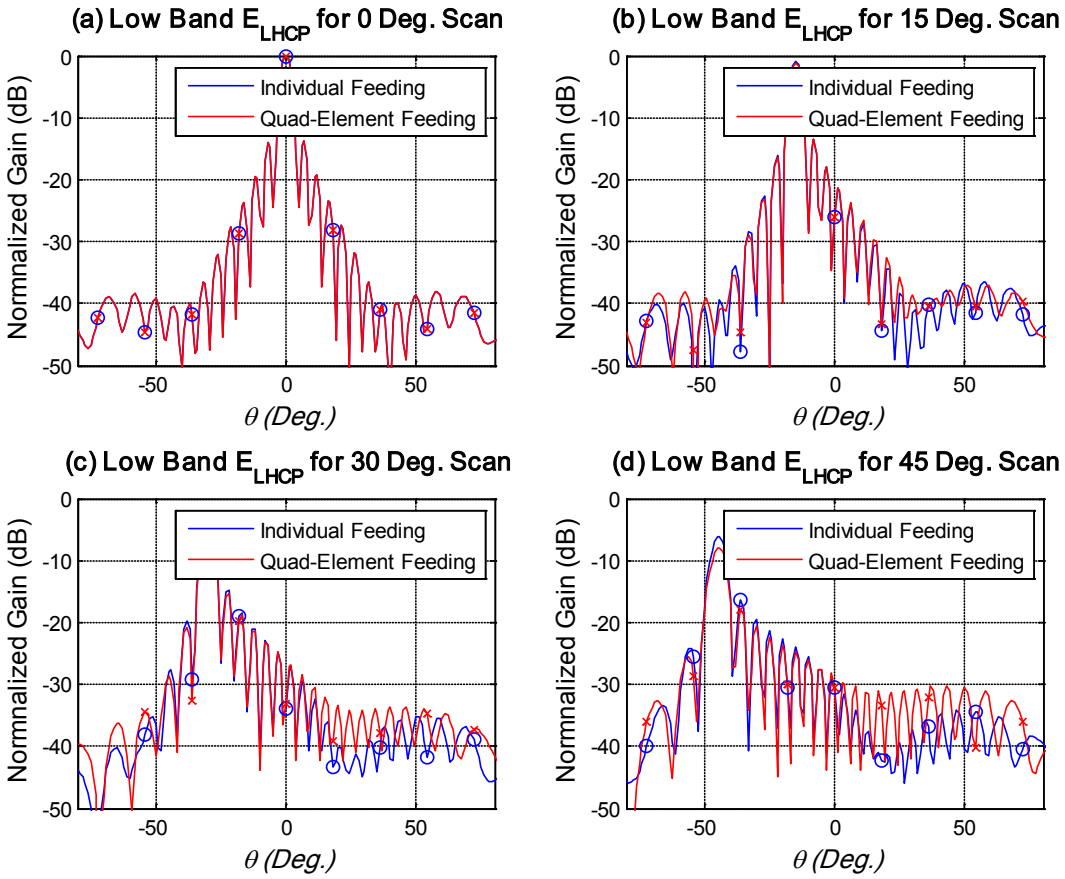

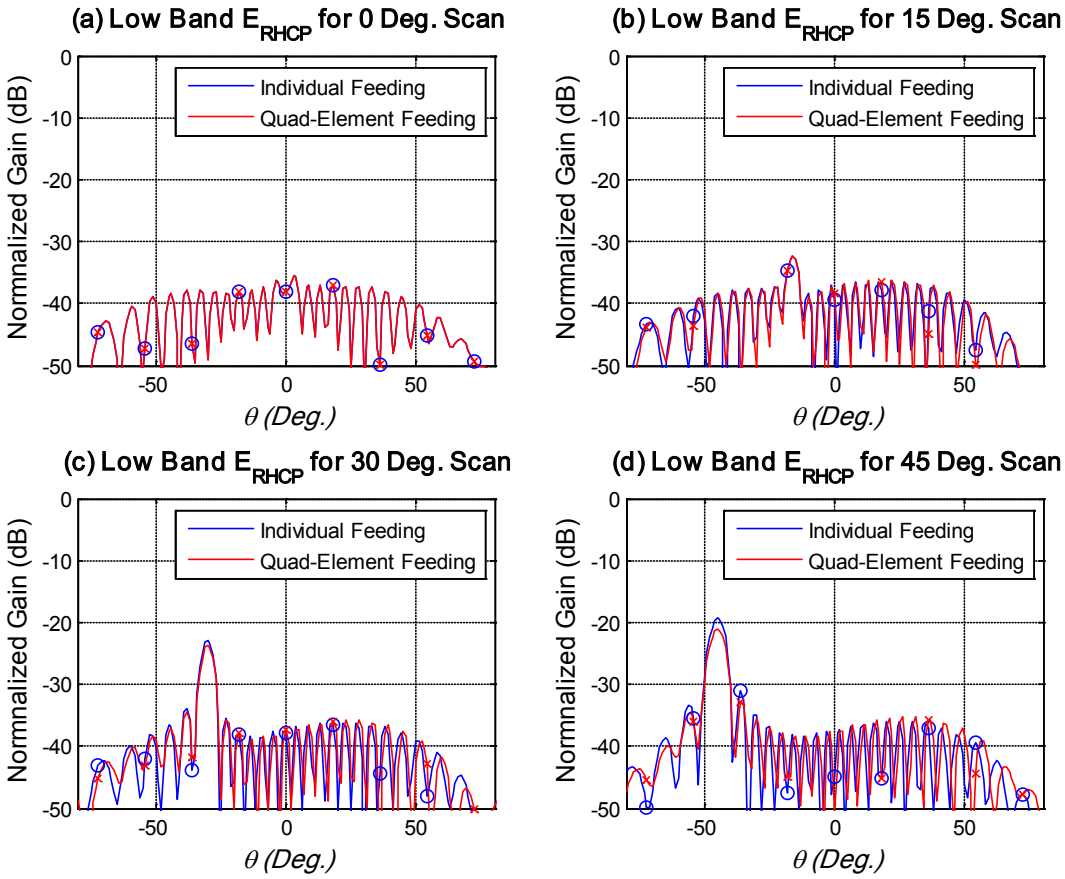
(a) Low Band E RHCP for 0 Deg. Scan
(b) Low Band E RHCP for 15 Deg. Scan
(c) Low Band E RHCP for 30 Deg. Scan
(d) Low Band E RHCP for 45 Deg. Scan
Individual Feeding
Quad-Element Feeding
Normalized Gain (dB)
θ (Deg.)
0
-10
-20
-30
-40
-50
-50
0
50

		θ_0=0°	θ_0=15°	θ_0=30°	θ_0=45°
3dB Beamwidth (BW_{3dB})	Ind. Feed	5°	5°	5°	6°
	Quad. Feed	5°	5°	5°	6°
	Approx.*	4.1116°	4.2567°	4.7477°	N/A
θ_{MAX}	Ind. Feed	0°	-15°	-30°	-44°
	Quad. Feed	0°	-15°	-30°	-44°
Normalized Maximum Value ($F(\theta_{MAX})_{MAX}$)	Ind. Feed	0dB	-1.0082dB	-3.2867dB	-6.1916dB
	Quad. Feed	0dB	-1.2239dB	-4.1249dB	-7.9137dB
Cross-pol. discrimination (XPD)	Ind. Feed	38.1352dB	31.8272dB	19.4971dB	13.3938dB
	Quad. Feed	38.1352dB	31.5952dB	19.5731dB	13.4108dB

Low Band RHCP φ=0°

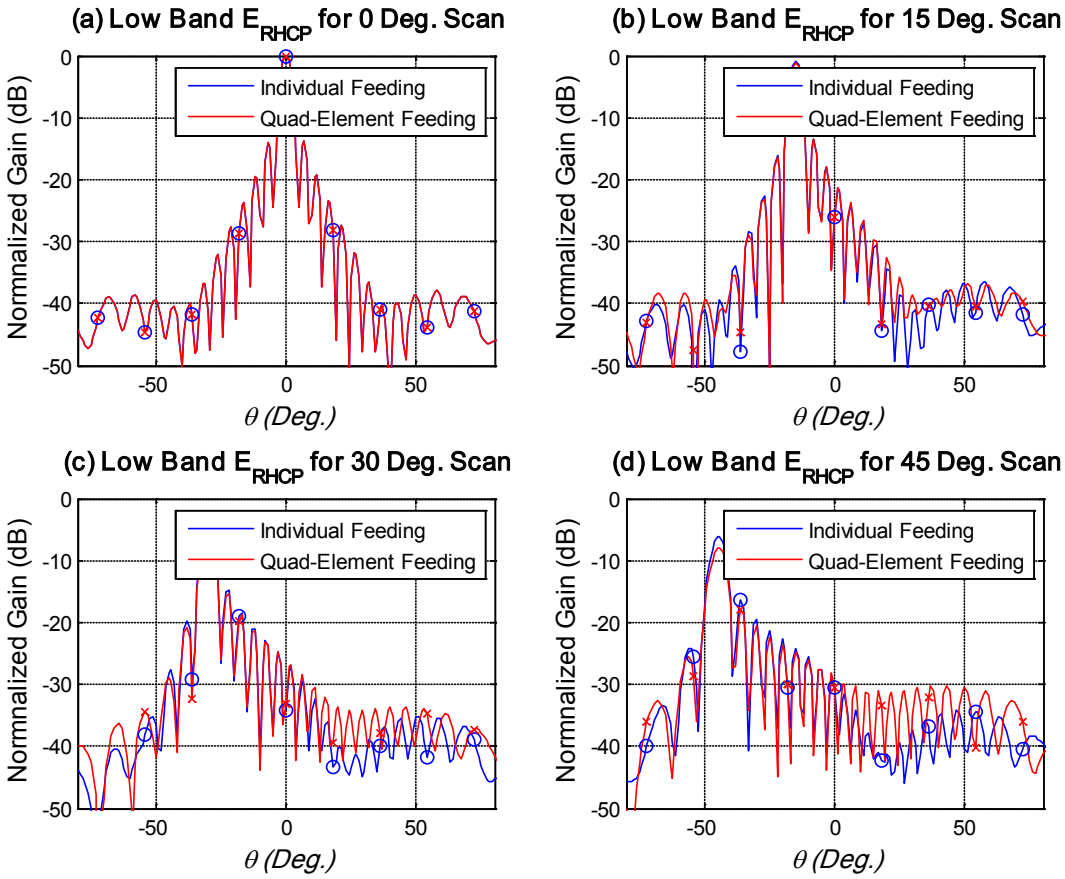

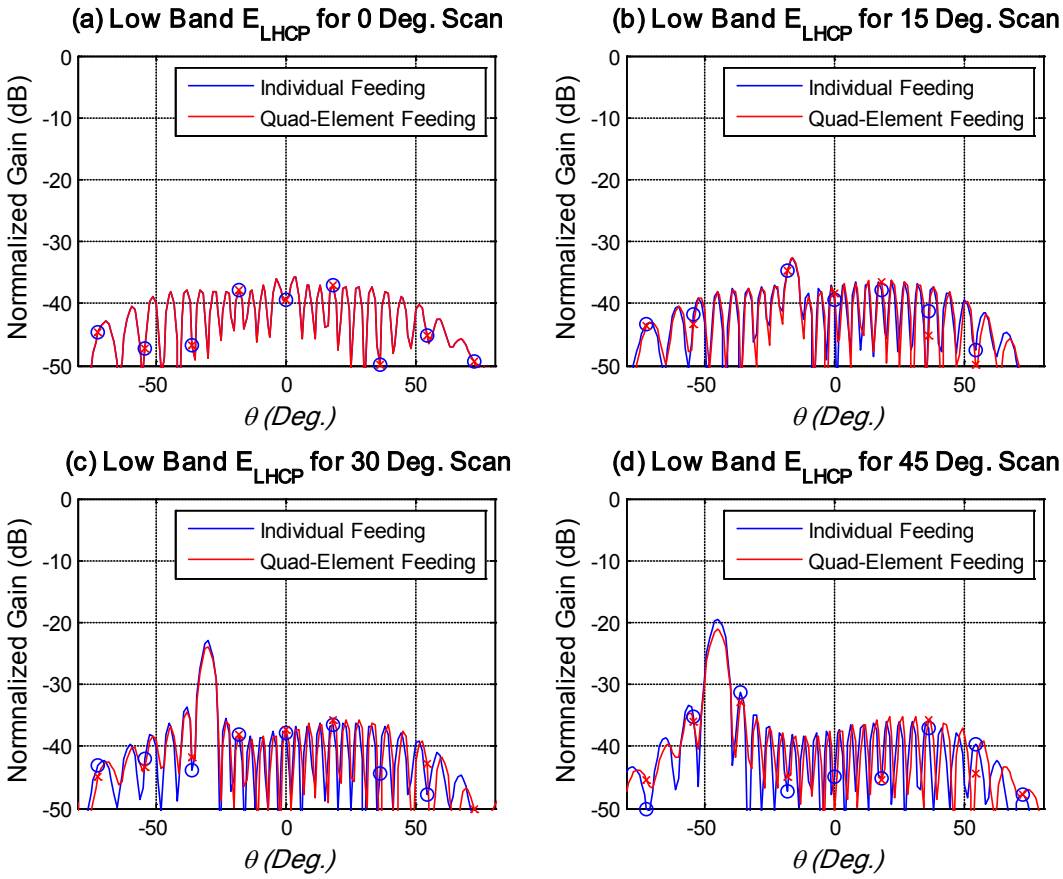
(a) Low Band E_LHCP for 0 Deg. Scan
(b) Low Band E_LHCP for 15 Deg. Scan
(c) Low Band E_LHCP for 30 Deg. Scan
(d) Low Band E_LHCP for 45 Deg. Scan
Individual Feeding
Quad-Element Feeding
Normalized Gain (dB)
θ (Deg.)
0
-10
-20
-30
-40
-50
-50
0
50

		θ_0=0°	θ_0=15°	θ_0=30°	θ_0=45°
3dB Beamwidth (BW_{3dB})	Ind. Feed	5°	5°	5°	6°
	Quad. Feed	5°	5°	5°	6°
	Approx.*	4.1116°	4.2567°	4.7477°	N/A
θ_{MAX}	Ind. Feed	0°	-15°	-30°	-44°
	Quad. Feed	0°	-15°	-30°	-44°
Normalized Maximum Value ($F(\theta_{MAX})_{MAX}$)	Ind. Feed	0dB	-1.0130dB	-3.2958dB	-6.2126dB
	Quad. Feed	0dB	-1.2287dB	-4.1343dB	-7.9345dB
Cross-pol. discrimination (XPD)	Ind. Feed	39.3959dB	32.5617dB	19.6964dB	13.4998dB
	Quad. Feed	39.3959dB	32.2726dB	19.7682dB	13.5090dB

Low Band RHCP φ=90°

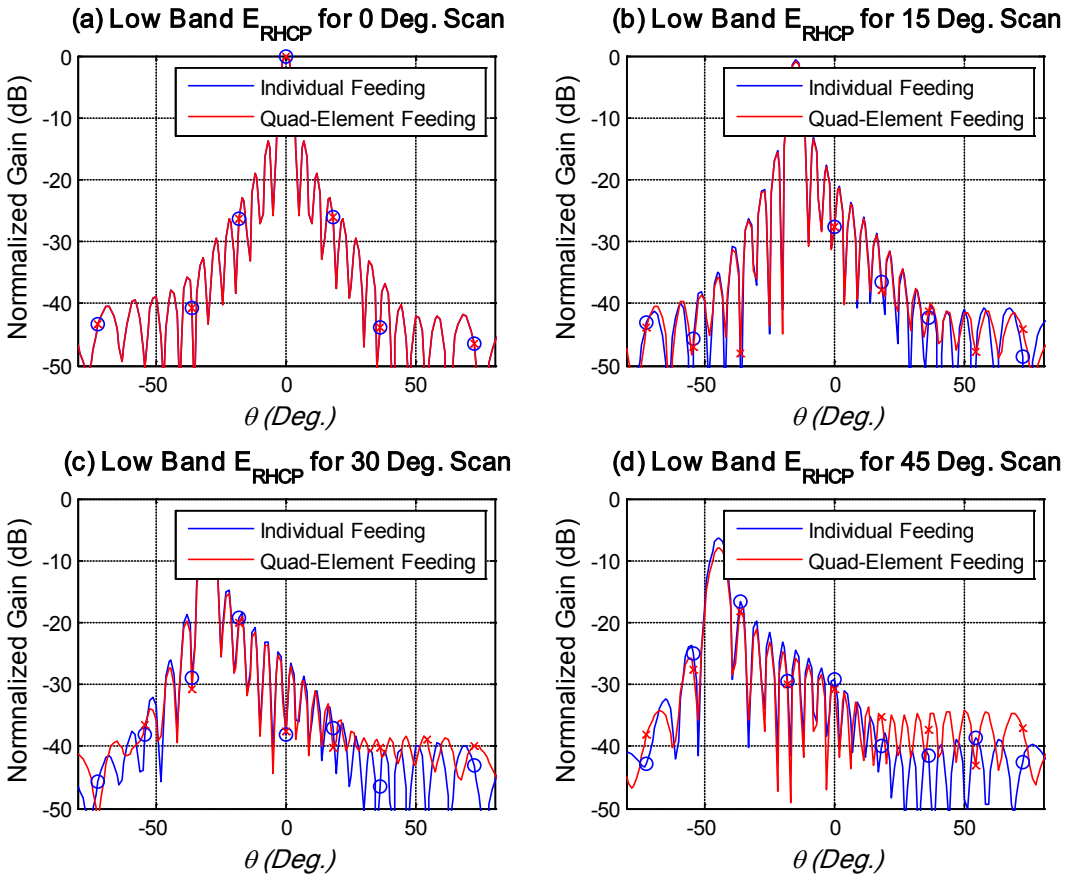

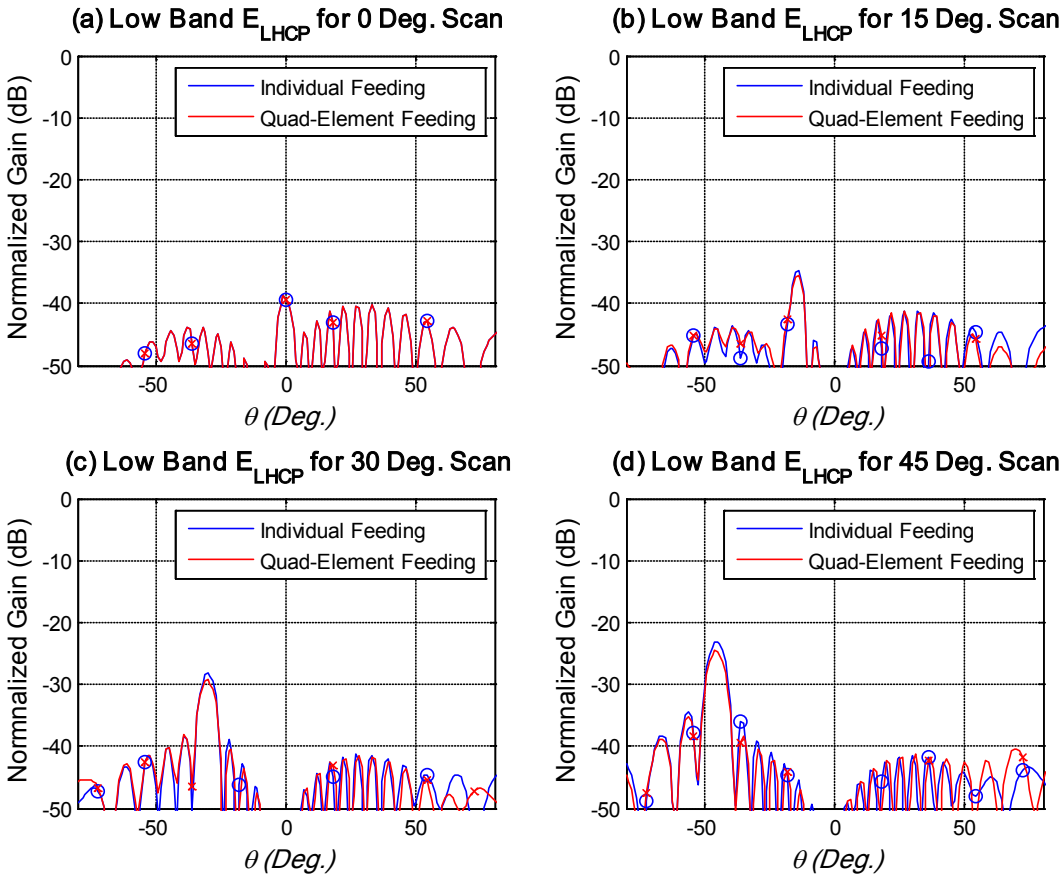
(a) Low Band E_LHCP for 0 Deg. Scan
(b) Low Band E_LHCP for 15 Deg. Scan
(c) Low Band E_LHCP for 30 Deg. Scan
(d) Low Band E_LHCP for 45 Deg. Scan
Individual Feeding
Quad-Element Feeding
Normalized Gain (dB)
θ (Deg.)
0
-10
-20
-30
-40
-50
-50
0
50

		θ_0=0°	θ_0=15°	θ_0=30°	θ_0=45°
3dB Beamwidth (BW_{3dB})	Ind. Feed	5°	5°	5°	6°
	Quad. Feed	5°	5°	5°	6°
	Approx.*	4.1116°	4.2567°	4.7477°	N/A
θ_{MAX}	Ind. Feed	0°	-15°	-30°	-44°
	Quad. Feed	0°	-15°	-30°	-44°
Normalized Maximum Value ($F(\theta_{MAX})_{MAX}$)	Ind. Feed	0dB	-0.7094dB	-2.9917dB	-6.3323dB
	Quad. Feed	0dB	-0.9163dB	-3.7821dB	-7.1405dB
Cross-pol. discrimination (XPD)	Ind. Feed	39.3959dB	34.3332dB	25.1529dB	17.1405dB
	Quad. Feed	39.3959dB	34.7057dB	25.4894dB	17.2563dB

High Band LHCP φ=0°

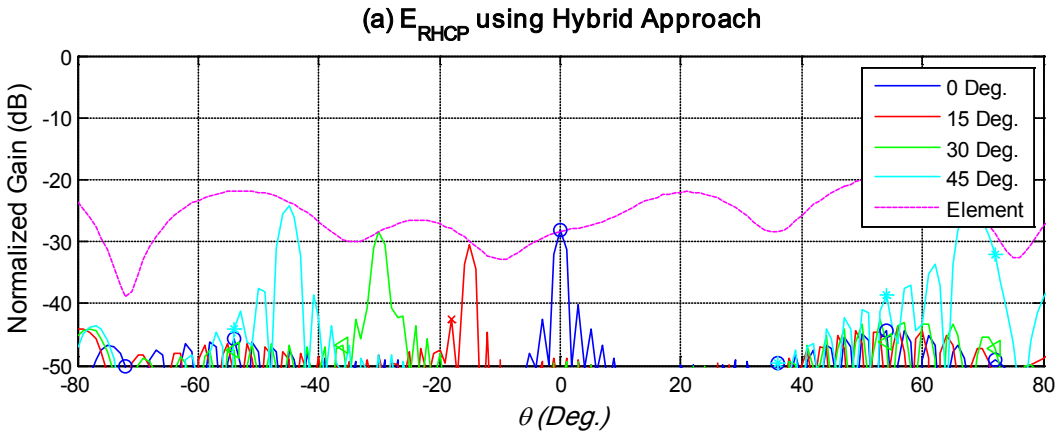

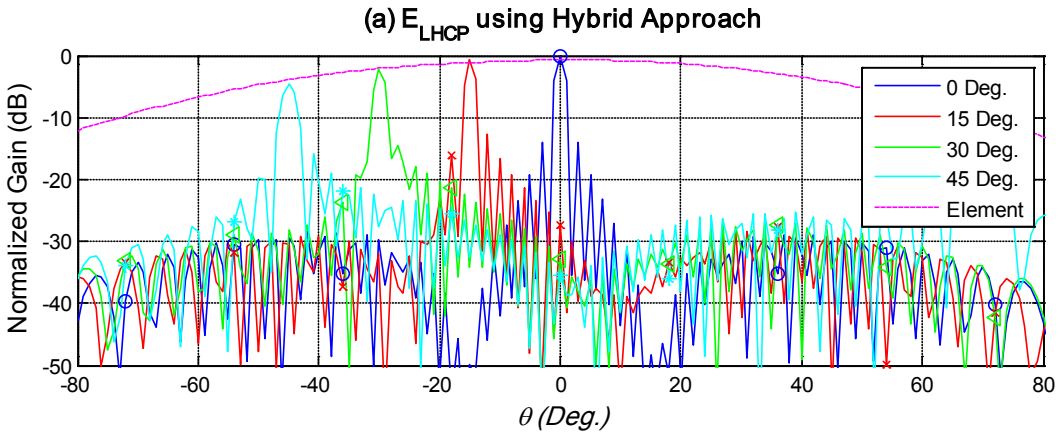

		θ_0=0°	θ_0=15°	θ_0=30°	θ_0=45°
3dB Beamwidth (BW_{3dB})	Calculated	2°	2°	2°	3°
	Approx.*	1.7368°	1.7981°	2.0055°	N/A
θ_{MAX}	Calculated	0°	-15°	-30°	-45°
Normalized Maximum Value ($F(\theta_{MAX})_{MAX}$)	Calculated	0dB	-0.7101dB	-2.3196dB	-4.5642dB
Cross-pol. discrimination (XPD)	Calculated	28.1364dB	29.6973dB	26.1502dB	19.6024dB

High Band LHCP φ=90°

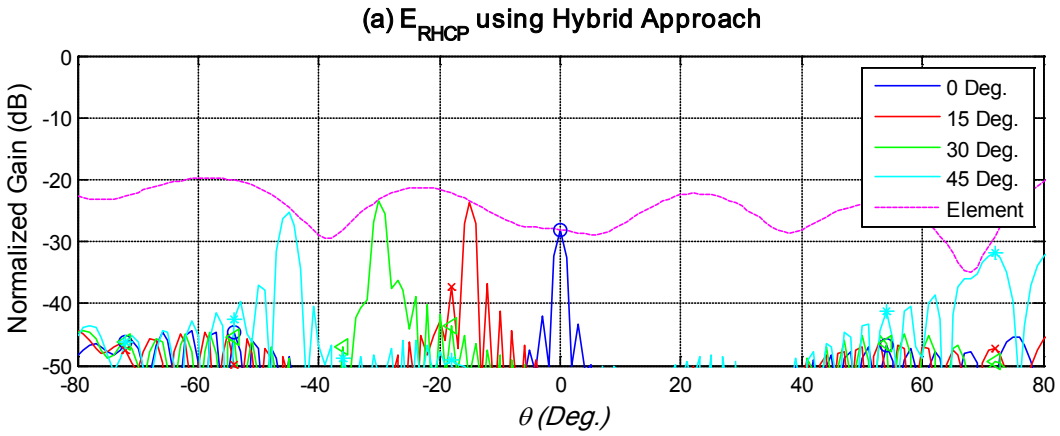

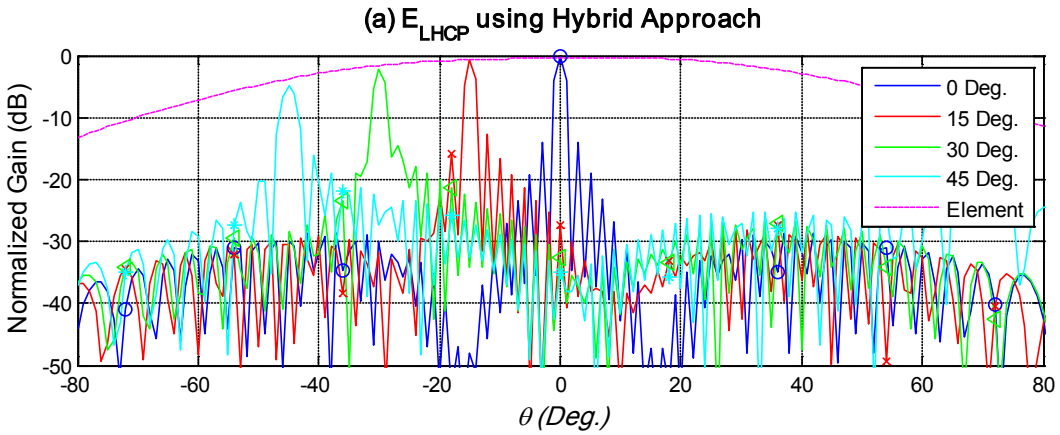

		θ_0=0°	θ_0=15°	θ_0=30°	θ_0=45°
3dB Beamwidth (BW_{3dB})	Calculated	2°	2°	2°	3°
	Approx.*	1.7368°	1.7981°	2.0055°	N/A
θ_{MAX}	Calculated	0°	-15°	-30°	-45°
Normalized Maximum Value ($F(\theta_{MAX})_{MAX}$)	Calculated	0dB	-0.6191dB	-2.1533dB	-4.8102dB
Cross-pol. discrimination (XPD)	Calculated	28.1364dB	23.0574dB	21.3860dB	20.4223dB

High Band RHCP φ=0°

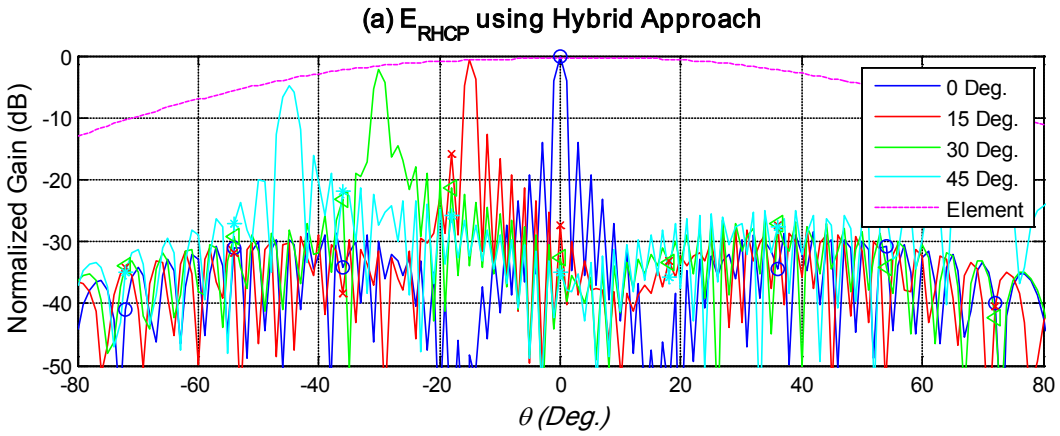

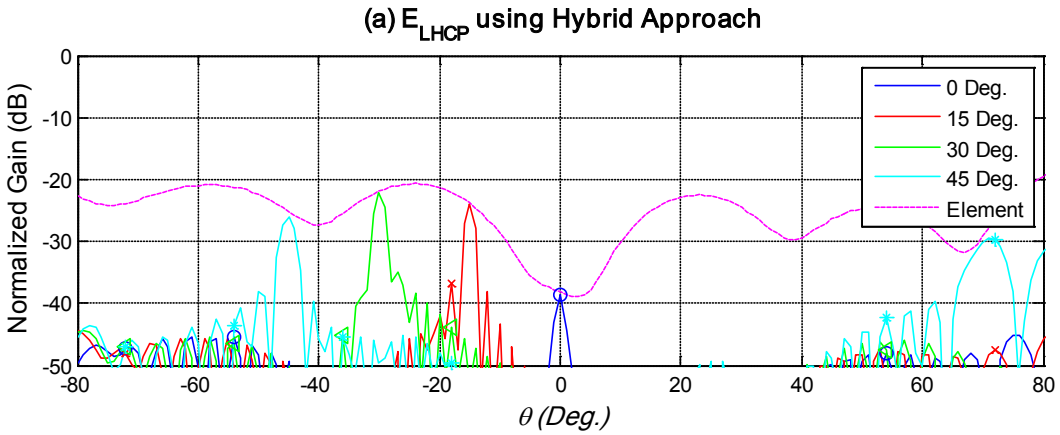

		θ_0=0°	θ_0=15°	θ_0=30°	θ_0=45°
3dB Beamwidth (BW_{3dB})	Calculated	2°	2°	2°	3°
	Approx.*	1.7368°	1.7981°	2.0055°	N/A
θ_{MAX}	Calculated	0°	-15°	-30°	-45°
Normalized Maximum Value ($F(\theta_{MAX})_{MAX}$)	Calculated	0dB	-0.6357dB	-2.1858dB	-4.7685dB
Cross-pol. discrimination (XPD)	Calculated	38.6918dB	23.2877dB	20.0557dB	21.2861dB

High Band RHCP φ=90°

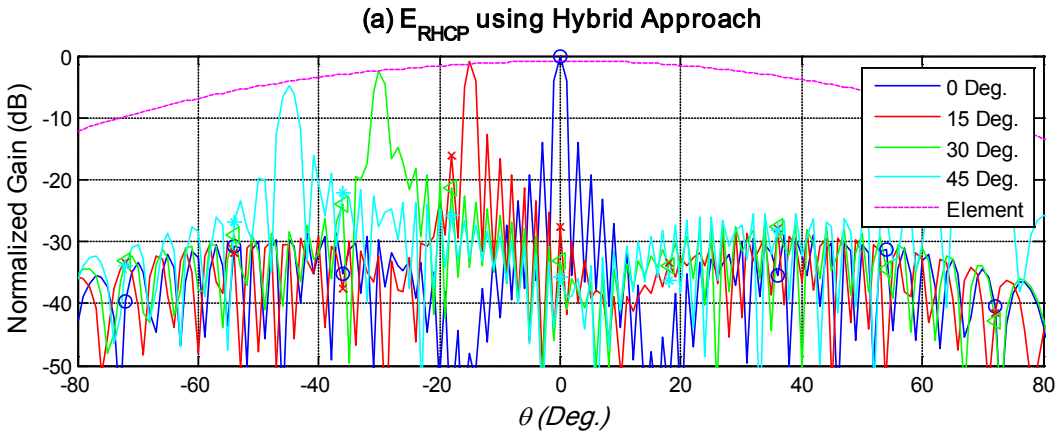

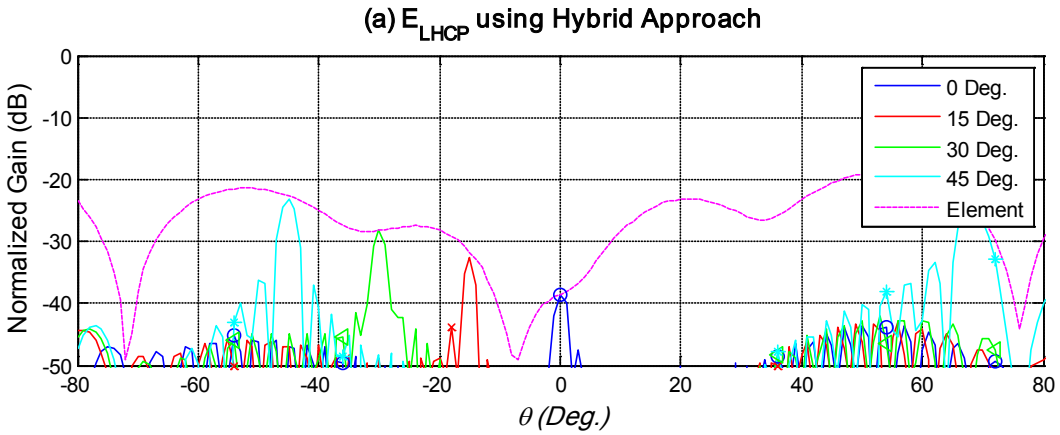

		θ_0=0°	θ_0=15°	θ_0=30°	θ_0=45°
3dB Beamwidth (BW_{3dB})	Calculated	2°	2°	2°	3°
	Approx.*	1.7368°	1.7981°	2.0055°	N/A
θ_{MAX}	Calculated	0°	-15°	-30°	-45°
Normalized Maximum Value ($F(\theta_{MAX})_{MAX}$)	Calculated	0dB	-0.7941dB	-2.5521dB	-4.7473dB
Cross-pol. discrimination (XPD)	Calculated	38.6918dB	31.6850dB	25.6196dB	18.2955dB

APPENDIX C: Active Element Patterns for 3x3 Array Simulations

The array calculation tool used in this dissertation requires the simulation of a 3x3 array to obtain the necessary active element patterns for the pattern calculation of an arbitrary array size. Each active element pattern is used to represent the pattern for elements in a specified geometrical region within the array. A comprehensive collection of the active element patterns is provided in this appendix. Refer to Chapter 4 for details.

Low Band RHCP (φ=0°)

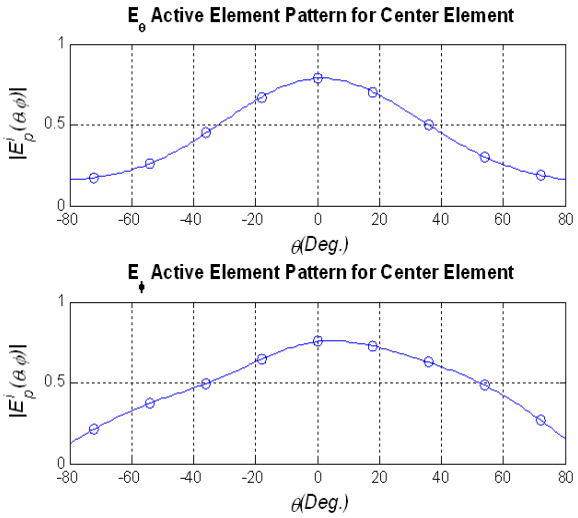

(a) Linearly polarized components of active element pattern

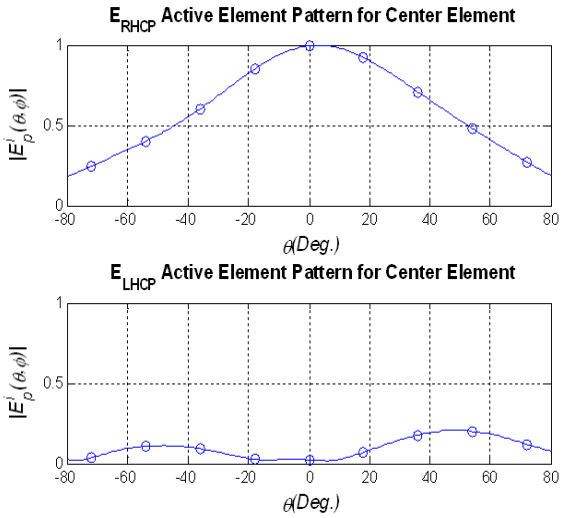

(b) Circularly polarized components of active element pattern

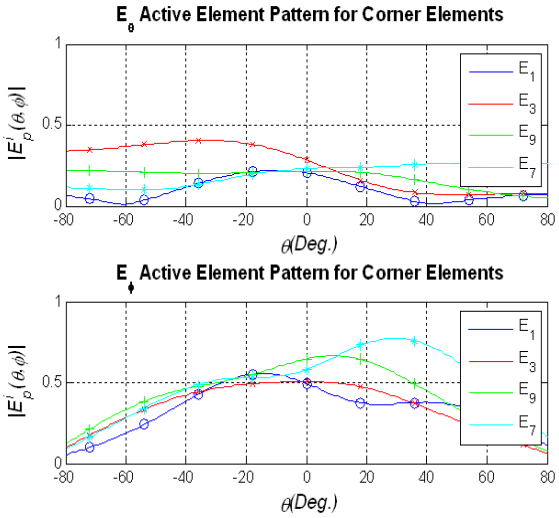

(a) Linearly polarized components of active element pattern

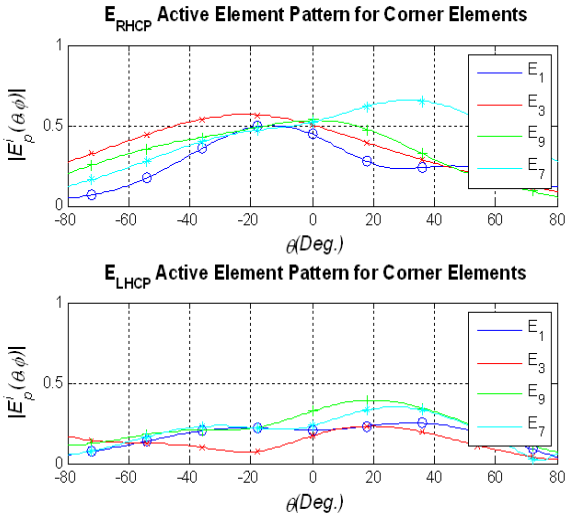

(b) Circularly polarized components of active element pattern

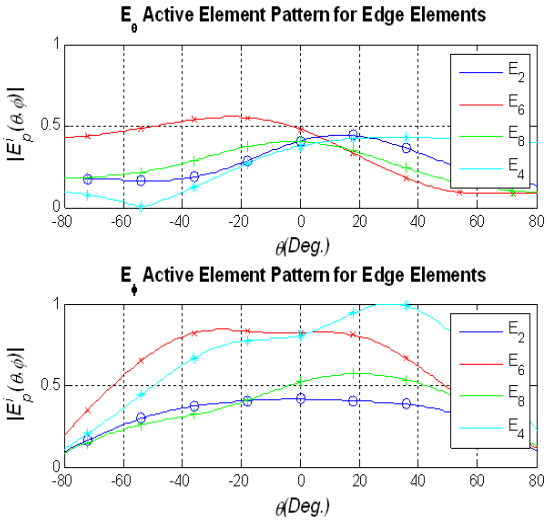

(a) Linearly polarized components of active element pattern

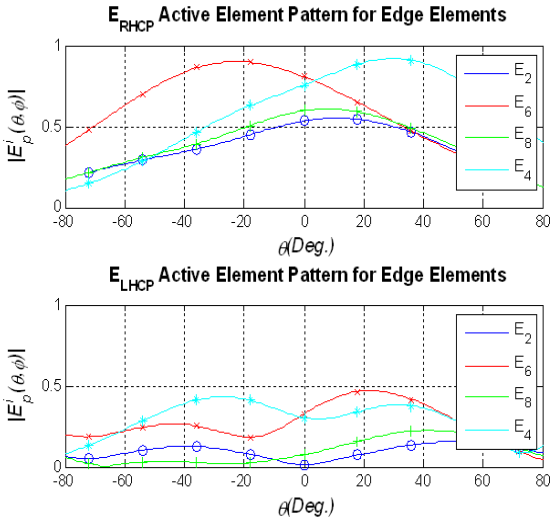

(b) Circularly polarized components of active element pattern

Low Band RHCP (φ=90°)

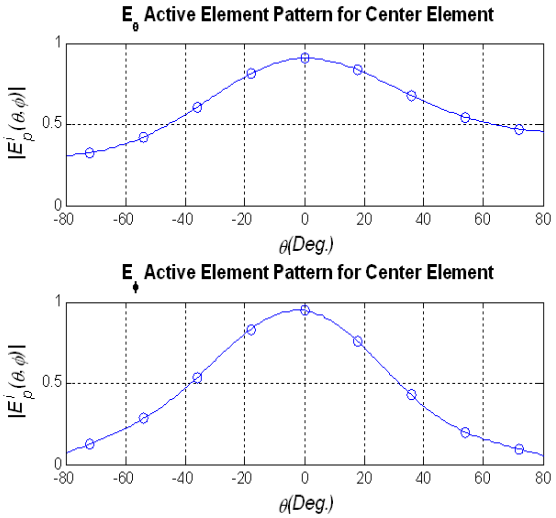

(a) Linearly polarized components of active element pattern

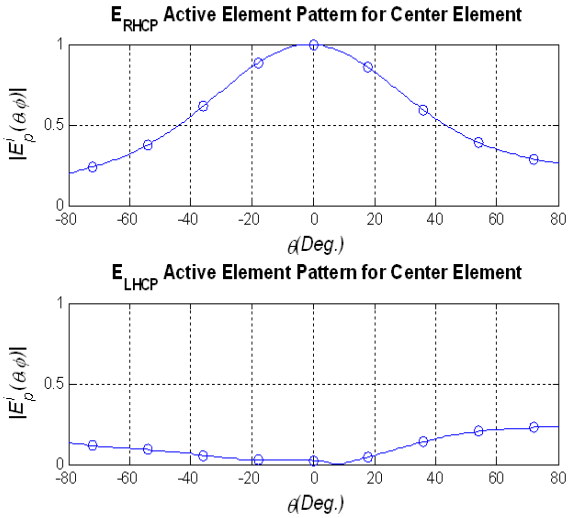

(b) Circularly polarized components of active element pattern

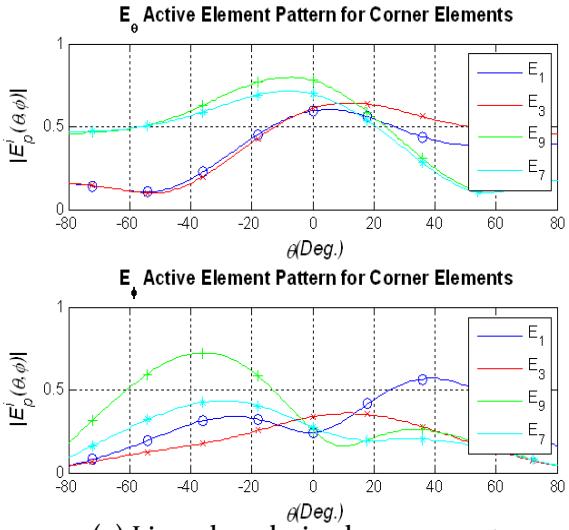

(a) Linearly polarized components of active element pattern

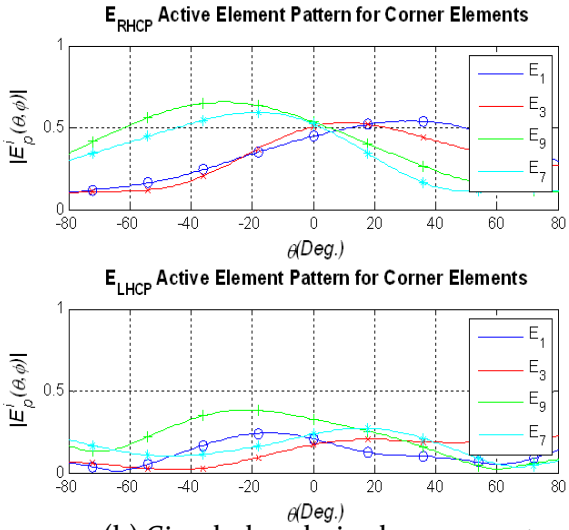

(b) Circularly polarized components of active element pattern

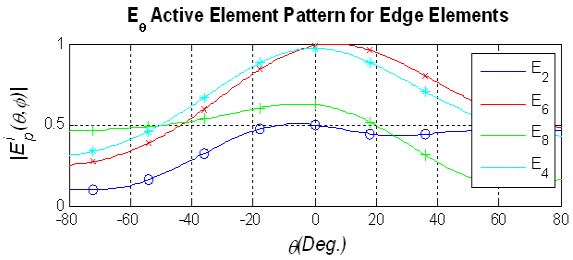

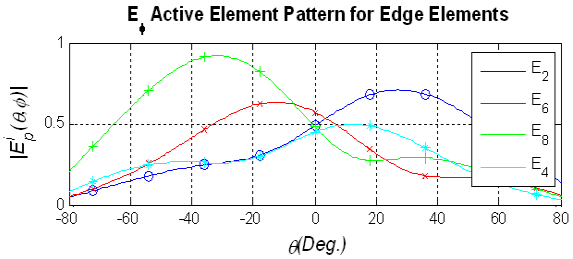

(a) Linearly polarized components of active element pattern

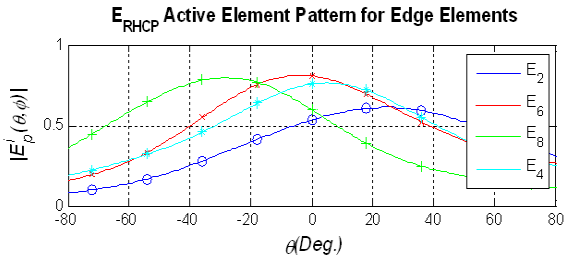

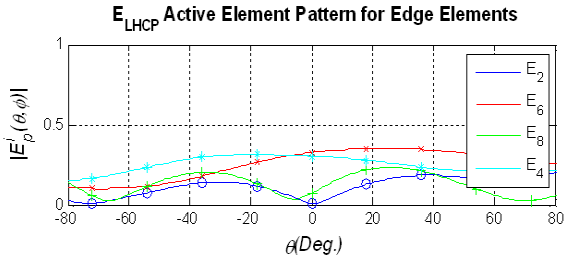

(b) Circularly polarized components of active element pattern

Low Band LHCP (φ=0°)

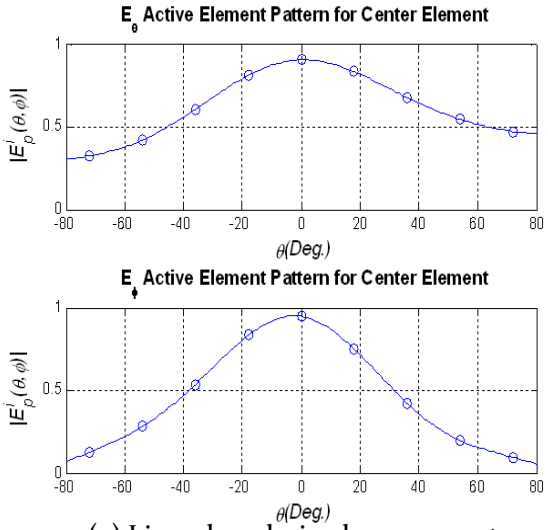

(a) Linearly polarized components of active element pattern

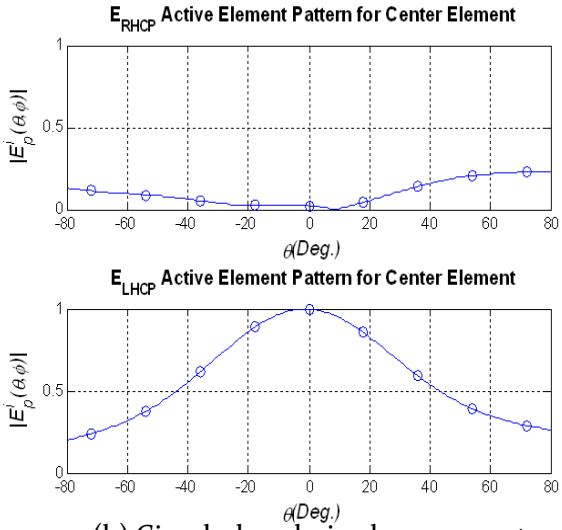

(b) Circularly polarized components of active element pattern

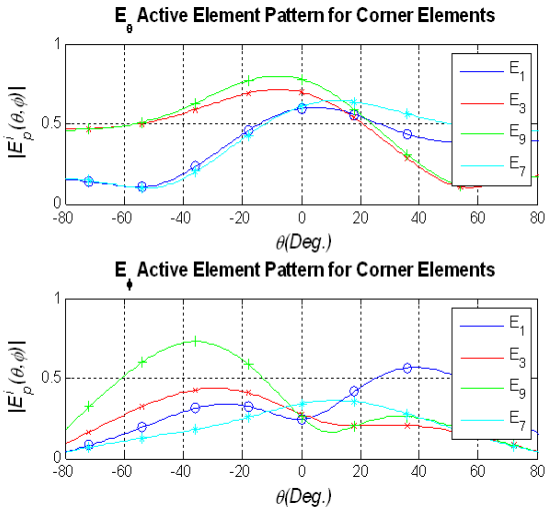

(a) Linearly polarized components of active element pattern

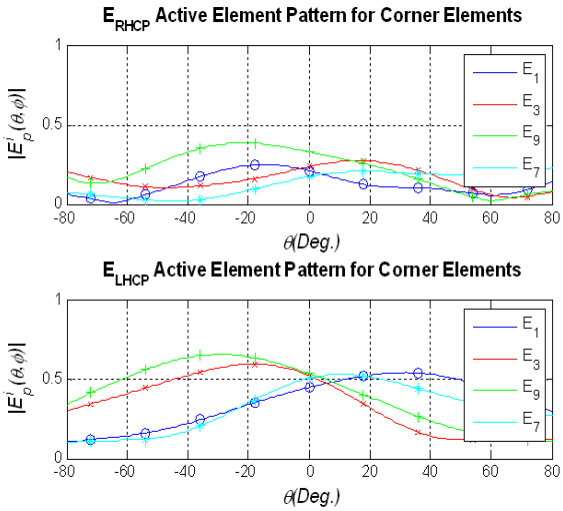

(b) Circularly polarized components of active element pattern

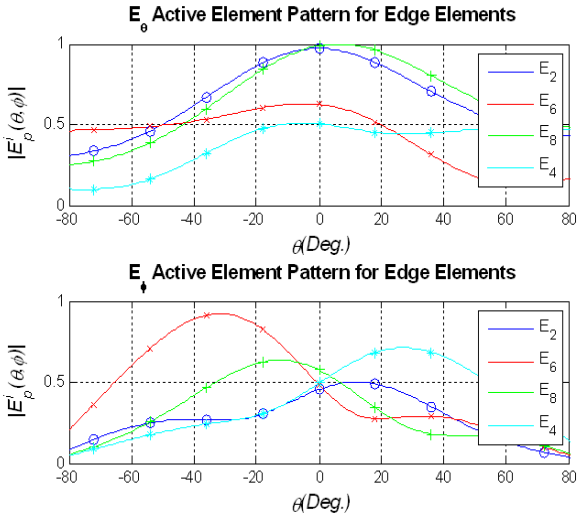

(a) Linearly polarized components of active element pattern

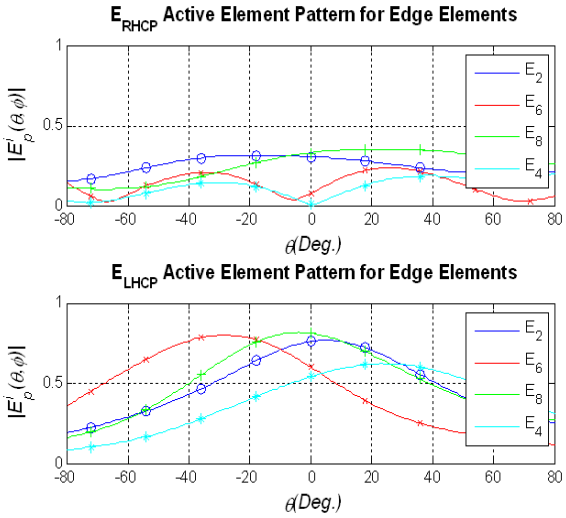

(b) Circularly polarized components of active element pattern

Low Band LHCP (φ=90°)

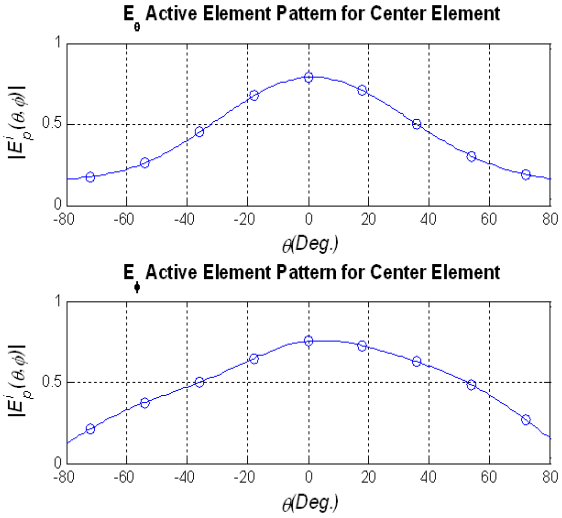

(a) Linearly polarized components of active element pattern

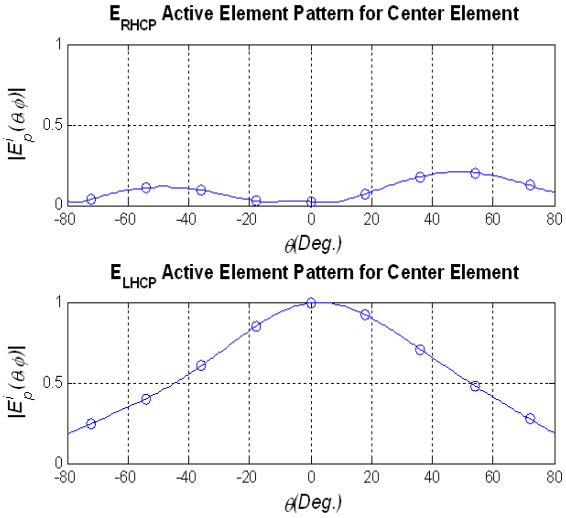

(b) Circularly polarized components of active element pattern

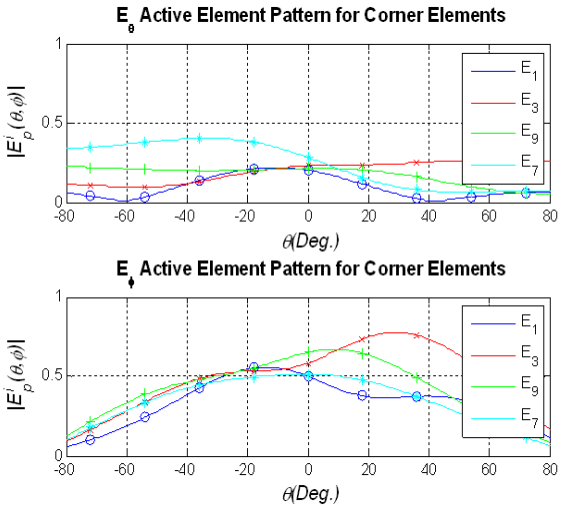

(a) Linearly polarized components of active element pattern

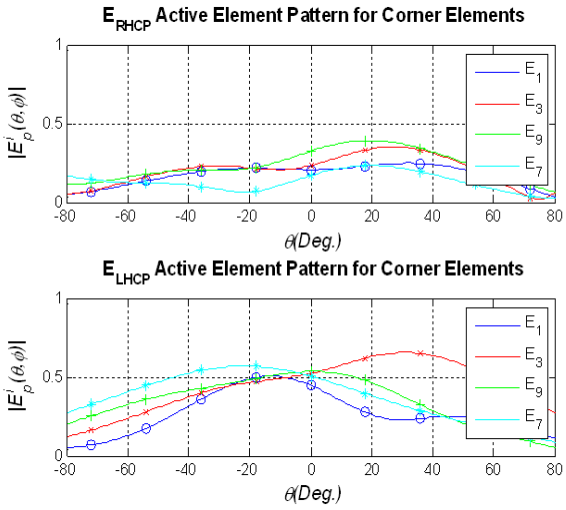

(b) Circularly polarized components of active element pattern

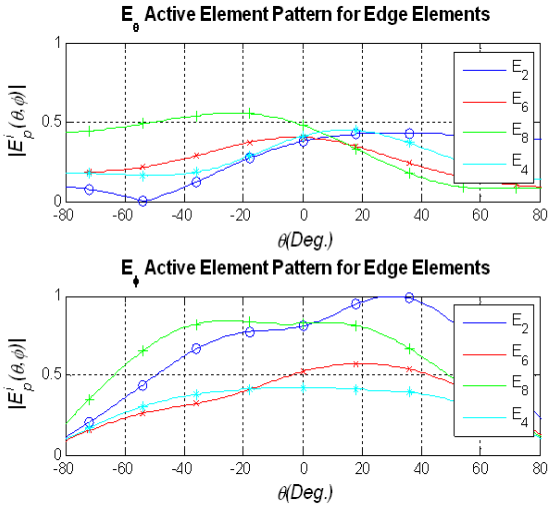

(a) Linearly polarized components of active element pattern

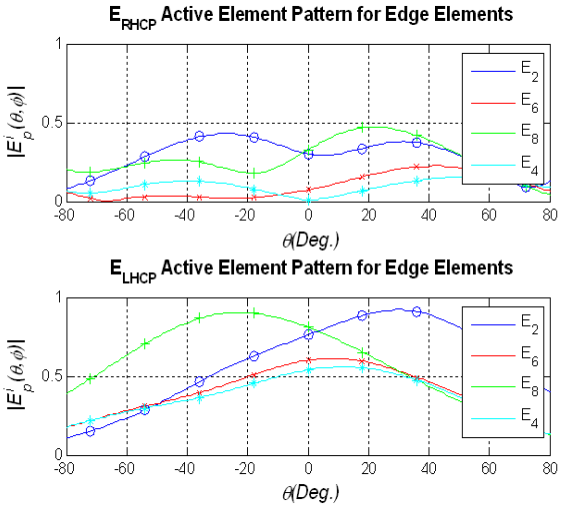

(b) Circularly polarized components of active element pattern

High Band RHCP (φ=0°)

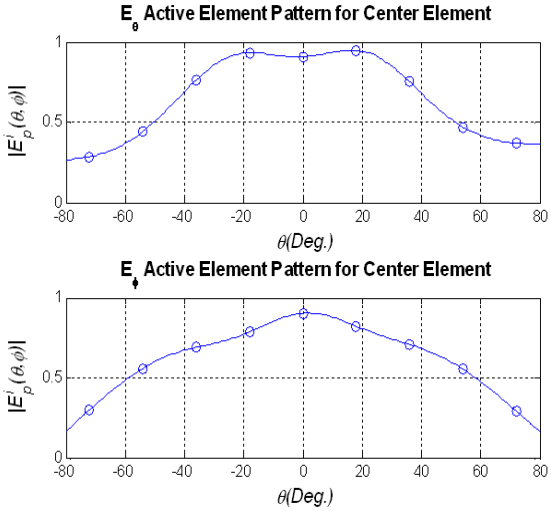

(a) Linearly polarized components of active element pattern

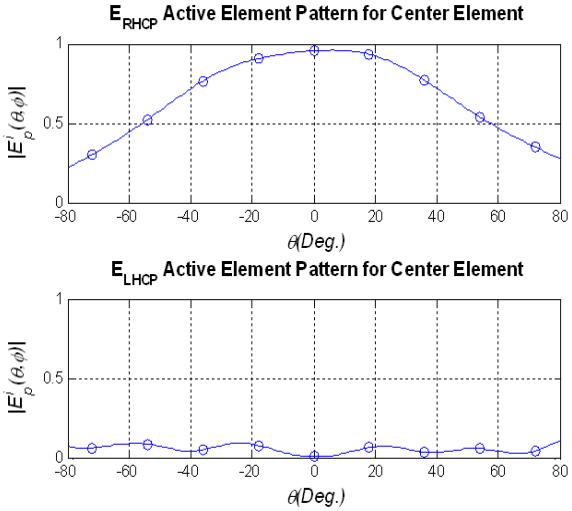

(b) Circularly polarized components of active element pattern

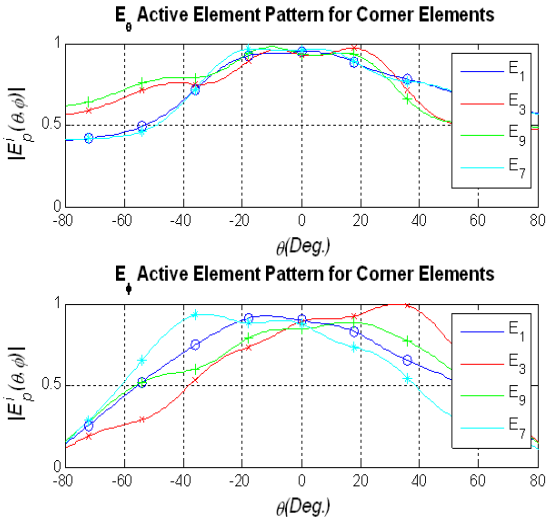

(a) Linearly polarized components of active element pattern

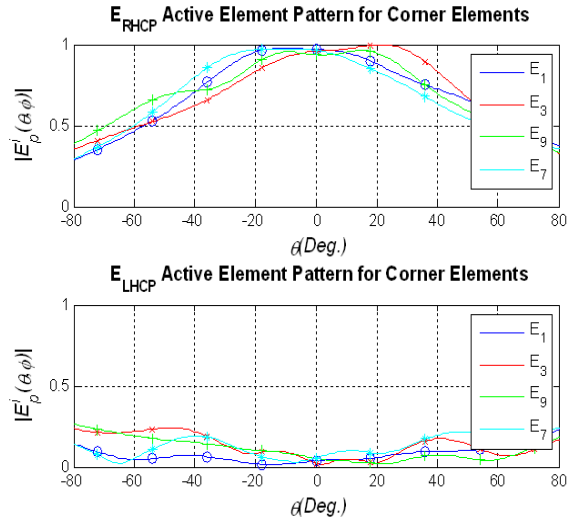

(b) Circularly polarized components of active element pattern

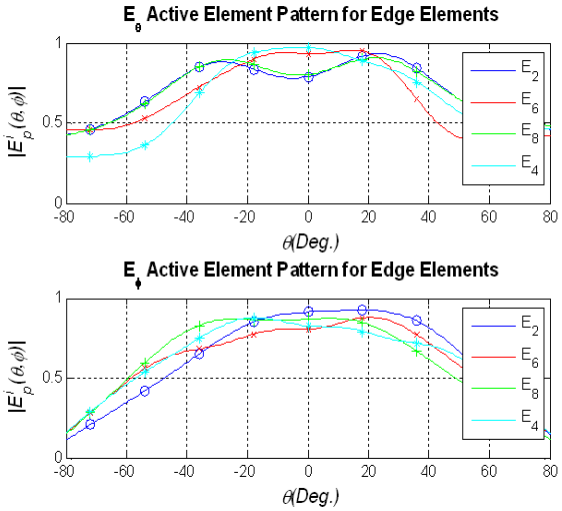

(a) Linearly polarized components of active element pattern

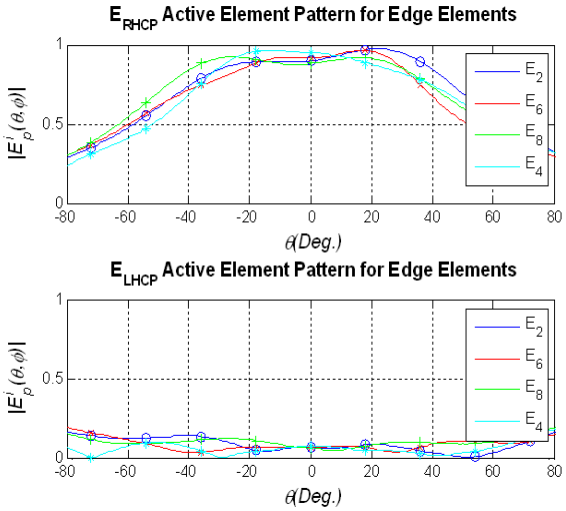

(b) Circularly polarized components of active element pattern

High Band RHCP (φ=90°)

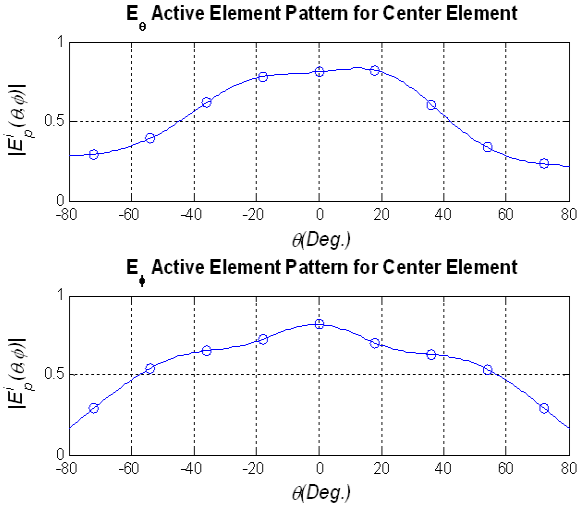

(a) Linearly polarized components of active element pattern

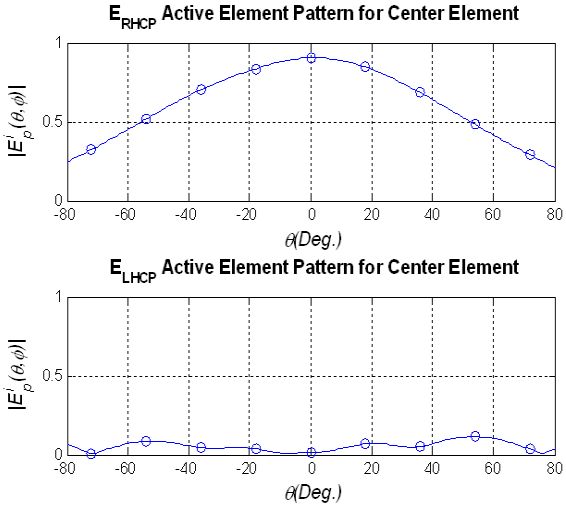

(b) Circularly polarized components of active element pattern

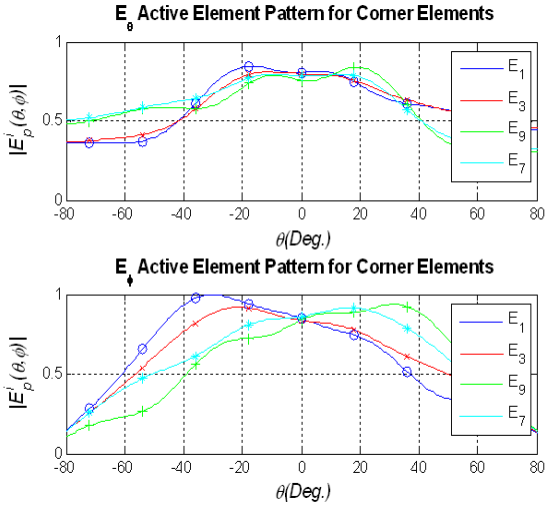

(a) Linearly polarized components of active element pattern

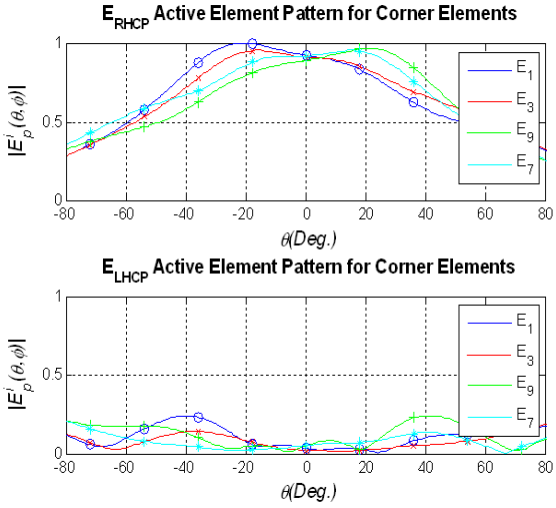

(b) Circularly polarized components of active element pattern

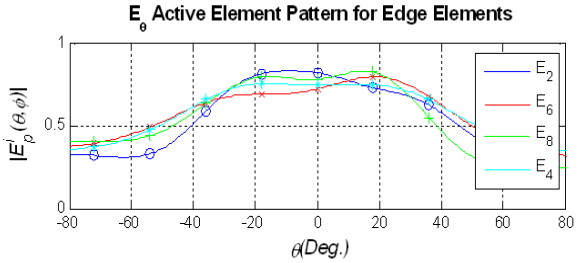

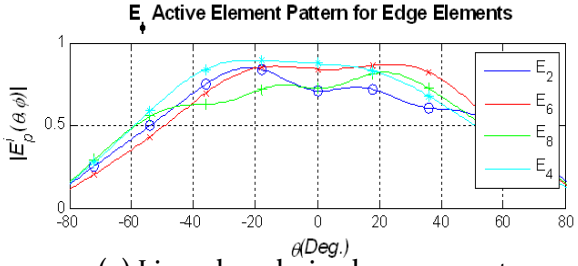

(a) Linearly polarized components of active element pattern

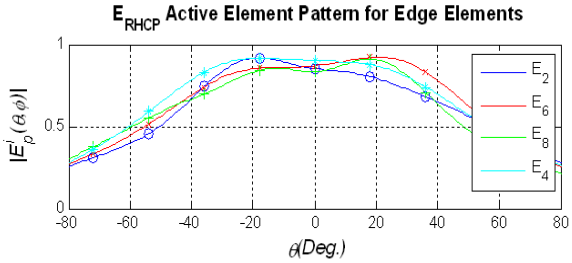

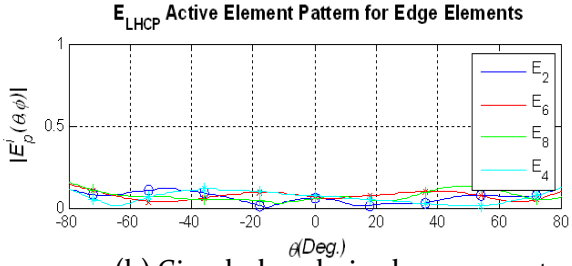

(b) Circularly polarized components of active element pattern

High Band LHCP (φ=0°)

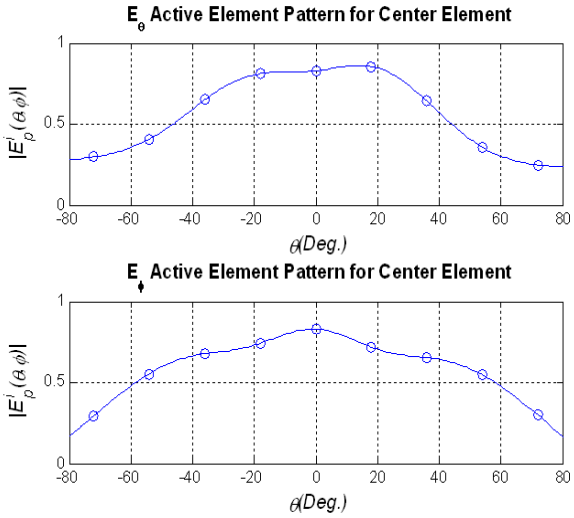

(a) Linearly polarized components of active element pattern

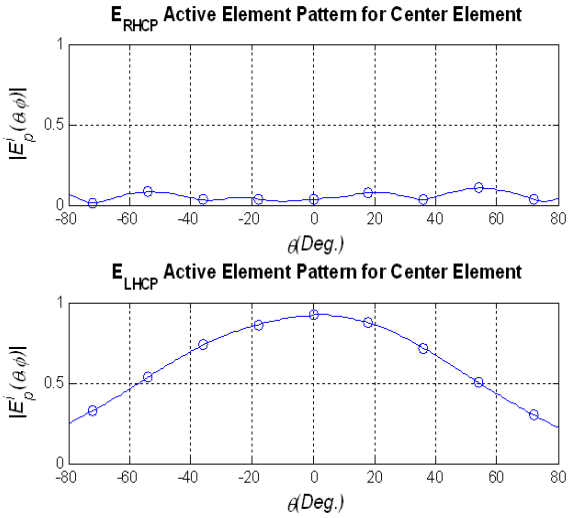

(b) Circularly polarized components of active element pattern

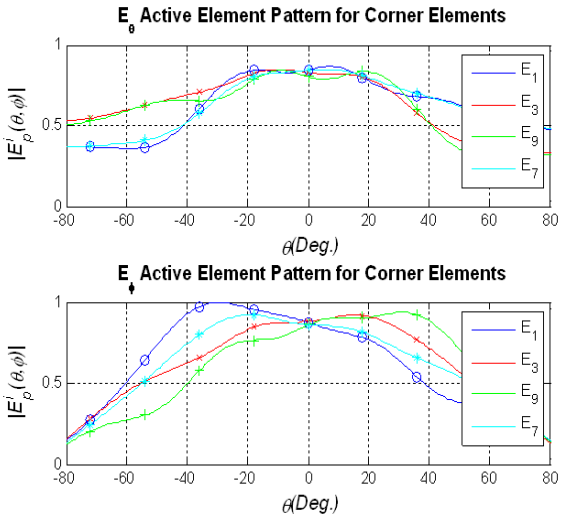

(a) Linearly polarized components of active element pattern

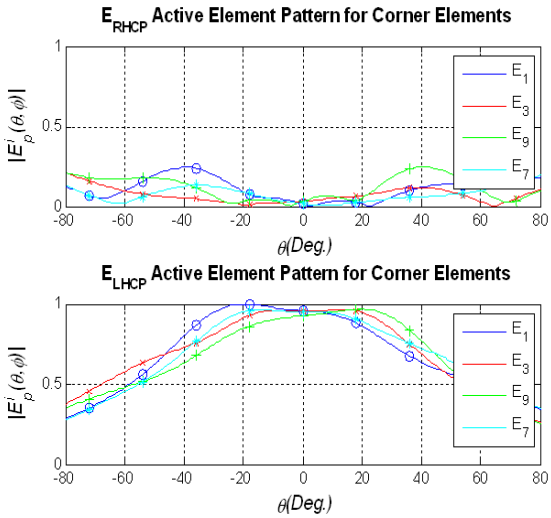

(b) Circularly polarized components of active element pattern

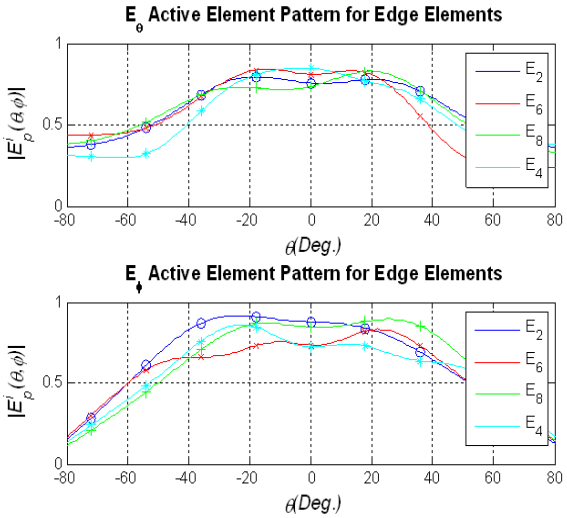

(a) Linearly polarized components of active element pattern

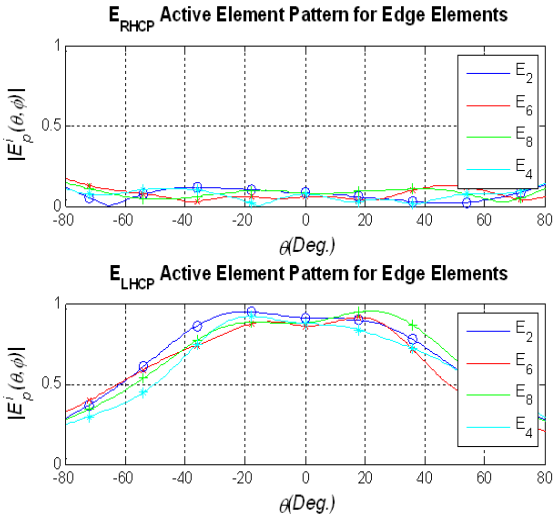

(b) Circularly polarized components of active element pattern

High Band LHCP (φ=90°)

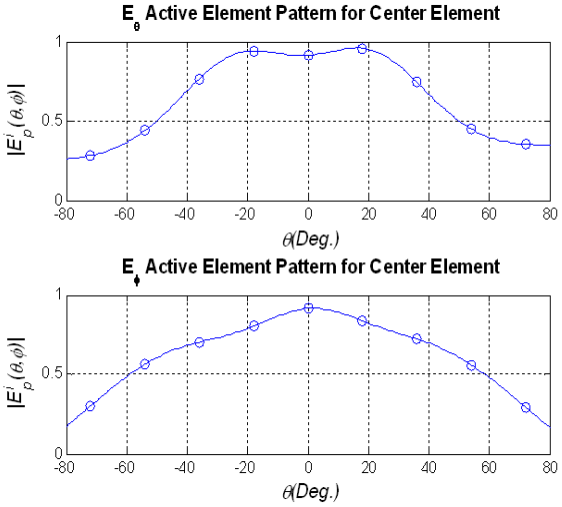

(a) Linearly polarized components of active element pattern

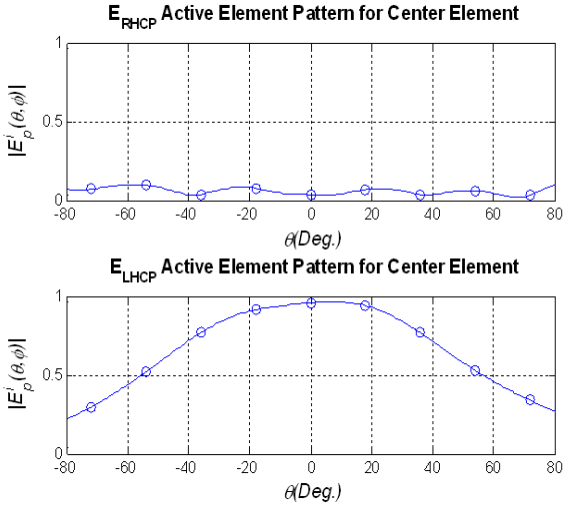

(b) Circularly polarized components of active element pattern

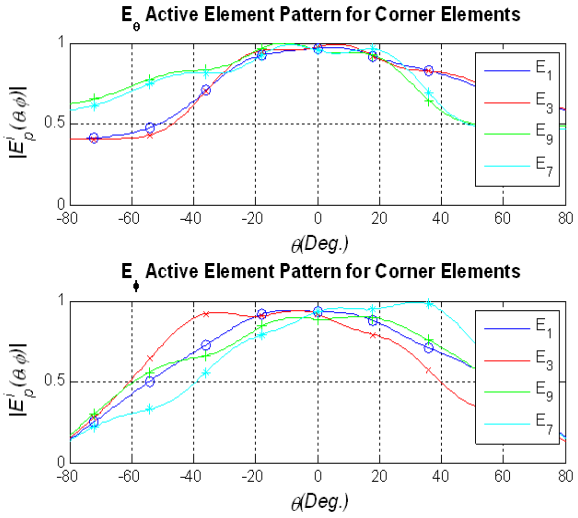

(a) Linearly polarized components of active element pattern

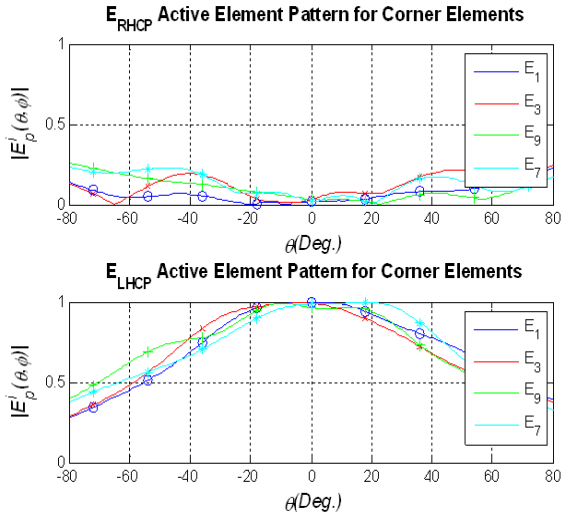

(b) Circularly polarized components of active element pattern

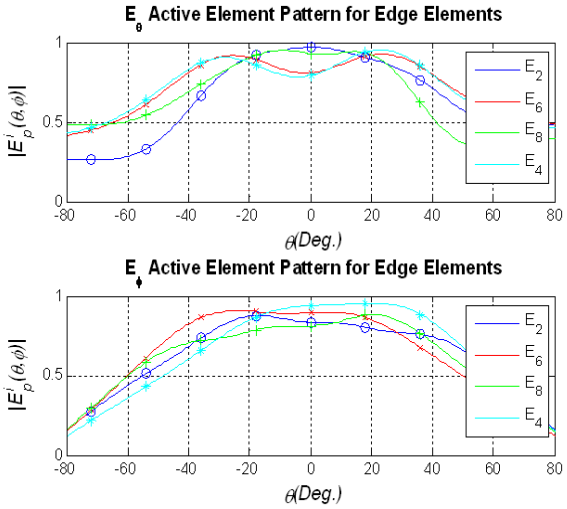

(a) Linearly polarized components of active element pattern

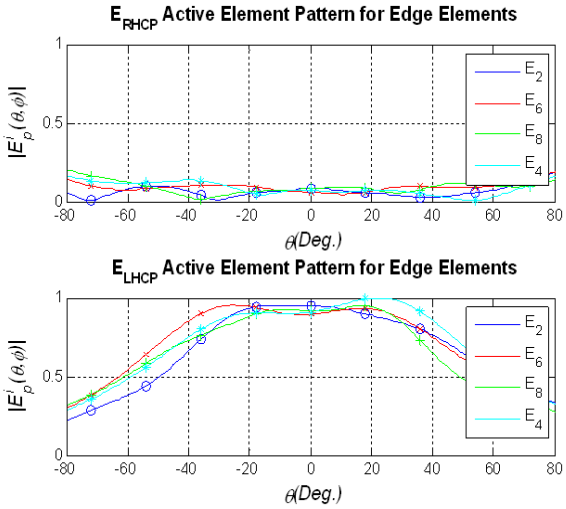

(b) Circularly polarized components of active element pattern

PUBLICATIONS LIST

Journal Articles

1. Dorsey, W. Mark; Zaghloul, Amir I.; "Dual-Substrate Capacitive Loading for Size Reduction in Shorted Annular Ring Antennas", Accepted to IEEE Transactions on Antennas and Propagation.
2. Dorsey, W. Mark; Zaghloul, Amir I.; Dorsey, "Perturbed Square Ring Slot with Reconfigurable Polarization", Accepted to IEEE Letters on Antennas and Wireless Propagation.
3. Dorsey, W. Mark; Zaghloul, Amir I.; "Dual-Band, Dual-Circularly Polarized Antenna Element for ISM Band Applications", in progress.
4. Dorsey, W. Mark; Zaghloul, Amir I.; "Dual-Band, Dual-Circularly Polarized Phased Array for Wide Scan Angle Applications", in progress.

Refereed Conference Papers

1. Dorsey, W. Mark; Zaghloul, Amir I.; "Size Reduction and Bandwidth Enhancement of Shorted Annular Ring (SAR) Antenna", *IEEE International Symposium on Antennas and Propagation*, pp. 897-900, Honolulu, Hawaii, 9-15 June 2007.
2. Zaghloul, Amir I.; Dorsey, W. Mark .; "Dual-Band Reduced-Size Circularly-Polarized Co-Planar Printed-Circuit Antenna Element", *URSI 2007*, Ottawa, ON, Canada July 2007.
3. Dorsey, W. Mark; Valenzi, John A.; Zaghloul, Amir I.; " Dual-Substrate Capacitive Loading Technique in Linearly and Circulary Polarized Annular Ring Antennas", *2007 Antenna Applications Symposium*, Monticello, Il, September 2007.
4. Dorsey, W. Mark; Zaghloul, Amir I.; Parent, Mark G.; "Perturbed Square Ring Slot with Reconfigurable Polarization", *IEEE International Symposium on Antennas and Propagation*, San Diego, CA, July 2008.
5. Dorsey, W. Mark; Zaghloul, Amir I.; "Dual-Polarized Dual-Band Antenna Element for ISM Band Application", *IEEE International Symposium on Antennas and Propagation*, Charleston, SC, June 2009.
6. Zaghloul, Amir I.; Dorsey, W. Mark .; "Evolutionary Development of A Dual-Band, Dual-Polarization, Low-Profile Printed Circuit Antenna," Invited Paper, International Conference on Electromagnetics in Advanced Applications (ICEAA), Torino, Italy, September 2009.

Invention Disclosures

1. Dorsey, W. Mark; Zaghloul, Amir I.; "Dual-Substrate Capacitive Loading Technique and Bandwidth Enhancement in Linearly and Circularly Polarized Shorted Annular Ring Antennas", February 1, 2007, Navy Case Number 98,610.
2. Dorsey, W. Mark; Zaghloul, Amir I.; Parent, Mark G.; "Perturbed Square Ring Slot Antenna with Reconfigurable Polarization", February 20, 2008, Navy Case Number 99,108.
3. Zaghloul, Amir I.; Dorsey, W. Mark; "Low-Profile, Printed Circuit Antenna Element with Dual-Polarization at Dual-Frequency Bands and Array Application", October 15, 2008.

NRL Memorandum Reports

1. Dorsey, W. Mark; Zaghloul, Amir I.; "Dual-Band Array Calculations Using Hybrid Approach", Naval Research Laboratory Memorandum Report, February 2009.